Modeling and inversion of seismic data using multiple scattering, renormalization and homotopy methods

Xingguo Huang

Thesis for the degree of Philosophiae Doctor (PhD)
University of Bergen, Norway
2020

UNIVERSITY OF BERGEN

Modeling and inversion of seismic data using multiple scattering, renormalization and homotopy methods

Xingguo Huang

Thesis for the degree of Philosophiae Doctor (PhD)
at the University of Bergen

Date of defense: 14.05.2020

Year: 2020

Title: Modeling and inversion of seismic data using multiple scattering, renormalization and homotopy methods

Name: Xingguo Huang

Print: Skipnes Kommunikasjon / University of Bergen

Scientific environment

The author has carried out the research reported in this dissertation at the Department of Earth Sciences, University of Bergen, Norway, at University of California, Santa Cruz, Earth and Planetary Sciences, Modeling and Imaging Laboratory, USA and at NORCE Norwegian Research Centre, Bergen, Norway.

Main supervisor: Prof. Morten Jakobsen (UiB).

Co-supervisors: Dr. Geir Nævdal (NORCE), Dr. Kjersti Solberg Eikrem (NORCE).

This research has received support from the Research Council of Norway for the Petromaks II project 267769/E3 (Bayesian inversion of 4D seismic waveform data for quantitative integration with production data).

Acknowledgements

When starting to write my PhD thesis and looking back to the past two and half years of my PhD studies, I realize that it would not have been possible to finish my PhD without the help of many friends and colleagues.

Firstly, I would like to express my deepest gratitude to my supervisor Morten Jakobsen, for giving me the opportunity to pursue PhD studies at University of Bergen and collaboration research at University of California, Santa Cruz, and for guiding me throughout the PhD studies. I would say I am lucky to meet such a supervisor. Morten is very clever and nice supervisor, who is not only my supervisor but also my good friend, helping me from work to life. My words cannot express how blessed I am your PhD student.

I am grateful to Ru-Shan Wu, Stewart Greenhalgh, Einar Iversen, Geir Nævdal, Kjersti Solberg Eikrem and Xiao-bi Xie at UC Santa Cruz, ETH Zürich, UiB and NORCE for supporting me during my studies. When I had a weekly meeting at NORCE, I learned from Geir and Kjersti for Bayesian inversion, they gave me valuable expertise, suggestions and ideas for the PhD project work. Without their kind help, I cannot finish this thesis. Ru-Shan always gave me insightful suggestions and comments for the research work from his strong theoretical background. Stewart has been always giving me unconditional support in the past few years, especially in my hard time and helping me improving the papers. I enjoy the lunch time with Einar, a really nice person, we came closest to discussing the ray theory and become good friends. He always gave me kind help and unconditional support in my PhD studies. When I stayed at UCSC, Xiao-Bi gave me a lot of support and useful discussion. All of them gave me strong support and recommendation in my job searching.

Thanks a lot Malte Sommer, Ole Meyer, Kui Xiang, Bjørn Burr Nyberg, Vilde Dimmen, Johannes Wiest,Tore Aadland and Nuno Vieira da Silva, I am grateful for our conversations, your advice and your kind help. My colleagues and friends at University of Bergen made my life and stay smooth and I thank all of you. Thanks Nuno, your inputs for my papers improved the work significantly. A long stay at UC Santa Cruz made me learn a lot. There are a group of people from different geophysical background, which really contributed to my PhD research work. The colleagues in the group helped me a lot.

The unconditional love and support of my wife Shaoyue kept me going through both the happy and sad times. You are intelligent, generous, I know how much effort you've made to your career, and how you are valued at your job. But for family reason, you also have the courage to come to my side and try new work. It's the love and care you've given me for the past 7 years, that have helped me finish the PhD studies. Special thanks to my parents in law, my parents and my brother, you always support me unconditionally during my PhD studies. Unfortunately, there is no enough space to thank all my friends, but that doesn't mean I forget your help to me.

Abstract

Seismic scattering theory plays an important role in seismic forward modeling and is the theoretical foundation for various seismic imaging methods. Full waveform inversion is a powerful technique for obtaining a high-resolution model of the subsurface. One objective of this thesis is to develop convergent scattering series solutions of the Lippmann-Schwinger equation in strongly scattering media using renormalization and homotopy methods. Other objectives of this thesis are to develop efficient full waveform inversion methods of time-lapse seismic data and, to investigate uncertainty quantification in full waveform inversion for anisotropic elastic media based on integral equation approaches and the iterated extended Kalman filter.

The conventional Born scattering series is obtained by expanding the Lippmann-Schwinger equation in terms of an iterative solution based on perturbation theory. Such an expansion assumes weak scattering and may have the problems of convergence in strongly scattering media. This thesis presents two scattering series, referred to as convergent Born series (CBS) and homotopy analysis method (HAM) scattering series for frequency-domain seismic wave modeling. For the convergent Born series, a physical interpretation from the renormalization prospective is given. The homotopy scattering series is derived by using homotopy analysis method, which is based on a convergence control parameter (h) and a convergence control operator (H) that one can use to ensure convergence for strongly scattering media. The homotopy scattering scattering series solutions of the Lippmann-Schwinger equation, which is convergent in strongly scattering media. The homotopy scattering series is a kind of unified scattering series theory that includes the conventional and convergent Born series as special cases. The Fast Fourier Transform (FFT) is employed for efficient implementation of matrix-vector multiplication for the convergent Born series and the homotopy scattering series.

This thesis presents homotopy methods for ray based seismic modeling in strongly anisotropic media. To overcome several limitations of small perturbations and weak anisotropy in obtaining the traveltime approximations in anisotropic media by expanding the anisotropic eikonal equation in terms of the anisotropic parameters and the elliptically anisotropic eikonal equation based on perturbation theory, this study applies the homotopy analysis method to the eikonal equation. Then this thesis presents a retrieved zero-order deformation equation that creates a map from the anisotropic eikonal equation to a linearized partial differential equation system. The new traveltime approximations are derived by using the linear and nonlinear operators in the retrieved zero-order deformation equation. Flexibility on variable anisotropy parameters is naturally incorporated into the linear differential equations, allowing a medium of arbitrarily anisotropy.

This thesis investigates efficient target-oriented inversion strategies for improving full waveform inversion of time-lapse seismic data based on extending the distorted Born iterative T-matrix inverse scattering to a local inversion of a small region of interest (e. g. reservoir under production). The target-oriented approach is more efficient for inverting the monitor data. The target-oriented

inversion strategy requires properly specifying the wavefield extrapolation operators in the integral equation formulation. By employing the T-matrix and the Gaussian beam based Green's function, the wavefield extrapolation for the time-lapse inversion is performed in the baseline model from the survey surface to the target region. I demonstrate the method by presenting numerical examples illustrating the sequential and double difference strategies.

To quantify the uncertainty and multiparameter trade-off in the full waveform inversion for anisotropic elastic media, this study applies the iterated extended Kalman filter to anisotropic elastic full waveform inversion based on the integral equation method. The sensitivity matrix is an explicit representation with Green's functions based on the nonlinear inverse scattering theory. Taking the similarity of sequential strategy between the multi-scale frequency domain full waveform inversion and data assimilation with an iterated extended Kalman filter, this study applies the explicit representation of sensitivity matrix to the the framework of Bayesian inference and then estimate the uncertainties in the full waveform inversion. This thesis gives results of numerical tests with examples for anisotropic elastic media. They show that the proposed Bayesian inversion method can provide reasonable reconstruction results for the elastic coefficients of the stiffness tensor and the framework is suitable for accessing the uncertainties and analysis of parameter trade-offs.

List of papers

Paper 1. **Huang X.**, Jakobsen M., and Wu R. S. (2019). On the applicability of a renormalized Born series for seismic wave modelling in strongly scattering media. *Journal of Geophysics and Engineering*, doi:10.1093/jge/gxz105.

Paper 2. Jakobsen M., **Huang X.** and Wu R. S. (2020). Homotopy analysis of the Lippmann-Schwinger equation for seismic wavefield modeling in strongly scattering media. *Geophysical Journal International*, Minor Revision.

Paper 3. **Huang X.** and Greenhalgh S. (2019). Traveltime approximation for strongly anisotropic media using the homotopy analysis method. *Geophysical Journal International*, 216 (3): 1648-1664.

Paper 4. **Huang X.**, Jakobsen M., Eikrem K. S. and Nævdal G. (2019) Target-oriented inversion of time-lapse seismic waveform data. *Communication in Computational Physics*, doi: 10.4208/cicp.OA-2018-0143.

Paper 5. **Huang X.**, Eikrem K. S., Jakobsen M. and Nævdal G. (2020) Bayesian seismic full waveform inversion in anisotropic elastic media using an integral equation approach. *Geophysics*, in revision.

Contents

Chapter 1

Introduction

1.1 Seismic modeling

Seismic forward modeling plays an important role in seismic survey design, imaging, inversion and interpretation. The goal of seismic forward modeling is to generate the seismograms based on assumed subsurface structures. Nowadays, full waveform inversion has become a more popular technique for obtaining an accurate velocity structure of the subsurface. Seismic full waveform inversion depends on the data fitting of the recorded and modeled seismogram (Tarantola and Valette, 1982a; Tarantola, 1986). The applicability of such a technique relies on the fact that the seismograms are used for fitting based on the forward modeling. As a result, one of the challenges for seismic inversion in complex structures, e. g. salt structure, is to accurately model the seismogram.

Seismic forward modeling can be mainly divided into three categories (Carcione, 2007): direct methods (Robertsson, 1996), integral equation methods (see e. g., Zhdanov, 2002; Jakobsen and Wu, 2016; Malovichko et al., 2017; Jakobsen and Wu, 2018) and asymptotic methods (Ĉervenỳ, 2001). The direct methods use the numerical techniques, e. g. the finite difference method and finite element method, to solve the full acoustic or elastic wave equation directly. Direct methods can obtain highly accurate full wavefields and can be used for complex subsurface structures and strong velocity contrast regions. Although the approaches produce highly accurate results, the computational cost is still expensive and the memory requirements are high.

Asymptotic methods are traditional methods which are widely used for Kirchhoff and beam imaging due to their efficiency. They have well known limitation of asymptotic approximations based on ray theory rather than the full wavefields. Such methods can also identify the specific events from the seismograms whereas the direct methods just calculate the full wavefields. Ray theory based methods require an accurate computation of traveltimes. To develop efficient time-lapse inversion methods and full waveform inversion methods in anisotropic elastic media, I use the ray theory to calculate the background Green's functions in the integral equation approach. When calculating the Green's functions in the background media, computing traveltimes is very important, which ensures that the modeled waveform is not more than half a cycle out of phase with the recorded waveform. The traveltimes can be obtained by solving the eikonal equation, which is a nonlinear partial differential equation under the high frequency asymptotic ray theory assumption.

There are several approaches to solve the eikonal equation, such as ray tracing methods (see e. g., Červenỳ, 1972; Červenỳ and Pšenčík, 1983; Moser, 1991; Vinje et al., 1993; Ĉervenỳ, 2001;

Červenỳ et al., 2007; Bai et al., 2007; Iversen and Tygel, 2008; Červenỳ et al., 2012) and the finite difference method (see e. g., Vidale, 1988; Sethian and Popovici, 1999; Cao and Greenhalgh, 1994; Sethian, 1996; Rawlinson and Sambridge, 2004a,b; Noble et al., 2014). The ray tracing method computes the traveltimes by integration along rays, in which the initial condition must be specified. The main advantages include easy implementation and high efficiency. However, it gives a non-uniform distribution of traveltimes, and the presence of shadow zones can lead to problems. Moreover, due to the different directions of the group velocity (ray direction) and the phase velocity (wavefront normal direction) vectors, solving the ray tracing system becomes complicated in anisotropic media. The finite difference (FD) method has been recognized as an efficient and accurate computational scheme for calculating the traveltimes. In the framework of the FD method, two approaches, the fast marching method (Sethian, 1996; Sethian and Popovici, 1999; Alkhalifah and Fomel, 2001; Huang et al., 2016b; Huang and Sun, 2018) and the fast sweeping method (Zhao, 2005), have been widely used for calculating the traveltimes. In recent years, efforts have been made to solve the anisotropic eikonal equations (Luo and Qian, 2012; Waheed et al., 2015; Bouteiller et al., 2017; Han et al., 2017; Waheed and Alkhalifah, 2017). In addition, some interesting results for moveout approximations have been obtained based on the weak-anisotropy (WA) parameters (Pšenčík and Farra, 2017; Farra and Pšenčík, 2017). However, it is challenging to use the finite difference method to solve the eikonal equation for anisotropic media because of the additional anisotropic parameters involved. This is especially true because solving the quartic equation and finding the roots of a quartic equation at each computational step is difficult (Alkhalifah, 2011a; Stovas and Alkhalifah, 2012).

Most traveltime approximations employ perturbation theory to calculate the traveltimes in anisotropic media (Ursin, 1982; Gjøystdal et al., 1984; Červenỳ et al., 1984; Alkhalifah, 2011a,b; Červenỳ et al., 2012; Waheed et al., 2013; Iversen et al., 2018). Alkhalifah (2011a,b) derived the traveltime approximations and used them for scanning anisotropic parameters in transversely isotropic media with a vertical-symmetry axis (VTI) and transversely isotropic media with a tilted symmetry axis (TTI) media. Much work has been done along this direction of traveltime development. Even in the case of strongly anisotropic media, the perturbation theory is used. Many researchers have applied the perturbation theory and have made significant progress (Stovas and Alkhalifah, 2012; Waheed et al., 2013; Alkhalifah, 2013; Masmoudi and Alkhalifah, 2016; Xu et al., 2017). Later, this approach has been extended to an orthorhombic medium (Stovas et al., 2016) and attenuating VTI medium (Hao and Alkhalifah, 2017). Rather than calculating the real traveltimes, recently, Huang et al. (2018) used perturbation theory to calculate the omplex traveltime by solving the highly nonlinear complex eikonal equation. They successfully applied perturbation theory to the complex eikonal equations in orthorhombic and VTI media and derived a system of linear equations for the complex traveltime computation. It should be appreciated that in the derived linear system, it become possible to develop analytic solutions in an orthorhombic medium (Huang and Greenhalgh, 2018) and numerical solutions in a VTI medium (Huang et al., 2018). This approach relies on the availability of the perturbation theory with the assumption of small contrast to the complex eikonal equations in anisotropic media.

One potential weakness of the above perturbation theories is the assumption of small anisotropic parameters. This is because most of the traveltime approximations make use of a power series expansion in terms of the anisotropic parameters. When the traveltime computation is performed in strongly anisotropic media, in which the degree of anisotropy is beyond a small perturbation from the anisotropic background medium, the calculated traveltimes are no longer accurate. In such cases, overcoming the weak anisotropy assumption is necessary.

Table 1.1: Multiple scattering theory can be applied to various partial differential equations (Gonis and Butler, 2012)

Equation	$L\left\|\psi\right\rangle = -\left\|S\right\rangle$	
1	Schrödinger equation	$(-\bigtriangledown^2 + V - E)\left\|\psi\right\rangle = 0$
2	Dirac equation	$(-i\alpha \cdot \bigtriangledown + \beta + V - W)\left\|\psi\right\rangle = 0$
3	Laplace equation	$\bigtriangledown \cdot \epsilon \bigtriangledown \left\|\psi\right\rangle = 0$
4	Poisson equation	$\bigtriangledown^2 \left\|\psi\right\rangle = -4\pi\rho$
5	Debye-Huckel equation	$(-\bigtriangledown^2 + \lambda^2)\left\|\psi\right\rangle = 0$
6	Vector wave equation	$\bigtriangledown \times [\bigtriangledown \times \mathbf{E}] - \kappa^2\epsilon\left(\mathbf{r}\right)\mathbf{E} = 0$
7	Helmholtz equation	$(\bigtriangledown^2 + k^2)\left\|\psi\right\rangle = 0$

Integral equation methods are another class of seismic modeling methods (Aki, 1980; Zhdanov, 2002). An attractive feature of the integral equation method is that only the anomalous volume (scattering volume) needs to be discretized, which leads to more efficient computation (Malovichko et al., 2017). From the perspective of applicability to inversion, the integral equation approach has actually several advantages compared with the differential equation approach: (1) it is naturally target oriented (Huang et al., 2018), (2) it gives the sensitivity matrix directly in terms of Green's functions (Jakobsen and Ursin, 2015) which is convenient for uncertainty estimation (Eikrem et al., 2019) and (3) it is compatible with the use of domain decomposition and renormalization methods from modern physics (Jakobsen and Wu, 2016; Jakobsen et al., 2018). On the other hand, the integral equations involving dividing the medium into background and anomalous parts, have some significant limitations, such as the expensive computation of the matrix inversion.

1.2 Aspects of multiple scattering theory

Scattering theory is the basis for various seismic modeling and inversion methods. Seismic scattering theory provides a solution of the wave equation, which can be transformed into Lippmann-Schwinger integral equation. The Lippmann-Schwinger equation has long been used in the mathematical physics community as a basis for solving scattering problems. This Lippmann-Schwinger integral equation, which relates the reflection response measured on one side to wavefields inside the medium, provides solutions of the wave equations. Typically, the wave propagation can be described by the following equation

$$L\left\|\psi\right\rangle = -\left\|S\right\rangle. \tag{1.1}$$

Here $\left\|\psi\right\rangle$ is the state, L is the linear operator and $\left\|S\right\rangle$ represents the source signal. We express the wave equation in operator notation using Dirac's bra-ket notation for linear operators and state-vectors (Taylor, 1972). Table 1.1 shows that multiple scattering theory can be applied to various linear partial differential equations. Assuming $\left\|\psi\right\rangle = \left\|\psi_0\right\rangle + \left\|\psi_s\right\rangle$, where $\left\|\psi_0\right\rangle$ is the state in the background media and $\left\|\psi_s\right\rangle$ is the scattered state, and substituting the above equation into Equation (1.1) gives the Lippmann-Schwinger equation (Taylor, 1972)

$$\left\|\psi\right\rangle = \left\|\psi_0\right\rangle + G_0 V\left\|\psi\right\rangle, \tag{1.2}$$

where G_0 is the Green's functions in reference media and V is the potential. The key idea is to transform the inhomogeneous Helmholtz equation into the equivalent Lippmann-Schwinger integral equation, where the actual wavefields can be constructed by reference wavefields in a relatively

simple reference medium and the perturbation operator in a corresponding perturbation potential. The Lippmann-Schwinger equation can in principle be solved very accurately using the full integral operators. Solving the Lippman-Schwinger equation for $|\psi\rangle$ is formally very simple, giving

$$|\psi\rangle = (1 - G_0 V)^{-1} |\psi_0\rangle \,, \tag{1.3}$$

Following the quantum mechanical potential scattering approach (Taylor, 1972), Jakobsen (2012) introduced a transition operator T

$$VG = TG_0 \tag{1.4}$$

Because the background medium is arbitrary, it follows that (Taylor, 1972; Jakobsen, 2012)

$$T = V + VG_0T \tag{1.5}$$

Thus, the T-operator satisfies an integral equation of the Lippmann-Schwinger type, independent of the source-receiver configuration. Equation (1.5) has the following formal solution

$$T = V \left(1 - G_0 V\right)^{-1} \tag{1.6}$$

which represents a full numerical solution of the Lippman-Schwinger equation that includes all the effects of multiple scattering. However, solving the full integral equation requires the inversion of a full matrix, which is very expensive and the memory demands are high. Different iterative solutions of the Lippmann-Schwinger equation have been proposed, but not all of these are guaranteed to converge independent of the strength of the velocity perturbations and the size of the model relative to the wavelength.

Another way to solve the Lippman-Schwinger equation is by the iteration method. A forward scattering series solution of the integral equations is a popular approach to solve the Lippmann-Schwinger equation for seismic modeling. It generates seismic wavefields, including primaries, free surface multiples and internal multiples, based on the reference wavefieds and the perturbation operator. There are various approximate solutions of the integral equations, such as Born approximation, extended Born approximation (Liu et al., 2001), quasi-linear, quasi-analytical and localized quasi-analytical approximations (Zhdanov and Fang, 1996; Zhdanov, 2002) for seismic modeling. An instructive approach is to generate the Born scattering series using a succession of propagations in the relative simple reference medium and different terms in the scattering series. After an infinite number of iterations, this procedure leads to

$$|\psi\rangle = (1 + G_0V + G_0VG_0V + G_0VG_0VG_0V + G_0VG_0VG_0VG_0V + ...) |\psi_0\rangle \,, \tag{1.7}$$

which is known as the Born series.

The different terms in the Born scattering series means the scattering interactions. The main difference between the approximate solutions and the Born scattering series is that the Born scattering series includes multiple scattering. The forward scattering series is based on scattering theory, which is a form of perturbation theory (Weglein et al, 2009). The Born series has the assumption of weak scattering (Wu and Toksöz, 1987; Kouri and Vijay, 2003). Convergence issues may occur in strong scattering in high-contrast areas, such as salt structures. It is important for seismic imaging in such high-contrast regions to address the weak-scattering.

Figure 1.1 (a) shows an example for strongly scattering model, SEG/EAGE salt model. Figure 1.2 shows the wavefields using the full integral equation solution, with the background model shown in Figure 1.1 (b). Figure 1.3 shows the wavefields using the Born series, which shows the conventional Born series is divergent for such a strongly scattering model.

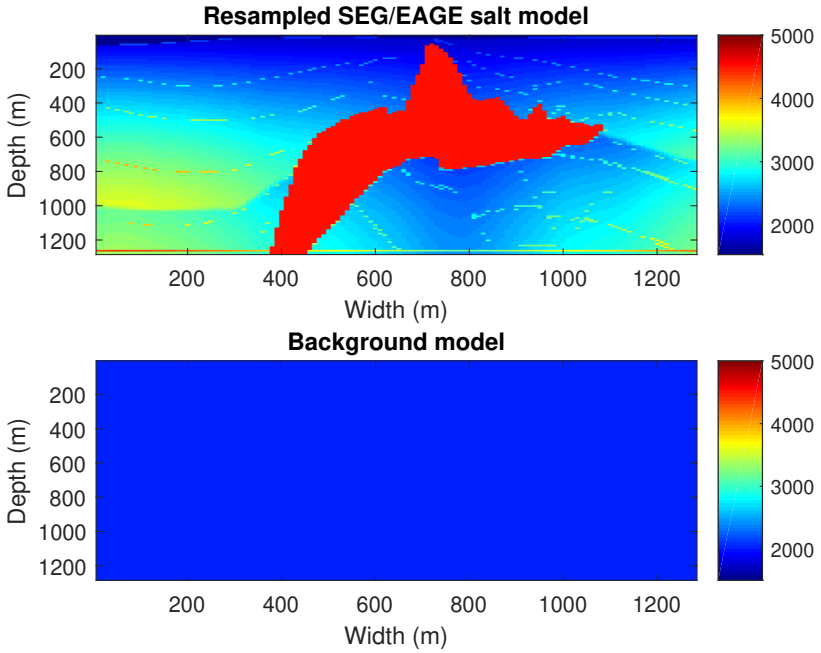

Figure 1.1: (a) The velocity (m/s) of resampled version of the SEG/EAGE salt model and (b) background model.

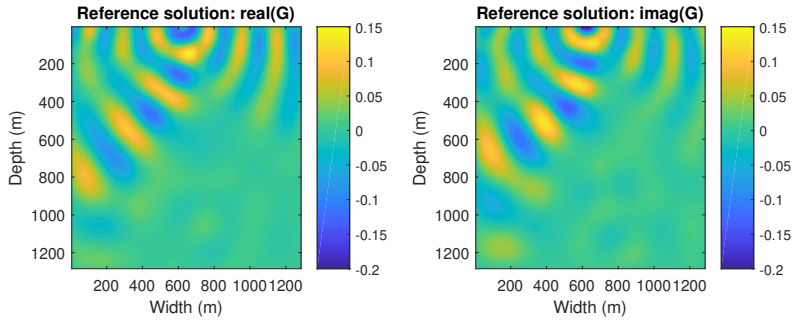

Figure 1.2: Frequency-domain wavefields with the frequency of 10 Hz for the SEG/EAGE salt model using the full integral equation solution.

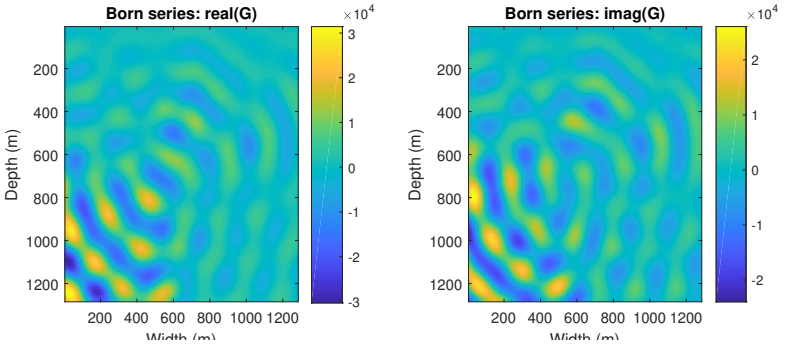

Figure 1.3: Frequency-domain wavefields with the frequency of 10 Hz for the SEG/EAGE salt model using the Born series.

1.3 Renormalization

Historically, the scattering problem was solved using perturbation theory, where it was found that the series did not always converge. Instead the sum would diverge towards infinity as more and more terms were included. This was the famous 'renormalization' problem. One important approach to address the divergence issue is to renormalize the Born series using various renormalization schemes (Eftekhar et al., 2018).

To obtain a convergent scattering scattering series in the presence of strong contrasts, it may be required to perform some kind of renormalization (Abubakar et al., 2003; Kouri and Vijay, 2003; Kirkinis, 2008, 2012; Osnabrugge et al., 2016). The term renormalization is often associated with quantum field theory and related mathematical structures (Delamotte, 2004; Hollowood, 2013), but within the context of classical wave phenomena the term renormalization may simply refer to a rearrangement of the different terms in Born series so that infinities cancel each other in each term in the scattering series. Renormalization can be performed on a term-by-term basis or more generally on the basis of the renormalization group (RG) (Hollowood, 2013). Jakobsen and Wu (2016) derived a renormalized scattering series by considering a T-matrix representation of the De Wolf series (Wu et al., 2007). Wu et al. (2016) has described applications of renormalization group theory in the context of seismic envelope inversion in the time domain. Jakobsen et al. (2018) derived a renormalized Born series using the RG theory.

The goal of the renormalization is to remove the divergence by adding a small correction to each term in the Born series. After adding the correction, when summing the whole series, the sum of the corrections gives an infinity that exactly cancels the infinity in the pure Born series. Following the lecture notes of (Moore, 2008), I will give an introduction for the renormalization process. I start with defining the eigenstates of (Moore, 2008)

$$G_0 V \left|z_n\right\rangle = z_n \left|z_n\right\rangle , \tag{1.8}$$

where z_n is the n th complex eigenvalue. By assuming a discrete spectrum for convenience, the operator $G_0 V$ can be expressed as

$$G_0 V = \sum_n \frac{\left|z_n\right\rangle \left\langle z_n\right|}{1 - z_n}. \tag{1.9}$$

Note that the series expansion $(1 - z)^{-1}$ only converges for $|z| < 1$. This is because a series expansion converges only as far from the expansion point as the nearest singularity in the function being

expanded. Here the expansion point is $z = 0$ and the singularity is at $z = 1$. The series expansion of $(1 - G_0V)^{-1}$ can be expressed as (Moore, 2008)

$$\begin{array}{rcl}(1-G_0V)^{-1} & = & \sum_n u\left(1-|z_n|\right)|z_n\rangle\langle z_n|\left(1+z_n+z_n^2+...\right) \\ & & +\sum_n u\left(|z_n-1|\right)\frac{|z_n\rangle\langle z_n|}{1-z_n}.\end{array} \tag{1.10}$$

where $u(x)$ is the unit step function. For the case $|z_n| > 1$, we can expand in powers of $\frac{1}{z_n}$, as

$$\begin{array}{rcl}\frac{1}{1-z_n} & = & -\frac{1}{z_n}\frac{1}{1-\frac{1}{z_n}} \\ & = & -\frac{1}{z_n}\left(1+z_n^{-1}+z_n^{-2}+...\right).\end{array} \tag{1.11}$$

Combining the two series gives (Moore, 2008)

$$\begin{array}{rcl}(1-G_0V)^{-1} & = & \sum_n |z_n\rangle\langle z_n|\sum_{m=0}^{\infty}\left(z_n^m+u\left(|z_n-1|\right)\left[-z_n^m+\left(-z_n^{-m-1}\right)\right]\right) \\ & = & \sum_{m=0}^{\infty}\sum_n |z_n\rangle\langle z_n|\left[z_n^m-u\left(|z_n-1|\right)\left(z_n^m+z_n^{-m-1}\right)\right] \\ & = & \sum_{m=0}^{\infty}\left[\left(G_0V\right)-R_m\right].\end{array} \tag{1.12}$$

where

$$R_m=\sum_n u\left(|z_n-1|\right)|z_n\rangle\langle z_n|\left(z_n^m+z_n^{-m-1}\right). \tag{1.13}$$

Then the renormalized series will converge normally. In practice, the renormalization is difficult because we cannot know the eigenvalues and eigenvectors of G_0V.

There are several approaches to develop a renormalized scattering series. There have been successful attempts to introduce the De Wolf approximation (De Wolf, 1971; de Wolf, 1985) into seismic scattering theory (Wu and Huang, 1995). The renormalized scattering series is derived by Jakobsen and Wu (2016) using the T-matrix and De Wolf series. Renormalization group method has been applied to seismic waveform inversion (Wu et al., 2015) and envelope inversion (Wu et al., 2016). Significant progress has been made by Yao et al. (2015) by dividing the renormalized Lippmann-Schwinger equation into two sub-Volterra type integral equations by introducing wavefield separation technology. Recently, by employing the renormalization group (RG) theory, we developed a renormalized version of Born series. Numerical tests showed that this solution can be convergent for large-contrast media (Jakobsen et al., 2018, 2020). Our renormalization group approach is based on the use of an auxillary set of scale-dependent scattering potentials, which gradually evolve toward the real physical scattering potential.

Renormalization group (RG) theory was originally proposed by Gell-Mann and Low (1954) in theoretical physics to remove divergences and singularities in perturbation theory in quantum field theory. Historically, Gell-Mann and Low (1954) proposed the idea of a "floating renormalization point" to deal with divergent terms in perturbative expansions within quantum field theory, and pointed out that the physical quantity should be independent of the choice of the renormalization points. They expressed the so-called renormalization group law as

$$H\left(g\left(\Lambda\right),\Lambda\right)=H\left(g\left(\Lambda'\right),\Lambda'\right), \tag{1.14}$$

where H is the local effective Hamiltonian which is a functional of a quantum field, representing the local (short range) interaction at the corresponding scale Λ

$$\frac{dH\left(g\left(\Lambda\right),\Lambda\right)}{d\ln\Lambda}=0, \tag{1.15}$$

which means that the system is scale invariant. From the perspective of statistical physics, Wilson (1971) developed the RG approach into a general tool for dealing with infinities and interactions

across different length scales. As a result, the RG method has found useful applications in a range of different subjects, ranging from quantum field theory to solid state physics via turbulent fluid flow.

Scientists found that the renormalization group has significant application in obtaining stable properties of physical systems (Goldenfeld, 1992). The RG theory (Wilson, 1971) has been widely used to remove divergence in quantum physics, critical phenomena, dynamical systems and statistical mechanics, etc. The idea was extended to obtain the global asymptotic solutions to nonlinear differential equations and asymptotic analysis of differential equations (Goldenfeld, 1992; Chen et al., 1994, 1996). Kunihiro (1995) established the relation between the traditional envelope theory and the RG theory and gave the geometrical interpretation of RG theory. RG theory has proved to be extremely useful in renormalizing perturbation series (Yakhot and Orszag, 1986; Pelissetto and Vicari, 2002; Delamotte, 2004; Kirkinis, 2008, 2012). Renormalization theory was applied to overcome the divergence problem in the direct inverse scattering series in different ways. I extend the forward scattering series to calculate the wavefields by localizing the background wavefields.

1.4 Homotopy analysis method

Historically, there are various ways to solve nonlinear problems, such as perturbation theory, the artificial small parameter methods, the δ-expansion method, and Adomian's decomposition method. Perturbation theory is based on the existence of small or large parameters or variables. A major limitation of perturbation theory is that perturbation theory uses a small perturbation parameter to transfer a nonlinear problem into an infinite number of linear sub-problems and then approximates it by the sum of solutions of the first several sub-problems. In particular, for strongly nonlinear problem, such a theory is often inapplicable. The artificial small parameter methods avoid the assumption of small parameter by introducing a artificial small parameter. Lyapunov (1992) considered the equation

$$\frac{dx}{dt} = A(t)\, x, \tag{1.16}$$

where $A(t)$ is a time periodic matrix. Lyapunov (1992) introduced an artificial parameter to replace this equation with the equation

$$\frac{dx}{dt} = \varepsilon A(t)\, x, \tag{1.17}$$

and then calculated power series expansions over for the solutions that will converge for ε.

The domian's decomposition method (Adomian, 1976; Adomian and Adomian, 1984) is also a powerful analytic technique for strongly nonlinear problems. This method is valid for ordinary and partial differential equations, no matter whether they contain small/large parameters, and thus is rather general. The major advantage of this is that the Adomian approximation series converge quickly. However, convergence regions of the power series given by the domian's decomposition method are small.

The homotopy analysis method (HAM) was proposed by Liao (1992b, 1999, 2003, 2012) for solving nonlinear differential equations in mathematical physics. However, the development of related globally convergent homotopy methods for solving nonlinear equations started around 1976 (Watson, 1989). Historically, there have been several attempts to apply homotopy methods to model and invert geophysical data (Watson, 1989). In any case, the homotopy methods allows one to solve operator equations of any kind by using ideas and concepts of topology, which is a branch of pure and

applied mathematics dealing with quantities that are preserved during continuous deformations. A homotopy describes a continuous transformation between two states and has been compared with the concept of scale-invariance in renormalization group theory (Palit and Datta, 2016; Pfeffer, 2019). The homotopy analysis method have been used to solve a range of different nonlinear problems, ranging from heat conduction problems (Abbasbandy, 2006) to problems within theoretical physics. Most applications of the homotopy analysis method is based on a differential operator formulation, but there have also been successful attempts to solve integral equations of the Fredholm and Volterra types using the homotopy analysis method (Hetmaniok et al., 2014). From the late 1990s to 2010s, due to the advantages of HAM over perturbation theory, it has been widely used in the mathematical and physical sciences, including nonlinear oscillations (Liao, 1992a,b; Liao and Chwang, 1998; Liao, 2004), boundary layer flows (Liao, 1999, 2002), heat transfer (Liao, 2003; Wang et al., 2003), nonlinear water waves (Liao, 1992a; Liao et al., 2016) and nonlinear gravity waves (Liao, 2011). This implies that the new HAM formulation can be potentially used for strongly nonlinear problems, e. g. strongly anisotropic media and strongly scattering media.

Unlike perturbation theory, the homotopy analysis method constructs analytic solutions that are not only independent of any physical parameters but also can guarantee the convergence of the series solution. The main advantage of HAM is that it can be used for highly nonlinear differential equations. The homotopy analysis method can be used to solve operator equations of the form (Liao, 2003)

$$N\left[\psi\right] = 0, \tag{1.18}$$

where N denotes a nonlinear operator and ψ is the unknown function. The basic idea of the homotopy analysis method is to so-called zeroth-order deformation equation to transform a nonlinear equation into a linear equation system and construct a series solution. Liao (2003) constructs the so-called zeroth-order deformation equation

$$\left(1-\lambda\right) L\left[\Phi\left(\lambda\right) - \psi_0\right] = \lambda h H \Phi\left(\lambda\right), \tag{1.19}$$

where $\lambda \in [0,1]$ is the so-called embedding parameter, $h \neq 0$ is the so-called convergence control parameter, H is a convergence control operator, ψ_0 is our initial guess of the solution and L is an auxiliary linear operator that can be selected arbitrarily as long as $L\left[0\right] = 0$.

Hence developing analytic solutions with the homotopy analysis method, which involves transforming the nonlinear differential equations into a system of linear equations, improves the accuracy of the solutions. The homotopy analysis method explains how the analytic solutions of the nonlinear equation can be obtained by transforming the nonlinear equation into a linear equation system. Expanding the solution in Taylor series with respect to a embedding parameter and inserting the series into the zeroth-order deformation equation leads to linear equation system, which is used to construct the coefficients of the series. Then, one can obtain the exact solution. With suitable embedding parameter, auxiliary parameter and the auxiliary linear operator, the series will converge to exact solution. By analogy with the homotopy analysis process, the first guess approximation is chosen, then the approximation changes until it satisfies the original nonlinear equation. This means that the assumed series expansion solution changes from the initial solution to the exact solution. With the embedding parameter getting larger and larger, the series expansion solution approaches the exact solution smoothly, meaning that, at $\lambda = 1$, the exact solution can be obtained. The homotopy analysis process can be divided into the following steps: (1) choosing the linear operator L; (2) construction of the zero-order deformation equation; (3) determination of the coefficients of the series expansion; (4) obtaining the exact solution by setting $\lambda = 1$.

In this thesis, the fundamental theory for inverse scattering problems using the renormalized and

homotopy scattering series is established and its significant advantages compared to optimization inversion methods are illustrated. This thesis also applies the homotopy analysis method to develop the traveltime approximation in strongly anisotropic media.

1.5 Seismic inversion

1.5.1 Full waveform inversion

Full waveform inversion is a powerful tool for high resolution subsurface imaging. It was originally proposed by Tarantola and Valette (1982b) to estimate an earth model by a data-fitting procedure, which minimizes the difference between the modeled data and recorded data, which can be performed in the time domain (Tarantola, 1986) or the frequency domain (Pratt et al., 1996). Compared to other seismic inversion techniques, such as traveltime tomography (Zhang and Toksöz, 1998) and AVO inversion (Buland and Omre, 2003; Downton, 2005), full waveform inversion tries to exploit the full waveform information of the seismic data (Virieux and Operto, 2009). There are still some challenges in full waveform inversion, including huge computational cost, sensitivity to the initial model and convergence problems in strongly scattering media, although it has been applied successfully.

Essentially, seismic full waveform inversion can be viewed as a seismic inverse scattering problem since the scattering theory provides the relations between the model parameter perturbation and the seismic waveform (Tarantola, 1986; Virieux and Operto, 2009). Since the 1980s, the direct inversion approach based on the linearized wave equation using the seismic scattering method has been widely used (Berkhout, 2012). Actually, seismic inversion in general and full waveform inversion in particular is a balancing act between linearization and nonlinearization of inverse theory. The seismic data from the excitation of seismic waves is nonlinear with respect to the real Earth parameter. The weak scattering assumption combined with imperfections of the forward and inverse scattering theory make inverse problems ill-posed. Solving a seismic inversion problem means to investigate the seismic data to find model parameters, which can be achieved by various inversion methods. It depends on simplified methods including the linearization of inverse theory formulation and the assumption of weak scattering and the linearization forward scattering theory. Full waveform inversion can be equivalent to the seismic inverse scattering theory in the sense that the sensitivity operator has a single scattering assumption, which is a major limitation of full waveform inversion to a weak scattering medium when multiple scattering is present.

There are various alternative approaches to full waveform inversion in the context of integral equations, known as the scattering integral approach (Tao and Sen, 2013), contrast source inversion (Van Den Berg and Kleinman, 1997) and distorted Born T-matrix inversion (Jakobsen and Ursin, 2015; Jakobsen and Wu, 2018). Integral equation methods or multiple scattering theory have several advantages compared with the finite difference and finite element methods: (1) It is only required to discretize the scattering region of interest where the anomaly is located. This is in contrast to the finite difference method where it is required to discretize the entire model, unless the special grid injection method is used. (2) The grid blocks can be selected somewhat larger in the integral equation approach compared with the finite difference approach. (3) The inversion can be focused on the target region of interest, if the rest of the model is assumed known and absorbed into the reference model. (4) The integral equation approach allows for the use of sophisticated renormalization and domain decomposition from theoretical physics for reducing the starting model sensitivity and the

computational cost (Kouri and Vijay, 2003; Wu and Zheng, 2014; Jakobsen and Ursin, 2015; Jakobsen and Wu, 2016, 2018). (5) The sensitivity matrix is given explicitly in terms of Greens functions in the reference medium, which is very convenient for Bayesian inversion and uncertainty estimation. (6) The acoustic and elastic wave equations can all be represented by integral equations of the Lippmann-Schwinger form, suggesting that one can use essentially the same methods for mono- and multi-parameter FWI. I will use the distorted Born iterative T-matrix method (DBIT) for full waveform inversion (Jakobsen and Ursin, 2015), which is based on integral equation formulations. Similar to the classic full waveform inversion method, our approach uses the linear relation between the medium contrast and the data due to the use of the Born approximation in the sensitivity matrix. The key idea is to reduce a nonlinear inverse problem to a sequence of linear inverse problems. However, the nonlinear relationship between the subsurface parameters and the recorded data is incorporated in the updated wavefields. Also, the T-matrix completion method can be used (Jakobsen and Wu, 2017).This thesis will develop target-oriented inversion and Bayesian inversion methods. The features described here make it applicable to target-oriented inversion and Bayesian full waveform inversion by combining the integral equation based full waveform inversion and the iterated extended Kalman filter method.

1.5.2 Target-oriented inversion of time-lapse data

Time-lapse seismic surveying is a widely used tool for dynamic reservoir monitoring and assessing the reservoir fluid movements (Landrø, 2001; Landrø et al., 2003; Landrø and Stammeijer, 2004; Lumley, 2010). In the last couple of decades, we have witnessed an increased use of time-lapse seismic data. Traditionally, the result of successful interpretation of time-lapse seismic data has been a better understanding of the oil saturation in the reservoir, leading to identification of the water-flooded areas and pockets of remaining oil, and an improved understanding of compartmentalization of the reservoir. This has been crucial in making decisions for drilling new wells. The success in use of time-lapse seismic data can be judged by the willingness to invest in such data.

Many oil companies have experienced that the information about fluid pressure and saturation changes that are contained in the time-lapse seismic data can help to decrease the uncertainty in the statistical estimates of the porosity and permeability fields. Typically, this is done by performing a quantitative integration of time-lapse seismic and production data using an ensemble-based method (Skjervheim et al., 2005, 2006; Jakobsen et al., 2007; Eikrem et al., 2016). Since reservoir production and time-lapse seismic data are typically densely (sparsely) sampled in time and space, respectively; one can say that these two data types complement each other. Therefore, one should really expect an improved dynamic reservoir characterization by performing a joint inversion of time-lapse seismic and production data. However, dynamic reservoir characterization or seismic history matching is still considered a difficult task; due to the large scale of the problem and due to the fact that one needs to quantify the uncertainty in the time-lapse seismic data as well as the production data.

Full waveform inversion is a powerful tool to estimate the physical parameters of the subsurface (Virieux and Operto, 2009). Recent studies have shown the applicability of full waveform inversion for time-lapse seismic inverse problem (Zheng et al., 2011; Routh et al., 2012; Asnaashari et al., 2015; Yang et al., 2016; Kamei and Lumley, 2017; Yuan et al., 2017). There are different strategies for applying full waveform inversion to time-lapse data, such as the sequential difference strategy (Asnaashari et al., 2015) and double difference strategy (Zhang and Huang, 2013). The sequential difference strategy independently inverts different data sets in the time-lapse data (shown in Figure

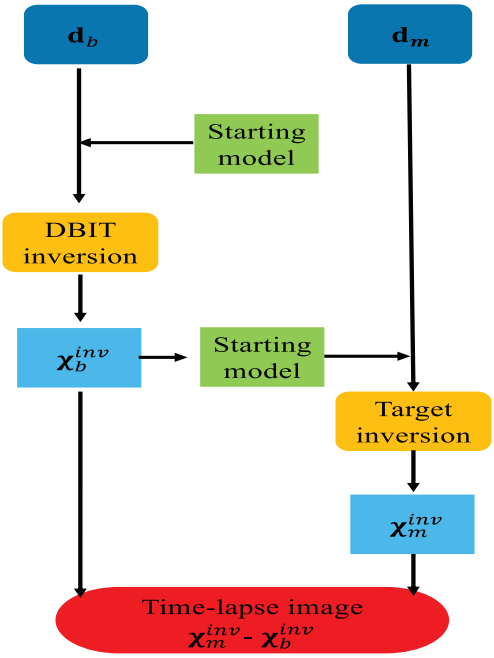

Figure 1.4: Schematic diagram of the sequential difference strategy.

1.3). Then the perturbation can be obtained by a subtraction between the inverted baseline and monitor models. The double difference strategy (shown in Figure 1.4), was originally proposed by Waldhauser and Ellsworth (2000) in the traveltime tomography for improving the earthquake source location. It has become a popular strategy to invert directly for time-lapse changes using the difference of time-lapse data. Recently, the integral equation formulations were applied to the time-lapse seismic data and to estimate the uncertainty (Eikrem et al., 2017). However, time-lapse full waveform inversion requires repeated inversion of monitoring data. Thus, a major limitation of time-lapse full waveform inversion is that the computational cost is expensive.

Target-oriented inversion refers to the situation in which the model space is reduced to the target of interest, and hence the inversion speed can be improved by localizing the inversion in a target-oriented fashion (Valenciano et al., 2006). Techniques to perform target-oriented inversion can be classified into two major categories: 1) performing seismic redatuming by propagating the seismic survey data to the region of interest; 2) generating the local wavefields that can be used to update the wavefields when reconstructing the velocity. The technique that generates the local wavefields is by far the most widespread approach and this thesis focuses on this approach by using the integral equation approach.

The integral equation formulation of full waveform inversion provides significant advantages over other methods for target-oriented inversion since it allows the sensitivity matrix to be expressed explicitly in terms of the Green's functions. The distorted Born iterative T-matrix method was introduced as a general FWI method by Jakobsen and Ursin (2015). They suggested that it could be very suitable for time-lapse inversion, since the T-matrix approach is naturally target-oriented, in the sense that the inversion can be focused on any target if the rest of the model is assumed known.

Target-oriented inversion is particularly appealing for time-lapse full waveform inversion. The reason is that the effects of production on the reservoir changes are considered as small perturbations of

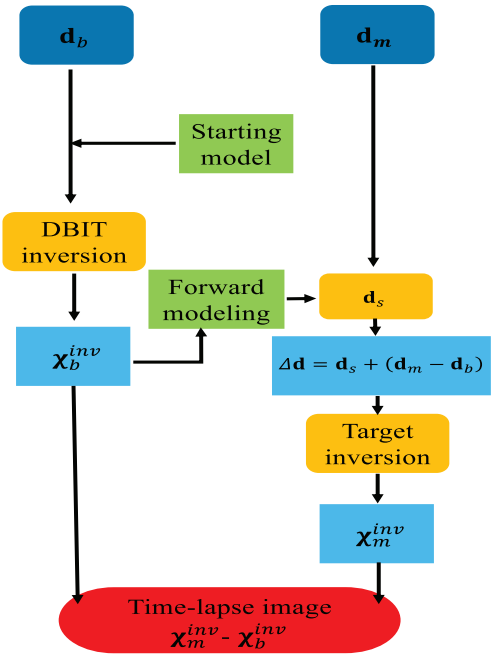

Figure 1.5: Schematic diagram of the double difference strategy.

the earth model (Kirchner and Shapiro, 2001), which is localized and only occur in a small region. Thus starting from the baseline model for time-lapse inversion is a good candidate and can reduce the computation cost. There are several attempts to focus the inversion on a small region. Borisov et al. (2015) used the finite-difference injection method to develop an efficient 3-D time-lapse full waveform inversion. Willemsen et al. (2016) derived a local solver for full waveform inversion of a small region of interest. Malcolm and Willemsen (2016) have developed local solvers for localized inversion. Broggini et al. (2017) derived the immersive boundary conditions for local wavefield computations. Yuan et al. (2017) performed a localized waveform inversion time-lapse survey by combining the wavefield injection and extrapolation. Unlike the methods above, we develop a target-oriented waveform inversion scheme based on the distorted Born iterative T-matrix method (Jakobsen and Ursin, 2015) and Gaussian beam based Green's function (Cerveny, 2005; Huang et al., 2016a,b; Huang and Greenhalgh, 2018; Huang and Sun, 2018; Huang et al., 2018; Huang, 2018). Figure 1.5 shows the scheme of the target-oriented inversion.

1.5.3 Anisotropic elastic full waveform inversion

Interest in anisotropic full waveform inversion has increased considerably within the FWI community in the past few years. Seismic anisotropy is particularly important to account for phase and amplitude information related to different scales of heterogeneous media with fine layering (Backus, 1962), aligned fractures (Ali and Jakobsen, 2011; Huang and Greenhalgh, 2019) and aligned clay minerals (Jakobsen and Johansen, 2000; Schoenberg and Sayers, 1995). Small scale heterogeneities less than the smallest wavelength are responsible for the direction of wave propagation. In the process of FWI, it is the variation in the velocity with respect to the direction of propagation (Virieux and Operto, 2009; Lee et al., 2010; Plessix and Cao, 2011; Operto et al., 2013; Alkhalifah et al.,

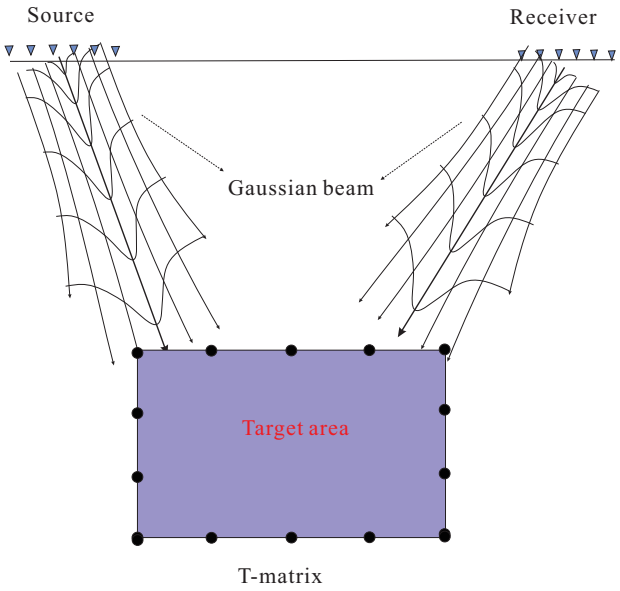

Figure 1.6: Target-oriented inversion.

2016), which leads to medium anisotropy, and contributes to short and long offset data (Plessix and Cao, 2011). If anisotropy is not considered when present, then the traveltime is not calculated accurately. This leads to inaccurate inversion.

Some recent effort has been focused on developing methods for anisotropic FWI but in different ways. The most widely used method includes anisotropy in the forward modeling that accounts for the kinematics in FWI with the acoustic approximation (Plessix and Cao, 2011; Silva et al., 2016; Gholami et al., 2013; Alkhalifah and Plessix, 2014). This is because performing anisotropic elastic FWI is still very challenging, especially for 3-D cases. This type of approach requires that the S-waves are viewed as artifacts and the S-wave velocity is zero. However, in real wave physics of anisotropic elastic media, the acoustic approximation is inapplicable. The use of both anisotropic and elastic FWI methods, in which both elasticity and anisotropy are considered (Burridge et al., 1998; Lee et al., 2010; Köhn et al., 2015; Kamath and Tsvankin, 2016; Oh and Alkhalifah, 2016; He and Plessix, 2017; Oh and Alkhalifah, 2018; Jakobsen et al., 2019), mitigates the need to address the real earth. However, it is well known that increase in the number of parameters will further make the non-linear inversion approach more complicated (Tarantola, 1986; Brossier et al., 2009), which is referred to as multiparameter trade-off or crosstalk problem. Also, the lack of low frequencies, the inaccuracy of initial velocity models and noise (Operto et al., 2013) will increase the uncertainty of inversion. Different approaches have been devised for addressing the trade-off problems, but very few researchers have taken a quantitative way to the trade-offs.

1.5.4 Uncertainty quantification

Uncertainty quantification of seismic images is a key component for merging of seismic and production data in the seismic history matching of reservoir models. Because of this, quantifying the uncertainty of inversion results has become increasingly important for the industry (Gouveia and Scales, 1998; Chen et al., 2007; Landrø, 2002; Martin et al., 2012). The quantification of uncertain-

ties in time-lapse seismic data is highly non-trivial, since the so-called seismic data are often the result of a complicated seismic processing or inversion task. Utilizing time-lapse seismic data for updating reservoir models has been done at different levels. In most cases, inverted elastic properties or changes in the elastic properties (e.g., acoustic impedance, S-wave impedance, Poisson's ratio) are used as data for history matching (Eikrem et al., 2016). In some cases, a further inversion step is done and the data for history matching are in forms of pressure and saturation changes, or saturation fronts or changes in fluid contacts. Another alternative is to use seismic amplitudes and/or time-shifts as data. Some attempts have been made to compare results of using different data types, but the conclusions seem to be largely case dependent. In any case, we think that the use of full waveform inversion methods can help us to obtain a better understanding of the propagation of uncertainties along the seismic processing chain (Eikrem et al., 2016).

Full waveform inversion has emerged as a very promising method for obtaining images of the seismic or elastic parameters of the underground (Abubakar et al., 2003; Virieux and Operto, 2009; Tao and Sen, 2013; Asnaashari et al., 2014). Because the FWI method makes use of the full waveforms and not only the travel times and amplitudes, the FWI method is expected to result in images of the seismic or elastic parameters of the underground which are of higher quality and resolution than traditional travel time and seismic amplitude versus offset (AVO) inversion (Buland and Omre, 2003; Virieux and Operto, 2009; Jakobsen and Ursin, 2015). However, uncertainties arise in practical applications. On the one hand, the full waveform inversion is affected by different factors, such as noisy seismic data, nonlinear forward modeling and inaccurate initial model. These factors contribute to the uncertainty of inversion. Thus, uncertainty quantification of velocity fields is clearly essential for interpreting inverted subsurface models. On the other hand, it is necessary for making a more justifiable and reliable conclusion on identifying pockets of oil and gas to quantify the model uncertainties. To our best knowledge, only few reports have been given on uncertainty quantification in the context of full waveform inversion approach. It is generally assumed that a deterministic model can be obtained by the full waveform inversion. Such a method can be used to estimate the velocity uncertainties by finding statistical solutions for the unknown model parameters (Tarantola and Valette, 1982a; Tarantola, 2005).

Bayesian inference, which allows accounting for uncertainties, provides a systematic framework for obtaining probabilistic solutions of geophysical inverse problems. A prior probability distribution of the model parameters, such as velocity, density, has to be given to find the posterior probability distribution of the subsurface model parameters. In this procedure, a prior density $P(\mathbf{m})$ is chosen for the model parameter $\mathbf{m}$. A likelihood $\mathcal{P}(\mathbf{d} \mid \mathbf{m})$ needs also to be given for the model parameter $\mathbf{m}$ and observation data $\mathbf{d}$. Based on the Bayes' theorem, the mathematical formulation for the posterior distribution can be expressed as (Tarantola, 2005)

$$\mathcal{P}(\mathbf{m} \mid \mathbf{d}) = \frac{\mathcal{P}(\mathbf{d} \mid \mathbf{m})\,\mathcal{P}(\mathbf{m})}{\int \mathcal{P}(\mathbf{d} \mid \mathbf{m})\,\mathcal{P}(\mathbf{m})\,d\mathbf{m}}, \tag{1.20}$$

where $\int \mathcal{P}(\mathbf{d} \mid \mathbf{m})\,\mathcal{P}(\mathbf{m})\,d\mathbf{m}$ is the evidence.

A critical aspect of the Bayesian inversion is the calculation of the posterior covariance matrix. Actually, when obtaining the global minimum solution of an optimization problem, the inverse Hessian matrix can be viewed as the posterior covariance matrix (Tarantola, 2005). Several approaches to analyze the uncertainties based on analyzing the Hessian matrix or utilizing an approximate Hessian have been given (Liu et al., 2019; Liu and Peter, 2019). Fichtner and Trampert (2011a,b) showed the relation between the posterior covariance, the Hessian and the resolution matrix of seismic inversion. Fichtner and Leeuwen (2015) then applied Bayesian inference to seismic tomography using stochastic probing of the Hessian or resolution operators. The application of the Markov chain

Monte Carlo (MCMC) method to seismic inversion problems in the framework of Bayesian inference was reported (Martin et al., 2012). Bui-Thanh et al. (2013) and Petra et al. (2014) estimated the uncertainty for solutions of linearized infinite-dimensional statistical inverse problems. For a detained review of uncertainty assessment in seismic tomography problems, see Rawlinson et al. (2014). Zhu et al. (2016) also successfully applied full waveform inversion to uncertainty estimation by using a point spread function method and a priori information from depth migration. Compared to the deterministic inversion, the Bayesian inversion is computationally more involved as there is some extra computational cost for the covariance matrix.

We turn now to the situation where full waveform inversion has been recently used to estimate velocity uncertainties in the Bayesian framework. In this case, the formulations in Bayesian full waveform inversion are different from that in the classic deterministic full waveform inversion. Several publications on this topic are from different prospectives. Aleardi and Mazzotti (2017) developed a hybrid method that combines the genetic algorithm and a Gibbs sampler to estimate the posterior probability distributions. An approach to recover the Bayesian posterior model probability density function of subsurface elastic parameters and further effort to mitigate the problem of data uncertainty are presented (Ray et al., 2016, 2017). The Reversible Jump Hamiltonian Monte Carlo (Ray et al., 2016) was successfully applied to uncertainty quantification and some results on the Marmousi model were shown (Biswas and Sen, 2017). Fang et al. (2018) presented a method for uncertainty quantification with weak partial-differential-equation constraints. Also, uncertainty assessment in velocity models and images can be found in Ely et al. (2018). Recently, Thurin et al. (2017) made significant progress on the original application of the ensemble-based Kalman filter method to full waveform inversion and demonstrated impressive results on uncertainty estimation with the Marmousi model. Eikrem et al. (2019) developed a method with the iterated extended Kalman filter method for time-lapse seismic full-waveform inversion. In any case, to the best of our knowledge, there is no report in the literature that gives an uncertainty quantification of inverted velocities in anisotropic elastic media by means of full waveform inversion.

1.6 Thesis contributions and overview

The first goal of this thesis is to develop seismic forward modeling methods for strongly scattering and strongly anisotropic media. The second goal of the thesis is to develop efficient methods for time-lapse full waveform inversion. Another goal is to estimate the uncertainty and multiparameter trade-offs in anisotropic elastic full waveform inversion.

The first contribution in papers 1 and 2 is extending the convergent Born series approach to seismic forward scattering problems for strongly scattering media and developing the homotopy Born series using homotopy analysis method that is guaranteed to converge independent of the contrast and comparing them with the full integral equation method. The convergent Born series is obtained by localizing the Green's function with a damping factor and adding a preconditioner. From the technical point of view, the convergent Born series removes the divergence by localizing the wavefields and controlling convergence using a preconditioner, which is like a renormalization process. A physical interpretation of the convergent Born series from the physical renormalization prospective is given. Using several examples of numerical results for frequency-domain wavefields, this study shows that the convergent Born series can produce the same results for wavefields as the full integral equation method in strongly scattering media. Also, we use the homotopy analysis method (HAM) to derive a general scattering series solution of the Lippmann-Schwinger equation which

is guaranteed to converge, independent of the scattering potential. We found that the conventional Born series and the convergent Born series are special cases of the new scattering series based on HAM.

The second contribution in paper 3 is establishing the fundamental theory of the linear partial differential equations for solving the VTI and TTI eikonal equations and developing traveltime approximations for strongly anisotropic media. By applying the homotopy analysis method to anisotropic eikonal equations, this study extends the HAM to geophysical problems for strongly anisotropic media. They open up new approaches for applications of the homotopy analysis method to geophysical problems. The extension leads to a broader application of the derived formulations to the strongly anisotropic media and helps improve the accuracy of traveltime approximations.

Next, in paper 4, we develop an efficient target-oriented inversion method for time-lapse full waveform inversion by combining the T-matrix approach of the integral equation with the Gaussian beam Green's functions. The key idea is to perform local inversion for a small region which reduces the computational cost significantly. The inversion scheme with different degrees of noisy data is examined. We compare two time-lapse inversion strategies, called the double difference strategy and the sequential strategy and show the double different strategy has advantages over the sequential difference strategy.

Another contribution in paper 5 is a Bayesian framework for full waveform inversion in anisotropic elastic media for uncertainty quantification using the iterated extended Kalman filter. This study applies the Bayesian inference to the earlier elastodynamic generalization of the distorted Born iterative T-matrix method for anisotropic elastic full waveform inversion, which is based on the integral equation method. By employing the iterated extended Kalman filter in the Bayesian framework, the uncertainty characteristics can be exploited simultaneously with the velocity model building. We also explore the multiparameter trade-off analysis.

Appendix A includes a SEG abstract. This abstract presents a comparison of two scattering series, referred to as convergent Born series (CBS) and renormalized Born series (RBS) using the renormalization group theory (Jakobsen et al., 2018, 2020), for frequency-domain seismic modeling in strong scattering media. The results from both the CBS and RG theory can agree with the reference full integral method. We conclude that from the specific model in this abstract, the CBS converges faster. Currently, the convergence speed of the scattering series using RG theory has been improved significantly.

Chapter 2

Conclusions and future perspectives

In papers 1 and 2, this thesis extended the convergent Born scattering series to seismic modeling for strongly scattering media and derived the homotopy Born scattering series by employing the homotopy analysis method. This thesis analyzed the convergence properties of both the scattering series by comparing them with the full integral equation. This analysis builds a connection between the convergent Born series and conventional Born series. The investigation establishes the theoretical foundation of convergent Born series for inverse scattering problems in strongly scattering media.

In paper 3, the thesis derived the linear differential equation system that retrieves the eikonal equations for VTI and TTI media and the traveltime approximations. This methodology first transforms the strongly nonlinear eikonal equation in strongly anisotropic media into a linear differential equation system by employing the homotopy analysis method, then uses the zero-order deformation equation and Taylor's series expansion to construct the traveltime approximations. This thesis tested the method using synthetic models and showed that the formulations have advantages over the traditional perturbation theory.

In paper 4, this thesis presented a methodology for target-oriented inversion of time-lapse seismic waveform data. This method obviates the need to repeat the full model inversion for monitor surveys in time-lapse seismic inversion. The integral equation method with the T-matrix and the asymptotic Green's function with Gaussian beams were applied to construct the local wavefields in the region of interest. This thesis showed that inversion with the target-oriented scheme significantly reduces the computational cost. This thesis discussed two strategies for time-lapse inversion.

In paper 5, this thesis developed a Bayesian full waveform inversion method for inverting the stiffness parameters and estimating the uncertainty in anisotropic elastic media. The integral equations based on the nonlinear inverse scattering theory are used to construct the explicit sensitivity matrix in terms of Green's functions. The iterated extended Kalman filter is used to solve the Bayesian inversion problem. The FWI is performed in frequency domain and the sequential strategy is used for the data assimilation process.

The renormalized and homotopy scattering series developed in this thesis and in recent work (Jakobsen et al., 2020) can be generalized to anisotropic elastic media, since the corresponding wave equation can also be transformed into an integral equation of the Lippmann-Schwinger type. Having developed a convergent forward scattering series, the next step could be to apply this series in the context of inverse scattering theory. In principle, it can be extended to inverse scattering problems using the renormalized and homotopy scattering series. In theory, one can also use the wavefields produced by the scattering series for inversion. Weglein et al. (2003) have pioneered in-

verse acoustic scattering methods that do not require an assumed propagation velocity model within the medium. Their approach is based on the Born series solution of the Lippmann-Schwinger equation and a concomitant expansion of the interaction in orders of the data. In principle, the method is completely general and requires no prior information about the target or the propagation details of the probe signal within the target. The only fundamental limitation of the approach appears to the convergence of the conventional Born series. Potential extension of convergent inverse scattering series using the HAM scattering series to inverse scattering problem is also interesting. However, it is not obvious that the inverse scattering series will converge even though the forward scattering series is convergent.

There is another approach to inverse scattering theories in strongly scattering media, referred to as Gel'fand-Levitan-Marchenko theory in addition to the renormalization scattering theory. Gel'fand-Levitan-Marchenko theory provides an exact solution of the 1-D Schrodinger equation, which can be transformed into the acoustic wave equation in the 1-D case. The Gel'fand-Levitan-Marchenko (GLM) equation has long been used in the mathematical physics community as a basis for solving inverse scattering problems (Ware and Aki, 1969; Burridge, 1980; Coen, 1981; Wu and He, 2019). This Gel'fand-Levitan-Marchenko equation, which relates the reflection response measured on one side to wavefields inside the medium, provides exact solutions of the Schrodinger equations. The method may be called exact since in principle, the inversion method is not approximate. Recent studies have shown that the GLM method provide superior capability for inverse scattering problems compared to the optimization method. This is mainly due to the fact that this method can address multiple reflections, which is particularly important in reflection seismology. Multiple reflections are often caused by a strong scattering region, e. g. salt bodies, and they can have a strong influence on seismic inversion. The GLM method, however, is restricted to the one dimensional case in the context of one side reflection seismology. An attempt to generalize the Marchenko equation to 3D, which is the so-called Newton-Marchenko (NM) equation has been done but this 3D inverse scattering based on the NM equation requires omnidirectional reflection and transmission measurements. Hence, despite the fact that the NM equation is very useful for this class of inverse problems, it is not applicable to single-sided reflection seismology. One of the main physical requirements is the transformation of the acoustic wave equation into the 3-D Schrodinger type equation although Ware and Aki (1969) used the Liouville transformation to transform the acoustic wave equation into a Schrodinger equation in the 1-D case (Wu and He, 2019). Wapenaar et al. (2013) have pioneered the focusing scheme for 3-D inverse scattering problems that only requires the direct wave and reflection response in one sided observations. This focusing scheme is based on the one of Broggini and Snieder (2012), and Wapenaar et al. (2013) is an extension of the theory of Rose (2001, 2002) who uses an iterative scheme to solve the Marchenko equation for 1-D wavefield focusing. Extension of the focusing scheme leads to an iterative scheme to calculate the focused events in the wavefield for the virtual source consisted of primaries and internal multiples (Wapenaar et al., 2014). The focusing method derived by Rose (2001, 2002) for single-sided illumination with sources and receivers on one side of the medium was successfully applied to the seismic imaging problem. The only fundamental limitation of the approach is that to construct the focusing functions for wavefield focusing, a smooth velocity model is required, which is impossible to obtain in the inverse scattering problem for velocity reconstruction. Developing inverse scattering theory in this direction is the next goal.

Recent work shows that introducing an approximate inverse of the Born modelling operator, into the objective function can help reduce the artifacts in the full waveform inversion. In theory, this operator tends asymptotically towards the identity matrix. As a result of the introduction of the operator, the artifacts generated by second order scattering and the trade-off can be reduced. As a

modification of this approach, one can use the asymptotic methods developed in this thesis, which account for multi-arrivals in strongly anisotropic media, to replace the migration operator in the framework of the inversion and apply it to full waveform inversion.

The Bayesian full waveform inversion can be used for resolution analysis. Resolution quantification in Bayesian full waveform inversion is important for interpretation of the inversion results. There is still an important need for further development of methods due to the following factors: (1) The linearization approximation in the FWI is not applicable to the nonlinear data set with the real Earth. (2) The sensitivity matrix is not computed explicitly in FWI, which presents the local analysis for resolution quantification (Fichtner and Trampert, 2011b). (3) Recently probabilistic methods are not applicable to large scale FWI problem. The key point to resolution analysis is the Hessian matrix as the inverse Hessian operator is equivalent to the posterior covariance of the minimization problem when the solution is close to the global minimum. Recent approaches rely on parameterized or low-rank approximations of the Hessian operator. Application of the exact Hessian matrix based on the scattering integral method in terms of explicit Green's functions to Bayesian FWI can overcome the linear approximation. From the scattering prospective, the exact Hessian can account for the second order scattering effects.

Bibliography

Abbasbandy, S. (2006). The application of homotopy analysis method to nonlinear equations arising in heat transfer. *Physics Letters A 360*(1), 109–113. 9

Abubakar, A., P. Van Den Berg, and J. Fokkema (2003). Towards non-linear inversion for characterization of time-lapse phenomena through numerical modelling. *Geophysical Prospecting 51*(4), 285–293. 6, 15

Adomian, G. (1976). Nonlinear stochastic differential equations. *Journal of Mathematical Analysis and Applications 55*(2), 441–452. 8

Adomian, G. and G. Adomian (1984). A global method for solution of complex systems. *Mathematical Modelling 5*(4), 251–263. 8

Aki, K. (1980). Quantitative seismology. *Theory and Method*, 304–308. 3

Aleardi, M. and A. Mazzotti (2017). 1D elastic full-waveform inversion and uncertainty estimation by means of a hybrid genetic algorithm–Gibbs sampler approach. *Geophysical Prospecting 65*(1), 64–85. 16

Ali, A. and M. Jakobsen (2011). On the accuracy of rüger's approximation for reflection coefficients in HTI media: implications for the determination of fracture density and orientation from seismic AVAZ data. *Journal of Geophysics and Engineering 8*(2), 372–393. 13

Alkhalifah, T. (2011a). Scanning anisotropy parameters in complex media. *Geophysics 76*(2), U13–U22. 2

Alkhalifah, T. (2011b). Traveltime approximations for transversely isotropic media with an inhomogeneous background. *Geophysics 76*(3), WA31–WA42. 2

Alkhalifah, T. (2013). Traveltime approximations for inhomogeneous transversely isotropic media with a horizontal symmetry axis. *Geophysical Prospecting 61*(3), 495–503. 2

Alkhalifah, T. and S. Fomel (2001). Implementing the fast marching eikonal solver: spherical versus Cartesian coordinates. *Geophysical Prospecting 49*(2), 165–178. 2

Alkhalifah, T., N. Masmoudi, and J.-W. Oh (2016). A recipe for practical full-waveform inversion in orthorhombic anisotropy. *The Leading Edge 35*(12), 1076–1083. 13

Alkhalifah, T. and R.-É. Plessix (2014). A recipe for practical full-waveform inversion in anisotropic media: An analytical parameter resolution study. *Geophysics 79*(3), R91–R101. 14

Asnaashari, A., R. Brossier, S. Garambois, F. Audebert, P. Thore, and J. Virieux (2014). Time-lapse seismic imaging using regularized full-waveform inversion with a prior model: which strategy? *Geophysical prospecting 63*(1), 78–98. 15

Asnaashari, A., R. Brossier, S. Garambois, F. Audebert, P. Thore, and J. Virieux (2015). Time-lapse seismic imaging using regularized full-waveform inversion with a prior model: which strategy? *Geophysical prospecting 63*(1), 78–98. 11

Backus, G. E. (1962). Long-wave elastic anisotropy produced by horizontal layering. *Journal of Geophysical Research 67*(11), 4427–4440. 13

Bai, C.-Y., S. Greenhalgh, and B. Zhou (2007). 3D ray tracing using a modified shortest-path method. *Geophysics 72*(4), T27–T36. 2

Berkhout, A. (2012). Combining full wavefield migration and full waveform inversion, a glance into the future of seismic imaging. *Geophysics 77*(2), S43–S50. 10

Biswas, R. and M. Sen (2017). 2D full-waveform inversion and uncertainty estimation using the reversible jump Hamiltonian Monte Carlo. In *SEG Technical Program Expanded Abstracts 2017*, pp. 1280–1285. Society of Exploration Geophysicists. 16

Borisov, D., S. C. Singh, and N. Fuji (2015). An efficient method of 3-D elastic full waveform inversion using a finite-difference injection method for time-lapse imaging. *Geophysical Journal International 202*(3), 1908–1922. 13

Bouteiller, L. P., M. Benjemaa, L. Métivier, and J. Virieux (2017). An accurate discontinuous galerkin method for solving point-source eikonal equation in 2-D heterogeneous anisotropic media. *Geophysical Journal International 212*(3), 1498–1522. 2

Broggini, F. and R. Snieder (2012). Connection of scattering principles: A visual and mathematical tour. *European Journal of Physics 33*(3), 593. 19

Broggini, F., M. Vasmel, J. O. Robertsson, and D.-J. van Manen (2017). Immersive boundary conditions: Theory, implementation, and examples. *Geophysics 82*(3), T97–T110. 13

Brossier, R., S. Operto, and J. Virieux (2009). Seismic imaging of complex onshore structures by 2D elastic frequency-domain full-waveform inversion. *Geophysics 74*(6), WCC105–WCC118. 14

Bui-Thanh, T., O. Ghattas, J. Martin, and G. Stadler (2013). A computational framework for infinite-dimensional Bayesian inverse problems Part i: The linearized case, with application to global seismic inversion. *SIAM Journal on Scientific Computing 35*(6), A2494–A2523. 16

Buland, A. and H. Omre (2003). Bayesian linearized avo inversion. *Geophysics 68*(1), 185–198. 10, 15

Burridge, R. (1980). The Gelfand-Levitan, the Marchenko, and the Gopinath-Sondhi integral equations of inverse scattering theory, regarded in the context of inverse impulse-response problems. *Wave motion 2*(4), 305–323. 19

Burridge, R., M. V. de Hoop, D. Miller, and C. Spencer (1998). Multiparameter inversion in anisotropic elastic media. *Geophysical Journal International 134*(3), 757–777. 14

Cao, S. and S. Greenhalgh (1994). Finite-difference solution of the eikonal equation using an efficient, first-arrival, wavefront tracking scheme. *Geophysics 59*(4), 632–643. 2

Carcione, J. M. (2007). *Wave fields in real media: Wave propagation in anisotropic, anelastic, porous and electromagnetic media*, Volume 38. Elsevier. 1

Červenỳ, V. (1972). Seismic rays and ray intensities in inhomogeneous anisotropic media. *Geophysical Journal of the Royal Astronomical Society 29*(1), 1–13. 1

Ĉervenŷ, V. (2001). Seismic ray theory. 1

Cerveny, V. (2005). *Seismic ray theory*. Cambridge university press. 13

Červenỳ, V., E. Iversen, and I. Pšenčík (2012). Two-point paraxial traveltimes in an inhomogeneous anisotropic medium. *Geophysical Journal International 189*(3), 1597–1610. 2

Červenỳ, V., L. Klimeš, and I. Pšenčík (1984). Paraxial ray approximations in the computation of seismic wavefields in inhomogeneous media. *Geophysical Journal International 79*(1), 89–104. 2

Červenỳ, V., L. Klimeš, and I. Pšenčík (2007). Seismic ray method: Recent developments. *Advances in Geophysics 48*, 1–126. 2

Červenỳ, V. and I. Pšenčík (1983). Gaussian beams in two-dimensional elastic inhomogeneous media. *Geophysical Journal International 72*(2), 417–433. 1

Chen, L. Y., N. Goldenfeld, and Y. Oono (1994). Renormalization group theory for global asymptotic analysis. *Physical review letters 73*(10), 1311. 8

Chen, L.-Y., N. Goldenfeld, and Y. Oono (1996). Renormalization group and singular perturbations: Multiple scales, boundary layers, and reductive perturbation theory. *Physical Review E 54*(1), 376. 8

Chen, P., T. H. Jordan, and L. Zhao (2007). Full three-dimensional tomography: a comparison between the scattering-integral and adjoint-wavefield methods. *Geophysical Journal International 170*(1), 175–181. 14

Coen, S. (1981). The inverse problem of the shear modulus and density profiles of a layered earth. *Journal of Geophysical Research: Solid Earth 86*(B7), 6052–6056. 19

De Wolf, D. (1971). Electromagnetic reflection from an extended turbulent medium: cumulative forward-scatter single-backscatter approximation. *IEEE transactions on Antennas and Propagation 19*(2), 254–262. 7

de Wolf, D. (1985). Renormalization of EM fields in application to large-angle scattering from randomly continuous media and sparse particle distributions. *IEEE transactions on Antennas and Propagation 33*(6), 608–615. 7

Delamotte, B. (2004). A hint of renormalization. *American Journal of Physics 72*(2), 170–184. 6, 8

Downton, J. E. (2005). *Seismic parameter estimation from AVO inversion*. University of Calgary, Department of Geology and Geophysics. 10

Eftekhar, R., H. Hu, and Y. Zheng (2018). Convergence acceleration in scattering series and seismic waveform inversion using nonlinear Shanks transformation. *Geophysical Journal International 214*(3), 1732–1743. 6

Eikrem, K. S., G. Nævdal, and M. Jakobsen (2019). Iterated extended Kalman filter method for time-lapse seismic full-waveform inversion. *Geophysical Prospecting 67*(2), 379–394. 3, 16

Eikrem, K. S., G. Nævdal, M. Jakobsen, and Y. Chen (2016). Bayesian estimation of reservoir properties—effects of uncertainty quantification of 4D seismic data. *Computational Geosciences 20*(6), 1211–1229. 11, 15

Eikrem, K, S., M. Jakobsen, and G. Nævdal (2017). Bayesian inversion of time-lapse seismic waveform data using an integral equation method. In *IOR 2017-19th European Symposium on Improved Oil Recovery*. 12

Ely, G., A. Malcolm, and O. V. Poliannikov (2018). Assessing uncertainties in velocity models and images with a fast nonlinear uncertainty quantification method. *Geophysics 83*(2), R63–R75. 16

Fang, Z., C. Da Silva, R. Kuske, and F. J. Herrmann (2018). Uncertainty quantification for inverse problems with weak partial-differential-equation constraints. *Geophysics 83*(6), R629–R647. 16

Farra, V. and I. Pšenčík (2017). Weak-anisotropy moveout approximations for P-waves in homogeneous TOR layers. *Geophysics 82*(4), WA23–WA32. 2

Fichtner, A. and T. v. Leeuwen (2015). Resolution analysis by random probing. *Journal of Geophysical Research: Solid Earth 120*(8), 5549–5573. 15

Fichtner, A. and J. Trampert (2011a). Hessian kernels of seismic data functionals based upon adjoint techniques. *Geophysical Journal International 185*(2), 775–798. 15

Fichtner, A. and J. Trampert (2011b). Resolution analysis in full waveform inversion. *Geophysical Journal International 187*(3), 1604–1624. 15, 20

Gell-Mann, M. and F. E. Low (1954). Quantum electrodynamics at small distances. *Physical Review 95*(5), 1300. 7

Gholami, Y., R. Brossier, S. Operto, A. Ribodetti, and J. Virieux (2013). Which parameterization is suitable for acoustic vertical transverse isotropic full waveform inversion? Part 1: Sensitivity and trade-off analysis. *Geophysics 78*(2), R81–R105. 14

Gjøystdal, H., J. Reinhardsen, and B. Ursin (1984). Traveltime and wavefront curvature calculations in three-dimensional inhomogeneous layered media with curved interfaces. *Geophysics 49*(9), 1466–1494. 2

Goldenfeld, N. (1992). Lectures on phase transition and the renormalization group, Addison-Weslley. *Reading, Mass*. 8

Gonis, A. and W. H. Butler (2012). *Multiple scattering in solids*. Springer Science & Business Media. 3

Gouveia, W. P. and J. A. Scales (1998). Bayesian seismic waveform inversion: Parameter estimation and uncertainty analysis. *Journal of Geophysical Research: Solid Earth 103*(B2), 2759–2779. 14

Han, S., W. Zhang, and J. Zhang (2017). Calculating qP-wave traveltimes in 2-D TTI media by high-order fast sweeping methods with a numerical quartic equation solver. *Geophysical Journal International 210*(3), 1560–1569. 2

Hao, Q. and T. Alkhalifah (2017). An acoustic eikonal equation for attenuating transversely isotropic media with a vertical symmetry axisacoustic attenuating VTI media. *Geophysics 82*(1), C9–C20. 2

He, W. and R.-É. Plessix (2017). Analysis of different parameterisations of waveform inversion of compressional body waves in an elastic transverse isotropic Earth with a vertical axis of symmetry. *Geophysical Prospecting 65*(4), 1004–1024. 14

Hetmaniok, E., D. Słota, T. Trawiński, and R. Wituła (2014). Usage of the homotopy analysis method for solving the nonlinear and linear integral equations of the second kind. *Numerical Algorithms 67*(1), 163–185. 9

Hollowood, T. J. (2013). *Renormalization Group and Fixed Points: In Quantum Field Theory*. Springer. 6

Huang, X. (2018). Extended beam approximation for high-frequency wave propagation. *IEEE Access 6*, 37214–37224. 13

Huang, X. and S. Greenhalgh (2018). Linearized formulations and approximate solutions for the complex eikonal equation in orthorhombic media and applications of complex seismic traveltime. *Geophysics 83*(3), C115–C136. 2, 13

Huang, X. and S. Greenhalgh (2019). Traveltime approximation for strongly anisotropic media using the homotopy analysis method. *Geophysical Journal International 216*(3), 1648–1664. 13

Huang, X., M. Jakobsen, K. S. Eikrem, and G. Nævdal (2018). A target-oriented scheme for efficient inversion of time-lapse seismic waveform data. In *SEG Technical Program Expanded Abstracts 2018*, pp. 5352–5356. Society of Exploration Geophysicists. 3

Huang, X. and H. Sun (2018). Numerical modeling of gaussian beam propagation and diffraction in inhomogeneous media based on the complex eikonal equation. *Acta Geophysica 66*(4), 497–508. 2, 13

Huang, X., H. Sun, and J. Sun (2016a). Born modeling for heterogeneous media using the Gaussian beam summation based green's function. *Journal of Applied Geophysics 131*, 191–201. 13

Huang, X., J. Sun, and S. Greenhalgh (2018). On the solution of the complex eikonal equation in acoustic VTI media: a perturbation plus optimization scheme. *Geophysical Journal International 214*(2), 907–932. 2, 13

Huang, X., J. Sun, and Z. Sun (2016b). Local algorithm for computing complex travel time based on the complex eikonal equation. *Physical Review E 93*(4), 043307. 2, 13

Iversen, E. and M. Tygel (2008). Image-ray tracing for joint 3D seismic velocity estimation and time-to-depth conversion. *Geophysics 73*(3), S99–S114. 2

Iversen, E., B. Ursin, T. Saksala, J. Ilmavirta, and M. V. de Hoop (2018). Higher-order Hamilton–Jacobi perturbation theory for anisotropic heterogeneous media: dynamic ray tracing in Cartesian coordinates. *Geophysical Journal International 216*(3), 2044–2070. 2

Jakobsen, M. (2012). T-matrix approach to seismic forward modelling in the acoustic approximation. *Studia Geophysica et Geodaetica 56*(1), 1–20. 4

Jakobsen, M., E. Ivan, Psencik, Iversen, and B. Ursin (2019). Transition operator approach to seismic full-waveform inversion in arbitrary anisotropic elastic media. *Communications in Computational Physics*, doi:10.4208/cicp.OA–2018–0197. 14

Jakobsen, M. and T. A. Johansen (2000). Anisotropic approximations for mudrocks: A seismic laboratory study. *Geophysics 65*(6), 1711–1725. 13

Jakobsen, M., J.-A. Skjervheim, and S. I. Aanonsen (2007). Characterization of fractured reservoirs by effective medium modelling and joint inversion of seismic and production data. *Journal of Seismic Exploration 16*(2), 177. 11

Jakobsen, M. and B. Ursin (2015). Full waveform inversion in the frequency domain using direct iterative T-matrix methods. *Journal of Geophysics and Engineering 12*(3), 400. 3, 10, 11, 12, 13, 15

Jakobsen, M. and R. Wu (2016). Renormalized scattering series for frequency-domain waveform modelling of strong velocity contrasts. *Geophysical Journal International 206*(2), 880–899. 1, 3, 6, 7, 11

Jakobsen, M. and R.-S. Wu (2017). Multiscale T-matrix completion method for FWI in the absence of a good starting model. In *SEG Technical Program Expanded Abstracts 2017*, pp. 1274–1279. Society of Exploration Geophysicists. 11

Jakobsen, M. and R.-S. Wu (2018). Accelerating the T-matrix approach to seismic full-waveform inversion by domain decomposition. *Geophysical Prospecting 66*(6), 1039–1059. 1, 10, 11

Jakobsen, M., R.-S. Wu, and X. Huang (2018). Seismic waveform modeling in strongly scattering media using renormalization group theory. *SEG Technical Program Expanded Abstracts 2018 1*(1), 5007–5011. 3, 6, 7, 17

Jakobsen, M., R.-S. Wu, and X. Huang (2020). Convergent scattering series solution of the inhomogeneous helmholtz equation via renormalization group and homotopy continuation approaches. *Journal of Computational Physics*, 109343. 7, 17, 18

Kamath, N. and I. Tsvankin (2016). Elastic full-waveform inversion for VTI media: Methodology and sensitivity analysis. *Geophysics 81*(2), C53–C68. 14

Kamei, R. and D. Lumley (2017). Full waveform inversion of repeating seismic events to estimate time-lapse velocity changes. *Geophysical Journal International 209*(2), 1239–1264. 11

Kirchner, A. and S. A. Shapiro (2001). Fast repeat-modelling of time-lapse seismograms. *Geophysical prospecting 49*(5), 557–569. 13

Kirkinis, E. (2008). Renormalization group interpretation of the Born and Rytov approximations. *JOSA A 25*(10), 2499–2508. 6, 8

Kirkinis, E. (2012). The renormalization group: a perturbation method for the graduate curriculum. *SIAM Review 54*(2), 374–388. 6, 8

Köhn, D., O. Hellwig, D. De Nil, and W. Rabbel (2015). Waveform inversion in triclinic anisotropic media—a resolution study. *Geophysical Journal International 201*(3), 1642–1656. 14

Kouri, D. J. and A. Vijay (2003). Inverse scattering theory: Renormalization of the Lippmann-Schwinger equation for acoustic scattering in one dimension. *Physical Review E 67*(4), 046614. 4, 6, 11

Kunihiro, T. (1995). A geometrical formulation of the renormalization group method for global analysis. *Progress of theoretical physics 94*(4), 503–514. 8

Landrø, M. (2001). Discrimination between pressure and fluid saturation changes from time-lapse seismic data. *Geophysics 66*(3), 836–844. 11

Landrø, M. (2002). Uncertainties in quantitative time-lapse seismic analysis. *Geophysical Prospecting 50*(5), 527–538. 14

Landrø, M. and J. Stammeijer (2004). Quantitative estimation of compaction and velocity changes using 4D impedance and traveltime changes. *Geophysics 69*(4), 949–957. 11

Landrø, M., H. H. Veire, K. Duffaut, and N. Najjar (2003). Discrimination between pressure and fluid saturation changes from marine multicomponent time-lapse seismic data. *Geophysics 68*(5), 1592–1599. 11

Lee, H.-Y., J. M. Koo, D.-J. Min, B.-D. Kwon, and H. S. Yoo (2010). Frequency-domain elastic full waveform inversion for VTI media. *Geophysical Journal International 183*(2), 884–904. 13, 14

Liao, S. (1992a). Application of process analysis method to the solution of 2-D nonlinear progressive gravity waves. 9

Liao, S. (2003). *Beyond perturbation: introduction to the homotopy analysis method*. CRC press. 8, 9

Liao, S. (2012). *Homotopy analysis method in nonlinear differential equations*. Springer. 8

Liao, S., D. Xu, and M. Stiassnie (2016). On the steady-state nearly resonant waves. *Journal of Fluid Mechanics 794*, 175–199. 9

Liao, S. J. (1992b). *The proposed homotopy analysis technique for the solution of nonlinear problems*. Ph. D. thesis, Ph. D. Thesis, Shanghai Jiao Tong University Shanghai. 8, 9

Liao, S.-J. (1999). A uniformly valid analytic solution of two-dimensional viscous flow over a semi-infinite flat plate. *Journal of Fluid Mechanics 385*, 101–128. 8, 9

Liao, S.-J. (2002). An analytic approximation of the drag coefficient for the viscous flow past a sphere. *International Journal of Non-Linear Mechanics 37*(1), 1–18. 9

Liao, S.-J. (2004). An analytic approximate approach for free oscillations of self-excited systems. *International Journal of Non-Linear Mechanics 39*(2), 271–280. 9

Liao, S.-J. (2011). On the homotopy multiple-variable method and its applications in the interactions of nonlinear gravity waves. *Communications in Nonlinear Science and Numerical Simulation 16*(3), 1274–1303. 9

Liao, S.-J. and A. Chwang (1998). Application of homotopy analysis method in nonlinear oscillations. *Journal of applied mechanics 65*(4), 914–922. 9

Liu, Q. and D. Peter (2019). Square-root variable metric based elastic full-waveform inversion—Part 2: uncertainty estimation. *Geophysical Journal International 218*(2), 1100–1120. 15

Liu, Q., D. Peter, and C. Tape (2019). Square-root variable metric based elastic full-waveform inversion–Part 1: Theory and validation. *Geophysical Journal International 218*(2), 1121–1135. 15

Liu, Q. H., Z. Q. Zhang, and X. M. Xu (2001). The hybrid extended born approximation and CG-FFT method for electromagnetic induction problems. *IEEE transactions on geoscience and remote sensing 39*(2), 347–355. 4

Lumley, D. (2010). 4d seismic monitoring of co 2 sequestration. *The Leading Edge 29*(2), 150–155. 11

Luo, S. and J. Qian (2012). Fast sweeping methods for factored anisotropic eikonal equations: multiplicative and additive factors. *Journal of Scientific Computing 52*(2), 360–382. 2

Lyapunov, A. M. (1992). The general problem of the stability of motion. *International journal of control 55*(3), 531–534. 8

Malcolm, A. and B. Willemsen (2016). Rapid 4D FWI using a local wave solver. *The Leading Edge 35*(12), 1053–1059. 13

Malovichko, M., N. Khokhlov, N. Yavich, and M. Zhdanov (2017). Approximate solutions of acoustic 3D integral equation and their application to seismic modeling and full-waveform inversion. *Journal of Computational Physics 346*, 318–339. 1, 3

Martin, J., L. C. Wilcox, C. Burstedde, and O. Ghattas (2012). A stochastic Newton MCMC method for large-scale statistical inverse problems with application to seismic inversion. *SIAM Journal on Scientific Computing 34*(3), A1460–A1487. 14, 16

Masmoudi, N. and T. Alkhalifah (2016). Traveltime approximations and parameter estimation for orthorhombic media. *Geophysics 81*(4), C127–C137. 2

Moore, M. G. (2008). Introduction to scattering theory. *https://web.pa.msu.edu/people/mmoore/852scattering 65*(1), 1–28. 6, 7

Moser, T. (1991). Shortest path calculation of seismic rays. *Geophysics 56*(1), 59–67. 1

Noble, M., A. Gesret, and N. Belayouni (2014). Accurate 3-D finite difference computation of traveltimes in strongly heterogeneous media. *Geophysical Journal International 199*(3), 1572–1585. 2

Oh, J.-W. and T. Alkhalifah (2016). Elastic orthorhombic anisotropic parameter inversion: An analysis of parameterization elastic orthorhombic anisotropic FWI. *Geophysics 81*(6), C279–C293. 14

Oh, J.-W. and T. Alkhalifah (2018). Optimal full-waveform inversion strategy for marine data in azimuthally rotated elastic orthorhombic media. *Geophysics 83*(4), R307–R320. 14

Operto, S., Y. Gholami, V. Prieux, A. Ribodetti, R. Brossier, L. Metivier, and J. Virieux (2013). A guided tour of multiparameter full-waveform inversion with multicomponent data: From theory to practice. *The Leading Edge 32*(9), 1040–1054. 13, 14

Osnabrugge, G., S. Leedumrongwatthanakun, and I. M. Vellekoop (2016). A convergent Born series for solving the inhomogeneous Helmholtz equation in arbitrarily large media. *Journal of computational physics 322*, 113–124. 6

Palit, A. and D. P. Datta (2016). Comparative study of homotopy analysis and renormalization group methods on Rayleigh and van der pol equations. *Differential Equations and Dynamical Systems 24*(4), 417–443. 9

Pelissetto, A. and E. Vicari (2002). Critical phenomena and renormalization-group theory. *Physics Reports 368*(6), 549–727. 8

Petra, N., J. Martin, G. Stadler, and O. Ghattas (2014). A computational framework for infinite-dimensional Bayesian inverse problems, Part ii: Stochastic Newton MCMC with application to ice sheet flow inverse problems. *SIAM Journal on Scientific Computing 36*(4), A1525–A1555. 16

Pfeffer, T. (2019). *Homotopy and renormalization group approaches for strongly correlated systems*. Ph. D. thesis, lmu. 9

Plessix, R.-E. and Q. Cao (2011). A parametrization study for surface seismic full waveform inversion in an acoustic vertical transversely isotropic medium. *Geophysical Journal International 185*(1), 539–556. 13, 14

Pratt, R., Z.-M. Song, P. Williamson, and M. Warner (1996). Two-dimensional velocity models from wide-angle seismic data by wavefield inversion. *Geophysical Journal International 124*(2), 323–340. 10

Pšenčík, I. and V. Farra (2017). Reflection moveout approximations for P-waves in a moderately anisotropic homogeneous tilted transverse isotropy layer. *Geophysics 82*(5), C175–C185. 2

Rawlinson, N., A. Fichtner, M. Sambridge, and M. K. Young (2014). Seismic tomography and the assessment of uncertainty. In *Advances in Geophysics*, Volume 55, pp. 1–76. Elsevier. 16

Rawlinson, N. and M. Sambridge (2004a). Multiple reflection and transmission phases in complex layered media using a multistage fast marching method. *Geophysics 69*(5), 1338–1350. 2

Rawlinson, N. and M. Sambridge (2004b). Wave front evolution in strongly heterogeneous layered media using the fast marching method. *Geophysical Journal International 156*(3), 631–647. 2

Ray, A., S. Kaplan, J. Washbourne, and U. Albertin (2017). Low frequency full waveform seismic inversion within a tree based Bayesian framework. *Geophysical Journal International 212*(1), 522–542. 16

Ray, A., A. Sekar, G. M. Hoversten, and U. Albertin (2016). Frequency domain full waveform elastic inversion of marine seismic data from the alba field using a Bayesian trans-dimensional algorithm. *Geophysical Journal International 205*(2), 915–937. 16

Robertsson, J. O. (1996). A numerical free-surface condition for elastic/viscoelastic finite-difference modeling in the presence of topography. *Geophysics 61*(6), 1921–1934. 1

Rose, J. H. (2001). "single-sided" focusing of the time-dependent Schrödinger equation. *Physical Review A 65*(1), 012707. 19

Rose, J. H. (2002). 'single-sided'autofocusing of sound in layered materials. *Inverse problems 18*(6), 1923. 19

Routh, P., G. Palacharla, I. Chikichev, and S. Lazaratos (2012). Full wavefield inversion of time-lapse data for improved imaging and reservoir characterization. In *SEG Technical Program Expanded Abstracts 2012*, pp. 1–6. Society of Exploration Geophysicists. 11

Schoenberg, M. and C. M. Sayers (1995). Seismic anisotropy of fractured rock. *Geophysics 60*(1), 204–211. 13

Sethian, J. A. (1996). A fast marching level set method for monotonically advancing fronts. *Proceedings of the National Academy of Sciences 93*(4), 1591–1595. 2

Sethian, J. A. and A. M. Popovici (1999). 3-D traveltime computation using the fast marching method. *Geophysics 64*(2), 516–523. 2

Silva, N. V. d., A. Ratcliffe, V. Vinje, and G. Conroy (2016). A new parameter set for anisotropic multiparameter full-waveform inversion and application to a North Sea data set. *Geophysics 81*(4), U25–U38. 14

Skjervheim, J., B. Ruud, S. Aanonsen, G. Evensen, and T. Johansen (2006). Using the ensemble Kalman filter with 4D data to estimate properties and lithology of reservoir rocks. In *ECMOR X-10th European Conference on the Mathematics of Oil Recovery*. 11

Skjervheim, J.-A., G. Evensen, S. I. Aanonsen, B. O. Ruud, T.-A. Johansen, et al. (2005). Incorporating 4D seismic data in reservoir simulation models using ensemble Kalman filter. In *SPE Annual Technical Conference and Exhibition*. Society of Petroleum Engineers. 11

Stovas, A. and T. Alkhalifah (2012). A new traveltime approximation for TI media. *Geophysics 77*(4), C37–C42. 2

Stovas, A., N. Masmoudi, and T. Alkhalifah (2016). Application of perturbation theory to a P-wave eikonal equation in orthorhombic media eikonal equation in orthorhombic media. *Geophysics 81*(6), C309–C317. 2

Tao, Y. and M. K. Sen (2013). Frequency-domain full waveform inversion with a scattering-integral approach and its sensitivity analysis. *Journal of Geophysics and Engineering 10*(6), 065008. 10, 15

Tarantola, A. (1986). A strategy for nonlinear elastic inversion of seismic reflection data. *Geophysics 51*(10), 1893–1903. 1, 10, 14

Tarantola, A. (2005). *Inverse problem theory and methods for model parameter estimation*, Volume 89. siam. 15

Tarantola, A. and B. Valette (1982a). Generalized nonlinear inverse problems solved using the least squares criterion. *Reviews of Geophysics 20*(2), 219–232. 1, 15

Tarantola, A. and B. Valette (1982b). Inverse problems= quest for information. *J. geophys 50*(3), 150–170. 10

Taylor, J. R. (1972). Scattering theory, the quantum theory on nonrelativistic collisions, john willey & sons. *Inc., New York, London, Sydney, Toronto*. 3, 4

Thurin, J., R. Brossier, and L. Métivier (2017). An ensemble-transform Kalman filter: Full-waveform inversion scheme for uncertainty estimation. In *SEG Technical Program Expanded Abstracts 2017*, pp. 1307–1313. Society of Exploration Geophysicists. 16

Ursin, B. (1982). Quadratic wavefront and traveltime approximations in inhomogeneous layered media with curved interfaces. *Geophysics 47*(7), 1012–1021. 2

Valenciano, A. A., B. Biondi, and A. Guitton (2006). Target-oriented wave-equation inversion. *Geophysics 71*(4), A35–A38. 12

Van Den Berg, P. M. and R. E. Kleinman (1997). A contrast source inversion method. *Inverse problems 13*(6), 1607. 10

Vidale, J. (1988). Finite-difference calculation of travel times. *Bulletin of the Seismological Society of America 78*(6), 2062–2076. 2

Vinje, V., E. Iversen, and H. Gjøystdal (1993). Traveltime and amplitude estimation using wavefront construction. *Geophysics 58*(8), 1157–1166. 1

Virieux, J. and S. Operto (2009). An overview of full-waveform inversion in exploration geophysics. *Geophysics 74*(6), WCC1–WCC26. 10, 11, 13, 15

Waheed, bin, U., T. Alkhalifah, and H. Wang (2015). Efficient traveltime solutions of the acoustic TI eikonal equation. *Journal of Computational Physics 282*, 62–76. 2

Waheed, U. b. and T. Alkhalifah (2017). A fast sweeping algorithm for accurate solution of the tilted transversely isotropic eikonal equation using factorization. *Geophysics 82*(6), WB1–WB8. 2

Waheed, U. b., T. Alkhalifah, and A. Stovas (2013). Diffraction traveltime approximation for TI media with an inhomogeneous background. *Geophysics 78*(5), WC103–WC111. 2

Waheed, U. b., I. Pšenčík, V. Červenỳ, E. Iversen, and T. Alkhalifah (2013). Two-point paraxial traveltime formula for inhomogeneous isotropic and anisotropic media: Tests of accuracy. *Geophysics 78*(5), WC65–WC80. 2

Waldhauser, F. and W. L. Ellsworth (2000). A double-difference earthquake location algorithm: Method and application to the northern hayward fault, California. *Bulletin of the Seismological Society of America 90*(6), 1353–1368. 12

Wang, C., J. Zhu, S. Liao, and I. Pop (2003). On the explicit analytic solution of cheng–chang equation. *International Journal of Heat and Mass Transfer 46*(10), 1855–1860. 9

Wapenaar, K., F. Broggini, E. Slob, and R. Snieder (2013). Three-dimensional single-sided Marchenko inverse scattering, data-driven focusing, Green's function retrieval, and their mutual relations. *Physical Review Letters 110*(8), 084301. 19

Wapenaar, K., J. Thorbecke, J. Van Der Neut, F. Broggini, E. Slob, and R. Snieder (2014). Marchenko imaging. *Geophysics 79*(3), WA39–WA57. 19

Ware, J. A. and K. Aki (1969). Continuous and discrete inverse-scattering problems in a stratified elastic medium. i. plane waves at normal incidence. *The journal of the Acoustical Society of America 45*(4), 911–921. 19

Watson, L. T. (1989). Globally convergent homotopy methods: a tutorial. *Applied Mathematics and Computation 31*, 369–396. 8

Weglein, A. B., F. V. Araújo, P. M. Carvalho, R. H. Stolt, K. H. Matson, R. T. Coates, D. Corrigan, D. J. Foster, S. A. Shaw, and H. Zhang (2003). Inverse scattering series and seismic exploration. *Inverse problems 19*(6), R27. 18

Willemsen, B., A. Malcolm, and W. Lewis (2016). A numerically exact local solver applied to salt boundary inversion in seismic full-waveform inversion. *Geophysical Journal International 204*(3), 1703–1720. 13

Wilson, K. G. (1971). Renormalization group and critical phenomena. i. renormalization group and the Kadanoff scaling picture. *Physical review B 4*(9), 3174. 7, 8

Wu, R.-S. and H. He (2019). Extension of Gel'fand–Levitan–Marchenko solution for layered acoustic media to including oblique incidence for simultaneous ρ-v inversion. In *SEG Technical Program Expanded Abstracts 2019*, pp. 1475–1479. Society of Exploration Geophysicists. 19

Wu, R.-S. and L. Huang (1995). Reflected wave modeling in heterogeneous acoustic media using the De Wolf approximation. In *Mathematical Methods in Geophysical Imaging III*, Volume 2571, pp. 176–187. International Society for Optics and Photonics. 7

Wu, R.-S., J. Luo, and G. Chen (2016). Seismic envelope inversion and renormalization group theory: Nonlinear scale separation and slow dynamics. In *SEG Technical Program Expanded Abstracts 2016*, pp. 1346–1351. Society of Exploration Geophysicists. 6, 7

Wu, R.-S. and M. N. Toksöz (1987). Diffraction tomography and multisource holography applied to seismic imaging. *Geophysics 52*(1), 11–25. 4

Wu, R.-S., B. Wang, and C. Hu (2015). Renormalized nonlinear sensitivity kernel and inverse thin-slab propagator in T-matrix formalism for wave-equation tomography. *Inverse Problems 31*(11), 115004. 7

Wu, R.-S., X.-B. Xie, and X.-Y. Wu (2007). One-way and one-return approximations (De Wolf approximation) for fast elastic wave modeling in complex media. *Advances in Geophysics 48*, 265–322. 6

Wu, R.-S. and Y. Zheng (2014). Non-linear partial derivative and its De Wolf approximation for non-linear seismic inversion. *Geophysical Journal International 196*(3), 1827–1843. 11

Xu, S., A. Stovas, and Q. Hao (2017). Perturbation-based moveout approximations in anisotropic media. *Geophysical Prospecting 65*(5), 1218–1230. 2

Yakhot, V. and S. A. Orszag (1986). Renormalization group analysis of turbulence. i. basic theory. *Journal of scientific computing 1*(1), 3–51. 8

Yang, D., F. Liu, S. Morton, A. Malcolm, and M. Fehler (2016). Time-lapse full-waveform inversion with ocean-bottom-cable data: Application on Valhall field. *Geophysics 81*(4), R225–R235. 11

Yao, J., A.-C. Lesage, F. Hussain, and D. J. Kouri (2015). Scattering theory and volterra renormalization for wave modeling in heterogeneous acoustic media. In *SEG Technical Program Expanded Abstracts 2015*, pp. 3594–3600. Society of Exploration Geophysicists. 7

Yuan, S., N. Fuji, S. Singh, and D. Borisov (2017). Localized time-lapse elastic waveform inversion using wavefield injection and extrapolation: 2-D parametric studies. *Geophysical Journal International 209*(3), 1699–1717. 11, 13

Zhang, J. and M. N. Toksöz (1998). Nonlinear refraction traveltime tomography. *Geophysics 63*(5), 1726–1737. 10

Zhang, Z. and L. Huang (2013). Double-difference elastic-waveform inversion with prior information for time-lapse monitoring. *Geophysics 78*(6), R259–R273. 11

Zhao, H. (2005). A fast sweeping method for eikonal equations. *Mathematics of computation 74*(250), 603–627. 2

Zhdanov, M. S. (2002). *Geophysical inverse theory and regularization problems*, Volume 36. Elsevier. 1, 3, 4

Zhdanov, M. S. and S. Fang (1996). Three-dimensional quasi-linear electromagnetic inversion. *Radio Science 31*(4), 741–754. 4

Zheng, Y., P. Barton, and S. Singh (2011). Strategies for elastic full waveform inversion of time-lapse ocean bottom cable (obc) seismic data. In *SEG Technical Program Expanded Abstracts 2011*, pp. 4195–4200. Society of Exploration Geophysicists. 11

Zhu, H., S. Li, S. Fomel, G. Stadler, and O. Ghattas (2016). A bayesian approach to estimate uncertainty for full-waveform inversion using a priori information from depth migration. *Geophysics 81*(5), R307–R323. 16

Papers

I

OXFORD

Journal of Geophysics and Engineering

Journal of Geophysics and Engineering (2019) **00**, 1–22 doi:10.1093/jge/gxz105

On the applicability of a renormalized Born series for seismic wavefield modelling in strongly scattering media

Xingguo Huang [1,2,*], **Morten Jakobsen** [1] **and Ru-Shan Wu** [2]

[1] University of Bergen, Department of Earth Science, Allegaten 41, 5020 Bergen, Norway
[2] University of California, Earth and Planetary Sciences, Modeling and Imaging Laboratory, 1156 High Street, Santa Cruz, CA 95064, USA

*Corresponding author: Xingguo Huang. E-mail: xingguo.huang@uib.no, xingguo.huang19@gmail.com

Received 25 April 2019, revised 4 November 2019
Accepted for publication 15 November 2019

Abstract

Scattering theory is the basis for various seismic modeling and inversion methods. Conventionally, the Born series suffers from an assumption of a weak scattering and may face a convergence problem. We present an application of a modified Born series, referred to as the convergent Born series (CBS), to frequency-domain seismic wave modeling. The renormalization interpretation of the CBS from the renormalization group prospective is described. Further, we present comparisons of frequency-domain wavefields using the reference full integral equation method with that using the convergent Born series, proving that both of the convergent Born series can converge absolutely in strongly scattering media. Another attractive feature is that the Fast Fourier Transform is employed for efficient implementations of matrix–vector multiplication, which is practical for large-scale seismic problems. By comparing it with the full integral equation method, we have verified that the CBS can provide reliable and accurate results in strongly scattering media.

Keywords: seismic modeling, integral equation, wave scattering, renormalization theory

1. Introduction

The integral equation (IE) method based scattering theory (Aki & Richards 1980; Zhdanov 2002) is a powerful tool in the modeling of wave propagation, which has a wide application in data processing (Weglein *et al.* 1997, 2003), modeling (Innanen 2009), and seismic inversion (Wu & Zheng 2014; Snieder 1990; Berkhout 2012; Zhang & Weglein 2009; Alkhalifah & Wu 2016; Alkhalifah 2016; Wu & Alkhalifah 2017; Huang *et al.* 2019). An attractive features of the IE method is that only the anomalous volume (scattering volume) needs to be discretized, which leads to more efficient computation (Malovichko *et al.* 2017). The implementation of the IE method involves dividing the medium into background and anomalous parts (Zuberi & Alkhalifah 2014).

The Born series has an assumption of weak scattering (Wu & Toksoz 1987; Kouri & Vijay 2003). Convergence issues may occur in strongly scattering areas, such as salt structures. It is important for seismic imaging in such strong-contrast regions to address the weak-scattering assumption. One important approach that addresses the divergence problem is to renormalize the Born series using various renormalization approaches (Eftekhar *et al.* 2018).

There are several approaches to develop a convergent scattering series. There have been successful attempts to introduce the De Wolf approximation (De Wolf 1971, 1985) into seismic scattering series (Wu & Huang 1995). The renormalized scattering series is derived by Jakobsen & Wu (2016) using the T-matrix and De Wolf series. The T-matrix is a

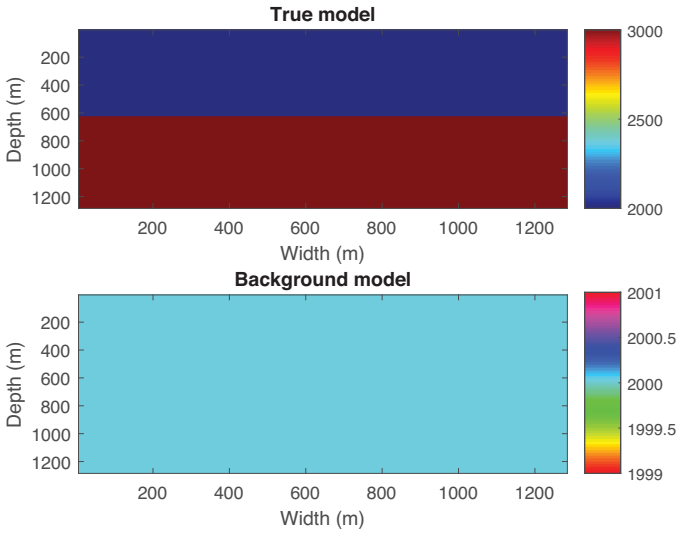

Figure 1. The two-layered and background models. The size of the model is 1280 m × 1280 m.

transition operator that includes all the effects of multiple scattering. Renormalization group method has been applied to seismic waveform inversion (Wu *et al.* 2015) and envelope inversion (Wu *et al.* 2016). Signicant progress has been made by Yao *et al.* (2015) by dividing the renormalized Lippmann–Schwinger equation into two sub-Volterra type integral equations and introducing wavefield separation. Recently, by employing the renormalization group (RG) theory, we developed a renormalized version of the Born series. Numerical tests showed that this solution can be convergent for large-contrast media (Jakobsen *et al.* 2018). Our renormalization group approach is based on the use of an auxillary set of scale-dependent scattering potentials, which gradually evolves toward the real physical scattering potential.

Another interesting convergent Born series (CBS) was proposed by Osnabrugge *et al.* (2016) to solve the Helmholtz equation. The convergent Born series can guarantee convergence by localizing the wavefields, in which the contracted preconditioner must be specified. Actually, the CBS can be understood as a kind of renormalized Born series based on the RG theory. In the early 1970s, the renormalization procedure was proposed by Gell-Mann & Low (1954) for problems of infinity and divergence. From the early 1970s (Wilson 1971), RG theory has been widely used to remove divergence in quantum physics, critical phenomena, dynamical systems and statistical mechanics, etc. The major purpose of the RG theory is to obtain stable properties of physical systems (Goldenfeld 1992). Based on the above fact, Chen *et al.* (1994, 1996) applied the RG approach to deriving global asymptotic solutions of differential equations. Since then, the RG theory has been well developed and significant progress in renormalizing perturbation series (Yakhot & Orszag 1986; Pelissetto & Vicari 2002; Delamotte 2004; Kirkinis 2008, 2012) has been made.

The purpose of this paper is to extend the CBS of Osnabrugge *et al.* (2016) to seismic scattering problems for strongly scattering media and compare the CBS with the full integral equation method. The convergent Born series is obtained by localizing the Green's function with a dampling factor. From the technical point of view, the CBS removes the divergence by localizing the wavefields and controlling convergence using a preconditioner. Thus, the CBS can be understood as a kind of renormalized Born series. After presenting the convergent Born series, we analyze the theoretical background of the convergent Born series from the renormalization group theory prospective and its nature of localization. Then, we give numerical results of frequency-domain wavefields. To quantatively compare the results from the CBS and full integral equation methods, we present numerical results for results of pressure wavefields in strongly scattering media.

2. Integral equations for the seismic scattering problem

2.1. *The Lippmann–Schwinger equation*

The Helmholtz equation can be written as (Morse & Feshback 1953):

$$\nabla^2\psi(\mathbf{r}) + k^2\psi(\mathbf{r}) = -s(\mathbf{r}), \tag{1}$$

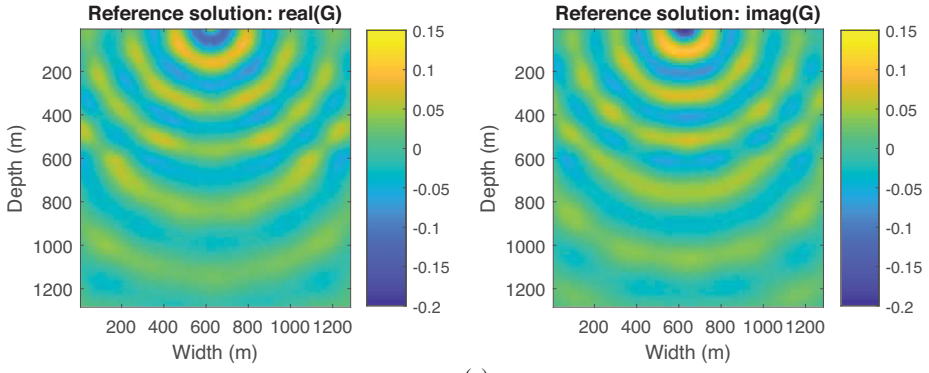

(a)

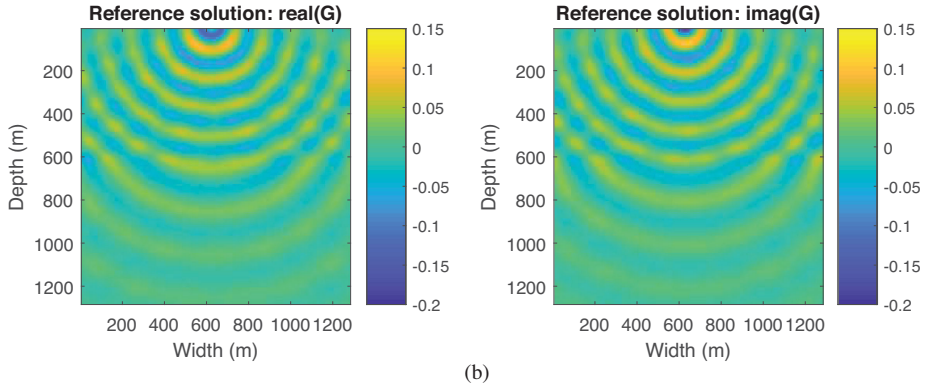

(b)

Figure 2. Frequency-domain wavefields for the frequency of (a) 10 Hz and (b) 15 Hz for the two-layer model using the IE method.

with the wavenumber k and source signal $s(\mathbf{r})$, where ∇ is the second-order differentiation. Defining $\psi_b(\mathbf{r})$ as the background field,

$$\nabla^2\psi_b(\mathbf{r}) + k_b^2\psi_b(\mathbf{r}) = -s(\mathbf{r}), \tag{2}$$

where k_b is the background wavenumber. The total wavefield $\psi(\mathbf{r})$ can expressed as

$$\psi(\mathbf{r}) = \psi_b(\mathbf{r}) + \psi_s(\mathbf{r}), \tag{3}$$

where k_s is the scattered wavenumber and $k_s = k - k_b$. Substituting equation (3) into (1), we have the following equation for the scattered wavefields $\psi_s(\mathbf{r})$:

$$-\nabla^2\psi_s(\mathbf{r}) - k_b^2\psi_s(\mathbf{r}) = k_s^2(\mathbf{r})\left(\psi_b(\mathbf{r}) + \psi_s(\mathbf{r})\right). \tag{4}$$

From equations (2) and (4), we get the scattered wavefields $\psi_s(\mathbf{r})$

$$\psi_s(\mathbf{r}) = k_b^2\int_D G_b(\mathbf{r},\mathbf{r}')\,\chi(\mathbf{r}')\,\psi(\mathbf{r}')\,d^3\mathbf{r}' \tag{5}$$

with

$$\chi(\mathbf{r}') = \frac{k^2 - k_b^2}{k_b^2}, \tag{6}$$

where the background Green's function G_b can also be calculated with analytical expressions for homogeneous media, and the ray theory (Cerveny 2005; Huang & Greenhalgh 2019), Gaussian beam (Huang *et al.* 2016a, b, 2018; Huang 2018) or finite difference method (Carcione 2007) for inhomogeneous media. Finally, we can get the Lippmann–Schwinger equation:

$$\psi(\mathbf{r}) = \psi_b(\mathbf{r}) + k_b^2\int_D G_b(\mathbf{r},\mathbf{r}')\,\chi(\mathbf{r}')\,\psi(\mathbf{r}')\,d^3\mathbf{r}'. \tag{7}$$

2.2. *The conventional Born series*

Equation (7) has the formal solution as

$$\psi(\mathbf{r},k) = \psi_b(\mathbf{r},k)\left(1 - k_b^2\int_D G_b(\mathbf{r},\mathbf{r}',k)\,\chi(\mathbf{r}')\,d^3\mathbf{r}'\right)^{-1}. \tag{8}$$

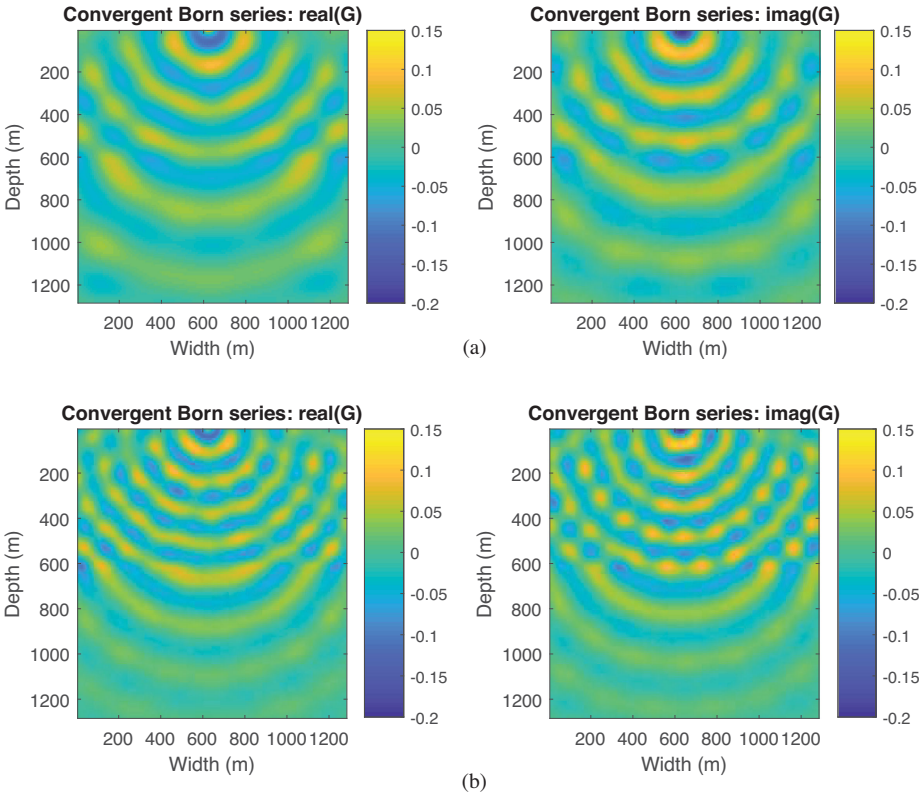

Figure 3. Frequency-domain wavefields for the frequency of (a) 10 Hz and (b) 15 Hz for the two-layered model using the CBS method.

This equation can be solved iteratively:

$$\psi(\mathbf{r}_g, \mathbf{r}_s, k) = \psi_b(\mathbf{r}_g, \mathbf{r}_s, k_b) + k_b^2 \int_D G_b(\mathbf{r}_g, \mathbf{r}')\chi(\mathbf{r}')\psi_b(\mathbf{r}', \mathbf{r}_s)\, d\mathbf{r}' + k_b^4 \int_D d\mathbf{r}' G_b(\mathbf{r}_g, \mathbf{r}')\chi(\mathbf{r}') \int_D d\mathbf{r}'' \times G_b(\mathbf{r}', \mathbf{r}'')\chi(\mathbf{r}'')\psi_b(\mathbf{r}'', \mathbf{r}_s) + \cdots \quad (9)$$

After taking the first-order term of the conventional Born series, we have the Born approximation:

$$\psi(\mathbf{r}_g, \mathbf{r}_s, k) = \psi_b(\mathbf{r}_g, \mathbf{r}_s, k) + k_b^2 \int_D G_b(\mathbf{r}_g, \mathbf{r}', k)\chi(\mathbf{r}')\psi_b(\mathbf{r}', \mathbf{r}_s, k) d\mathbf{r}'. \quad (10)$$

The Born series is the basis for seismic forward and inverse problems. However, because the Born series assumes weak scattering, it can only converge when the scattering potential is weak (Kirkinis 2008; Wu *et al.* 2007). For real applications, the strength of the contrast in the medium is relatively strong. Divergence may occur in media with strong contrasts.

2.3. *Convergent Born series*

This section revisits the equations for the CBS (Osnabrugge *et al.* 2016). Equations are presented for an arbitrary strong medium. The convergent Born series refers to the situation in which the value of the coefficient of each iteration term is less than unity. The key point for modification of the conventional Born series is to introduce a damping parameter ϵ and a preconditioner γ. Here, we review the derivation of the CBS. To this end, we start with the conventional Born series and apply the preconditioner to both sides of the conventional Born series. It should be noted that the damping parameter ϵ, which is related to the attenuation of the wavefields in the background medium, is also important for the convergence.

In operator form, the Born series (9) can be written as follows:

$$\psi = G\chi\psi + GS, \quad (11)$$

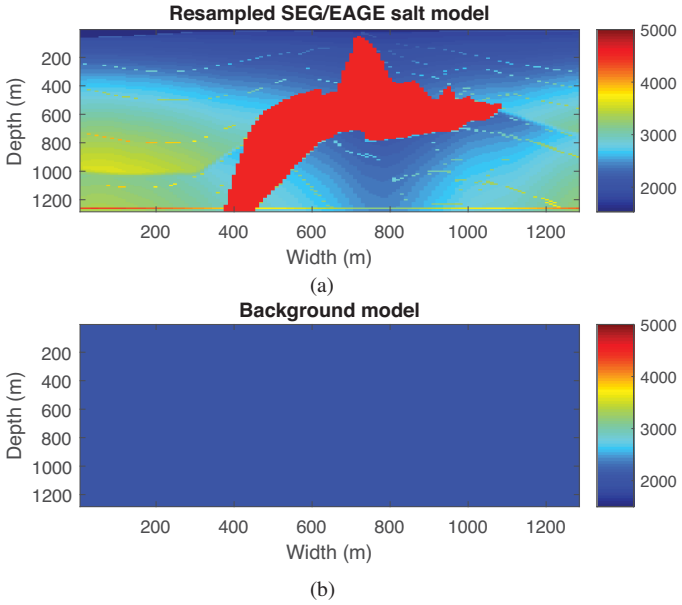

Figure 4. (a) Resampled version of the SEG/EAGE salt model and (b) background model.

where S is the source term, which represents the source wavelet in frequency-space domain, and G is the Green's operator, which represents the Green's function G_b in equation (9). Note that S and ψ are vectors, and G is dense operator filled with various Green's functions. χ is a diagonal matrix. By applying a preconditioner γ to both sides of equation (11), Osnabrugge *et al.* (2016) obtained

$$\gamma\psi = \gamma G\chi\psi + \gamma GS. \tag{12}$$

Then, we reformulate equation (12) as

$$\psi = \Lambda\psi + \gamma GS, \tag{13}$$

with

$$\Lambda = \gamma G\chi - \gamma + 1, \tag{14}$$

where

$$\gamma(\mathbf{r}) = \frac{i}{\epsilon}\chi(\mathbf{r}). \tag{15}$$

The combination of the parameters γ and ϵ can ensure that the largest eigenvalue of Λ is smaller than unity. The details of choice of parameter ϵ will be discussed in the section Implementation. The modified Born series is explained by the following renormalized Born series:

$$\psi = \left(1 + \Lambda + \Lambda^2 + \Lambda^3 + \cdots\right)\gamma GS. \tag{16}$$

The iteration form solution is $\psi = \Lambda\psi + \gamma GS$ with the initial solution $\psi_b = \gamma GS$. The background Green's function can be written as (Osnabrugge *et al.* 2016)

$$G_b(k) = \frac{1}{|k|^2 - k_b^2 - i\epsilon}, \tag{17}$$

and in the real-space domain (Osnabrugge *et al.* 2016)

$$G_b = \frac{e^{i|\mathbf{r}|\sqrt{k_b^2 + i\epsilon}}}{4\pi|\mathbf{r}|}, \tag{18}$$

where k is the wavenumber vector in the real medium.

Because of the introduction of the coefficient of each iteration term Λ and preconditioner γ into the Born series, the modified Born series is convergent. Mathematically, Osnabrugge *et al.* (2016) demonstrated that the modified Born series can converge by combining the two parameters and given the suggestions of choice of the parameters in the optimum scale.

Here, we aim to apply the CBS method to seismic wave modeling problems and provide the renormalization interpretation of the convergent Born series. Due the strong contrast in the seismic problems, it is more challenging. We perform numerical tests and investigate how to choose the coefficient Λ and preconditioner γ for each iteration term, and the dependence on the parameter ϵ. We will look at how the parameter ϵ changes for different models with different strong scattering cases.

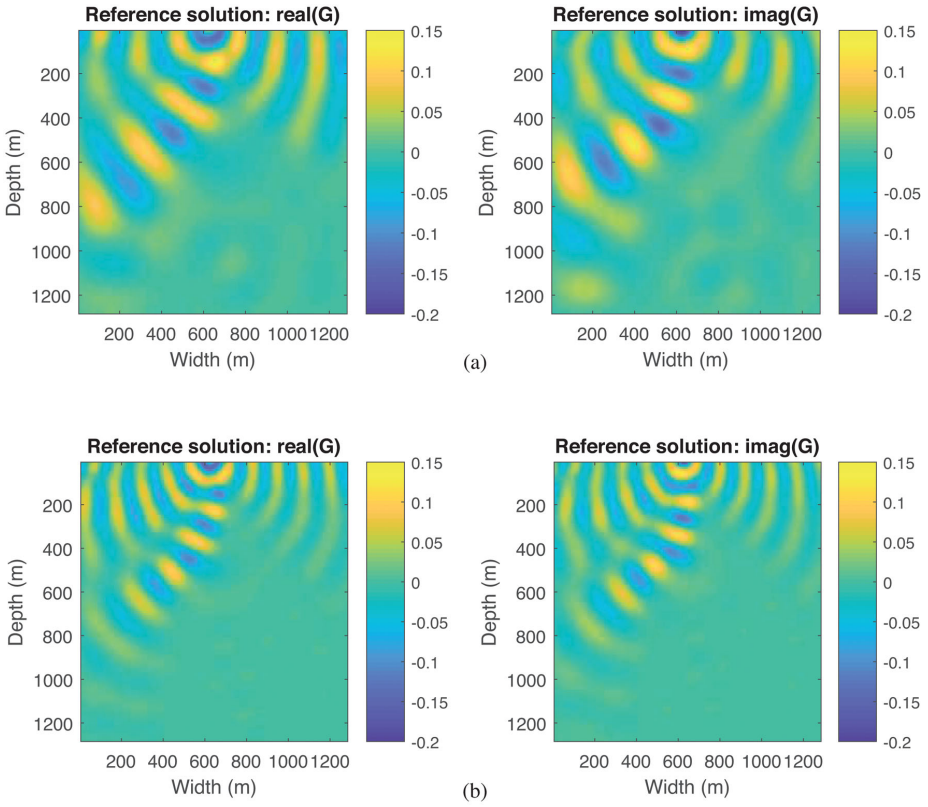

Figure 5. Frequency-domain wavefields for the frequency of (a) 10 Hz and (b) 15 Hz for the SEG/EAGE salt model using the full integral equation method.

3. Interpretation of the convergent Born series

In this section, we discuss the convergent Born series from the renormalization perspective.

3.1. *Step-by-step local interaction*

The modified version of the Born series developed by Osnabrugge *et al.* (2016) is called the convergent Born series. In this modified Born series, a preconditioner γ is introduced. By combining the preconditioner γ and parameter ϵ, the iteration computation satisfies the convergence condition of the Born series.

Actually, the concepts of the locality of wavefields explain how step-by-step propagators prevent the CBS from divergence. From equation (13), we can see that for the conventional Born series, each term involves integrations over the whole volume, which leads to the divergence problems of strongly scattering medium. The CBS makes the total energy in the background medium localized and finite so the volume integral in each term will not blow up. It compensates the damped wavefield by introducing an imaginary part with an opposite sign into the scattering potential V. This means that in the latter procedure the wavefield will grow when interacting with the scattering potential, and therefore compensate the energy loss during propagation in the background medium. In this way, those interactions always act locally, and thus can be regarded as short-range interactions. The iterations will continue until the wavefields cover the whole region with accepted accuracy. Physically, this can be explained as the renormalization process. According to Wilson's RG theory, one can first integrate out the local interactions and then derive the effective action operator, and then go to the next level to calculate the local interactions based on the effective interaction operator. The RG procedure in CBS is more like the mathematician's renormalization procedure

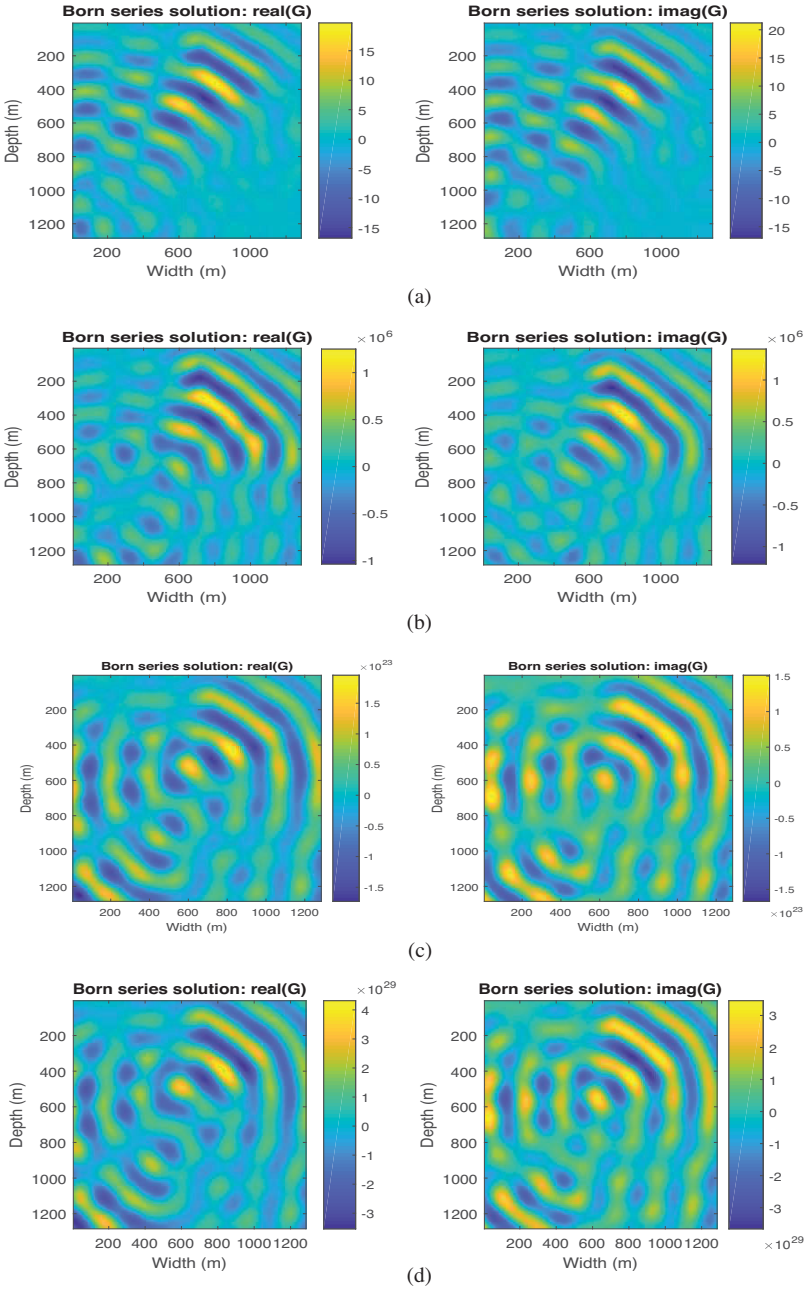

Figure 6. Frequency-domain wavefields with the frequency of 10 Hz for the SEG/EAGE salt model using the BS method with (a) 20, (b) 50, (c) 80 and (d) 100 iterations.

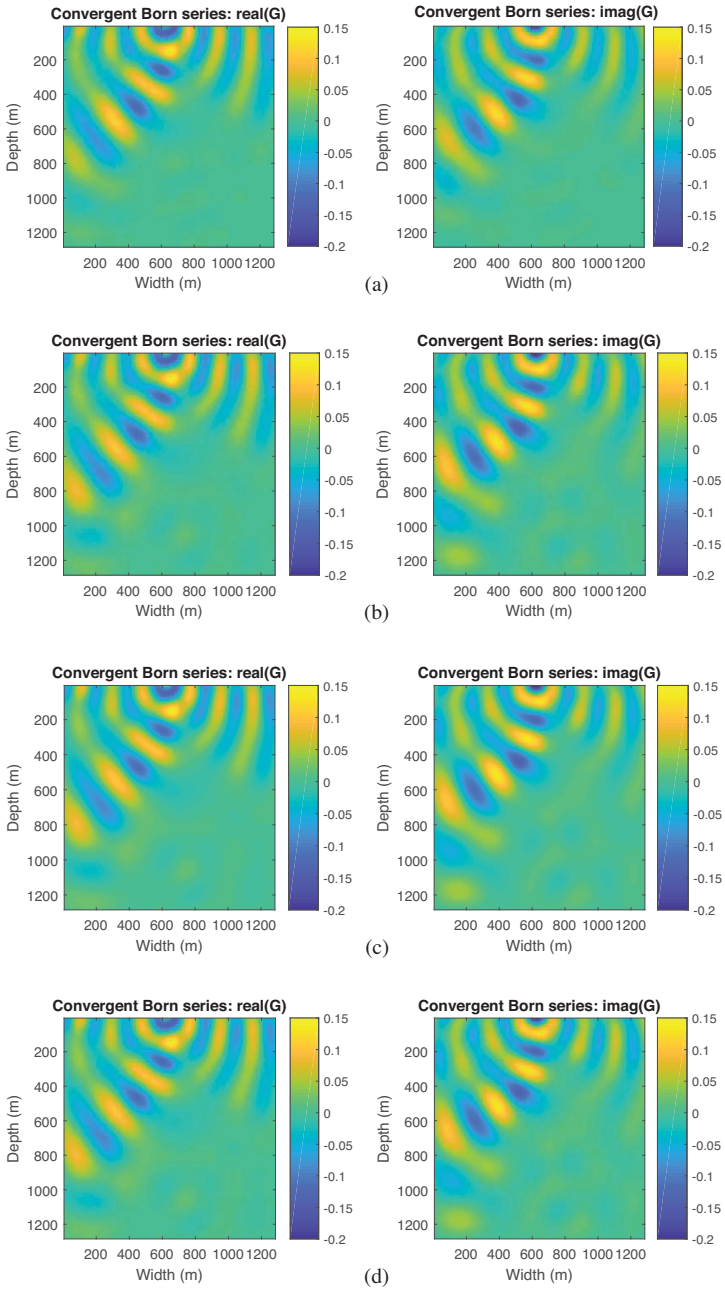

Figure 7. Frequency-domain wavefields with the frequency of 10 Hz for the SEG/EAGE salt model using the CBS method with (a) 20, (b) 50, (c) 80 and (d) 100 iterations.

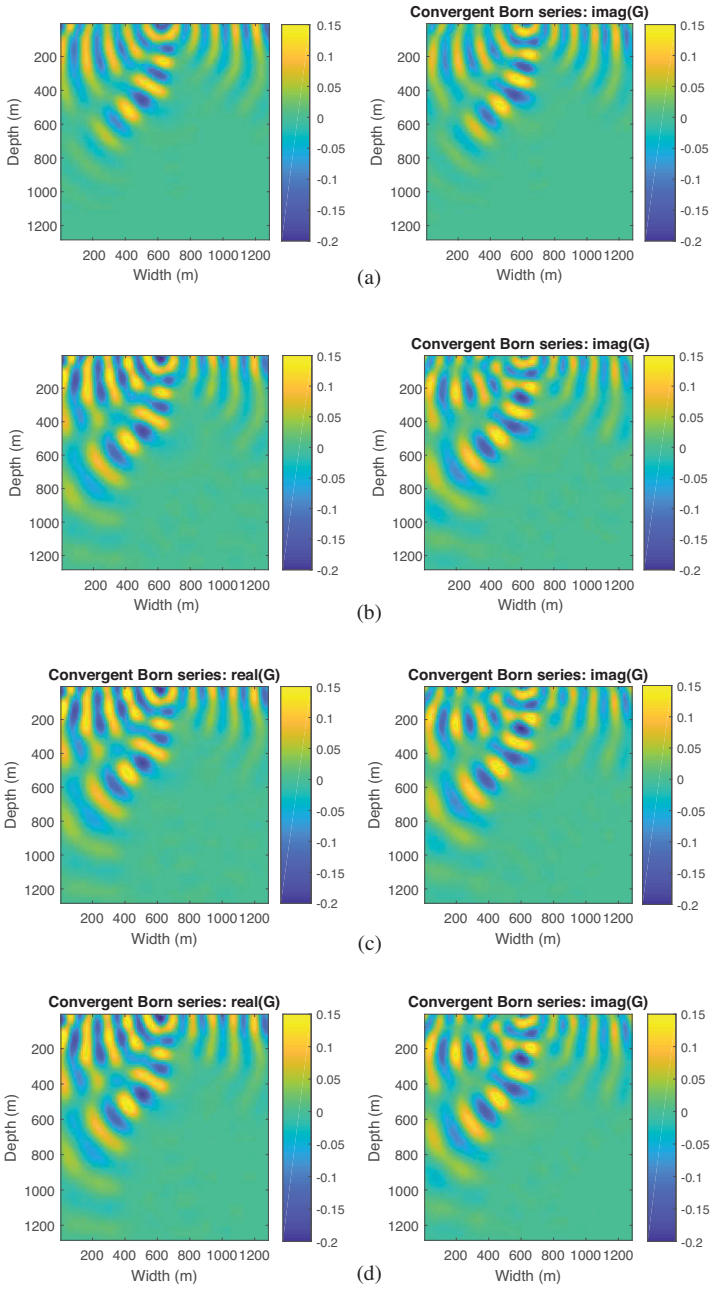

Figure 8. Frequency-domain wavefields with the frequency of 15 Hz for the SEG/EAGE salt model using the CBS method with (a) 20, (b) 50, (c) 80 and (d) 100 iterations.

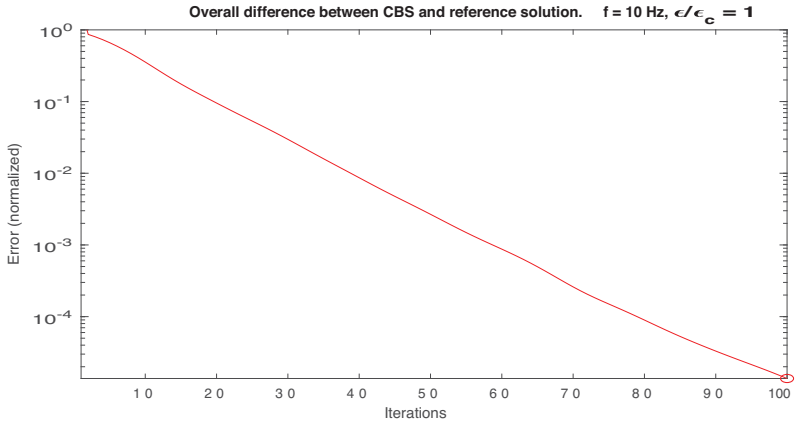

(a)

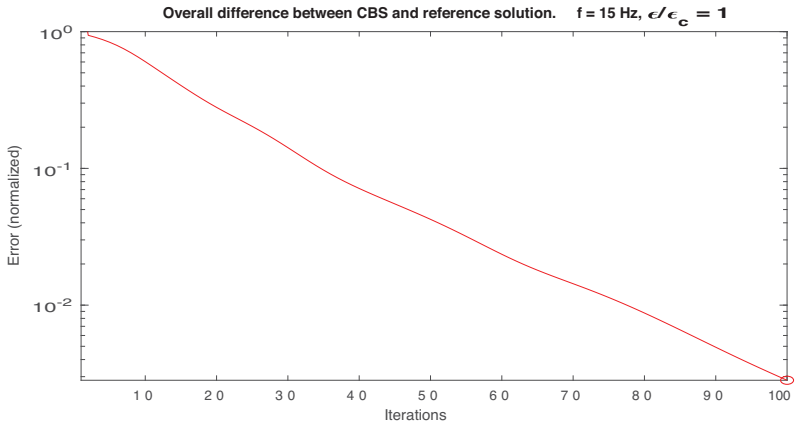

(b)

Figure 9. Convergence property of the CBS for the (a) 10 Hz and (b) 15 Hz simulations of the two-layer model.

(Chen *et al.* 1996) using RG theory as a floating initial condition. At each step, the calculated field is treated as a new initial wavefield for further propagation. This is different from Wilson's multi-scale RG procedure.

4. Implementation

In this section, we give the coordinate representation for the CBS. The advantage of this representation is that it is easy to relate two adjacent scattering potentials. Using the coordinate representation, equation (13) can be rewritten as

$$\psi(\mathbf{r}) = \gamma(\mathbf{r})\, G(\mathbf{r})\, S + \Lambda(\mathbf{r}, \mathbf{r}')\, \psi(\mathbf{r}). \tag{19}$$

The entire model is discretized into $N_x \times N_z$ in the two-dimensional case. Then, we have

$$\psi_{m,n}(\mathbf{r}) = \gamma(\mathbf{r})\, G_{m,n}(\mathbf{r})\, S + \sum_{m=1}^{N_x} \sum_{n=1}^{N_z} \Lambda_{m,n}(\mathbf{r}, \mathbf{r}')\, \psi_{m,n}(\mathbf{r}), \tag{20}$$

where $i = 1, \ldots, N_x$ and $j = 1, \ldots, N_z$.

It should be noted that, to compute the wavefields at the receivers along the surface, we need to compute the wavefields from the sources to any subsurface point and the background Green's functions from receivers to any subsurface point. For computing the wavefields at any subsurface point, we need compute the wavefields in the background

medium and the Green's functions from any subsurface point to any subsurface point (the Green's function from volume to volume G_{VV}). Then we need compute Λ, which is used for the high-order terms of the CBS. The workflow for implementing the renormalized Born series can be found in Algorithm 1.

Algorithm 1 Pseudo code for renormalized Born series

Initialisation: frequency, maximum iteration number $N_{\max}$ and the parameter ϵ
m = **true model,** m_0 = **background model;**
for $n = 0$ **to** $n = N_{\max}$ **do**
  $\chi = k^2 - k_0^2 - i\epsilon$
  $kb = \sqrt{k_0^2 + i\epsilon}$
  $n = n + 1$
  if $n == 0$ **then**
    $G_{VV}^{(b)} = Green(VV, kb)$
    $G_{VS}^{(b)} = Green(VS, kb)$
    $G_{VR}^{(b)} = Green(VR, kb)$
    $\psi^{(b)} = GS$
  end
  $\gamma(\mathbf{r}) = \frac{i}{\epsilon}\chi(\mathbf{r})$
  $\Lambda = \gamma G_{VV}\chi - \gamma + 1$
  $\psi = \Lambda\psi + \gamma G_{VS}S$
  dr=Error $(\psi_{CBS}, \psi_{FullIntegral})$
end for

5. Choice of parameter ϵ in the scale of seismic modeling

An important issue for the CBS is to choose the parameter ϵ. From the analysis in the above section, it can be found that the stronger the scatters (large-contrast), the higher the required parameter ϵ. This is because to eliminate the divergence the wavefields should be strongly localized. From equation (19), one can see that the higher the parameter ϵ, the stronger the attenuation of the background Green's functions. This means that there is a compromise between the demand on the convergence of the CBS and the computational cost. After conducting numerical tests, we find that the parameter ϵ should be chosen as follows:

$$\epsilon = 0.1 \times \max|k^2 - k_b^2| \qquad \text{if} f < 3, \tag{21}$$

and

$$\epsilon = \max|k^2 - k_b^2| \qquad \text{if} f > 3. \tag{22}$$

After investigating the convergence of the convergent Born series, Fast-Fourier Transform (FFT) is used, which can accelerate the computation in the implementation. Following Osnabrugge *et al.* (2016), we employ the FFT technique for an efficient matrix-free implementation. The FFT method has been used for integral equation modeling (Liu *et al.* 2001; Gao & Torres-Verdin 2006). The matrix–vector multiplications can be expressed as

$$G\chi = \mathcal{F}^{-1}[\mathcal{F}[G]\mathcal{F}[\chi]], \tag{23}$$

where $\mathcal{F}$ is the forward 2D FFT operator and $\mathcal{F}^{-1}$ is the inverse 2D FFT operator. It should be noted that the product is performed in the size of $2N_x \times 2N_z$. The computational complexity is $O[N_xN_z log(N_xN_z)]$ and the memory complexity is $O[N_xN_z]$.

6. Synthetic results

6.1. Comparison of frequency-domain wavefields

In this section, we share the frequency-domain wavefields for different models, including two-layers and the SEG/EAGE salt models as well as, compare the convergence property of the CBS by calculating the normalized errors and share the pressure response along receiver line for different iterations. To demonstrate the accuracy of the CBS, we compare it with the full integral equation method (Jakobsen & Wu 2016). We have used homogeneous background media in the tests and the velocity is 2000 m s^{-1}.

We first compare the renormalized Born series against the T-matrix method in an acoustic two-layer model (figure 1). The model measures 1280 m × 1280 m with grid intervals for the simulations of 10 m × 10 m.

Snapshots of frequency-domain wavefields computed with the full integral equation method and the convergent Born series are shown in figures 2 and 3, respectively. In each figure, we show the wavefields of two frequencies, 10 Hz and 15 Hz. From figures 2 and 3, one can make the following observations: (1) the wavefields using all the methods display an obvious change around the boundary; (2) the wavefields using the CBS match well with those from the reference integral equation method.

Figure 4 shows the resampled SEG/EAGE salt model for this example. The model grid is 10 m × 10 m. The model represents a uniform mesh of 128 × 128 nodes. We have performed simulations of frequency-domain wavefields in which the frequencies of 10 Hz and 15 Hz are used. Figure 5 shows the wavefields for 10 Hz and 15 Hz obtained by the reference integral equation method with 100 iterations. Figure 6 shows the wavefield snapshots for 10 Hz obtained by the conventional Born series (BS) method with 20, 50, 80 and 100 iterations. Figures 7 and 8 show the wavefields at frequencies 10 Hz and 15 Hz, respectively, obtained by the CBS method with 20, 50 ,80 and 100 iterations. From figures 5, 7 and 8, one can observe that the results from the CBS method have a good match with the results from full integral

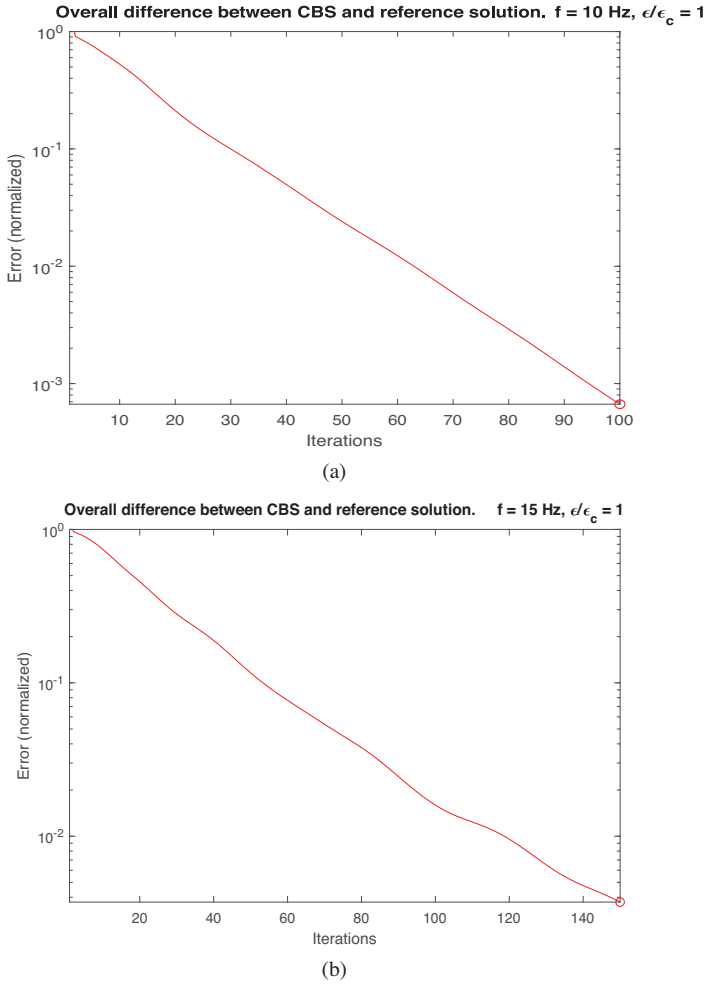

Figure 10. Convergence property of the CBS for (a) 10 Hz and (b) 15 Hz simulations of the SEG/EAGE salt model.

equation approach. All computations were performed on an Intel i7-7700. The CPU of the computer is 3.60 GHz with RAM 64 GB. The computational times of the full integral equation and CBS for 100 iterations are 859 s and 492 s, respectively.

6.2. Convergence property of the CBS

To investigate the convergence property of the CBS, we calculate the normalized error. Figures 9 and 10 show the results for the two-layered and the SEG/EAGE salt models, respectively . The figures show that the CBS has a similar convergence property in different models and frequencies, but the error decreases in a different way. With the same iterations, the error in the two-layered model is smaller than those of the SEG/EAGE salt model. From the figures, one can observe that after around 100 iterations the error of the CBS is very small. This suggests that the CBS can give a good match with the reference solution.

6.3. Frequency-domain wavefields with FFT

Because we use FFT in the implementation, some periodic boundary condition problems may occur (Osnabrugge *et al.* 2016). To prevent the reflection from the boundaries, we use an absorbing boundary condition in the implementation

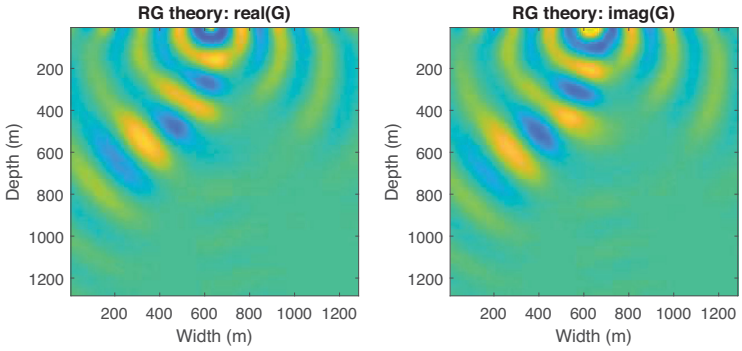

Figure 11. Frequency-domain wavefields for 10-Hz simulation of SEG/EAGE model using the CBS with FFT.

of the CBS. The absorbing boundary condition has been used in the context of wave modeling by different authors. More specifically, for the CBS, we use a width of absorbing boundary layer with grids of 40×40. Figure 11 shows the frequency-domain wavefields of 10 Hz using the CBS with FFT. We have estimated the computational cost. The computational times of the reference integral equation method is 492 s. The computational time of the CBS with FFT is 100 s.

6.4. Anomalous pressure response along receiver line

We now consider the same simulation as the SEG/EAGE salt models but for the synthetic pressure response along the receiver line. This example is designed to test the accuracy of the numerical scheme. Figure 12 shows the results for a two-layered model, in which the frequencies of 10 Hz and 15 Hz are used. Figures 13 and 14 show the pressure response in a salt model using the BS method with the frequency of 10 Hz for different iterations. Figures 15 and 16 show the pressure using the CBS method with the frequency of 10 Hz for the salt model. Figures 17 and 18 show the pressure using the CBS method with the frequency of 15 Hz for the salt model. For all the tests, the point source is placed at the same position. A receiver line is located at the surface. From figures 13 and 14, one can observe that the results from the BS method do not agree with the pressure wavefields from the full integral equation method. From figures 15–18, we observe that the pressure response using the CBS works very well compared with the result using the reference integral equation method.

7. Discussion

Before we discuss the convergence, computational complexity and potential application of the CBS, we would like to clarify that we have presented the theory and performed the numerical tests in the frequency domain because scattering theory is naturally formulated in the frequency domain and we do not have to generate time-domain waveforms to perform inversion in the frequency domain. The main reason for using a homogeneous reference medium is that we want to use FFT, which depends on the fact that the Greens function for a homogeneous medium is directly related to the difference between x and x'. Another point is that the contrast is frequency-dependent. In our tests, we used different frequencies and investigated different choices of parameter ϵ.

The application of the BS to seismic forward modeling requires small contrasts to achieve convergence. Here, by applying a preconditioner to the both sides of the BS and introducing the parameter ϵ to the background Green's function, the convergence of the BS is guaranteed. Figures 19 and 20 show the difference of frequency-domain wavefields for SEG/EAGE salt model using full integral equation and CBS methods. Osnabrugge *et al.* (2016) have already provided a general proof of convergence, we have used numerical examples to verify that the general proof holds for our specific models. However, for the case where the contrast is very large, e.g. salt areas, more iterations are needed to achieve convergence. This is also related to the choice of the parameter ϵ. The stronger the scatters (large-contrast), the higher the needed parameter ϵ.

Compared to the conventional BS there is no additional computational cost for each term in the real-space implementation. It should be noted that the accuracy of the wavefields depend on the number of iteration. This is different from the full IE method. One important thing we would like to mention is that, due to the FFT implementation for the CBS, the computational cost is reduced significantly. The computational complexity for such an implementation

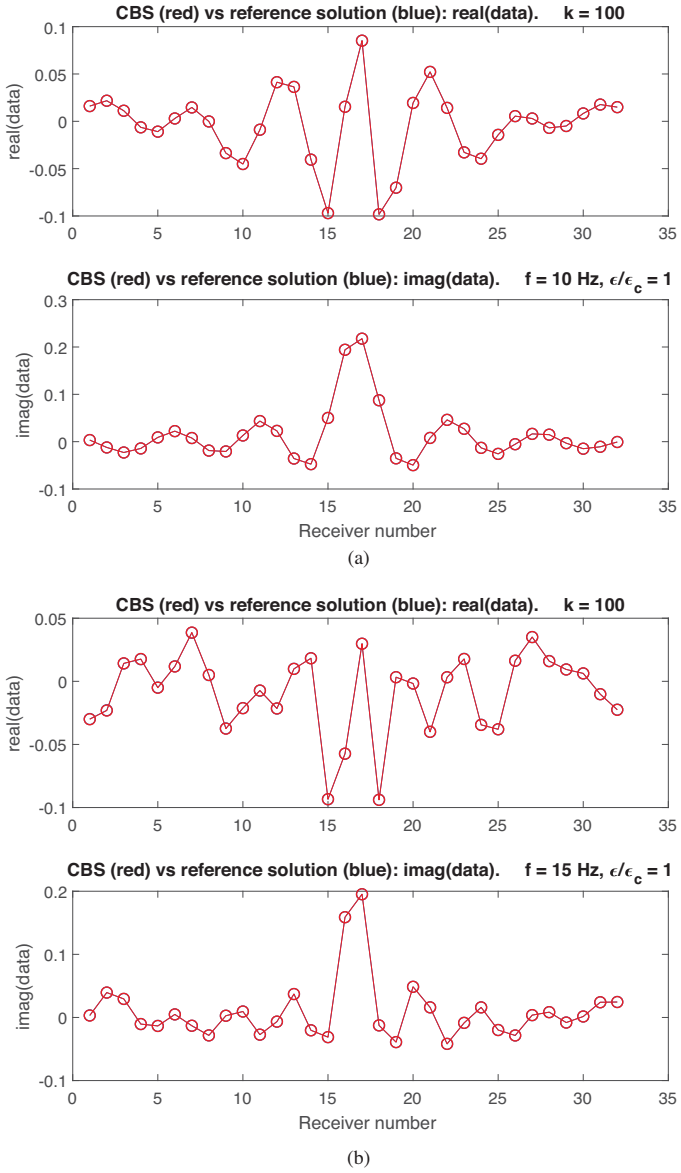

Figure 12. Comparison of pressure records for the two-layer model using the CBS and full integral equation methods with the frequencies of (a) 10 Hz and (b) 15 Hz, respectively.

is $O[N_xN_z log(N_xN_z)]$ and the memory complexity is $O[N_xN_z]$. Thus, the method can be in principle extended to the 3-D case.

We have presented and tested a new forward scattering series for seismic modeling. The method is suitable for numerical simulation of strongly scattering medium. The scattering series can be used for direct inverse scattering problems. Future research can look into the application of the CBS to the elastic case as well as in seismic inversion. The CBS in this paper can be considered as a stepping

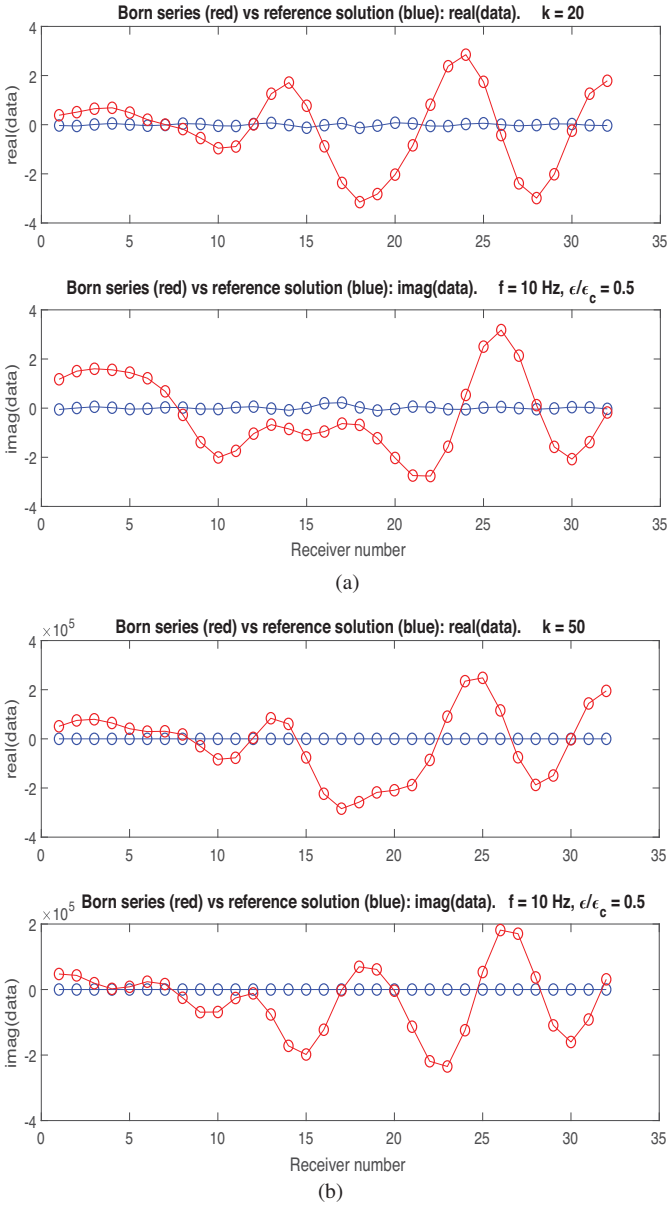

Figure 13. Comparison of pressure records for the SEG/EAGE salt model using the BS and full integral equation methods with the frequency of 10 Hz with a) 20, b) 50 iterations.

stone to developing modifications for one-way propagators. Also, it can be used to establish the Frechet derivatives for multi-scattering full waveform inversion (Alkhalifah & Wu 2016).

8. Conclusions

Seismic scattering theory is an effective method for seismic wave modeling and is the basis of seismic inversion. However, the Born series assumes weak scattering, which

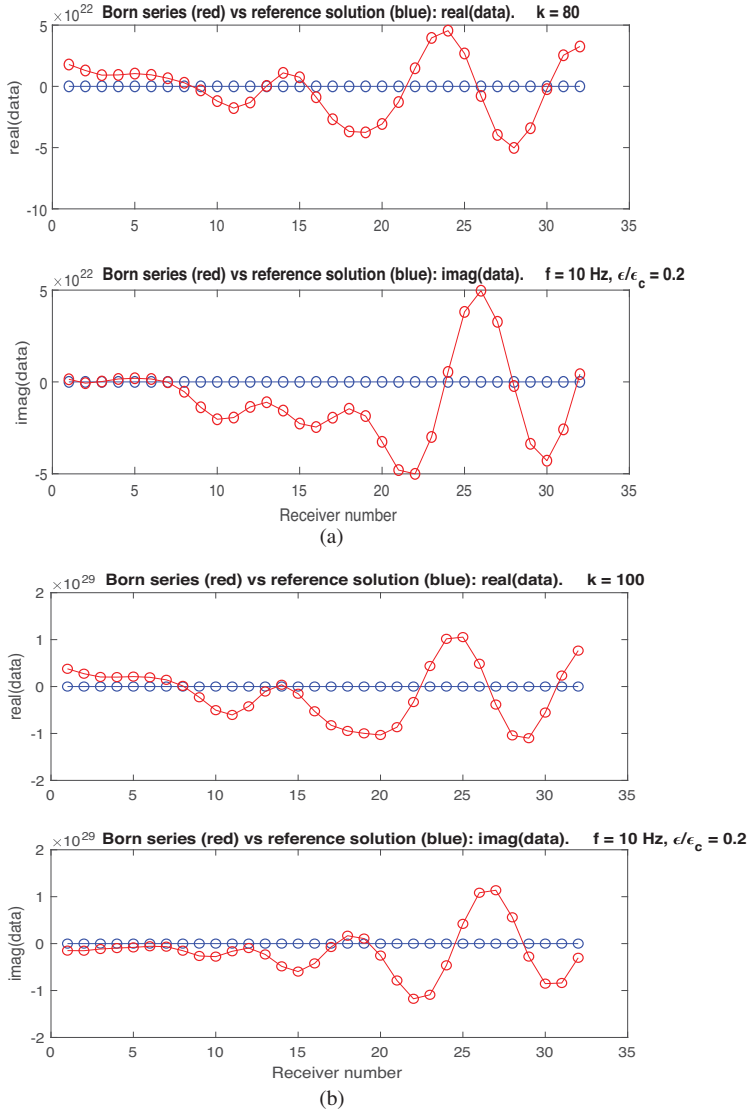

Figure 14. Comparison of pressure records for the SEG/EAGE salt model using the BS and full integral equation methods with the frequency of 10 Hz with (a) 80 and (b) 100 iterations.

renders the modeling and the inversion divergent for strong scattering media. We have presented the application of the so-called convergent Born series to seismic modeling problems. Numerical examples are presented, showing that, because of the introduction of a preconditioner into the traditional Born series, the Born series can be convergent for arbitrarily strong contrast medium. Compared to the integral equation method, the computational cost of the convergent Born series is cheaper, especially in the Fast Fourier Transform implementation. This method should be suitable for applications to inverse scattering and full waveform inversion.

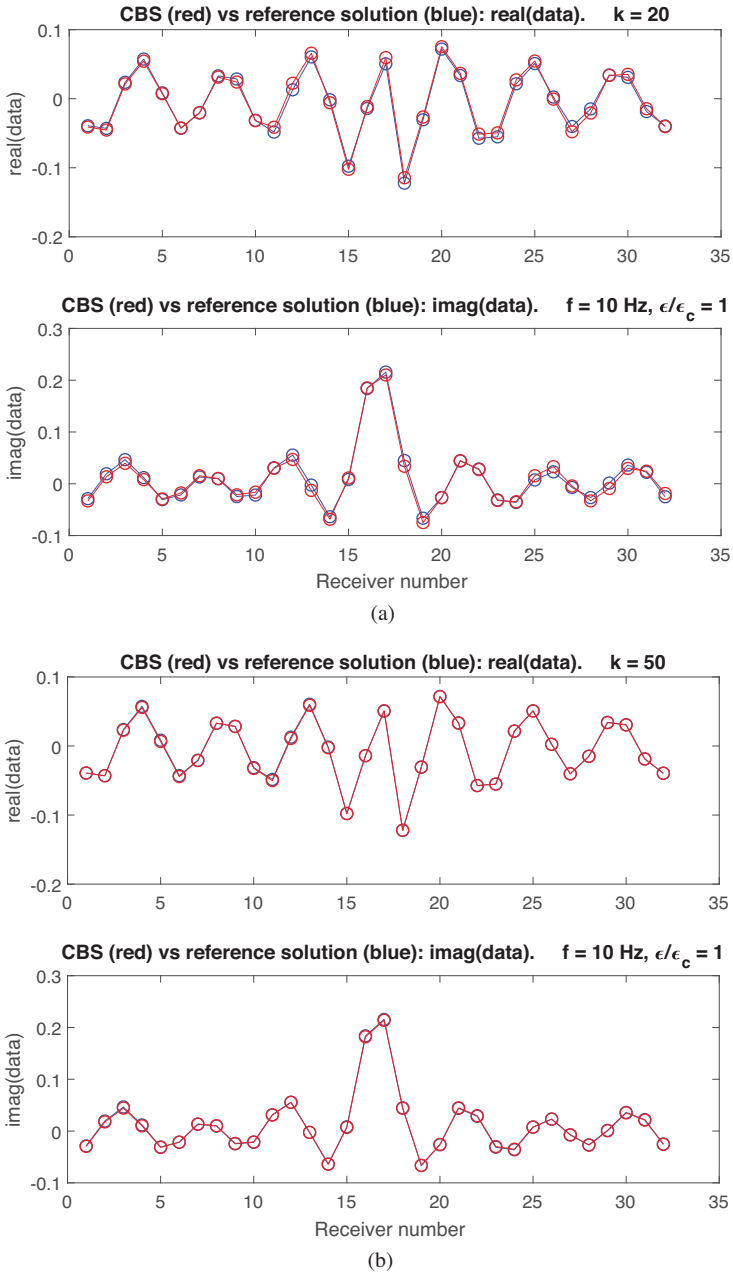

Figure 15. Comparison of pressure records for the SEG/EAGE salt model using the CBS and full integral equation methods with the frequency of 10 Hz with (a) 20 and (b) 50 iterations.

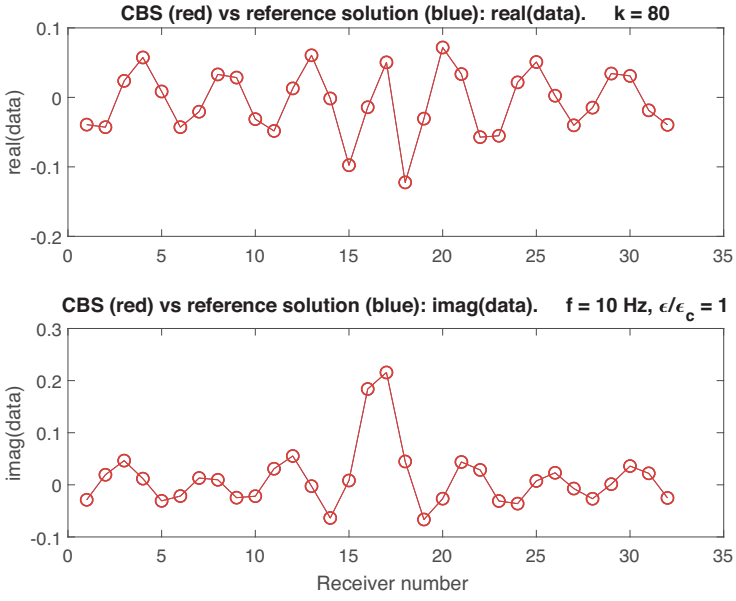

(a)

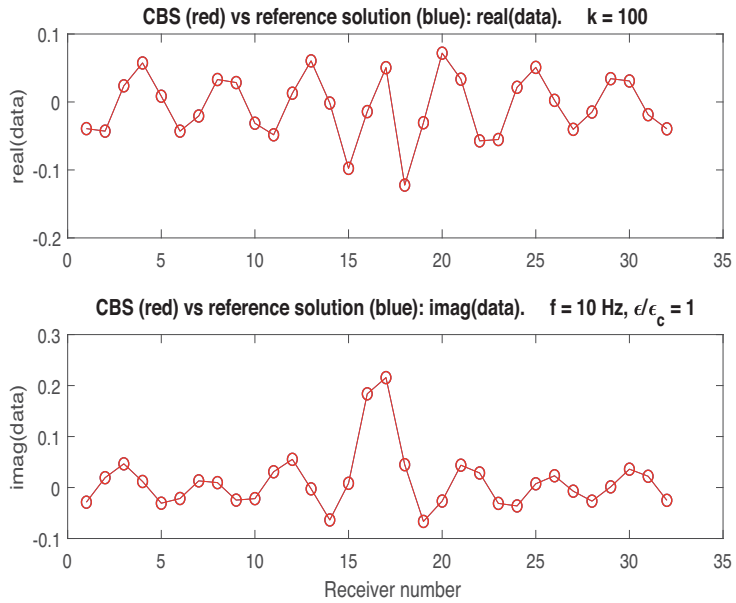

(b)

Figure 16. Comparison of pressure records for the SEG/EAGE salt model using the CBS and full integral equation methods with the frequency of 10 Hz with (a) 80, (b) 100 iterations.

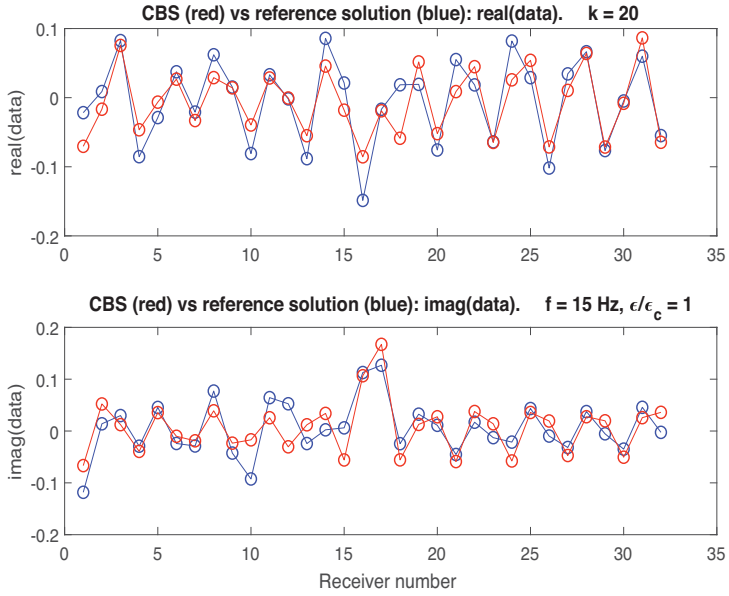

(a)

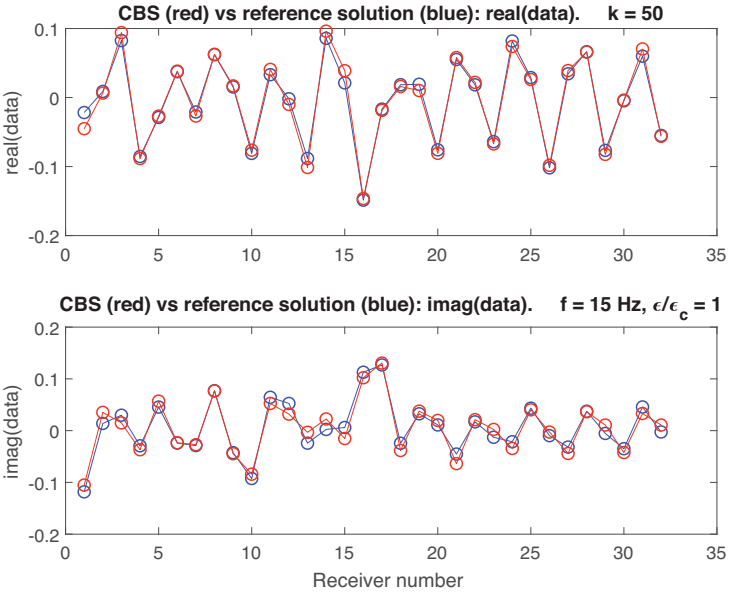

(b)

Figure 17. Comparison of pressure records for the SEG/EAGE salt model using the CBS and full integral equation methods with the frequency of 15 Hz with (a) 20, (b) 50 iterations.

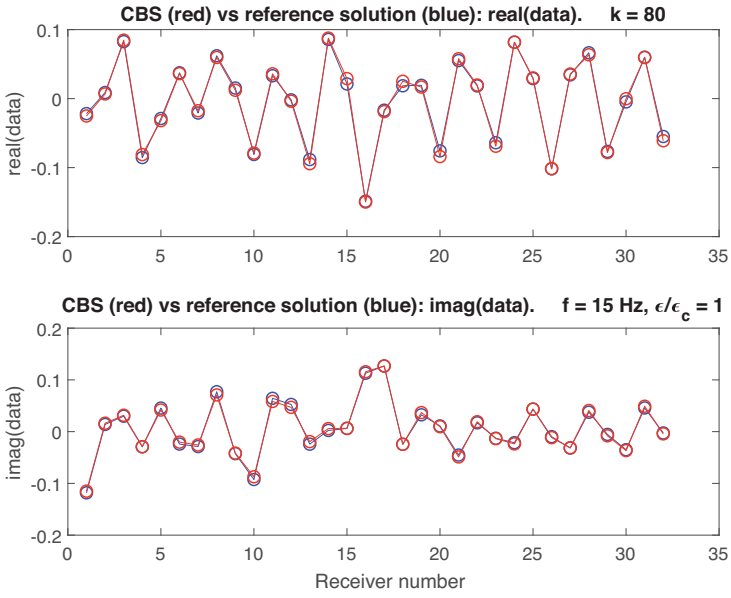

(a)

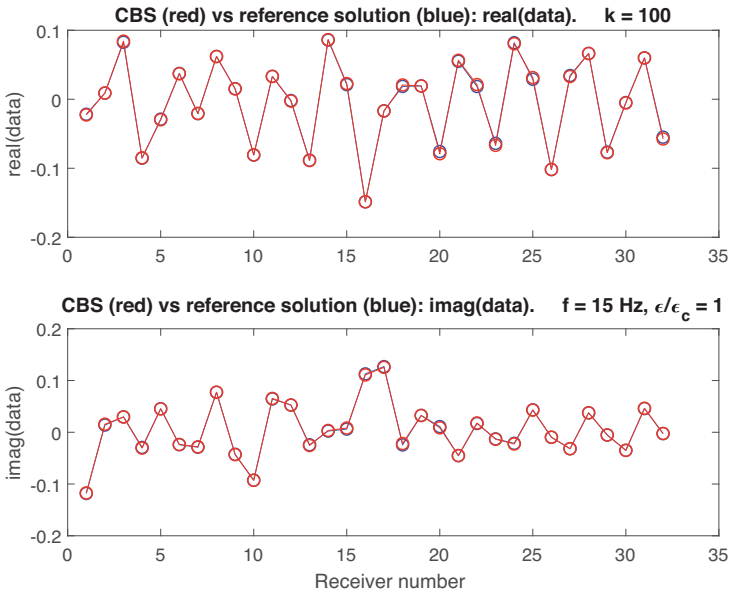

(b)

Figure 18. Comparison of pressure records for the SEG/EAGE salt model using the CBS and full integral equation methods with the frequency of 15 Hz with (a) 80 and (b) 100 iterations.

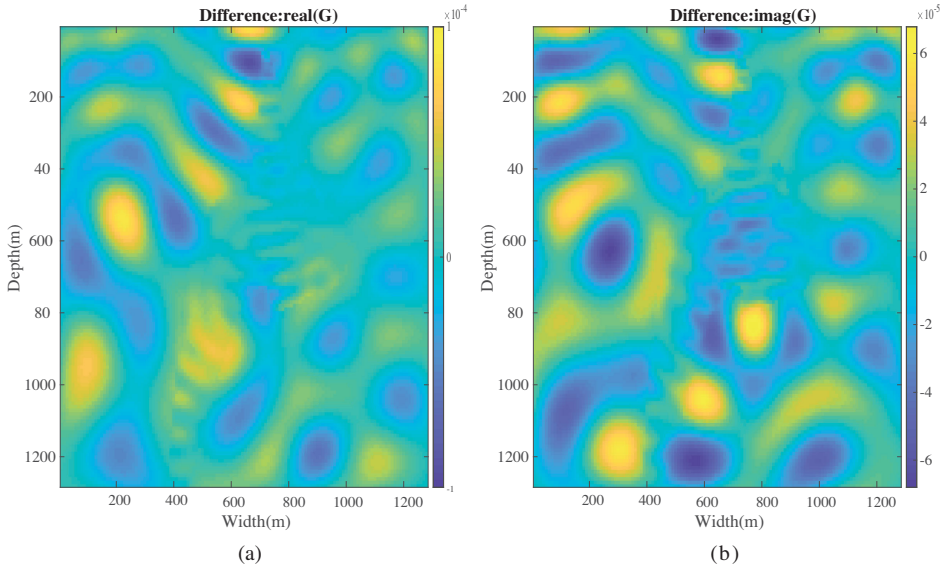

Figure 19. Difference of wavefields of real (a) and imaginary (b) parts using the CBS and full integral equation methods with the frequency of 10 Hz.

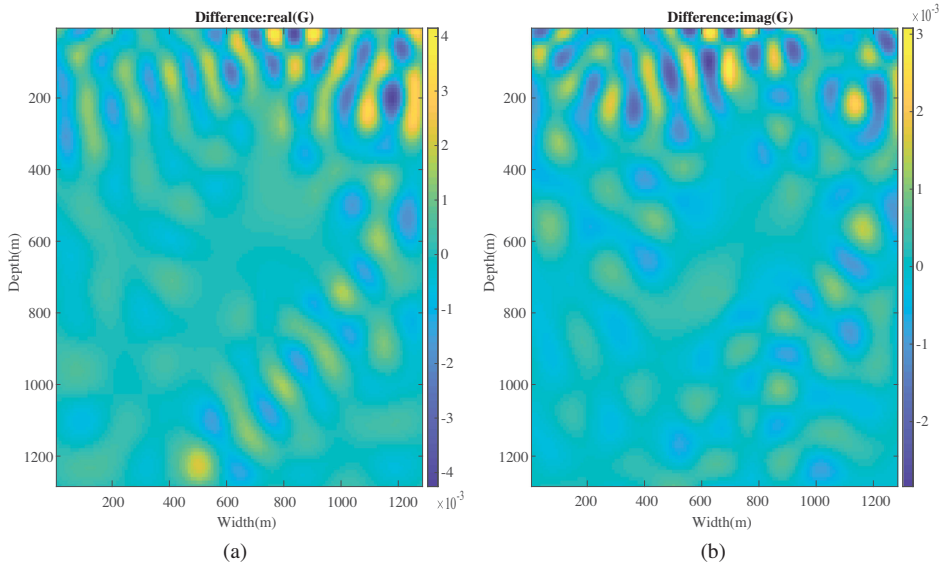

Figure 20. Difference of wavefields of real (a) and imaginary (b) parts using the CBS and full integral equation methods with the frequency of 15 Hz.

Acknowledgements

We thank the Research Council of Norway for the Petromaks II project 267769/E3 (Bayesian inversion of 4D seismic waveform data for quantitative integration with production data). We would like to acknowledge the WTOPI (Wavelet Transform On Propagation and Imaging for seismic exploration) Research Consortium sponsors for their financial support. Furthermore, we are grateful to Gerwin Osnabrugge at University of Twente, for very helpful discussion, the Editor and reviewers for their very constructive comments on the manuscript.

References

Aki, K. & Richards, P.G., 1980. *Quantitative Seismology*, W. H. Freeman and Company, 1st ed., 932, San Francisco, Calif.

Alkhalifah, T., 2016. Full-model wavenumber inversion: An emphasis on the appropriate wavenumber continuation, *Geophysics*, **81**, R89–R98.

Alkhalifah, T. & Wu, Z., 2016. Multiscattering inversion for low-model wavenumbers, *Geophysics*, **81**, R417–R428.

Berkhout, A., 2012. Combining full wavefield migration and full waveform inversion, a glance into the future of seismic imaging, *Geophysics*, **77**, S43–S50.

Carcione, J.M., 2007. *Wave Fields in Real Media: Wave Propagation in Anisotropic, Anelastic, Porous and Electromagnetic Media*, Elsevier.

Cerveny, V., 2005, *Seismic Ray Theory*, Cambridge University Press.

Chen, L.Y., Goldenfeld, N. & Oono, Y., 1994. Renormalization group theory for global asymptotic analysis, *Physical Review Letters*, **73**, 1311–1315.

Chen, L.Y., Goldenfeld, N. & Oono, Y., 1996. Renormalization group and singular perturbations: Multiple scales, boundary layers, and reductive perturbation theory, *Physical Review E*, **54**, 376–394.

De Wolf, D., 1971. Electromagnetic reflection from an extended turbulent medium: cumulative forward-scatter single backscatter approximation, *IEEE Transactions on Antennas and Propagation*, **19**, 254–262.

De Wolf, D., 1985. Renormalization of EM fields in application to largeangle scattering from randomly continuous media and sparse particle distributions, *IEEE Transactions on Antennas and Propagation*, **33**, 608–615.

Delamotte, B., 2004. A hint of renormalization, *American Journal of Physics*, **72**, 170–184.

Eftekhar, R., Hu, H. & Zheng, Y., 2018. Convergence acceleration in scattering series and seismic waveform inversion using nonlinear shanks transformation, *Geophysical Journal International*, **214**, 1732–1743.

Gao, G. & Torres-Verdin, C., 2006. High-order generalized extended Born approximation for electromagnetic scattering, *IEEE Transactions on Antennas and Propagation*, **54**, 1243–1256.

Gell-Mann, M. & Low, F.E., 1954. Quantum electrodynamics at small distances, *Physical Review*, **95**, 1300–1312.

Goldenfeld, N., 1992. *Lectures on Phase Transition and the Renormalization Group*, Addison-Wesley.

Huang, X., 2018. Extended beam approximation for high frequency wave propagation, *IEEE Access*, **6**, 37214–37224.

Huang, X. & Greenhalgh, S., 2019. Traveltime approximation for strongly anisotropic media using the homotopy analysis method, *Geophysical Journal International*, **216**, 1648–1664.

Huang, X., Jakobsen, M., Naevdal, G. & Eikrem, K.S., 2019. Target-oriented inversion of time-lapse seismic waveform data, *Communications in Computational Physics*, doi:10.4208/cicp.OA-2018-0143.

Huang, X., Sun, H. & Sun, J., 2016a. Born modeling for heterogeneous media using the gaussian beam summation based Green's function, *Journal of Applied Geophysics*, **131**, 191–201.

Huang, X., Sun, J. & Sun, Z., 2016b. Local algorithm for computing complex travel time based on the complex eikonal equation, *Physical Review E*, **93**, 043307.

Huang, X., Sun, J. & Greenhalgh, S., 2018. On the solution of the complex eikonal equation in acoustic vti media: a perturbation plus optimization scheme, *Geophysical Journal International*, **214**, 907–932.

Innanen, K.A., 2009. Born series forward modelling of seismic primary and multiple reflections: an inverse scattering shortcut, *Geophysical Journal International*, **177**, 1197–1204.

Jakobsen, M. & Wu, R., 2016. Renormalized scattering series for frequency-domain waveform modelling of strong velocity contrasts, *Geophysical Journal International*, **206**, 880–899.

Jakobsen, M., Wu, R.S. & Huang, X., 2018. Seismic waveform modeling in strongly scattering media using renormalization group theory, *SEG Technical Program Expanded Abstracts 2018*, **1**, 5007–5011.

Kirkinis, E., 2008. Renormalization group interpretation of the Born and Rytov approximations, *Journal of the Optical Society of America A*, **25**, 2499–2508.

Kirkinis, E., 2012. The renormalization group: a perturbation method for the graduate curriculum, *SIAM Review*, **54**, 374–388.

Kouri, D.J. & Vijay, A., 2003. Inverse scattering theory: Renormalization of the Lippmann–Schwinger equation for acoustic scattering in one dimension, *Physical Review E*, **67**, 046614.

Liu, Q.H., Zhang, Z.Q. & Xu, X.M., 2001. The hybrid extended Born approximation and CG-FFT method for electromagnetic induction problems, *IEEE Transactions on Geoscience and Remote Sensing*, **39**, 347–355.

Malovichko, M., Khokhlov, N., Yavich, N. & Zhdanov, M., 2017. Approximate solutions of acoustic 3D integral equation and their application to seismic modeling and full-waveform inversion, *Journal of Computational Physics*, **346**, 318–339.

Morse, P.M. & Feshback, H., 1953. Methods of theoretical physics, McGraw-Hill Science/Engineering/Math.

Osnabrugge, G., Leedumrongwatthanakun, S. & Vellekoop, I.M., 2016. A convergent Born series for solving the inhomogeneous Helmholtz equation in arbitrarily large media, *Journal of Computational Physics*, **322**, 113–124.

Pelissetto, A. & Vicari, E., 2002. Critical phenomena and renormalization-group theory, *Physics Reports*, **368**, 549–727.

Snieder, R., 1990. A perturbative analysis of non-linear inversion, *Geophysical Journal International*, **101**, 545–556.

Weglein, A.B., Araujo, F., Carvalho, P.M., Stiolt, R.H., Matson, K.K., Coates, R.T., Corrigan, D., Joster, D.J., Shaw, S.T. & Zhang, H., 2003. Inverse scattering series and seismic exploration, *Inverse problems*, **19**, R27–R83.

Weglein, A.B., Gasparotto, F.A., Carvalho, P.M. & Stolt, R.H., 1997. An inverse-scattering series method for attenuating multiples in seismic reflection data, *Geophysics*, **62**, 1975–1989.

Wilson, K.G., 1971. Renormalization group and critical phenomena. I. Renormalization group and the Kadanoff scaling picture, *Physical Review B*, **4**, 3174–3183.

Wu, R.S. & Huang, L., 1995. Reflected wave modeling in heterogeneous acoustic media using the De Wolf approximation, *Mathematical Methods in Geophysical Imaging III, International Society for Optics and Photonics*, **2571**, 176–187.

Wu, R.S., Luo, J. & Chen, G., 2016. Seismic envelope inversion and renormalization group theory: Nonlinear scale separation and slow dynamics, *SEG Technical Program Expanded Abstracts 2016*, **1**, 1346–1351.

Wu, R.S. & Toksoz, M.N., 1987. Difraction tomography and multisource holography applied to seismic imaging, *Geophysics*, **52**, 11–25.

Wu, R.S., Wang, B. & Hu, C., 2015. Renormalized nonlinear sensitivity kernel and inverse thin-slab propagator in T-matrix formalism for wave-equation tomography, *Inverse Problems*, **31**, 1–21.

Wu, R.S., Xie, X.B. & Wu, X.Y., 2007. One-way and one return approximations (De Wolf approximation) for fast elastic wave modeling in complex media, *Advances in Geophysics*, **48**, 265–322.

Wu, R.S. & Zheng, Y., 2014. Non-linear partial derivative and its De Wolf approximation for non-linear seismic inversion, *Geophysical Journal International*, **196**, 1827–1843.

Wu, Z. & Alkhalifah, T., 2017. Efficient scattering-angle enrichment for a nonlinear inversion of the background and perturbations components of a velocity model, *Geophysical Journal International*, **210**, 1981–1992.

Yakhot, V. & Orszag, S.A., 1986. Renormalization group analysis of turbulence. I. Basic theory, *Journal of Scientific Computing*, **1**, 3–51.

Yao, J., Lesage, A.C., Hussain, F. & Kouri, D.J., 2015. Scattering theory and Volterra renormalization for wave modeling in heterogeneous acoustic media, *SEG Technical Program Expanded Abstracts 2015*, **1**, 3594–3600.

Zhang, H. & Weglein, A.B., 2009. Direct nonlinear inversion of 1D acoustic media using inverse scattering subseries, *Geophysics*, **74**, WCD29–WCD39.

Zhdanov, M.S., 2002. *Geophysical Inverse Theory and Regularization Problems*, Elsevier.

Zuberi, M. & Alkhalifah, T., 2014. Generalized internal multiple imaging (GIMI) using Feynman-like diagrams, *Geophysical Journal International*, **197**, 1582–1592.

II

submitted to *Geophys. J. Int.*

Homotopy analysis of the Lippmann-Schwinger equation for seismic wavefield modeling in strongly scattering media

Morten Jakobsen[1], Xingguo Huang[1] and Ru Shan Wu[2]

[1]*Department of Earth Science, University of Bergen, Allegaten 41, 5020 Bergen, Norway;*

[2]*Institute of Earth and Planetary Physics, University of California, Santa Cruz, 95060 CA, USA.*

SUMMARY

We present an application of the homotopy analysis method for solving the integral equations of the Lippmann-Schwinger type, which occurs frequently in acoustic and seismic scattering theory. In this method, a series solution is created which is guaranteed to converge independent of the scattering potential. This series solution differs from the conventional Born series because it contains two auxiliary parameters ϵ and h and an operator H that can be selected freely in order to control the convergence properties of the scattering series. The ϵ-parameter which controls the degree of dissipation in the reference medium (that makes the wavefield updates localized in space) is known from the so-called convergent Born series theory; but its use in conjunction with the homotopy analysis method represents a novel feature of this work. By using $H = I$ (where I is the identity operator) and varying the convergence control parameters h and ϵ, we obtain a family of scattering series which reduces to the conventional Born series when $h = -1$ and $\epsilon = 0$. By using $H = \gamma$ where γ is a particular preconditioner and varying the convergence control parameters h and ϵ, we obtain another family of scattering series which reduces to the so-called convergent Born series when $h = -1$ and $\epsilon \geq \epsilon_c$ where ϵ_c is a critical dissipation parameter depending on the largest value of the scattering potential. This means that we have developed a kind of unified scattering series theory that includes the conventional and convergent Born series as special cases. By performing a series of 12 numerical experiments with a strongly scattering medium, we illustrate the effects of varying the (ϵ, h, H)-parameters on the convergence properties of the new homotopy scattering series. By using $(\epsilon, h, H) = (0.5, -0.8, I)$ we obtain a new scattering series that converges significantly faster than the convergent Born series. The use of a non-zero dissipation parameter ϵ seems to improve on the convergence properties of any scattering series, but one can now relax on the requirement $\epsilon \geq \epsilon_c$ from the convergent Born series theory, provided that a suitable value of the convergence control parameter h and operator H is used.

1 INTRODUCTION

There exist a range of different numerical methods for seismic wavefield modeling (Carcione, 2002), including differential equation methods (e.g., Robertsson et al., 2012) and integral equation methods (Pike and Sabatier, 2000; Oristaglio and Blok, 2012; Jakobsen, 2012; Jakobsen and Wu, 2016; Malovichko et al., 2018). The majority of researchers in the seismic community use differential equation methods (Carcione et al., 2002), but the integral equation approach has actually several advantages compared with the differential equation approach: (1) it is naturally target oriented (Haffinger et al., 2016; Huang et al., 2019), (2) it gives the sensitivity matrix directly in terms of Green's functions (Jakobsen and Ursin, 2015) which is convenient for uncertainty estimation (Eikrem et al., 2018) and (3) it is compatible with the use of domain decomposition and renormalization methods from modern physics (Jakobsen and Wu, 2016, 2018). However, the integral equation approach can be less efficient than the differential equation approach, depending on how it is implemented (Malovichka et al., 2018; Jakobsen and Wu, 2018; Jakobsen et al. 2019). An integral equation solution based on matrix inversion can be very accurate, but very memory-depending and costly (Jakobsen and Wu, 2018). Efficient implementations of the integral equations approach are typically based on the use of iterative methods and /or scattering series solutions (Jakobsen and Wu, 2016, Malovichko et al., 2018; Jakobsen et al., 2019, Huang et al., 2019b,c).

Many geophysicists are familiar with the scattering series of Born that one can easily obtain from the Lippmann-Schwinger equation via simple iteration (Jakobsen and Wu, 2016). However, the Born series represents an example of a so-called naive perturbation expansion which is only guaranteed to converge in the special case of relatively small contrasts (Kirkinis, 2008; Jakobsen and Wu, 2016). To obtain a convergent scattering scattering series in the presence of strong contrasts, it may be required to use a non-perturbative method for strongly nonlinear systems. Previously, researchers have developed convergent scattering series solutions of the Lippmann-Schwinger equation by using renormalization procedures (Abubakar and Habashy, 2003; Wu et al., 2007; Osnabrugge et al., 2016; Jakobsen et al., 2016; Jakobsen et al.. 2019). In this study, however, we have employed the so-called homotopy analysis method, which is based on concepts and ideas form topology (Liao, 2003; Hetmaniok et al., 2014).

The homotopy analysis method (HAM) used in this study was developed by Liao (1998, 2003, 2004, 2009, 2012, 2014). However, the development of related globally convergent homotopy methods for solving nonlinear equations started around 1976 (see Watson, 1989). Historically, there have been several attempts to apply homotopy methods to model and invert geophysical data (see Watson, 1989), but the paper of Huang and Greenhalgh (2019a) appears to represent the first geophysical application of the modern homotopy analysis method developed by Liao (2003), which differs from the

one discussed by Watson (1989). In any case, the homotopy methods allows one to solve operator equations of any kind by using ideas and concepts of topology, which is a branch of pure and applied mathematics dealing with quantities that are preserved during continuous deformations. A homotopy describes a continuous transformation between two states and has been compared with the concept of scale-invariance in renormalization group theory (Palit and Datta, 2016; Jakobsen et al., 2019a; Pfeffer, 2019). The homotopy analysis method have been used to solve a range of different nonlinear problems, ranging from heat conduction problems (Abbasbandy, 2006) to problems within theoretical physics (Pfeffer, 2019). Most applications of the homotopy analysis method is based on a differential operator formulation, but there have also been successful attempts to solve integral equations of the Fredholm and Volterra types using the homotopy analysis method (see Hetmanio et al., 2014).

Although the homotopy analysis method may potentially be very useful for practical nonlinear inversion of seismic waveform data (see Han et al., 2005; Fu and Han, 2006), we shall focus on the forward problem. This is partially because there is still an important need for more work on the nonlinear direct scattering problem (Jakobsen et al., 2019a,b) and the corresponding nonlinear inverse scattering problem is much more difficult to solve due to its ill-posed nature. It will be demonstrated that the homotopy analysis method can be used to construct a scattering series solution of the Lippmann-Schwinger equation in the context of seismic wavefield modeling. Although such convergent scattering series have been developed on the basis of renormalization methods in the past (Abubakar and Habashy 1983; Osnabrugge et al., 2016; Jakobsen et al., 2019a), we think it is interesting to study convergence properties of the direct scattering series solution from different perspectives, since this may give us new ideas and insights that may be useful for future studies of nonlinear inverse scattering as well as direct scattering problems.

In section 2, we present fundamental equations and establish our notation. In section 3, we present a general method for obtaining convergent series solutions of nonlinear operator equations that does not depend on any parameter being small. In section 4, we derive a convergent scattering series solution of the Lippmann-Schwinger equation. In section 5, we show that the conventional Born series and the renormalized Born series of Osnabrugget et al. (2016) and Huang et al. (2019) represents a special case of the HAM series. In section 6, we demonstrate that the HAM series converges for strongly scattering media where the conventional Born series diverges. In section 7, we also provide some ideas for further work.

2 THE LIPPMANN-SCHWINGER EQUATION AND CONVENTIONAL BORN SERIES

The scalar wave equation in the frequency domain (the inhomogeneous Helmholtz equation) can be written as (Morse and Feshbach, 1953; Osnabrugge et al., 2016; Huang et al., 2019b,c)

$$\left(\nabla^2 + k^2(\mathbf{x})\right)\psi(\mathbf{x}) = -S(\mathbf{x}), \tag{1}$$

where $k(\mathbf{x})$ is the wave number at position $\mathbf{x}$. Following Osnabrugge et al. (2016), we now decompose the actual medium with wavenumber $k(\mathbf{x})$ into an arbitrary homogeneous dissipative reference medium with complex wave number k_d given by $k_d^2 = k_0^2 + i\epsilon$ (where ϵ is an arbitrary small positive number) and a corresponding complex scattering potential $V(\mathbf{x})$ (with compensating gain, rather than dissipation). It follows that

$$\left(\nabla^2 + k_d^2\right)\psi(\mathbf{x}) = -S(\mathbf{x}) - V(\mathbf{x})\psi(\mathbf{x}), \tag{2}$$

where

$$V(\mathbf{x}) = k^2(\mathbf{x}) - k_d^2. \tag{3}$$

The second term on the right-hand side of equation (2) represents the so-called equivalent sources. By treating the contrast-sources just like real sources, one can derive the Lippmann-Schwinger equation (Jakobsen and Ursin, 2015)

$$\psi(\mathbf{x}) = \psi^{(0)}(\mathbf{x}) + \int_\Omega d\mathbf{x}' G^{(0)}(\mathbf{x} - \mathbf{x}')V(\mathbf{x}')\psi(\mathbf{x}'), \tag{4}$$

where $G^{(0)}(\mathbf{x} - \mathbf{x}')$ is the Green's function for the homogeneous reference medium, that satisfies

$$\left(\nabla^2 + k_d^2\right)G^{(0)}(\mathbf{x} - \mathbf{x}') = -\delta(\mathbf{x} - \mathbf{x}'). \tag{5}$$

Note that the introduction of a non-zero imaginary part ϵ to the squared wave number k_0^2 in the homogeneous reference medium makes the energy associated with Green's function finite and the wave fields more localized (Osnabrugge et al., 2016; Jakobsen et al., 2019a; Huang et al., 2019c). Although most workers tend to set ϵ to zero, the use of a non-zero ϵ parameter improves the convergence properties of any scattering series (Abubakar and Habashy, 2003; Osbabrugge et al., 2016; Huang et al., 2019c; Jakobsen et al., 2019a).

In symbolic operator notation, the Lippmann-Schwinger equation (4) can be written as

$$\psi = \psi^{(0)} + G^{(0)}V\psi, \tag{6}$$

where the scattering potential operator V is local (but see Jakobsen and Wu, 2017) and can be represented by a diagonal matrix in the real-space representation (Jakobsen and Ursin, 2015). The above equation has the following exact formal solution:

$$\psi = (I - G^{(0)}V)^{-1}\psi^{(0)} \tag{7}$$

where I is the identity operator.

The solution (7) is valid independently of the contrast volume, but it involves the inversion of a huge operator or matrix (in the coordinate representation), which can be very costly in the case of a realistic model. In principle, one could try to solve the Lippmann-Schwinger equation by iteration. The well-known Born series can be regarded as the simplest possible iterative solution of the Lippmann-Schwinger equation and can be presented as

$$\psi = \sum_{m=0}^{\infty} \psi_m \tag{8}$$

where $\psi_0 = \psi^{(0)}$ and

$$\psi_m = G^{(0)} V \psi_{m-1}, \quad m = 1, 2, 3, \ldots . \tag{9}$$

The Born series is very popular due to its simplicity. However, the Born series represents an example of a naive perturbation expansion (Kirkinis, 2008) which is only guaranteed to converge if the contrast is relatively small, in the sense that the largest eigenvalue of the operator $G^{(0)}V$ must be smaller than unity (Weinberg, 1983, Newton, 2002; Osnabrugge et al., 2016).

3 THE HOMOTOPY ANALYSIS METHOD

The homotopy analysis method can be used to solve operator equations of the form (Liao, 2003)

$$N\left[\psi\right] = 0, \tag{10}$$

where N denotes a nonlinear operator and ψ is the unknown function (or state vector). The first step is to define the homotopy operator $\mathcal{H}$ by (Liao, 2003)

$$\mathcal{H}\left[\Phi, \lambda\right] \equiv (1-\lambda) L\left[\Phi(\lambda) - \psi_0\right] - \lambda h H N\left[\Phi(\lambda)\right], \tag{11}$$

where $\lambda \in [0, 1]$ is the so-called embedding parameter, $h \neq 0$ is the so-called convergence control parameter, H is a convergence control operator (see section 4), ψ_0 is our initial guess of the solution to equation (10) and L is an auxiliary linear operator that can be selected arbitrarily as long as $L\left[0\right] = 0$.

By setting $\mathcal{H}\left[\Phi, \lambda\right] = 0$ we get the so-called zero-order deformation equation (Liao, 2003)

$$(1-\lambda) L\left[\Phi(\lambda) - \psi_0\right] = \lambda h H N\left[\Phi(\lambda)\right]. \tag{12}$$

If $\lambda = 0$ then $L\left[\Phi(0) - \psi_0\right] = 0$, which implies that $\Phi(0) = \psi_0$. If $\lambda = 1$ then $N\left[\Phi(1)\right] = 0$, which implies that $\Phi(1) = \psi$, where ψ is the solution of equation (10) we are looking for. A gradual change in the embedding parameter λ from 0 to 1 therefore means a continuous transition of $\Phi(\lambda)$ from the initial guess ψ_0 to the exact solution ψ of the original equation (10).

If we now expand the auxiliary field $\Phi(\lambda)$ into a Maclaurin series with respect to the embedding parameter λ then we obtain (Liao, 2003)

$$\Phi(\lambda) = \Phi(0) + \sum_{m=1}^{\infty} \frac{1}{m!} \frac{\partial^m \Phi(\lambda)}{\partial \lambda^m}|_{\lambda=0} \lambda^m. \tag{13}$$

By introducing the definition (Liao, 2003)

$$\psi_m \equiv \frac{1}{m!} \frac{\partial^m \Phi(\lambda)}{\partial \lambda^m}|_{\lambda=0}, \quad m = 1, 2, 3, ..., \tag{14}$$

the above equation (13) can be expressed as (Liao, 2003)

$$\Phi(\lambda) = \Phi(0) + \sum_{m=1}^{\infty} \psi_m \lambda^m. \tag{15}$$

If the above series (15) is convergent for $\lambda = 1$ then the solution we are looking for is given by (Liao, 2003)

$$\psi = \sum_{m=0}^{\infty} \psi_m. \tag{16}$$

It is of course not obvious that the series (15) is convergent for $\lambda = 1$, but by adjusting the auxiliary parameter h and the auxiliary operator H we can make sure that this series is indeed convergent (Liao, 2003).

In order to determine the different ψ_m terms , we now differentiate the left and right side of the 0th-order deformation equation (12) m times with respect to the auxiliary parameter λ, divide the result by $m!$ and set $\lambda = 0$. In this way suggested by Liao (2003), we obtain the so-called mth-order deformation equation ($m > 0$):

$$L\left[\psi_m - \chi_m \psi_{m-1}\right] = hHR_m, \tag{17}$$

where

$$\chi_m = \begin{cases} 0 & \text{if } m \leq 1 \\ 1 & \text{if } m \geq 2 \end{cases} \tag{18}$$

and

$$R_m = \frac{1}{(m-1)!} \left(\frac{\partial^{m-1}}{\partial \lambda^{m-1}} N \left[\sum_{i=0}^{\infty} \psi_i \lambda^i \right] \right)_{\lambda=0}. \tag{19}$$

The different R_m parameters will depend on the nature of the non-linear operator N. In the next section, we shall evaluate the R_m-parameters for the nonlinear operator corresponding with the Lippmann-Schwinger equation.

The selection of the convergence control parameter h is very important. In order to select a suitable value of h, one can either use the h-parameter curve method or an optimization method (Liao, 2003; Hetmaniok et al., 2014). We shall discuss the selection of h in connection with the results we have obtained for the homotopy analysis of the Lippmann-Schwinger equation.

4 HOMOTOPY ANALYSIS OF THE LIPPMANN-SCHWINGER EQUATION

Hetmaniok et al. (2014) discuss the usage of the homotopy analysis method for solving nonlinear and linear integral equations of the second kind. However, their analysis is restricted to 1D media and slightly different from the analysis presented below. In order to derive a convergent scattering series solution of the Lippmann-Schwinger equation based on the homotopy analysis method, we define the linear and nonlinear integral operators L and N by

$$L[\psi] = \psi, \quad N[\psi] = \psi - \psi^{(0)} - G^{(0)}V\psi, \tag{20}$$

By using the above definitions of the linear and nonlinear operators L and N in conjunction with the mth-order deformation equation 17, we obtain

$$\psi_m = \chi_m \psi_{m-1} + hHR_m. \tag{21}$$

By using the definition of the nonlinear operator N given in equation (20) in conjunction with the expression for the R_m parameters in equation (18), we get

$$R_m = \frac{1}{(m-1)!}\frac{\partial^{m-1}}{\partial\lambda^{m-1}}\left[\sum_{i=0}^{\infty}\psi_i\lambda^i - \psi^{(0)} - G^{(0)}V\sum_{i=0}^{\infty}\psi_i\lambda^i\right]_{\lambda=0}. \tag{22}$$

The above equation implies that

$$R_m = \frac{1}{(m-1)!}\left((m-1)!\psi_{m-1} - (1-\chi_m)\psi^{(0)} - (1-m)!G^{(0)}V\psi_{m-1}\right), \tag{23}$$

or

$$R_m = \psi_{m-1} - \frac{(1-\chi_m)}{(1-m)!}\psi^{(0)} - G^{(0)}V\psi_{m-1}. \tag{24}$$

By using the above expression for R_m in conjunction with the recursive formula (21), we obtain

$$\psi_1 = hH\left(\psi_0 - \psi^{(0)} - G^{(0)}V\psi_0\right), \tag{25}$$

and for $m \geq 2$:

$$\psi_m = \mathcal{M}\psi_{m-1}. \tag{26}$$

where

$$\mathcal{M} \equiv I + hH - hHG^{(0)}V. \tag{27}$$

Equations (25) and (A.1) for the first and higher-order terms in the homotopy analysis scattering series represents the main results of this paper. This homotopy analysis method iterative solution of the Lippmann-Schwinger equation differs from the conventional Born series via the convergence control parameter h and the operator H that can be selected arbitrarily to ensure that the series is convergent. The HAM series converges if the spectral radius σ of M is smaller than unity; which can occur even

if the spectral radius of the operator G_0V is larger than unity; that is, when the conventional scattering series of Born diverges.

5 COMPARISON WITH EXISTING ANALYTICAL RESULTS

If we use our freedom to set $\psi_0 = \psi(0)$, $h = -1$ and $H = I$ then the homotopy series in equations (25-26) reduces to the conventional Born series (9). As discussed earlier, the conventional Born series have a rather small range of convergence, since the largest eigenvalue of the operator $G^{(0)}V$ must be smaller than unity.

Osnabrugge et al. (2016) presented a modified Born series (CBS) which is guaranteed to converge independent of the scattering potential. If we set $\psi_0 = \gamma\psi^{(0)}$ where $\gamma = iV/\epsilon$ is the preconditionner of Osnabrugge et al. (2016) then it follows from equation (23) that

$$\psi_1 = hH\left(I - \gamma^{-1} - G^{(0)}V\right)\psi_0. \tag{28}$$

If we now set $h = -1$ and $H = \gamma$ then the above equation becomes

$$\psi_1 = M\psi_0, \tag{29}$$

where

$$M \equiv I - \gamma + \gamma G^{(0)}V. \tag{30}$$

Also, it follows from equation that

$$\psi_m = M\psi_{m-1}, \tag{31}$$

which implies that the convergent Born series of Osnabrugge et al. (2016) is a special case of our new HAM series.

A comparison of equations (26-27) and (30-31) clearly suggests that we have generalized the convergent Born series of Osnabrugge et al. (2016). We can construct a family of convergent Born series similar to the convergent Born series of Osnabrugge et al. (2016) if we set $H = \gamma$ but use different values of the convergence control parameter h. The CBS is based on the use of a dissipative reference medium, which makes the Green's function finite and localized (Osnabrugge et al., 2016; Huang et al., 2019c; Jakobsen et al., 2019a). Since our generalized convergent Born series based on HAM contains the additional convergence control parameter h, we can decrease the value of the dissipation parameter ϵ if we compensate by using a suitable h-value. The convergence control parameter h is a global convergence parameter, in the sense that it acts globally on the whole model, whereas the dissipation parameter ϵ can be regarded as a local convergence parameter, since a higher value for ϵ implies a higher degree of wavefield localization. By a suitable choice of the local and global convergence

control parameters ϵ and h we can accelerate the convergence of the HAM series. This point will be illustrated in the next section dealing with numerical experiments based on a strongly scattering seismic model.By introducing an imaginary part to the wavevector of the background medium, we make the total energy represented by the background Green's function finite and localized. The imaginary term in the background medium is compensated exactly by an imaginary term in the scattering potential. Therefore, the final solution remains the same as the solution without any dissipation.

6 NUMERICAL RESULTS AND DISCUSSION

We performed a series of 12 different numerical experiments to study the effects of the auxiliary parameters (ϵ, h, H) on the convergence properties of the homotopy analysis method for solving the Lippmann-Schwinger equation. The numerical experiments are based on a resampled version of the SEG/EAGE salt model (Figure 1, left). We used a homogeneous reference medium with wavespeed $c_0 = 2870$ m/s (Figure 1, right). We employed a single delta function source with frequency 10 Hz located in the middle of the top of the model and we used a grid size equal to 5 m in each direction. In each experiment, we used one of the combinations of the (ϵ, h, H) -parameters given in Table 1 and generated a scattering series solution of the Lippmann-Schwinger equation by using the recursive formula (25-27).

We quantified the convergence properties of the different scattering series by calculating the normalized overall error δ_k as a function of the number of iterations k, where

$$\delta_k = ||\sum_{i=1}^{k} \psi_i - \psi^{(r)}||/||\psi^{(r)}||, \tag{32}$$

and $\psi^{(r)}$ is a reference solution obtained by solving equation (7) via matrix inversion (see Figure 2), which is exact apart from very small numerical discretization errors (Jakobsen, 2012). In each numerical experiment, we iterated until the normalized overall error became smaller than 10^{-3} (in the case of convergence) or larger than 10 (in the case of divergence). However, this stopping criteria is of course flexible and dependent on the desired accuracy.

If the scattering series diverges then the resulting wavefield (Figure 3) will of course look very different from the reference wavefield (Figure 2). If the scattering series converges in the sense that the overall normalized error becomes smaller than 10^{-3} than the resulting wavefield (Figure 4) will necessarily be very similar to the true wavefield (Figure 2). Since the resulting wavefield is independent of the auxiliary parameters in the case of convergence, we focus on the behavour of δ_k rather than the wavefield itself.

In numerical experiments 1-6 (Figure 5) we assumed $H = I$ and varied the dissipation parameter ϵ and the convergence control parameter h. As discussed in the previous section, when $\epsilon = 0$ and $h =$

-1 the numerical results correspond with the conventional Born series, whereas the use of different ϵ- and h-values represents different modifications of the conventional Born series. Clearly, one can see from the blue curve in Figure 5 that the conventional Born series corresponding with $\epsilon = 0$ and $h = -1$ diverges for this strongly scattering medium. When $\epsilon = 0$ and $h = -0.95$ corresponding with the green curve in Figure 5, the scattering series still diverges. When $\epsilon = 0$ and $h = -0.9$ corresponding with the red curve in Figure 5, the scattering series is starting to converge, but extremely slowly. When $\epsilon = 0$ and $h = -0.8$ corresponding with the cyan curve in Figure 5, the scattering series converges faster. When $\epsilon = 0$ and $h = -0.1$ corresponding to the black curve in Figure 5, the scattering series is still convergent, but the convergence rate is much smaller than when using $h = -0.8$. When $\epsilon = 0.5$ and $h = -0.8$ corresponding to the black curve in Figure 5 than the scattering series converges faster than for all the other experiments 1-5. Therefore, it appears that the use of a non-zero ϵ-value in conjunction with an optimal h-value helps to accelerate an already convergent scattering series.

In numerical experiments 7-12 (Figure 6) we assumed $H = \gamma$ and varied the dissipation parameter ϵ as well as the convergence control parameter h. When $\epsilon \leq \epsilon_c$ where ϵ_c is a critical value depending on the velocity model and $h = -1$ then the numerical results corresponds with the convergent Born series of Osnabrugge et al. (2016), whereas the use of different ϵ and h-parameters correspond with different modifications of the convergent Born series of Osnabrugge et al. (2016). Clearly, one can see from the blue curve in Figure 6 that the convergent Born series of Osnabrugge et al. (2016) corresponding with $\epsilon = \epsilon_c$ and $h = -1$ is indeed convergent. When $h = -1$ but $\epsilon = 0.5\epsilon_c$ corresponding to the green curve in Figure 6, the scattering series is as expected divergent. When $\epsilon = 0.5\epsilon_c$ and $h = -0.5$ corresponding with the red curve in Figure 6, the scattering series is still divergent. However, when $\epsilon = 0.5\epsilon_c$ and $h = -0.25$ corresponding with the cyan curve in Figure 6, the scattering series become convergent again. When $\epsilon = 0.5\epsilon_c$ and $h = -0.125$ corresponding with the curve in Figure 6, the scattering series is still convergent, but the convergence rate is smaller than when using $h = -0.25$. When using $\epsilon = 0.25\epsilon_c$ corresponding with the black curve in Figure 6 the scattering series converges extremely slowly. Therefore, it appears that the ϵ and h-parameters corresponding with the original convergent Born series of Osnabrugge et al. (2016) are optimal when $H = \gamma$.

Figure 7 represents a comparison of the optimal HAM series (the black curve in Figure 6 corresponding to $\epsilon = 0.5$, $h = -0.8$ and $H = I$) and the original convergent Born series of Osbabrugge et al. (2016) (the blue curve in Figure 6 corresponding with $\epsilon = 1$, $h = -1$ and $H = -\gamma$). Clearly, one can see that the optimal HAM series requires much less iterations than the original convergent Born series. Therefore, one can say that we have generalized and improved on the convergent Born series of Osnabrugge et al. (2016) by using the homotopy analysis method.

The auxiliary parameters ϵ and h may be referred to as local and global convergence control pa-

rameters, respectively. This is because a non-zero ϵ value leads to dissipation in the reference medium (and gain in the scattering potential), which makes the wavefield update more localized in space; and different h-values are associated with different degrees of global wavefield scaling. Having both local and global convergence control parameters in addition to the auxiliary convergence control operator H makes this homotopy analysis method very general and flexible.

7 CONCLUDING REMARKS

We have used the homotopy analysis method (HAM) to derive a general scattering series solution of the Lippmann-Schwinger equation which is guaranteed to converge independent of the scattering potential, provided that one select the dissipation parameter ϵ as well as the convergence control parameter h and operator H in a suitable manner. We have found that the conventional Born series and the convergent Born series of Osnabrugge et al. (2016) are special cases of the new scattering series based on HAM. We have performed a series of 12 numerical experiments and found that a scattering series with $\epsilon = 0.5$, $h = -0.8$ and $H = I$ requires much less iterations to converge than the original convergent Born series of Osnabrugge et al. (2016). Other choices of the (ϵ, h, H) may lead to even higher convergence rate, but existing guidelines for selecting h and H (see Liao, 2003) needs to be modified in the presence of the new parameter ϵ.

Historically, this paper represents a rare example of the application of HAM for solving integral equations and the first example in the context of seismic wavefield modeling. The introduction of the dissipation parameter ϵ into the HAM formalism also represents a novel feature of this work. *Theoretically*, the embedding parameter λ reminds us about the running coupling constant in the renormalization group theory of Jakobsen et al. (2019a) as well as the homotopy parameter λ of Watson (1989), but these relations requires further investigation. *Computationally*, it is interesting to note that the computational cost of the reference solution (7) we have obtained via matrix inversion and the scattering series solution (25-27) scales like N^3 and N^2, respectively, where N is the number of grid blocks in a discretized seismic model. Since our formulation is based on a homogeneous reference medium, it allows for the use of efficient and memory-saving Fast Fourier Transform methods that scales like N and $N \log N$, respectively (see Osnabrugge et al., 2016; Jakobsen et al., 2019a). The present work can also be combined with convergence acceleration techniques (Eftekhar et al., 2018). *Practically*, it is important that the theory and method developed in this study can be generalized to anisotropic elastic media, since the corresponding wave equation can also be transformed into an integral equation of the Lippmann-Schwinger type (Jakobsen et al., 2019b). Having developed a convergent forward scattering series, the next step could be to apply this series in the context of inverse scattering theory. Weglein et al (2003) have pioneered inverse acoustic scattering methods that do not require an assumed propagation velocity model within the medium (Zou and Weglein, 2018). Their approach (Zhang and Weglein, 2009; Zou et al. 2019) is based on the Born series solution of the Lippmann-Schwinger equation and a concomitant expansion of the interaction in orders of the data. In principle, the method is completely general and requires no prior information about the target or the propagation details of the probe signal within the target. The only fundamental limitation of the approach appears to the convergence of the conventional Born series (Kouri, 2003). Weglein et al., (2003) have made significant progress using

this approach by introducing subseries. We hope to develop convergent inverse scattering series using the HAM scattering series. However, it is not obvious that the inverse scattering series will converge even though the forward scattering series is convergent. *Finally*, we note that the work reported here may be useful in future applications of the homotopy analysis method within the context of nonlinear inverse scattering to solve the so-called regularized normal equations (Jegen et al., 2001).

ACKNOWLEDGMENTS

We thank the Research Council of Norway for funding related to Petromaks II project 267769/E3 (Bayesian inversion of 4D seismic waveform data for quantitative integration with production data) and the National IOR Centre of Norway. Ru-Shan Wu would like to thank the sponsors of the WTOPI consortium for their continuous support.

REFERENCES

Abubakar, A. and Habashy, T., 2013. Three-dimensional visco-acoustic modeling using a renormalized integral equation iterative solver, *J. Comput. Phys.*, 249 (2013) 1–12.

Abasbandy, S., 2006. The application of homotopy analysis method to nonlinear equations arising in heat transfer, *Physics Letters A.*, **360**, 109-113.

Carcione, J.M., G.C. Herman, and Kroode, A.P.E., 2002, Seismic modeling, *Geophysics*, 67, 1304-1325.

Eftekhar, R., Hu, H. and Yingcai Zheng, Y., 2018. Convergence acceleration in scattering series and seismic waveform inversion using nonlinear Shanks transformation, *Geophysical Journal International*, **214**, 1732-1743.

Eikrem, K. S., Nævdal, G., and Jakobsen, M., 2019. Iterated extended kalman filter method for time-lapse seismic full-waveform inversion, *Geophysical Prospecting*, 67(2), 379–394.

Fu, H.S. and Han, B., 2006. A homotopy method for nonlinear inverse methods *Applied Mathematics and Computation*, **183**, 1270–1279.

Han, B., Fu, H.S. and Li, Z., 2005. A homotopy method for the inversion of a two- dimensional acoustic wave equation, *Inverse Problems in Science and Engineering*, **13**, 411-431.

Hetmaniok, E., Slota, D., Trawinski, T. and Witula, R., 2014. Usage of the homotopy analysis method for solving the nonlinear and linear integral equations of the second kind, *Mathematical Modelling and Analysis*, **21**, 350-370.

Huang, X. and Greenhalgh, S., 2019a. Traveltime approximation for strongly scattering media using the homotopy analysis method, *Geophysical Journal International*, **66**, 1749-1760.

Huang, X., Jakobsen, M., Naevdal, G., and Eikrem, K.S., 2019b. Target-oriented inversion of time-lapse seismic waveform data, *Communications in Computational Physics*,doi: 10.4208/cicp.OA-2018-0143.

Huang, X., Jakobsen, M. and Wu, R.S. 2019c. On the applicability of a renormalized Born series for seismic wavefield modelling in strongly scattering media, doi:10.1093/jge/gxz105.

Jegen, M.D. Mark, E. Everet, M.E. and Schultz, A., 2001. Using homotopy to invert geophysical data, *Geophysics*, **66** 1749-1760.

Jakobsen, M., 2012 T-matrix approach to seismic forward modelling in the acoustic approximation, *Studia Geophysica et Geodaetica*, **56**, 1-20

Jakobsen, M. and Ursin, B., 2015 Full waveform inversion in the frequency domain using direct iterative T-matrix methods, *Journal of Geophysics and Engineering*, **12**, 400–418.

Jakobsen, Morten; Wu, R.S., 2016. Renormalized scattering series for frequency-domain waveform modelling of strong velocity contrasts, *Geophysical Journal International*, **206**, 880-899.

Jakobsen, M., and R. S. Wu, 2018. Accelerating the T-matrix approach to full waveform inversion by domain decomposition, *Geophysical Prospecting*, **66**, 1039-1059.

Jakobsen, M., Wu, R.S. and Huang, X., 2019a. Convergent scattering series solutions of the scalar wave equation based on renormalization group theory: Application to seismic wavefields modeling, In revision.

Jakobsen, M., Psenik, I., Iversen, E. and Ursin, B., 2019b. Transition operator approach to seismic full waveform

inversion in anisotropic elastic media, *Communications in Computational Physics*, doi: 10.4208/cicp.OA-2018-0197.

Kirkinis, E., 2008. Renormalization group interpretation of the Born and Rytov approximations, *Journal of the Optical Society of America A*, **25**, 2499-2508.

Kouri, D.J. and Vijay, A., 2003. Inverse scattering theory: Renormalization of the Lippmann-Schwinger equation for acoustic scattering in one dimension, *Physical Review E*, **67**, 046614

Liao, S., 1998. Homotopy analysis method: a new analytical method for nonlinear problems, *Appl. Math. MEch. Engl. Ed.* , **19**, 957-962.

Liao, S., 2003. *Beyond Perturbation: Introduction to the Homotopy Analysis Method*, Chapman and Hall CRC Press, Boca Raton.

Liao, S., 2004. On the homotopy analysis method for nonlinear problems, *Appl. Math. Comput.*, **147**, 499-513.

Liao, S., 2009. Notes on the homotopy analysis method: some definitions and theorems, *Common. Nonlinear. Sci. Numer. Simulat*, **14**, 983-997.

Liao, S., 2012. *Homotopy analysis method in nonlinear differential equations*, Springer/Higher equation Press, Berlin/Bejing.

Liao, S., 2014. *Advances in the homotopy analysis method*, World Scientific Publishing, Singapore.

Morse, P.M. and Feshback, H., 1953. *Methods of theoretical physics*, McGraw-Hill Science/Engineering/Math.

Malovichkoa, M., Khokhlova, N., Yavicha, N. and Zhanov, M., 2018. Acoustic 3D modeling by the method of integral equations, *Computers and Geosciences*, **111**, 223–234

Newton, R.G., 2002. *Scattering theory of waves and particles*, Dover Publications

Oristaglio, M.L. and Blok, H., 2012. *Wavefield Imaging and Inversion in Electromagnetics and Acoustics*, Cambridge University Press.

Osnabrugge, G., Leedumrongwatthanakun, S. and Vellekoop, I.M., 2016. A convergent Born series for solving the inhomogeneous Helmholtz equation in arbitrarily large media, *Journal of Computational Physics*, **322**, 113-124.

Palit, A. and Datta, D.P., 2016. Comparative Study of Homotopy Analysis and Renormalization Group Methods on Rayleigh and Van der Pol Equations, *Differential equations and dynamical systems*, **24**, 417-443.

Pfeffer, T., 2019. *Homotopy and renormalization group approaches for strongly correlated systems*, Doctoral dissertation, lmu.

Pike, R. and Sabatier, P., 2000. *Scattering: Scattering and inverse scattering in pure and applied science*, Academic press.

Robertsson, J.O.A., Blanch, J.O., Nihei, K. and Tromp, J., 2012. *Numerical modeling of seismic wave propagation: Gridden two-way wave equation methods*, Society of Exploration Geophysicists.

Watson, L. T., 1989, Globally convergent homotopy methods: a tutorial, Applied Mathematics and Computation, **31**, 369-396.

Weinberg, S., 1963. Quasi-particles and the Born series, *Physical Review*, **131**, 1, 440-460.

Zhang, H., and Weglein, A. B. 2009. Direct nonlinear inversion of 1D acoustic media using inverse scattering

subseries, *Geophysics*, 74(6), WCD29-WCD39..

Weglein, A. B., Araújo, F. V., Carvalho, P. M., Stolt, R. H., Matson, K. H., Coates, R. T., ... and Zhang, H. 2003. Inverse scattering series and seismic exploration, *Inverse problems*, 19(6), R27.

Zou, Y. and Weglein, A.B., 2018. ISS Q compensation without knowing, estimating or determining Q and without using or needing low and zero frequency data, *Journal of Seismic Exploration*, 27: 593-608.

Zou, Y., Ma, C. and Weglein, A. B. 2019. A new multidimensional method that eliminates internal multiples that interfere with primaries, without damaging the primary, without knowledge of subsurface properties, for off-shore and on-shore conventional and unconventional plays, *SEG Technical Program Expanded Abstracts 2019*, 4525-4529.

Table 1. Convergence control parameters used in 4 different numerical experiments focusing on the convergence properties of the homotopy analysis method. The parameter ϵ_c is the critical value which is required for the convergent Born series of Osnabrugge et al. (2016) to converge. The color refers to the different colors used in Figure 5 (experiments 1-6) and Figure 6 (experiments 7-12).

Experiment	ϵ/ϵ_c	h	H	color	$\|M\|$	$\sigma(M)$
1	0.00	-1.000	I	1.46	1.06	b
2	0.00	-0.950	I	1.40	1.03	g
3	0.00	-0.900	I	1.35	0.99	r
4	0.00	-0.800	I	1.27	0.94	c
5	0.00	-0.100	I	1.01	0.97	m
6	0.50	-0.800	I	0.96	0.82	k
7	1.00	-1.000	γ	0.94	1.98	b
8	0.50	-1.000	γ	0.85	1.93	g
9	0.50	-0.500	γ	0-92	1.09	r
10	0.50	-0.250	γ	0.96	0.93	c
11	0.50	-0.125	γ	0.98	0.96	m
12	0.25	-0.125	γ	0.96	1.00	k

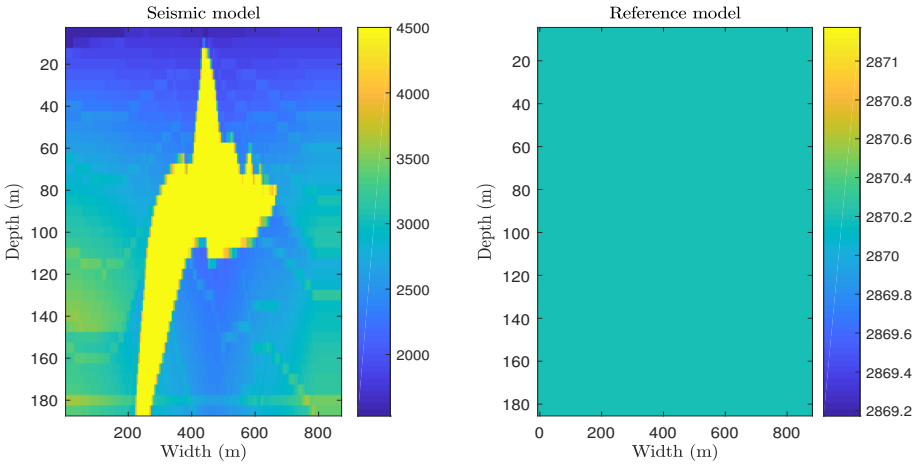

Figure 1. The true velocity model and the homogeneous reference model.

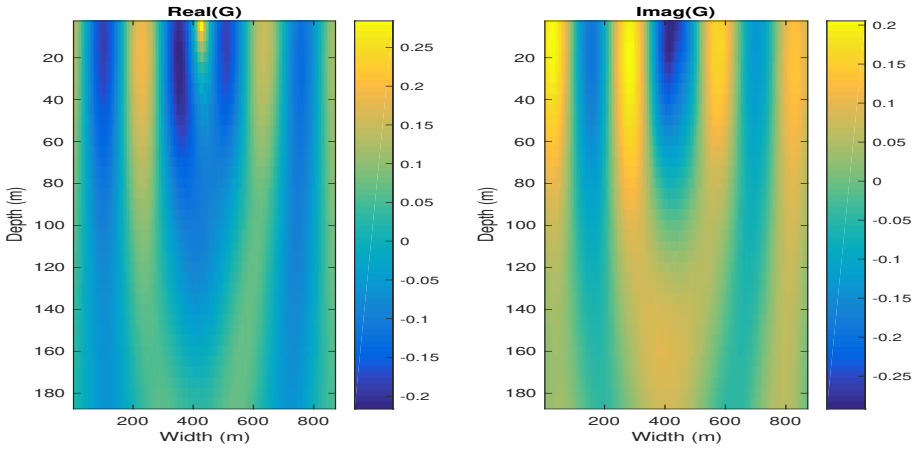

Figure 2. Real and imaginary parts of the frequency domain wavefield at 10 Hz computed by solving the Lippmann-Schwinger equation exactly using a real space matrix representation.

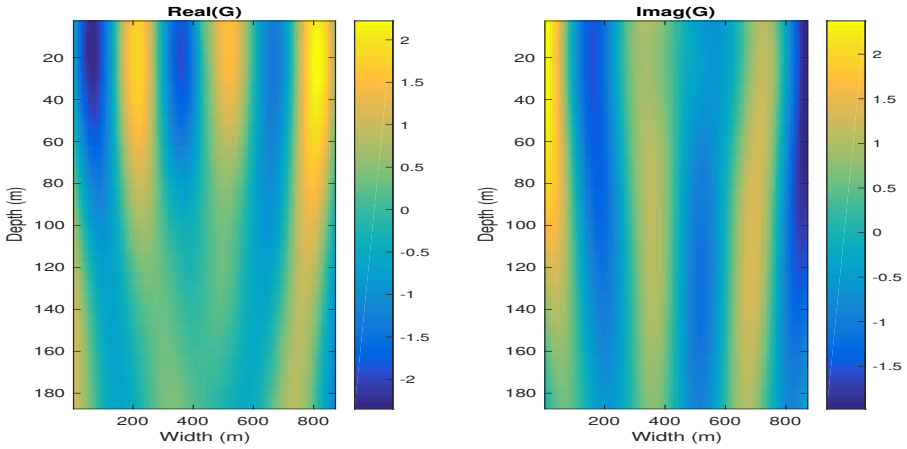

Figure 3. The real and imaginary parts of the frequency domain wavefield at 10 Hz computed using the HAM series with auxiliary parameters corresponding to experiment 1 in Table 1.

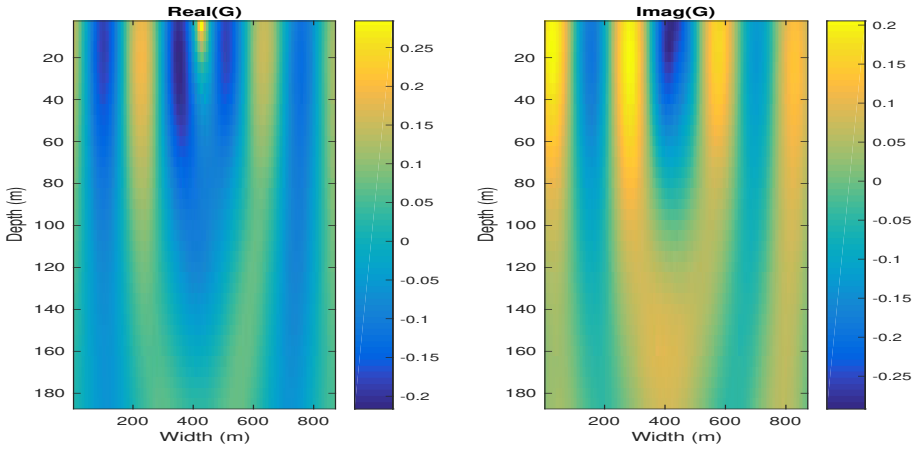

Figure 4. The real and imaginary parts of the frequency domain wavefield at 10 Hz computed using the HAM series with auxiliary parameters corresponding with experiment 2 in Table 1.

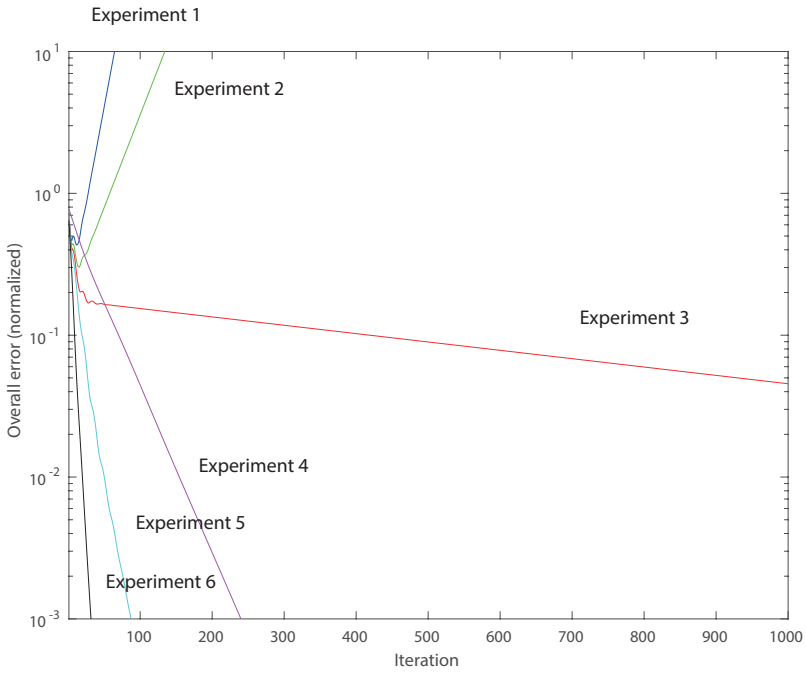

Figure 5. Comparison of overall errors vs the number of iterations for numerical experiments 1-6 described in Table 1.

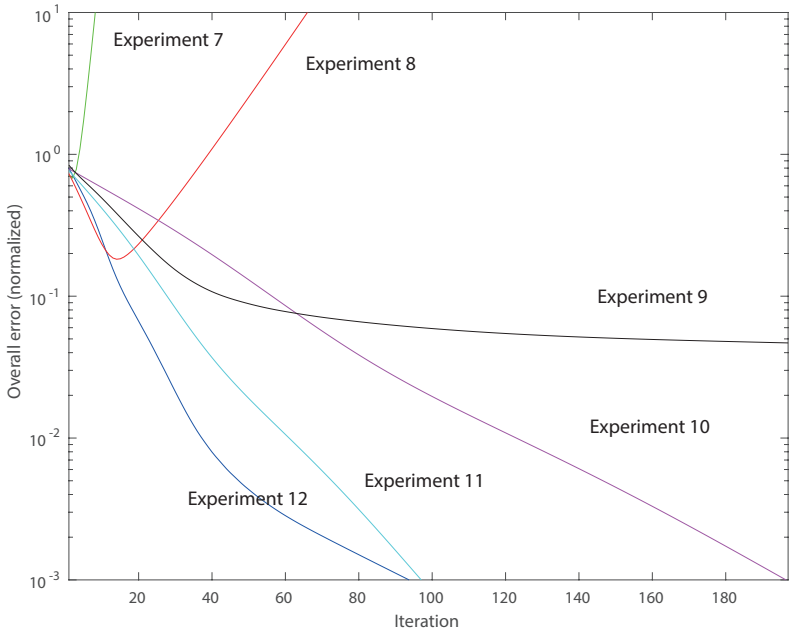

Figure 6. Comparison of overall errors vs the number of iterations for numerical experiments 7-12 described in Table 1.

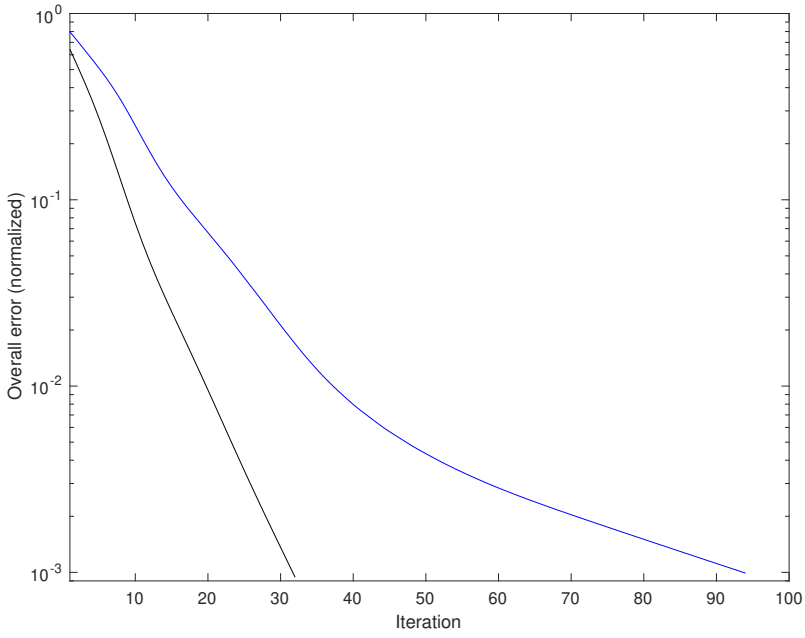

Figure 7. Comparison of overall errors vs the number of iterations for numerical experiment 6 (optimal HAM series with some dissipation in the reference medium) and 7 (original convergent Born series of Osnabrugge et al. 2016). Note that the optimal HAM series (black curve) requires much less iterations than the convergent Born series (blue curve) of Osnabrugge et al. (2016).

APPENDIX A: DESCRIPTION AND IMPLEMENTATION OF THE HAM SERIES

Similar to the conventional Born series, every iteration is associated with multiple scattering processes of different orders. However, we have reorganized the different terms in the conventional Born series so that the spectral radius of M is smaller than unity. This implies that each new term is smaller than the previous one, so that the scattering series does not diverge when the number of iterations becomes large. Mathematically, this is done by introducing an integral operator with spectral radius smaller than unity via the use of control parameter h and the convergence control operator H. The series converges if the spectral radius of the operator M is less than unity. We have also introduced an element of dissipation in the reference medium, which ensures that the energy associated with Greens function is finite and localized. It should be emphasized that the dissipation parameter ϵ can be selected arbitrary. This is because the dissipation is compensated exactly by a corresponding gain term in the scattering potential, suggesting that the final results are independent of this dissipation in the reference medium. The dissipation aspect of our HAM algorithm is similar to the convergent Born series of Osnabrugge et al. (2016). However, our convergent scattering series is more general than the convergent Born series, since the convergent control parameters can be selected rather arbitrary, as long as the spectral radius of the M-operator is smaller than unity. Some details for implementation of the new convergent scattering series using based on the HAM is provided in Algorithm 1. In addition, Table 1 shows the norm $\|M\|$ and spectral radius $\sigma\left(M\right)$ of the operator M with numerical experiments.

The HAM algorithm is represented by equations (25)-(27). However, the formulation in the main text is based on the real-space coordinate representation of the relevant integral operators. As discussed by Osnabrugge et al., (2016), the operation of Green's function with contrast-source terms has a convolution structure that can be implemented more efficiently by using the wave vector representation; that is, by using the Fast Fourier Transform (FFT) algorithm in this context. This is because convolution in real-space is equivalent to multiplication in the Fourier space, and the computational cost of the FFT-operation is much smaller than that of matrix multiplication and inversion.The memory requirements scales like N^2 and N when using the position and wave vector representations, respectively. The computational cost should theoretically scale like N^3 and $N\log N$ when using the position and wave vector representations, respectively. The iterative FFT algorithm is implemented as

$$\psi_m\left(\mathbf{r}\right) = hH(\psi^{(0)}\left(\mathbf{r}\right) - \psi_0\left(\mathbf{r}\right) - \text{ifft}\left[G^{(0)}\left(\mathbf{k}\right)\text{fft}\left[V\psi_m\left(\mathbf{r}\right)\right]\right]), \tag{A.1}$$

where fft and ifft are the forward and inverse fast Fourier transform operators, $\mathbf{k}$ is the Fourier transformed coordinates. Figures A1 and A2 show the frequency domain wavefield using exact solutions, the efficient and memory-saving FFT implementation with 100 iterations, respectively.

Algorithm 1 Pseudo code for the scattering series

Initialisation: frequency, maximum iteration number N_{max}, the parameter ϵ

true model and background model;

$V = k^2 - k_0^2 - i\epsilon$

$k_b = \sqrt{k_0^2 + i\epsilon}$

$\psi^{(0)} = G^{(0)} S$

$\psi = \psi^{(0)}$

$M = I + hH - hHG^{(0)}V$

$n = 1$

while $n < N_{max}$ **do**

  $n = n + 1$

  if $n == 1$ **then**

    $\psi_m = hH(\psi^{(0)} - \psi_0 - G^{(0)} V \psi^{(0)})$

  else

    $\psi_m = M\psi_m$

  end if

  $\psi = \psi + \psi_m$

end while

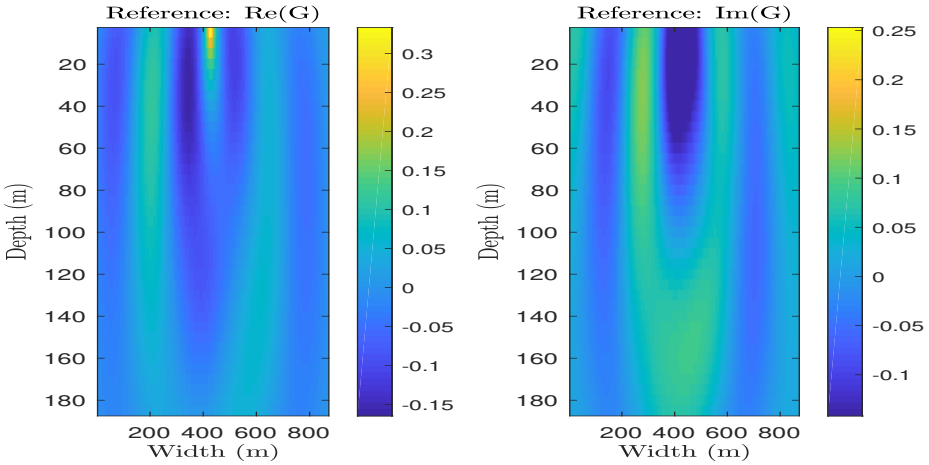

Figure A1. The real and imaginary parts of the frequency domain wavefield at 10 Hz computed by solving the Lippmann-Schwinger equation exactly using a real space matrix representation.

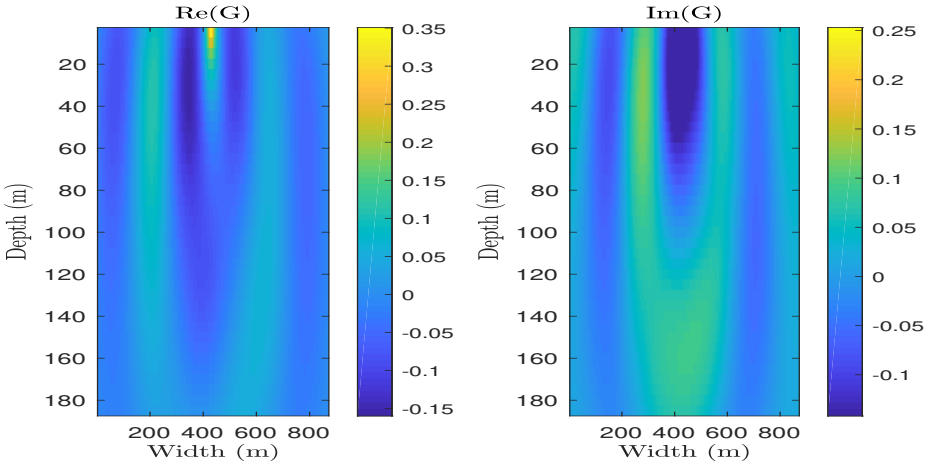

Figure A2. The real and imaginary parts of the frequency domain wavefield computed using the HAM series with auxiliary parameters corresponding with experiment 11 in Table 1.

III

Geophysical Journal International

Geophys. J. Int. (2019) **216,** 1648–1664
Advance Access publication 2018 December 13
GJI Marine geosciences and applied geophysics

doi: 10.1093/gji/ggy524

Traveltime approximation for strongly anisotropic media using the homotopy analysis method

Xingguo Huang[1] and Stewart Greenhalgh[2]

[1]*Department of Earth Science, University of Bergen, P.O. Box* 7803, 5020 *Bergen, Norway. E-mail: xingguo.huang19@gmail.com*
[2]*Department of Geosciences, King Fahd University of Petroleum and Minerals, Dhahran 31261, Saudi Arabia*

Accepted 2018 December 12. Received 2018 June 8; in original form 2018 November 15

SUMMARY

Traveltime approximation plays an important role in seismic data processing, for example, anisotropic parameter estimation and seismic imaging. By exploiting seismic traveltimes, it is possible to improve the accuracy of anisotropic parameter estimation and the resolution of seismic imaging. Conventionally, the traveltime approximations in anisotropic media are obtained by expanding the anisotropic eikonal equation in terms of the anisotropic parameters and the elliptically anisotropic eikonal equation based on perturbation theory. Such an expansion assumes a small perturbation and weak anisotropy. In a realistic medium, however, the assumption of small perturbation likely breaks down. We present a retrieved zero-order deformation equation that creates a map from the anisotropic eikonal equation to a linearized partial differential equation system based on the homotopy analysis method. By choosing the linear and nonlinear operators in the retrieved zero-order deformation equation, we develop new traveltime approximations that allow us to compute the traveltimes for a medium of arbitrarily strength anisotropy. A comparison of the traveltimes and their errors from the homotopy analysis method and from the perturbation method suggests that the traveltime approximations provide a more reliable result in strongly anisotropic media.

Key words: Non-linear differential equations; Seismic anisotropy; Wave propagation.

INTRODUCTION

Seismic anisotropy can arise due to various geological situations such as crystal orientation (Musgrave 1970), parallel cracked rocks (Crampin 1984), sedimentation near salt domes and thin layering in the subsurface (Schoenberg 1983; Tsvankin 1997, 2012). It is important for seismic exploration and investigations of the Earth's interior to recognize the anisotropy. One of the most common and effective approximations to an anisotropic subsurface is the transversely isotropic medium. Modelling seismic traveltimes is clearly essential for understanding and quantification of the kinematic properties of the propagating waves in such media. It finds many applications such as velocity analysis, anisotropic parameter estimation (Alkhalifah 2011a), traveltime tomography (Chapman & Pratt 1992; Zelt & Barton 1998; Zhou *et al.* 2008; Bai & Greenhalgh 2005), seismic migration (Huang *et al.* 2016a; Huang & Sun 2018) and full waveform inversion (Alkhalifah & Choi 2014; Silva *et al.* 2016). The seismic traveltimes can be obtained by solving the nonlinear partial differential equation under the high-frequency assumption; this is referred to as the eikonal equation.

There are several approaches to solve the eikonal equation, such as ray-tracing methods (see e.g. Červenỳ 1972, 2001; Červenỳ & Pšenčík 1983; Moser 1991; Vinje *et al.* 1993; Bai *et al.* 2007; Červenỳ *et al.* 2007, 2012; Iversen & Tygel 2008) and the finite-difference (FD) method (Vidale 1988; Cao & Greenhalgh 1994; Sethian 1996; Sethian & Popovici 1999; Rawlinson & Sambridge 2004a,b; Noble *et al.* 2014). The ray-tracing method computes the traveltimes by integration along rays in which the initial condition must be specified. The main advantages include easy implementation and high efficiency. However, it gives a non-uniform distribution of traveltimes, and the presence of shadow zones can lead to problems. Moreover, due to the different directions of the group velocity (ray direction) and the phase velocity (wave front normal direction) vectors , solving the ray-tracing system becomes complicated in the anisotropic media. The FD method has been recognized as an efficient and accurate computational scheme for calculating the traveltimes. In the framework of the FD method, two approaches, the fast marching method (Sethian 1996; Sethian & Popovici 1999; Alkhalifah & Fomel 2001; Huang *et al.* 2016b; Huang & Sun 2018) and the fast sweeping method (Zhao 2005), have been widely used for calculating the traveltimes. In recent years, efforts have been made to solve the anisotropic eikonal equations (Luo & Qian 2012; Waheed *et al.* 2015a,b; Bouteiller *et al.* 2017; Han *et al.* 2017; Waheed & Alkhalifah 2017). In addition, some interesting results for moveout approximations have been obtained based on the weak-anisotropy (WA)

parameters (Farra & Pšenčík 2017; Pšenčík & Farra 2017). However, it is challenging to use the FD method to solve the eikonal equation for the anisotropic media because of the additional anisotropic parameters involved. This is especially true because solving the quartic equation and finding the roots of a quartic equation at each computational step are difficult (Alkhalifah 2011a; Stovas & Alkhalifah 2012).

Perturbation theory has been widely used to develop traveltime approximations for calculating the traveltimes in anisotropic media. This approach was proposed by Alkhalifah (2011a,b) for deriving traveltime approximations and scanning anisotropic parameters in transversely isotropic media with a vertical symmetry axis (VTI) and transversely isotropic media with a tilted symmetry axis (TTI) media. Since then, many researchers have applied the perturbation theory and have made significant progress in developing the traveltime approximations. For instance, Stovas & Alkhalifah (2012) derive the traveltime approximations in TTI media by expanding the TTI eikonal equation in a power series in terms of the anellipticity parameter. Subsequent generalizations of the perturbation theory to a transversely isotropic medium can be found in Waheed *et al.* (2013), Alkhalifah (2013) and Masmoudi & Alkhalifah (2016). Xu *et al.* (2017) have applied perturbation theory to moveout approximations in an anisotropic medium. Later, this approach has been extended to an orthorhombic medium (Stovas *et al.* 2016) and attenuating VTI medium (Hao & Alkhalifah 2017).

Recently, we have extended the perturbation theory to the problem of complex traveltime computation. We have applied it to the complex eikonal equations in orthorhombic and VTI media and derived a system of linear equations for the complex traveltime computation. Based on the derived system, we have developed analytic solutions in an orthorhombic medium (Huang & Greenhalgh 2018) and numerical solutions in a VTI medium (Huang *et al.* 2018). The perturbation approach to the complex eikonal equation differs from the real eikonal equation in the following respects. First, we expand the real and imaginary parts of the complex traveltime in terms of the background traveltime and the coefficients separately and transform the problem of the highly nonlinear eikonal equations into one of solving a relatively simple eikonal equation for the background medium and a system of linear partial differential equations. Second, we use a perturbation scheme to solve the background complex eikonal equation for the background traveltimes. In this case, we successfully employed the perturbation theory to solve the complex eikonal equations in anisotropic media.

In reviewing all of the above perturbation theories, we find that most of the traveltime approximations make use of a power-series expansion in terms of the anisotropic parameters and make the assumption of small anisotropic parameters. This means that the degree of anisotropy does not exceed a small perturbation from the elliptically anisotropic background medium. A major limitation of the perturbation analysis technique is that it breaks down in regions with strong anisotropy.

The purpose of this paper is to establish the fundamental theory of the linear partial differential equations for solving the VTI and TTI eikonal equations and to develop traveltime approximations for strongly anisotropic media. To this end, we employ the homotopy analysis method (HAM), an analytic approximation method for highly nonlinear problems, to the nonlinear eikonal equations. The HAM was proposed by Liao (1992c, 1999, 2003a, 2012) for solving nonlinear problems encountered in mathematical physics. Different from the conventional perturbation theory, the HAM does not depend on any physical parameters and can guarantee the convergence of the series solution. This implies that the HAM can be used for arbitrarily high nonlinear problem. From the late 1990s to 2010s, due to the advantages of the HAM over perturbation theory, it has been widely used in the mathematical and physical sciences. Much work has been done on the HAM for nonlinear problems in developing analytic series solutions, for example, nonlinear oscillations (Liao 1992b, 2003b, 2004; Liao & Chwang 1998), boundary layer flows (Liao 1999, 2002), heat transfer (Liao 2003b; Wang *et al.* 2003), nonlinear water waves (Liao 1992a; Liao *et al.* 2016) and nonlinear gravity waves (Liao 2011). In this work, by applying the HAM to anisotropic eikonal equations, we extend the HAM to geophysical problems for anisotropic media.

In the following, we first review the theory of the HAM. After deriving linear partial differential equations in VTI and TTI media, we provide the theoretical background of the differences between the HAM and the perturbation theory and the nature of the derived linear equations. Then, we develop the analytic solutions of the VTI and TTI eikonal equations for traveltime approximations. Finally, we present numerical tests of the contours of the traveltimes and the relative errors which are aimed at quantifying the differences of the results from the HAM and the perturbation theory method and comparing the performance in strongly anisotropic media.

HOMOTOPY ANALYSIS METHOD

The HAM (Liao 2004) is an analytic approximation technique for generating series solutions to highly nonlinear problems. In this method, an embedding parameter q and a convergence control parameter h are chosen to transform the nonlinear equation into a sequence of linear equations. In this section, we review the mathematical formulations of the HAM and discuss the applicability of this method to solving nonlinear equations.

Consider a general nonlinear equation

$$\mathcal{N}[\tau(x,z)] = 0, \tag{1}$$

where $\mathcal{N}$ is a nonlinear operator, x and z are the independent variable parameters, and $\tau(x,z)$ is the exact solution of the nonlinear equation. For solving the above nonlinear equation, Liao (1992a,1992b) developed the zero-order deformation equation

$$(1-q)\,\mathcal{L}\left[t_q(x,z) - \tau_0(x,z)\right] = q\,h\mathcal{H}(x,z)\cdot\mathcal{N}\left[\tau_q(x,z)\right], \tag{2}$$

where $\mathcal{L}$ is an arbitrary linear operator, $\mathcal{H}(x, z)$ is an auxiliary function and $\tau_0(x, z)$ is the initial approximation. Eq. (2) shows that (1) the nonlinear problem is transformed into a linear problem; (2) the linear operator $\mathcal{L}$ plays a crucial role in the transformation; (3) there is a continuous mapping from $\tau(x, z, q)$ to $t(x, z, q)$.

It can be seen that when $q = 0$, eq. (2) becomes

$$\mathcal{L}\left[t_q(x, z) - \tau_0(x, z)\right] = 0, \tag{3}$$

and when $q = 1$, eq. (2) becomes

$$h\mathcal{H}(x, z) \cdot \mathcal{N}\left[\tau_q(x, z)\right] = 0. \tag{4}$$

From eqs (3) and (4), we have

$$t(x, z, 0) = \tau_0(x, z), \tag{5}$$

and

$$t(x, z, 1) = \tau(x, z). \tag{6}$$

Eqs (5) and (6) show that while the embedding parameter q changes from 0 to 1, the solution of the nonlinear eq. (1) varies from the initial approximation to the exact solution of the equation.

By means of Taylor's theorem, the solution of eq. (2) can be expressed as a power series in q to yield the series expansion solution

$$t_q(x, z) = \tau_0(x, z) + \sum_{m=1}^{\infty} \tau_m(x, z) q^m. \tag{7}$$

If now we assume that we can choose the embedding parameter, auxiliary parameter and the auxiliary linear operator to make the series converge at $q = 1$, then we can determine the coefficients by substituting it into eq. (2). Then returning to the situation in which $q = 1$ and from a combination of eqs (6) and (8), we have

$$\tau_q(x, z) = \tau_0(x, z) + \sum_{m=1}^{\infty} \tau_m(x, z). \tag{8}$$

The above solution refers to a situation in which only the coefficients $\tau_m(x, z)$ vary. The solution therefore depends on the initial approximation $\tau_0(x, z)$ and the coefficients $\tau_m(x, z)$. This differs from the perturbation theory in which the solution is a function of the coefficients and small parameters.

The HAM explains how the analytic solutions of the nonlinear equation can be obtained by transforming the nonlinear equation into a linear equation system. From eq. (2), we can observe that with suitable embedding parameter, auxiliary parameter and the auxiliary linear operator, the transformation relationship is always accepted. By analogy with the homotopy analysis process, the first guess approximation is chosen initially for satisfying eq. (3), then the approximation changes until it satisfies eq. (4). This means that the assumed series expansion solution (7) changes from the initial solution to the exact solution. With the embedding parameter q getting larger and larger, the series expansion solution (7) approaches the exact solution smoothly, meaning that, at $q = 1$, the exact solution can be obtained. The homotopy analysis process can be divided into the following steps: (1) choosing the linear operator $\mathcal{L}$; (2) construction of the zero-order deformation equation; (3) determination of the coefficients of the series expansion; (4) obtaining the exact solution by setting $q = 1$.

THEORY FOR TRAVELTIME CALCULATION IN ANISOTROPIC MEDIA USING HAM

In this section, we derive the linearized partial differential equation system for the traveltime solutions of the VTI and TTI eikonal equations by using the HAM. For the VTI eikonal equation, we assume to have the known initial traveltime solution, but just for an elliptically anisotropic medium, which we denote as the background traveltime solution. We start with Alkhalifah's acoustic eikonal equation for a VTI medium involving the anisotropic parameter η. Following recent work (Huang & Greenhalgh 2018; Huang *et al.* 2018), we choose the linear operator form as an elliptical anisotropic eikonal equation. Then, we propose the solution as a series expansion containing the embedding parameter q. For the TTI eikonal equation, the initial solution and linear operator are chosen in a similar way to the VTI eikonal equation. However, for the series expansion, we only keep two terms because if we keep high-order terms, the solution of the TTI eikonal equation is complicated.

Retrieved VTI eikonal equation

Following Alkhalifah (2000), the eikonal equation for VTI media can be written as

$$v^2(1 + 2\eta)\left(\frac{\partial \tau}{\partial x}\right)^2 + v_v^2\left(\frac{\partial \tau}{\partial z}\right)^2\left(1 - 2\eta v_v^2\left(\frac{\partial \tau}{\partial x}\right)^2\right) = 1. \tag{9}$$

Here, $\tau(x,z)$ is the traveltime at the position in the coordinates (x,z) , v is the P-wave normal-moveout (NMO) velocity ($v = v_v\sqrt{1+2\delta}$), v_v is the vertical P-wave velocity and η is the anellipticity parameter. According to eqs (2) and () and by choosing the linear operator as

$$\mathcal{L} = v^2\frac{\partial\tau_0}{\partial x}\frac{\partial\tau}{\partial x} + v_v^2\frac{\partial\tau_0}{\partial z}\frac{\partial\tau}{\partial z}, \tag{10}$$

and the nonlinear operator as

$$\mathcal{N} = v^2(1+2\eta)\left(\frac{\partial\tau}{\partial x}\right)^2 + v_v^2\left(\frac{\partial\tau}{\partial z}\right)^2\left(1-2\eta v^2\left(\frac{\partial\tau}{\partial x}\right)^2\right) - 1, \tag{11}$$

we obtain the following zero-order deformation equation for the eikonal equation in VTI media

$$(1-q)\left(v^2\frac{\partial\tau_0}{\partial x}\frac{\partial\tau}{\partial x} + v_v^2\frac{\partial\tau_0}{\partial z}\frac{\partial\tau}{\partial z} - \left(v^2\left(\frac{\partial\tau_0}{\partial x}\right)^2 + v_v^2\left(\frac{\partial\tau_0}{\partial z}\right)^2\right)\right) + q\left(v^2(1+2\eta)\left(\frac{\partial\tau}{\partial x}\right)^2 + v_v^2\left(\frac{\partial\tau}{\partial z}\right)^2\left(1-2\eta v^2\left(\frac{\partial\tau}{\partial x}\right)^2\right) - 1\right) = 0, \tag{12}$$

where τ_0 is the traveltime solution (initial approximation) for the elliptical anisotropic eikonal equation. To obtain the linear equation system, we assume

$$\tau = \tau_0 + \tau_1 q + \tau_2 q^2 + \tau_3 q^3, \tag{13}$$

where τ_1, τ_2 and τ_3 are the first-order, second-order and third-order coefficients, respectively. Then substituting eq. (13) into eq. (12), we obtain the linear partial differential equation for the first-order coefficient τ_1:

$$\left(\frac{\partial\tau_0}{\partial x}\right)\left(\frac{\partial\tau_1}{\partial x}\right)v^2 + \left(\frac{\partial\tau_0}{\partial z}\right)\left(\frac{\partial\tau_1}{\partial z}\right)v_v^2 = 2\eta\left(\frac{\partial\tau_0}{\partial x}\right)^2\left(\frac{\partial\tau_0}{\partial z}\right)^2 v_v^2v^2 - (2\eta+1)\left(\frac{\partial\tau_0}{\partial x}\right)^2 v^2 - \left(\frac{\partial\tau_0}{\partial z}\right)^2 v_v^2 + 1, \tag{14}$$

the linear partial differential equation for the second-order coefficient τ_2:

$$\begin{aligned}\left(\frac{\partial\tau_0}{\partial x}\right)\left(\frac{\partial\tau_2}{\partial x}\right)v^2 + \left(\frac{\partial\tau_0}{\partial z}\right)\left(\frac{\partial\tau_2}{\partial z}\right)v_v^2 &= 4\eta\left(\frac{\partial\tau_0}{\partial x}\right)^2\left(\frac{\partial\tau_0}{\partial z}\right)\left(\frac{\partial\tau_1}{\partial z}\right)v_v^2v^2 + 4\eta\left(\frac{\partial\tau_0}{\partial x}\right)\left(\frac{\partial\tau_0}{\partial z}\right)^2\left(\frac{\partial\tau_1}{\partial x}\right)v_v^2v^2\\ &\quad - 2(2\eta+1)\left(\frac{\partial\tau_0}{\partial x}\right)\left(\frac{\partial\tau_1}{\partial x}\right)v^2 - \left(\frac{\partial\tau_0}{\partial x}\right)\left(\frac{\partial\tau_1}{\partial x}\right)v^2 - \left(\frac{\partial\tau_0}{\partial z}\right)\left(\frac{\partial\tau_1}{\partial z}\right)v_v^2\end{aligned} \tag{15}$$

and the linear partial differential equation for the third-order coefficient τ_3:

$$\begin{aligned}\left(\frac{\partial\tau_0}{\partial x}\right)\left(\frac{\partial\tau_3}{\partial x}\right)v^2 + \left(\frac{\partial\tau_0}{\partial z}\right)\left(\frac{\partial\tau_3}{\partial z}\right)v_v^2 &= 4\eta\left(\frac{\partial\tau_0}{\partial x}\right)^2\left(\frac{\partial\tau_0}{\partial z}\right)\left(\frac{\partial\tau_2}{\partial z}\right)v_v^2v^2 + 2\eta\left(\frac{\partial\tau_0}{\partial x}\right)^2\left(\frac{\partial\tau_1}{\partial z}\right)^2 v_v^2v^2 + 4\eta\left(\frac{\partial\tau_0}{\partial x}\right)\left(\frac{\partial\tau_0}{\partial z}\right)^2\left(\frac{\partial\tau_2}{\partial x}\right)v_v^2v^2\\ &\quad + 8\eta\left(\frac{\partial\tau_0}{\partial x}\right)\left(\frac{\partial\tau_0}{\partial z}\right)\left(\frac{\partial\tau_1}{\partial x}\right)\left(\frac{\partial\tau_1}{\partial z}\right)v_v^2v^2 - 2(2\eta+1)\left(\frac{\partial\tau_0}{\partial x}\right)\left(\frac{\partial\tau_2}{\partial x}\right)v^2 + \left(\frac{\partial\tau_0}{\partial x}\right)\left(\frac{\partial\tau_2}{\partial x}\right)v^2\\ &\quad + 2\eta\left(\frac{\partial\tau_0}{\partial z}\right)^2\left(\frac{\partial\tau_1}{\partial x}\right)^2 v_v^2v^2 - \left(\frac{\partial\tau_0}{\partial z}\right)\left(\frac{\partial\tau_2}{\partial z}\right)v_v^2 - (2\eta+1)\left(\frac{\partial\tau_1}{\partial x}\right)^2 v^2 - \left(\frac{\partial\tau_1}{\partial z}\right)^2 v_v^2.\end{aligned} \tag{16}$$

The linearized partial differential equations, derived in this section, may be used directly for obtaining the coefficients τ_1, τ_2 and τ_3, once the initial traveltime solution τ_0 has been calculated. For each linear equation, we can solve the equation for the corresponding coefficient in terms of the anisotropic parameter. Thus, instead of solving the eikonal equation in VTI media directly, we can obtain the solutions by solving the above linearized partial differential equations.

Retrieved TTI eikonal equation

The eikonal equation for TTI media is given by (Alkhalifah 2000)

$$v^2(1+2\eta)\left(\frac{\partial\tau}{\partial x}\cos\theta + \frac{\partial\tau}{\partial z}\sin\theta\right)^2 + v_t^2\left(\frac{\partial\tau}{\partial z}\cos\theta - \frac{\partial\tau}{\partial x}\sin\theta\right)^2\left(1-2\eta v^2\left(\frac{\partial\tau}{\partial x}\cos\theta + \frac{\partial\tau}{\partial z}\sin\theta\right)^2\right) = 1, \tag{17}$$

where θ is the angle of the symmetry axis measured from the vertical direction and v_t is the tilted velocity. According to eqs (2) and (7) and by choosing the linear operator as

$$\mathcal{L} = v^2\frac{\partial\tau_0}{\partial x}\frac{\partial\tau}{\partial x} + v_t^2\frac{\partial\tau_0}{\partial z}\frac{\partial\tau}{\partial z} \tag{18}$$

and the nonlinear operator as

$$\mathcal{N} = v^2(1+2\eta)\left(\frac{\partial\tau}{\partial x}\cos\theta + \frac{\partial\tau}{\partial z}\sin\theta\right)^2 + v_t^2\left(\frac{\partial\tau}{\partial z}\cos\theta - \frac{\partial\tau}{\partial x}\sin\theta\right)^2\left(1-2\eta v^2\left(\frac{\partial\tau}{\partial x}\cos\theta + \frac{\partial\tau}{\partial z}\sin\theta\right)^2\right) - 1, \tag{19}$$

we obtain the following zero-order deformation equation for the eikonal equation in TTI media:

$$(1-q)\left(v^2\frac{\partial\tau_0}{\partial x}\frac{\partial\tau}{\partial x}+v_t^2\frac{\partial\tau_0}{\partial z}\frac{\partial\tau}{\partial z}-\left(v^2\left(\frac{\partial\tau_0}{\partial x}\right)^2+v_t^2\left(\frac{\partial\tau_0}{\partial z}\right)^2\right)\right)$$
$$+q\left(v^2(1+2\eta)\left(\frac{\partial\tau}{\partial x}\cos\theta+\frac{\partial\tau}{\partial z}\sin\theta\right)^2+v_t^2\left(\frac{\partial\tau}{\partial z}\cos\theta-\frac{\partial\tau}{\partial x}\sin\theta\right)^2\left(1-2\eta v^2\left(\frac{\partial\tau}{\partial x}\cos\theta+\frac{\partial\tau}{\partial z}\sin\theta\right)^2\right)-1\right)=0, \tag{20}$$

where τ_0 is the traveltime solution (initial approximation) for the elliptical anisotropic eikonal equation.

In a similar manner, by assuming

$$\tau=\tau_0+\tau_1 q+\tau_2 q^2, \tag{21}$$

we obtain the following linear partial differential equations for the first-order and second-order coefficients τ_1 and τ_2, respectively:

$$\begin{aligned}-\frac{\partial\tau_0}{\partial x}\frac{\partial\tau_1}{\partial x}v^2-\frac{\partial\tau_0}{\partial z}\frac{\partial\tau_1}{\partial z}v_t^2=&-2\eta\left(\frac{\partial\tau_0}{\partial x}\right)^4v^2v_v^2\sin^2\theta\cos^2\theta+4\eta\left(\frac{\partial\tau_0}{\partial x}\right)^3\frac{\partial\tau_0}{\partial z}v^2v_t^2\sin\theta\cos^3\theta-4\eta\left(\frac{\partial\tau_0}{\partial x}\right)\frac{\partial\tau_0}{\partial z}v^2v_t^2\sin^3\theta\cos\theta\\&-2\eta\left(\frac{\partial\tau_0}{\partial x}\right)^2\left(\frac{\partial\tau_0}{\partial z}\right)^2v^2v_t^2\sin^4\theta-2\eta\left(\frac{\partial\tau_0}{\partial x}\right)^2\left(\frac{\partial\tau_0}{\partial z}\right)^2v^2v_t^2\cos^4\theta\\&+8\eta\left(\frac{\partial\tau_0}{\partial x}\right)^2\left(\frac{\partial\tau_0}{\partial z}\right)^2v^2v_t^2\sin^2\theta\cos^2\theta\\&+(2\eta+1)\left(\frac{\partial\tau_0}{\partial x}\right)^2v^2\cos^2\theta+\left(\frac{\partial\tau_0}{\partial x}\right)^2v_t^2\sin^2\theta-4\eta\frac{\partial\tau_0}{\partial x}\left(\frac{\partial\tau_0}{\partial z}\right)^3v^2v_t^2\sin\theta\cos^3\theta\\&+4\eta\frac{\partial\tau_0}{\partial x}\left(\frac{\partial\tau_0}{\partial z}\right)^3v^2v_t^2\sin^3\theta\cos\theta\\&+2(2\eta+1)\left(\frac{\partial\tau_0}{\partial x}\right)^2v^2\sin\theta\cos\theta-2\frac{\partial\tau_0}{\partial x}\frac{\partial\tau_0}{\partial z}v_t^2\sin\theta\cos\theta-2\eta\left(\frac{\partial\tau_0}{\partial z}\right)^4v^2v_t^2\sin^2\theta\cos^2\theta\\&+(2\eta+1)\left(\frac{\partial\tau_0}{\partial z}\right)^2v^2\sin^2\theta+\left(\frac{\partial\tau_0}{\partial z}\right)^2v_t^2\cos^2\theta-1\end{aligned} \tag{22}$$

and

$$\begin{aligned}-\frac{\partial\tau_0}{\partial x}\frac{\partial\tau_2}{\partial x}v^2-\frac{\partial\tau_0}{\partial z}\frac{\partial\tau_2}{\partial z}v_t^2=&-8\eta\left(\frac{\partial\tau_0}{\partial x}\right)^3\frac{\partial\tau_1}{\partial x}v^2v_t^2\sin^2\theta\cos^2\theta+4\eta\left(\frac{\partial\tau_0}{\partial x}\right)^3\frac{\partial\tau_1}{\partial z}v^2v_t^2\sin\theta\cos^3-4\eta\left(\frac{\partial\tau_0}{\partial x}\right)^3\frac{\partial\tau_1}{\partial z}v^2v_t^2\sin^3\theta\cos\theta\\&+12\eta\left(\frac{\partial\tau_0}{\partial x}\right)^2\frac{\partial\tau_0}{\partial z}\frac{\partial\tau_1}{\partial x}v^2v_t^2\sin\theta\cos^3\theta-12\eta\left(\frac{\partial\tau_0}{\partial x}\right)^2\frac{\partial\tau_0}{\partial z}\left(\frac{\partial\tau_1}{\partial x}\right)v^2v_t^2\sin^3\theta\cos\theta\\&-4\eta\left(\frac{\partial\tau_0}{\partial x}\right)^2\frac{\partial\tau_0}{\partial z}\frac{\partial\tau_1}{\partial z}v^2v_t^2\sin^4\theta\\&-4\eta\left(\frac{\partial\tau_0}{\partial x}\right)^2\frac{\partial\tau_0}{\partial z}\frac{\partial\tau_1}{\partial z}v^2v_t^2\cos^4\theta+16\eta\left(\frac{\partial\tau_0}{\partial x}\right)^2\frac{\partial\tau_0}{\partial z}\frac{\partial\tau_1}{\partial z}v^2v_t^2\sin^2\theta\cos^2\theta\\&-4\eta\frac{\partial\tau_0}{\partial x}\left(\frac{\partial\tau_0}{\partial z}\right)^2\frac{\partial\tau_1}{\partial x}v^2v_t^2\sin^4\theta\\&-4\eta\frac{\partial\tau_0}{\partial x}\left(\frac{\partial\tau_0}{\partial z}\right)^2\frac{\partial\tau_1}{\partial x}v^2v_t^2\cos^4\theta+16\eta\left(\frac{\partial\tau_0}{\partial x}\right)\left(\frac{\partial\tau_0}{\partial z}\right)^2\frac{\partial\tau_1}{\partial x}v^2v_t^2\sin^2\theta\cos^2\theta\\&-12\eta\frac{\partial\tau_0}{\partial x}\left(\frac{\partial\tau_0}{\partial z}\right)^2\frac{\partial\tau_1}{\partial z}v^2v_t^2\sin\theta\cos^3\theta\\&+12\eta\frac{\partial\tau_0}{\partial x}\left(\frac{\partial\tau_0}{\partial z}\right)^2\frac{\partial\tau_1}{\partial z}v^2v_t^2\sin^3\theta\cos\theta+2\frac{\partial\tau_0}{\partial x}\frac{\partial\tau_1}{\partial x}v_t^2\sin^2\theta+2(2\eta+1)\frac{\partial\tau_0}{\partial x}\frac{\partial\tau_1}{\partial z}v^2\sin\theta\cos\theta\\&-2\frac{\partial\tau_0}{\partial x}\frac{\partial\tau_1}{\partial z}v_t^2\sin\theta\cos\theta\\&-4\eta\left(\frac{\partial\tau_0}{\partial z}\right)^3\frac{\partial\tau_1}{\partial x}v^2v_t^2\sin\theta\cos^3\theta+4\eta\left(\frac{\partial\tau_0}{\partial z}\right)^3\frac{\partial\tau_1}{\partial x}v^2v_t^2\sin^3\theta\cos\theta-8\eta\left(\frac{\partial\tau_0}{\partial z}\right)^3\frac{\partial\tau_1}{\partial z}v^2v_t^2\sin^2\theta\cos^2\theta\\&-2\frac{\partial\tau_0}{\partial z}\frac{\partial\tau_1}{\partial x}v_t^2\sin\theta\cos\theta+2(2\eta+1)\frac{\partial\tau_0}{\partial z}\frac{\partial\tau_0}{\partial z}v^2\sin^2\theta-\frac{\partial\tau_0}{\partial z}\frac{\partial\tau_1}{\partial z}v_t^2+2\frac{\partial\tau_0}{\partial z}\frac{\partial\tau_1}{\partial z}v_t^2\cos^2\theta.\end{aligned} \tag{23}$$

Differences between HAM and perturbation theory

There is another approach to solving the eikonal equation in an anisotropic medium without having to find the root of a quartic equation as in the FD method. The perturbation method using a Taylor series expansion is by far the most widespread approach developed by Alkhalifah (2011a,b) and Stovas & Alkhalifah (2012). Such an approach has been adopted by many researchers (Stovas & Alkhalifah 2012; Alkhalifah 2013; Waheed *et al.* 2013; Masmoudi & Alkhalifah 2016; Stovas *et al.* 2016) for solving anisotropic eikonal equations. Recently, we applied this method to the complex eikonal equation for the seismic complex traveltime (Huang & Greenhalgh 2018; Huang *et al.* 2018). The perturbation method enables transforming the nonlinear problem into linear problems that can be used to derive analytic solutions of the anisotropic eikonal equation or solved by the FD method for numerical solutions. This reduces to a simple iteration scheme for the linearized partial difference equation system. Now we discuss the differences between the HAM and perturbation method and show why the HAM can account for a strongly anisotropic medium.

For VTI media, the perturbation expansion based on the Taylor series expansion is given by (Alkhalifah 2011a)

$$\tau = \tau_0 + \tau_1\eta + \tau_2\eta^2, \tag{24}$$

where τ_1 and τ_2 are the first-order and second-order coefficients of the Taylor series expansion, respectively.

For TTI media, the perturbation expansion based on the Taylor series expansion is given by (Alkhalifah 2011b)

$$\tau = \tau_0 + \tau_\eta\eta + \tau_\theta \sin\theta + \tau_{\eta_2}\eta^2 + \tau_{\eta\theta}\eta\sin\theta + \tau_{\theta_2}\sin^2\theta, \tag{25}$$

where τ_η, τ_θ, τ_{η_2}, $\tau_{\eta\theta}$ and τ_{θ_2} are the coefficients. Another approach for the TTI eikonal equation given by Stovas & Alkhalifah (2012) is

$$\tau = \tau_0 + \tau_{\eta 1}\eta + \tau_{\eta 2}\eta^2, \tag{26}$$

where $\tau_{\eta 1}$ and $\tau_{\eta 2}$ are the first-order and second-order coefficients of the Taylor series expansion, respectively.

The most obvious difference between the HAM and the perturbation method is their different expansion parameters in the expansion series. In the case of the perturbation method shown as eqs (24)–(26), the traveltime is expressed as a Taylor series expansion with respect to the small anisotropic parameters η and θ. In the perturbation expansion, there is an assumption of small perturbation, meaning that the anisotropic parameter is small. In the case of the HAM, the series expansion depends on the embedding parameter q. Contrary to the perturbation method, which is characterized by a Taylor series expansion that becomes the solution after obtaining the coefficients, the series expansion using the HAM approaches the exact solution with an increasing embedding parameter q, arriving at the exact analytic solution where $q = 1$.

Comparison of eqs (13) and (21) with eqs (24)–(26) implies two options for solving the anisotropic eikonal equations. One is to take the traveltime with respect to the anisotropic parameters; the other is to use the series expansion with respect to the embedding parameter q. A major feature of the former approach is the handling of lateral variation in η and θ. The perturbation method is only good for estimating constant η in a velocity analysis framework. However, the two methods have different capabilities for computing the traveltime in anisotropic media with lateral variation because of the different forms of the series expansions. In this case, since there is not the assumption of small perturbation in the HAM, this method can be used for a strongly anisotropic medium.

TRAVELTIME APPROXIMATION

One primary aim of this paper is to develop an analytic solution of the eikonal equation in homogeneous VTI and TTI media. To this end, we start with the initial traveltime solution satisfying the elliptical anisotropic eikonal equation and apply this solution to the linearized partial differential equations derived in the last section to obtain the coefficients of the series expansions (13) and (21). Then, we obtain the analytic solution of the eikonal equations in the anisotropic medium.

Analytical formulae for traveltime in VTI media

The analytic formula for the elliptical anisotropic eikonal equation is given by (Alkhalifah 2011a)

$$\tau_0 = \sqrt{\frac{x^2}{v^2} + \frac{z^2}{v_v^2}}. \tag{27}$$

Substituting eq. (27) into eq. (14), we obtain

$$\tau_1 = -\frac{2\eta v_v^4 x^4 \sqrt{\frac{x^2}{v^2} + \frac{z^2}{v_v^2}}}{\left(v^2 z^2 + v_v^2 x^2\right)^2}. \tag{28}$$

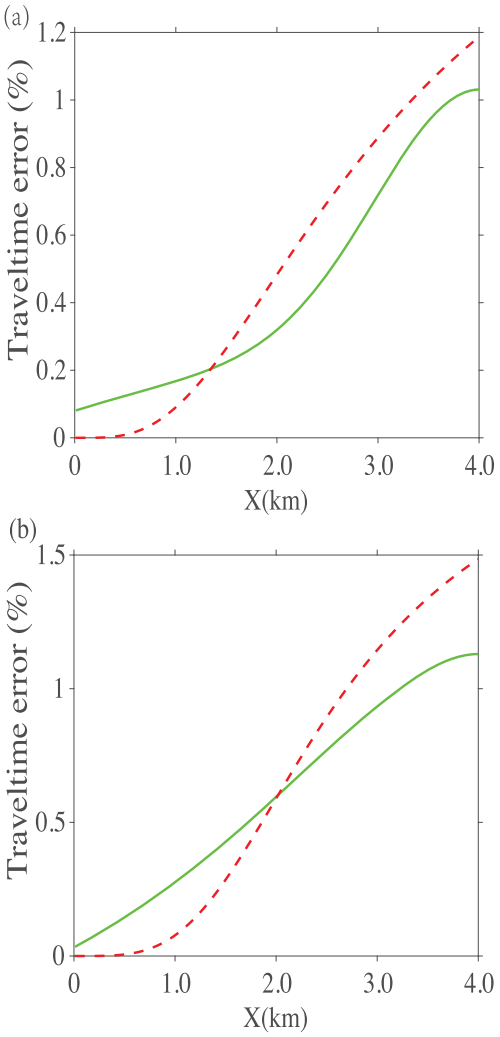

Figure 1. Comparison of the percentage traveltime error as a function of offset at the depth of 2 km using the perturbation method (dash red line) and the homotopy analysis method (solid green line) in VTI media with $C_{11} = 6.3$, $C_{13} = 2.25$, $C_{33} = 4.51$, $C_{44} = 1.0$, $C_{66} = 1.5$ ($\eta = 0.28$, $\varepsilon = 0.19$ and $\delta = -0.05$) for panel (a) and $C_{11} = 25.7$, $C_{13} = 15.2$, $C_{33} = 15.4$, $C_{44} = 4.2$, $C_{66} = 9.0$ ($\eta = -0.16$, $\varepsilon = 0.33$ and $\delta = 0.72$) for panel (b).

Also, applying eqs (27) and (28) to eq. (15), we have

$$\tau_2 = \frac{2\eta v_v^4 x^4 \sqrt{\frac{x^2}{v^2} + \frac{z^2}{v_v^2}} \left(v^4 z^4 + 2(14\eta + 1) v^2 v_v^2 x^2 z^2 + (4\eta + 1) v_v^4 x^4\right)}{\left(v^2 z^2 + v_v^2 x^2\right)^4}. \tag{29}$$

Furthermore, inserting eqs (27)–(29) into eq. (16) gives

$$\tau_3 = -\frac{4\eta v_v^4 x^4 \sqrt{\frac{x^2}{v^2} + \frac{z^2}{v_v^2}} \left(v^8 z^8 + 2(29\eta + 2) v^6 v_v^2 x^2 z^6 + 3(\eta(248\eta + 41) + 2) v^4 v_v^4 x^4 z^4 + 2(\eta(36 - 13\eta) + 2) v^2 v_v^6 x^6 z^2 + (2\eta + 1)(5\eta + 1) v_v^8 x^8\right)}{\left(v^2 z^2 + v_v^2 x^2\right)^6}. \tag{30}$$

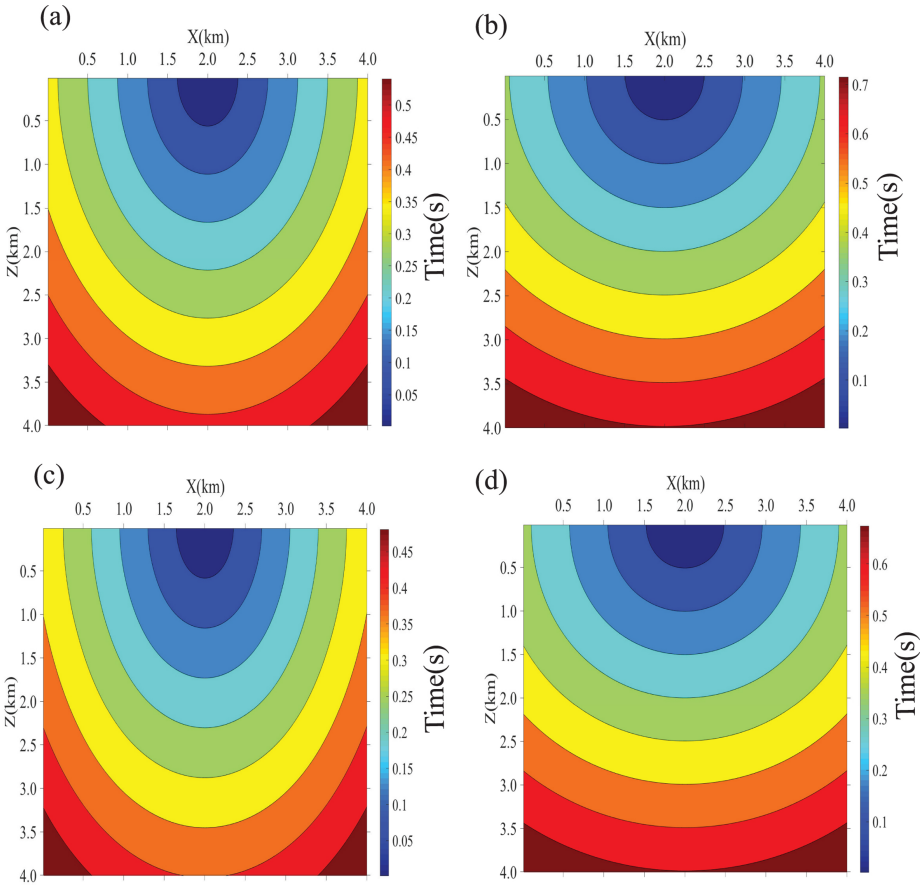

Figure 2. Colour plot of contours of the traveltime in VTI media. (a and c) The homotopy analysis method; (b and d) the perturbation method. The elastic parameters are $C_{11} = 35.7$, $C_{13} = 15.2$, $C_{33} = 15.4$, $C_{44} = 4.2$, $C_{66} = 9.0$ ($\eta = 0.03$, $\varepsilon = 0.66$ and $\delta = 0.58$) for panels (a) and (b), and $C_{11} = 40.7$, $C_{13} = 17.2$, $C_{33} = 15.4$, $C_{44} = 4.2$, $C_{66} = 9.0$ ($\eta = 0.04$, $\varepsilon = 0.82$ and $\delta = 0.81$) for panels (c) and (d).

Analytical formulae for traveltime in TTI media

For the analytic solution of the TTI eikonal equation, we employ the same initial traveltime solution to obtain the corresponding coefficients. The analytic formula for the elliptical anisotropic eikonal equation can be written as

$$\tau_0 = \sqrt{\frac{x^2}{v^2} + \frac{z^2}{v_t^2}}. \tag{31}$$

A derivation for the analytic solutions for the traveltime in homogeneous TTI media based on the initial solution for an elliptical anisotropic background medium is provided in the Appendix.

RESULTS

Comparison of HAM with perturbation method

To validate and test the accuracy of the analytic formulae using the HAM, we first compute the traveltimes in homogeneous VTI media. Here we use the group velocity formulae given by Zhou & Greenhalgh (2004) to construct the wave fronts. The phase velocity is given by

$$c_1 = \sqrt{P \pm \sqrt{P^2 - Q}} \tag{32}$$

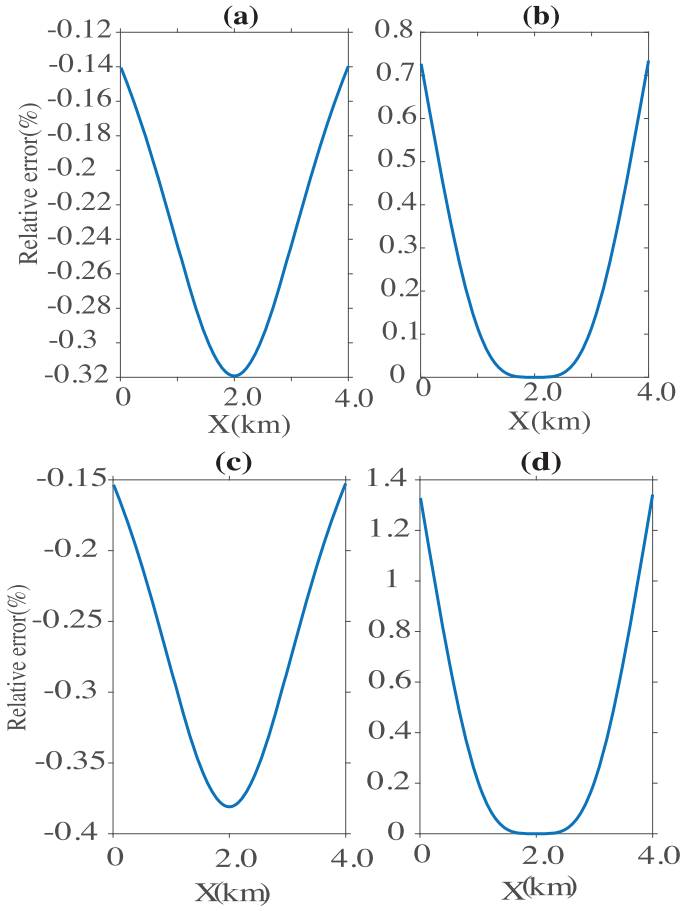

Figure 3. The percentage relative errors of the traveltime at a depth of 2 km for homogeneous VTI media using the homotopy analysis method (panels a and c) and perturbation method (panels b and d).The size of the model is 4 km × 4 km. The source is located at (2 km, 10 m). The elastic parameters are $C_{11} = 35.7$, $C_{13} = 15.2$, $C_{33} = 15.4$, $C_{44} = 4.2$, $C_{66} = 9.0$ ($\eta = -0.03$, $\varepsilon = 0.66$ and $\delta = 0.72$) for panels (a) and (b), and $C_{11} = 40.7$, $C_{13} = 17.2$, $C_{33} = 15.4$, $C_{44} = 4.2$, $C_{66} = 9.0$ ($\eta = -0.04$, $\varepsilon = 0.82$ and $\delta = 0.81$) for panels (c) and (d).

where

$$P = \frac{Q_1 + Q_2}{2},\ Q = Q_1 Q_2 - Q_3 \tag{33}$$

with

$$\begin{cases} Q_1 = C_{44} + (C_{11} - C_{44}) \sin^2 \vartheta \\ Q_2 = C_{33} + (C_{44} - C_{33}) \sin^2 \vartheta \\ Q_3 = 0.25(C_{13} + C_{44})^2 \sin^2 2\vartheta \end{cases}. \tag{34}$$

Then, the group velocity can be written as

$$U_1 = \sqrt{c_1^2 + \left(\frac{\partial c_1}{\partial \vartheta}\right)^2} \tag{35}$$

where

$$\frac{\partial c_1}{\partial \vartheta} = \frac{1}{2c_1}\left[\frac{\partial P}{\partial \vartheta} \pm \frac{1}{\sqrt{P^2 - Q}}\left(P\frac{\partial P}{\partial \vartheta} - 0.5\frac{\partial Q}{\partial \vartheta}\right)\right] \tag{36}$$

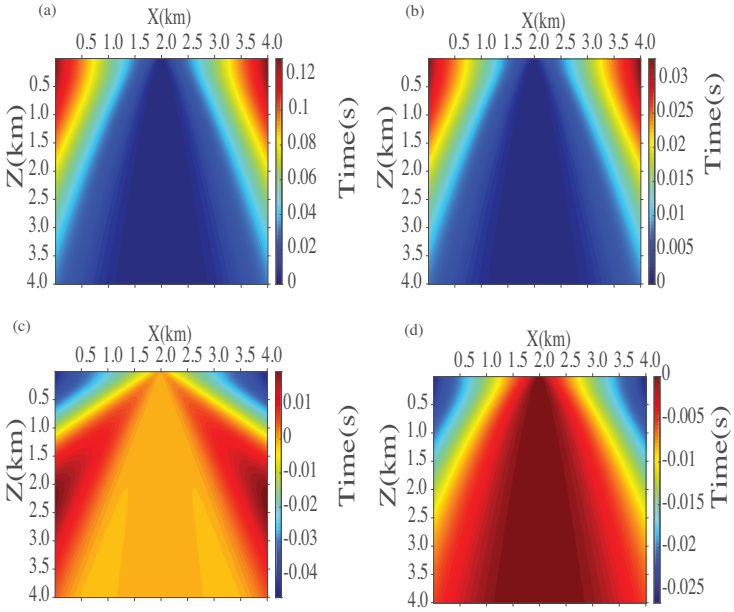

Figure 4. Colour plot of coefficients of the traveltime expansion. Panels (a) and (b) show the first-order expansion coefficient; panels (c) and (d) show the second-order expansion coefficient. The elastic parameters are $C_{11} = 25.7$, $C_{13} = 15.2$, $C_{33} = 15.4$, $C_{44} = 4.2$, $C_{66} = 9.0$ ($\eta = 0.16$, $\varepsilon = 0.33$ and $\delta = 0.81$) for panels (a) and (c), and $C_{11} = 35.7$, $C_{13} = 17.2$, $C_{33} = 15.4$, $C_{44} = 4.2$, $C_{66} = 9.0$ ($\eta = 0.1$, $\varepsilon = 0.66$ and $\delta = 0.92$) for panels (b) and (d).

with

$$\frac{\partial P}{\partial \vartheta} = 0.5\,(C_{11} - C_{33})\sin 2\vartheta \tag{37}$$

and

$$\frac{\partial Q}{\partial \vartheta} = [Q_1\,(C_{44} - C_{33}) + Q_2\,(C_{11} - C_{44})]\sin 2\vartheta - 0.5\,(C_{13} + C_{44})^2 \sin 4\vartheta\,. \tag{38}$$

We will use the traveltimes constructed using the above formulae as the reference traveltimes and compare the relative error of traveltimes using the HAM and the perturbation method.

Fig. 1 shows the comparison of the traveltime error as a function of offset at the depth of 2 km using the perturbation method (red dash line) and the HAM (green solid line) in VTI media with $C_{11} = 6.3$, $C_{13} = 2.25$, $C_{33} = 4.51$, $C_{44} = 1.0$, $C_{66} = 1.5$ ($\eta = 0.28$, $\varepsilon = 0.19$ and $\delta = -0.05$) for (a) and $C_{11} = 25.7$, $C_{13} = 15.2$, $C_{33} = 15.4$, $C_{44} = 4.2$, $C_{66} = 9.0$ ($\eta = -0.16$, $\varepsilon = 0.33$ and $\delta = 0.72$) for (b). The size of the model is 4 km × 4 km and the source is located at (10 m, 10 m). In this computation, we use the traveltimes from the exact solution (Zhou & Greenhalgh 2004) in the actual medium as the reference traveltimes. From Fig. 1, we can observe that the relative errors of both methods increase gradually with increasing distance in the x-direction. At around 4 km in the x-direction, the relative error arrives at the maximum value of 1. This can be easily explained. The larger the distance from the source, the larger errors will be. However, when the distance in the x-direction is less than 2 km, the values of the relative error using the HAM are bigger than those from the perturbation method. For a large offset, the results using the formulae from the HAM have a higher accuracy.

Traveltimes in strongly anisotropic media

To examine the capabilities of the analytic formulae developed in this paper and compare the results with the results from the perturbation method, we compute the traveltimes and their relative errors in more strongly anisotropic media. The size of the model is 4 km × 4 km and the source is located at (2 km, 10m). Fig. 2 shows a colour plot of the contours of the traveltimes. Figs 2(a) and (c) show the results using the HAM and Figs 2(b) and (d) show the results using the perturbation method. The elastic parameters are $C_{11} = 35.7$, $C_{13} = 15.2$, $C_{33} = 15.4$, $C_{44} = 4.2$, $C_{66} = 9.0$ ($\eta = 0.03$, $\varepsilon = 0.66$ and $\delta = 0.58$) for (a) and (b), and $C_{11} = 40.7$, $C_{13} = 17.2$, $C_{33} = 15.4$, $C_{44} = 4.2$, $C_{66} = 9.0$ ($\eta = 0.04$, $\varepsilon = 0.82$ and $\delta = 0.81$) for (c) and (d). From Fig. 2, it can be seen that although all the formulae yield smooth, continuous

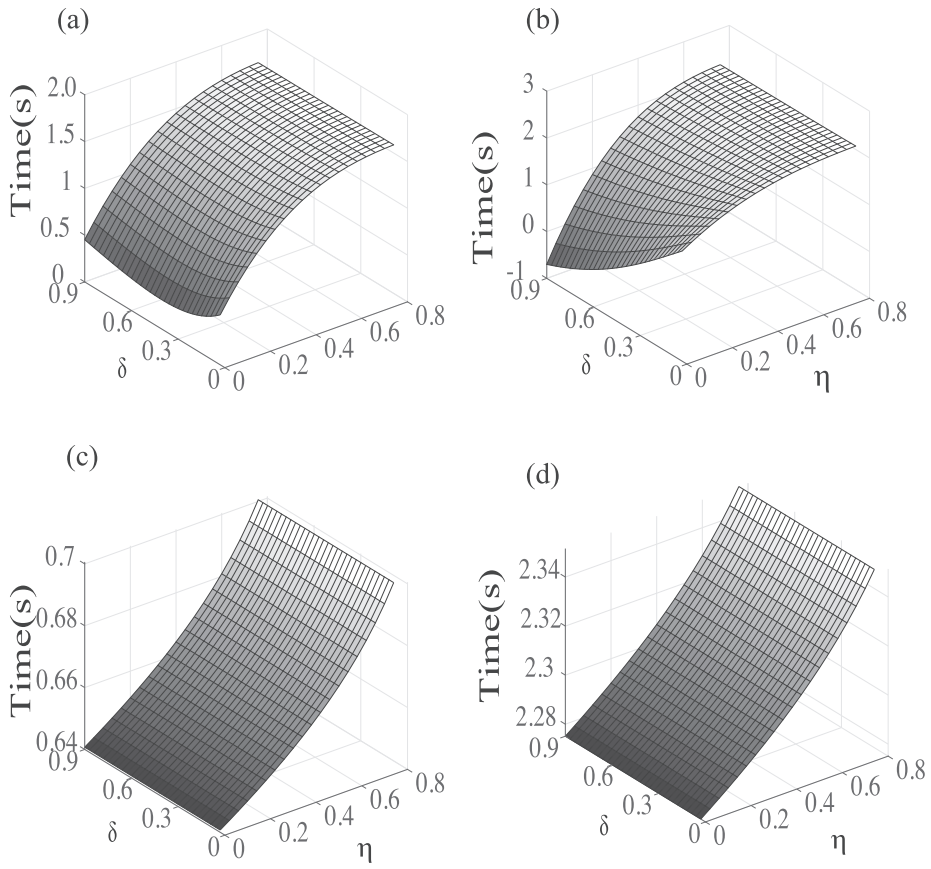

Figure 5. Effects of the anisotropic parameters on the traveltimes. The size of the model is 4 km × 4 km and the source is located at (2 km, 10 m). Panels (a) and (b) show results using the homotopy analysis method at the locations of (1 km, 1 km) and (2.5 km, 4 km); panels (c) and (d) show the results using the perturbation method at the locations of (1 km, 1 km) and (2.5 km, 4 km).

contours of the traveltime, there is some difference in the region far from the source. Comparing Figs 2(a) and (c) with Figs 2(b) and (d), one can recognize the difference between the results from the two methods. Specifically, by applying the chosen embedding parameter q and the HAM, the traveltime formulae can include the anisotropic parameters. By contrast, the analytic formulae with the perturbation method cannot give an accurate result in a strongly anisotropic medium but only give the results with a small perturbation of the anisotropic parameter. The difference in the results is caused mainly by the anisotropic parameters in which the traveltimes have different sensitivity behaviours to the various anisotropic parameters.

Fig. 3 shows the comparison of the relative errors of the traveltimes at a depth of 2 km using the perturbation method (b and d) and HAM (a and c). The experiments show that traveltime formulae with different methods can yield differing accuracy in the traveltime computation. From Fig. 3, one can observe that the formulae using the HAM give more satisfactory results because the relative errors are relatively small. For the results from the formulae from the HAM, when the distance in the direction of the x-axis changes from 0 to 2 m, the errors become larger; however, when the distance changes from 2 to 4 m, the errors decrease with increasing distance. For the results at a large offset, the errors using the formulae from the perturbation analysis are larger than those from the HAM.

Exact series expansion coefficients

In this section, we have computed the coefficients of the series expansion. We use the same model size 4 km × 4 km as the last section but the source is located at (2 km, 10 m). Fig. 4 shows a colour plot of the coefficients of the traveltimes expansion in VTI media. Figs 4(a) and (b)

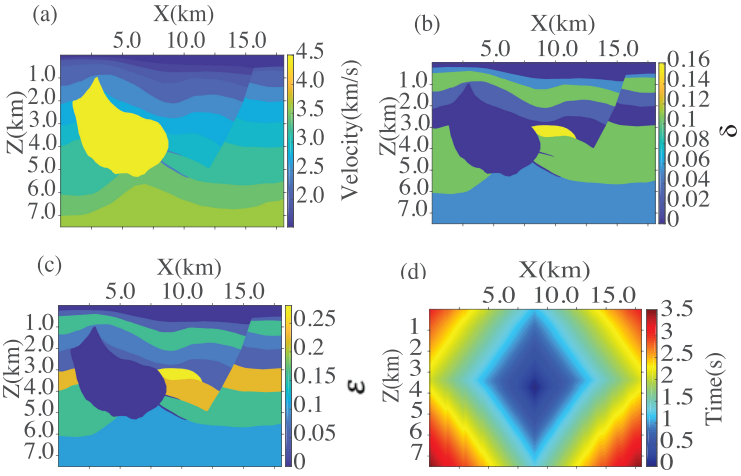

Figure 6. Colour plot of the traveltime using a modified Hess model with variable η. The size of the model is (18 km, 7.5 km). The source is located at the centre of the model (9 km, 3.75 km). Plot (a) shows velocity model, plot (b) shows δ model, plot (c) shows η model and plot (d) shows the traveltime.

show the results of the first-order coefficients and Figs 4(c) and (d) show the results of the second-order coefficients. The elastic parameters are $C_{11} = 25.7$, $C_{13} = 15.2$, $C_{33} = 15.4$, $C_{44} = 4.2$, $C_{66} = 9.0$ ($\eta = 0.16$, $\varepsilon = 0.33$ and $\delta = 0.81$) for (a) and (c), and $C_{11} = 35.7$, $C_{13} = 17.2$, $C_{33} = 15.4$, $C_{44} = 4.2$, $C_{66} = 9.0$ ($\eta = 0.1$, $\varepsilon = 0.66$ and $\delta = 0.92$) for (b) and (d). From Fig. 4, differences between the first-order coefficients and the second-order coefficients are notable. Whereas for the first-order coefficients, the large values are concentrated in the region along the vertical direction from the source, the values of the second-order coefficients are relatively large near the boundaries on both sides of the model. However, there is some similarity in shape between the first-order coefficients and the second-order coefficients, which shows similar effects of the coefficients on the traveltimes in VTI media.

Effects of anisotropic parameters

Finally, we perform numerical tests to analyse the effects of the anisotropic parameters on the traveltimes. The size of the model is 4 km × 4 km and the source is located at (2 km, 10 m). The NMO velocity is 2 km s^{-1} and the anisotropic parameters are $\eta = 0.2$ and $\delta = 0.2$, respectively. Figs 5(a) and (c) show colour plots of the traveltimes at a fixed location of (1 km, 1 km). Figs 5(b) and (d) show the colour plots of the traveltimes at a fixed location of (2.5 km, 4.0 km). From Fig. 5, one can observe that there are some common features: (1) whether using the HAM or the perturbation theory, there are more substantial effects on the traveltimes with an increasing anisotropic parameter η; (2) the maximum values for both methods occur in the region where the values of the anisotropic parameters η and δ are maximal. As for the locations of (1 km, 1 km) and (2.5 km, 4.0 km), the images are similar. As expected, the effects increase as the anisotropic parameters increase.

All the numerical tests so far have been based on the constant η. In real cases, however, η will be variable. One of the advantages of the approach is to deal with the variable η. We computed the traveltime in the Hess VTI model with variable η. Fig. 6 shows a colour plot of the traveltime using a modified Hess model with variable η. The size of the model is (18 km, 7.5 km). The source is located at the centre of the model (9 km, 3.75 km). Plot (a) shows the velocity model, plot (b) shows the δ model, plot (c) shows the η model and plot (d) shows the traveltime.

DISCUSSION AND CONCLUSION

We have presented a methodology and formulations for retrieving the eikonal equations for VTI and TTI media. The main advantage of the new HAM formulation in this paper is that it can be used for strongly anisotropic media. The formulation involves the initial approximation for the traveltimes, which is given by an analytical formulation or estimated by a numerical method. The derived linear equations involve the anisotropic parameters. We have derived the traveltime approximations for computing the traveltimes in VTI and TTI media using the HAM. We have demonstrated that the traveltime approximations based on the HAM can be used for computing the traveltimes in strongly anisotropic media. A comparison between traveltime approximations from the HAM and the perturbation theory has been carried out which shows that in strongly anisotropic media, the former has a higher accuracy. Finally, we have shown the effects of the coefficients of the series

solutions and the anisotropic parameters on the traveltimes. Because the HAM does not rely on the small perturbation assumption, we think that it is promising for applications to geophysical problems, for example, renormalization of scattering series.

ACKNOWLEDGEMENTS

XH acknowledges the Research Council of Norway for the Petromaks II project 267769/E3 (Bayesian inversion of 4D seismic waveform data for quantitative integration with production data). The authors are greatly grateful to Einar Iversen for insightful suggestions and valuable discussions. Some of the work was performed when XH had a visit from the University of Bergen to work for his PhD project at the University of California, Santa Cruz. We would like to thank the editor, Herve Chauris, the reviewer Tariq Alkhalifah and an anonymous reviewer for their insightful and constructive comments on the manuscript.

REFERENCES

Alkhalifah, T., 2000. An acoustic wave equation for anisotropic media, *Geophysics,* **65**(4), 1239–1250.

Alkhalifah, T., 2011a. Scanning anisotropy parameters in complex media, *Geophysics,* **76**(2), U13–U22.

Alkhalifah, T., 2011b. Traveltime approximations for transversely isotropic media with an inhomogeneous background, *Geophysics,* **76**(3), WA31–WA42.

Alkhalifah, T., 2013. Traveltime approximations for inhomogeneous transversely isotropic media with a horizontal symmetry axis, *Geophys. Prospect.,* **61**(3), 495–503.

Alkhalifah, T. & Choi, Y., 2014. From tomography to full-waveform inversion with a single objective function, *Geophysics,* **79**(2), R55–R61.

Alkhalifah, T. & Fomel, S., 2001. Implementing the fast marching eikonal solver: spherical versus cartesian coordinates, *Geophys. Prospect.,* **49**(2), 165–178.

Bai, C.-Y. & Greenhalgh, S., 2005. 3-D non-linear travel-time tomography: imaging high contrast velocity anomalies, *Pure appl. Geophys.,* **162**(11), 2029–2049.

Bai, C.-Y., Greenhalgh, S. & Zhou, B., 2007. 3D ray tracing using a modified shortest-path method, *Geophysics,* **72**(4), T27–T36.

Bouteiller, L.P., Benjemaa, M., Métivier, L. & Virieux, J., 2017. An accurate discontinuous galerkin method for solving point-source eikonal equation in 2-D heterogeneous anisotropic media, *Geophys. J. Int.,* **212**(3), 1498–1522.

Cao, S. & Greenhalgh, S., 1994. Finite-difference solution of the eikonal equation using an efficient, first-arrival, wavefront tracking scheme, *Geophysics,* **59**(4), 632–643.

Chapman, C.T. & Pratt, R., 1992. Traveltime tomography in anisotropic media I. Theory, *Geophys. J. Int.,* **109**(1), 1–19.

Crampin, S., 1984. Effective anisotropic elastic constants for wave propagation through cracked solids, *Geophys. J. Int.,* **76**(1), 135–145.

Červený, V., 1972. Seismic rays and ray intensities in inhomogeneous anisotropic media, *Geophys. J. R. astr. Soc.,* **29**(1), 1–13.

Červený, V., 2001. *Seismic Ray Theory,* Cambridge Univ. Press.

Červený, V. & Pšenčík, I., 1983. Gaussian beams in two-dimensional elastic inhomogeneous media, *Geophys. J. Int.,* **72**(2), 417–433.

Červený, V., Klimeš, L. & Pšenčík, I., 2007. Seismic ray method: recent developments, *Adv. Geophys.,* **48,** 1–126.

Červený, V., Iversen, E. & Pšenčík, I., 2012. Two-point paraxial traveltimes in an inhomogeneous anisotropic medium, *Geophys. J. Int.,* **189**(3), 1597–1610.

Farra, V. & Pšenčík, I., 2017. Weak-anisotropy moveout approximations for P-waves in homogeneous TOR layers, *Geophysics,* **82**(4), WA23–WA32.

Han, S., Zhang, W. & Zhang, J., 2017. Calculating qP-wave traveltimes in 2-D TTI media by high-order fast sweeping methods with a numerical quartic equation solver, *Geophys. J. Int.,* **210**(3), 1560–1569.

Hao, Q. & Alkhalifah, T., 2017. An acoustic eikonal equation for attenuating transversely isotropic media with a vertical symmetry axis, *Geophysics,* **82**(1), C9–C20.

Huang, X. & Greenhalgh, S., 2018. Linearized formulations and approximate solutions for the complex eikonal equation in orthorhombic media and applications of complex seismic traveltime, *Geophysics,* **83**(3), C115–C136.

Huang, X. & Sun, H., 2018. Numerical modeling of Gaussian beam propagation and diffraction in inhomogeneous media based on the complex eikonal equation, *Acta Geophys.,* **66**(4), 497–508.

Huang, X., Sun, H. & Sun, J., 2016a. Born modeling for heterogeneous media using the Gaussian beam summation based Green's function, *J. appl. Geophys.,* **131,** 191–201.

Huang, X., Sun, J. & Sun, Z., 2016b. Local algorithm for computing complex travel time based on the complex eikonal equation, *Phys. Rev. E,* **93**(4), 1–10, doi:10.1103/PhysRevE.93.043307.

Huang, X., Sun, J. & Greenhalgh, S., 2018. On the solution of the complex eikonal equation in acoustic VTI media: a perturbation plus optimization scheme, *Geophys. J. Int.,* **214**(2), 907–932.

Iversen, E. & Tygel, M., 2008. Image-ray tracing for joint 3D seismic velocity estimation and time-to-depth conversion, *Geophysics,* **73**(3), S99–S114.

Liao, S., 1992a. Application of process analysis method to the solution of 2-D nonlinear progressive gravity waves, *J. Ship Res.,* **36,** 30–37.

Liao, S., 1992b. A second-order approximate analytical solution of a simple pendulum by the process analysis method, *J. Appl. Mech.,* **59**(4), 970–975.

Liao, S., 2003a. *Beyond Perturbation: Introduction to the Homotopy Analysis Method,* CRC Press.

Liao, S., 2012. *Homotopy Analysis Method in Nonlinear Differential Equations,* Springer.

Liao, S., Xu, D. & Stiassnie, M., 2016. On the steady-state nearly resonant waves, *J. Fluid Mech.,* **794,** 175–199.

Liao, S.J., 1992c. The proposed homotopy analysis technique for the solution of nonlinear problems, *PhD thesis*, Shanghai Jiao Tong University, Shanghai.

Liao, S.-J., 1999. A uniformly valid analytic solution of two-dimensional viscous flow over a semi-infinite flat plate, *J. Fluid Mech.,* **385,** 101–128.

Liao, S.-J., 2002. An analytic approximation of the drag coefficient for the viscous flow past a sphere, *Int. J. Non-Linear Mech.,* **37**(1), 1–18.

Liao, S.-J., 2003b. An analytic approximate technique for free oscillations of positively damped systems with algebraically decaying amplitude, *Int. J. Non-Linear Mech.,* **38**(8), 1173–1183.

Liao, S.-J., 2004. An analytic approximate approach for free oscillations of self-excited systems, *Int. J. Non-Linear Mech.,* **39**(2), 271–280.

Liao, S.-J., 2011. On the homotopy multiple-variable method and its applications in the interactions of nonlinear gravity waves, *Commun. Nonlinear Sci. Numer. Simul.,* **16**(3), 1274–1303.

Liao, S.-J. & Chwang, A., 1998. Application of homotopy analysis method in nonlinear oscillations, *J. Appl. Mech.,* **65**(4), 914–922.

Luo, S. & Qian, J., 2012. Fast sweeping methods for factored anisotropic eikonal equations: multiplicative and additive factors, *J. Sci. Comput.,* **52**(2), 360–382.

Masmoudi, N. & Alkhalifah, T., 2016. Traveltime approximations and parameter estimation for orthorhombic media, *Geophysics,* **81**(4), C127–C137.

Moser, T., 1991. Shortest path calculation of seismic rays, *Geophysics,* **56**(1), 59–67.

Musgrave, M.J.P., 1970. *Crystal Acoustics: Introduction to the Study of Elastic Waves and Vibrations in Crystal,* Holden-Day.

Noble, M., Gesret, A. & Belayouni, N., 2014. Accurate 3-D finite difference computation of traveltimes in strongly heterogeneous media, *Geophys. J. Int.,* **199**(3), 1572–1585.

Pšenčík, I. & Farra, V., 2017. Reflection moveout approximations for P-waves in a moderately anisotropic homogeneous tilted transverse isotropy layer, *Geophysics,* **82**(5), C175–C185.
Rawlinson, N. & Sambridge, M., 2004a. Multiple reflection and transmission phases in complex layered media using a multistage fast marching method, *Geophysics,* **69**(5), 1338–1350.
Rawlinson, N. & Sambridge, M., 2004b. Wave front evolution in strongly heterogeneous layered media using the fast marching method, *Geophys. J. Int.,* **156**(3), 631–647.
Schoenberg, M., 1983. Reflection of elastic waves from periodically stratified media with interfacial slip, *Geophys. Prospect.,* **31**(2), 265–292.
Sethian, J.A., 1996. A fast marching level set method for monotonically advancing fronts, *Proc. Natl. Acad. Sci. USA,* **93**(4), 1591–1595.
Sethian, J.A. & Popovici, A.M., 1999. 3-D traveltime computation using the fast marching method, *Geophysics,* **64**(2), 516–523.
Silva, N.V.D., Ratcliffe, A., Vinje, V. & Conroy, G., 2016. A new parameter set for anisotropic multiparameter full-waveform inversion and application to a north sea data set, *Geophysics,* **81**(4), U25–U38.
Stovas, A. & Alkhalifah, T., 2012. A new traveltime approximation for TI media, *Geophysics,* **77**(4), C37–C42.
Stovas, A., Masmoudi, N. & Alkhalifah, T., 2016. Application of perturbation theory to a P-wave eikonal equation in orthorhombic media eikonal equation in orthorhombic media, *Geophysics,* **81**(6), C309–C317.
Tsvankin, I., 1997. Anisotropic parameters and P-wave velocity for orthorhombic media, *Geophysics,* **62**(4), 1292–1309.
Tsvankin, I., 2012. *Seismic Signatures and Analysis of Reflection Data in Anisotropic Media,* Society of Exploration Geophysicists.
Vidale, J., 1988. Finite-difference calculation of travel times, *Bull. seism. Soc. Am.,* **78**(6), 2062–2076.
Vinje, V., Iversen, E. & Gjøystdal, H., 1993. Traveltime and amplitude estimation using wavefront construction, *Geophysics,* **58**(8), 1157–1166.
Waheed, U.B. & Alkhalifah, T., 2017. A fast sweeping algorithm for accurate solution of the tilted transversely isotropic eikonal equation using factorization, *Geophysics,* **82**(6), WB1–WB8.
Waheed, U.B., Alkhalifah, T. & Stovas, A., 2013. Diffraction traveltime approximation for TI media with an inhomogeneous background, *Geophysics,* **78**(5), WC103–WC111.
Waheed, B.U., Yarman, C.E. & Flagg, G., 2015a. An iterative, fast-sweeping-based eikonal solver for 3D tilted anisotropic media, *Geophysics,* **80**(3), C49–C58.
Waheed, U.B, Alkhalifah, T. & Wang, H., 2015b. Efficient traveltime solutions of the acoustic TI eikonal equation, *J. Comput. Phys.,* **282,** 62–76.
Wang, C., Zhu, J., Liao, S. & Pop, I., 2003. On the explicit analytic solution of Cheng–Chang equation, *Int. J. Heat Mass Transfer,* **46**(10), 1855–1860.
Xu, S., Stovas, A. & Hao, Q., 2017. Perturbation-based moveout approximations in anisotropic media, *Geophys. Prospect.,* **65**(5), 1218–1230.
Zelt, C.A. & Barton, P.J., 1998. Three-dimensional seismic refraction tomography: a comparison of two methods applied to data from the Faeroe basin, *J. geophys. Res.,* **103**(B4), 7187–7210.
Zhao, H., 2005. A fast sweeping method for eikonal equations, *Math. Comput.,* **74**(250), 603–627.
Zhou, B. & Greenhalgh, S., 2004. On the computation of elastic wave group velocities for a general anisotropic medium, *J. Geophys. Eng.,* **1**(3), 205–215.
Zhou, B., Greenhalgh, S. & Green, A., 2008. Nonlinear traveltime inversion scheme for crosshole seismic tomography in tilted transversely isotropic media, *Geophysics,* **73**(4), D17–D33.

APPENDIX: TRAVELTIME APPROXIMATION IN TTI MEDIA

In this appendix, we derive the traveltime approximations based on the HAM. Substituting eqs (31) into (22), we obtain

$$\tau_1 = \frac{1}{v^2 v_t^2 \left(x^2 v_t^2 + v^2 z^2\right)^2} \left(\sqrt{\frac{x^2 v_t^2 + v^2 z^2}{v^2 v_t^2}} \left(-2\eta v^8 z^4 \sin^2\theta + 2\eta v^8 z^4 \sin^2\theta \cos^2\theta + v^8 z^4 \left(-\sin^2\theta\right) \right. \right. \tag{A1}$$
$$v^6 x^2 z^2 \left(-\sin^2\theta\right) v_t^2 - 2v^6 x z^3 \sin\theta \cos\theta v_t^2 + v^6 z^4 v_t^2 - v^6 z^4 \cos^2\theta v_t^2 - 2\eta v^6 x^2 z^2 \sin^2\theta v_t^2 - 4\eta v^6$$
$$x z^3 \sin\theta \cos\theta v_t^2 + 4\eta v^6 x z^3 \sin\theta \cos^3\theta v_t^2 - 4\eta v^6 x z^3 \sin^3\theta \cos\theta v_t^2 - 2v^4 x^3 z \sin\theta \cos\theta v_t^4 + 2v^4 x^2 z^2 v_t^4$$
$$-2v^4 x^2 z^2 \cos^2\theta v_t^4 + 2v^4 x z^3 \sin\theta \cos\theta v_t^4 - 4\eta v^4 x^3 z \sin\theta \cos\theta v_t^4 - 2\eta v^4 x^2 z^2 \cos^2\theta v_t^4 + 2\eta v^4 x^2 z^2$$
$$\cos^4\theta v_t^4 - 8\eta v^4 x^2 z^2 \sin^2\theta \cos^2\theta v_t^4 + 2\eta v^4 x^2 z^2 \sin^4\theta v_t^4 + v^2 x^4 v_t^6 - v^2 x^4 \cos^2\theta v_t^6 + 2v^2 x^3 z \sin\theta$$
$$\cos\theta v_t^6 v^2 x^2 z^2 \sin^2\theta v_t^6 - 2\eta v^2 x^4 \cos^2\theta v_t^6 - 4\eta v^2 x^3 z \sin\theta \cos^3\theta v_t^6 + 4\eta v^2 x^3 z \sin^3\theta \cos\theta v_t^6 -$$
$$\left. \left. 2\eta x^4 \sin^2\theta \cos^2\theta v_t^8 + x^4 \sin^2\theta v_t^8 \right) + v^6 z^4 v_t^2 + 2v^4 x^2 z^2 v_t^4 + v^2 x^4 v_t^6 \right)$$

and

$$\tau_2 = \tau_{21} + \tau_{22} + \tau_{23} + \tau_{24} + \tau_{25}, \tag{A2}$$

where

$$\tau_{21} = 8\eta^2 v^{16} z^8 \sin^4\theta - 24\eta^2 v^{16} z^8 \sin^4\theta \cos^2\theta + 8\eta v^{16} z^8 \sin^4\theta - 12\eta v^{16} z^8 \sin^4\theta \cos^2\theta \quad \text{(A3)}$$
$$+2v^{16} z^8 \sin^4\theta + 16\eta^2 v^{16} z^8 \sin^4\theta \cos^4\theta + 8v^{14} x^2 z^6 \sin^4\theta v_t^2 - 3v^{14} z^8 \sin^2\theta v_t^2 + 8v^{14} z^8 \sin^2\theta$$
$$\cos^2\theta v_t^2 + 32\eta v^{14} x^2 z^6 \sin^4\theta v_t^2 - 44\eta v^{14} x^2 z^6 \sin^4\theta \cos^2\theta v_t^2 + 8\eta v^{14} xz^7 \sin^5\theta \cos\theta v_t^2$$
$$-6\eta v^{14} z^8 \sin^2\theta v_t^2 + 34\eta v^{14} z^8 \sin^2\theta \cos^2\theta v_t^2 - 28\eta v^{14} z^8 \sin^2\theta \cos^4\theta v_t^2 + 16\eta v^{14} z^8$$
$$\sin^4\theta \cos^2\theta v_t^2 + 32\eta^2 v^{14} x^2 z^6 \sin^4\theta v_t^2 - 88\eta^2 v^{14} x^2 z^6 \sin^4\cos^2\theta v_t^2 + 64\eta^2 v^{14} x^2 z^6 \sin^4\theta$$
$$\cos^4\theta v_t^2 + 16\eta^2 v^{14} xz^7 \sin^5\theta \cos\theta v_t^2 + 16\eta^2 v^{14} z^8 \sin^2\theta \cos^2\theta v_t^2 - 32\eta^2 v^{14} z^8 \sin^2\theta \cos^4\theta$$
$$v_t^2 + 16\eta^2 v^{14} z^8 \sin^2\theta \cos^6\theta v_t^2 + 32\eta^2 v^{14} z^8 \sin^4\theta \cos^2\theta v_t^2 - 32\eta^2 v^{14} z^8 \sin^4\theta \cos^4\theta v_t^2$$
$$+16\eta^2 v^{14} z^8 \sin^6\theta \cos^2\theta v_t^2 + 10v^{12} x^4 z^4 \sin^4\theta v_t^4 + 8v^{12} x^3 z^5 \sin^3\theta \cos\theta v_t^4 - 9v^{12} x^2 z^6 \sin^2\theta$$
$$v_t^4 + 20v^{12} x^2 z^6 \sin^2\theta \cos^2\theta v_t^4 - 6v^{12} xz^7 \sin\theta \cos\theta v_t^4 + 8v^{12} xz^7 \sin\theta \cos^3\theta v_t^4 + v^{12} z^8 v_t^4$$
$$-3v^{12} z^8 \cos^2\theta v_t^4 + 2v^{12} z^8 \cos^4\theta v_t^4 - 8v^{12} z^8 \sin^2\theta \cos^2\theta v_t^4 + 40\eta v^{12} x^4 z^4 \sin^4\theta v_t^4 - 32\eta$$
$$v^{12} x^4 z^4 \sin^4\theta \cos^2\theta v_t^4 + 32\eta v^{12} x^3 z^5 \sin^3\theta \cos\theta v_t^4 - 80\eta v^{12} x^3 z^5 \sin^3\theta \cos^3\theta v_t^4 + 56\eta$$
$$v^{12} x^3 z^5 \sin^5\theta \cos\theta v_t^4 - 18\eta v^{12} x^2 z^6 \sin^2\theta v_t^4 + 68\eta v^{12} x^2 z^6 \sin^2\theta \cos^2\theta v_t^4 - 20\eta v^{12} x^2 z^6$$
$$\sin^2\theta \cos^4\theta v_t^4 - 16\eta v^{12} x^2 z^6 \sin^4\theta \cos^2\theta v_t^4 + 4\eta v^{12} x^2 z^6 \sin^6\theta v_t^4 - 12\eta v^{12} xz^7 \sin\theta \cos\theta$$
$$v_t^4 + 52\eta v^{12} xz^7 \sin\theta \cos^3\theta v_t^4 - 40\eta v^{12} xz^7 \sin\theta \cos^5\theta v_t^4 - 20\eta v^{12} xz^7 \sin^3\theta \cos\theta v_t^4 + 80\eta v^{12}$$
$$xz^7 \sin^3\theta \cos^3\theta v_t^4 - 16\eta v^{12} xz^7 \sin^5\theta \cos\theta v_t^4 - 16\eta v^{12} z^8 \sin^2\theta \cos^2\theta v_t^4 + 16\eta v^{12} z^8 \sin^2\theta$$
$$\cos^4\theta v_t^4 - 16\eta v^{12} z^8 \sin^4\theta \cos^2\theta v_t^4 + 40\eta^2 v^{12} x^4 z^4 \sin^4\theta v_t^4 - 64\eta^2 v^{12} x^4 z^4 \sin^4\theta \cos^2\theta v_t^4$$
$$+32\eta^2 v^{12} x^3 z^5 \sin^3\theta \cos\theta v_t^4 - 160\eta^2 v^{12} x^3 z^5 \sin^3\theta \cos^3\theta v_t^4 + 192\eta^2 v^{12} x^3 z^5 \sin^3\theta \cos^5\theta$$
$$v_t^4 + 112\eta^2 v^{12} x^3 z^5 \sin^5\theta \cos\theta v_t^4 - 192\eta^2 v^{12} x^3 z^5 \sin^5\theta \cos^3\theta v_t^4 + 16\eta^2 v^{12} x^2 z^6 \sin^2\theta \cos^2\theta$$
$$v_t^4 + 48\eta^2 v^{12} x^2 z^6 \sin^2\theta \cos^4\theta v_t^4 - 64\eta^2 v^{12} x^2 z^6 \sin^2\theta \cos^6\theta v_t^4 - 32\eta^2 v^{12} x^2 z^6,$$

$$\tau_{22} = \sin^4\theta \cos^2\theta v_t^4 + 192\eta^2 v^{12} x^2 z^6 \sin^4\theta \cos^4\theta v_t^4 + 8\eta^2 v^{12} x^2 z^6 \sin^6\theta v_t^4 - 64\eta^2 v^{12} x^2 z^6 \sin^6\theta \quad \text{(A4)}$$
$$\cos^2\theta v_t^4 + 32\eta^2 v^{12} xz^7 \sin\theta \cos^3\theta v_t^4 - 64\eta^2 v^{12} xz^7 \sin\theta \cos^5\theta v_t^4 + 32\eta^2 v^{12} xz^7 \sin\theta \cos^7\theta v_t^4$$
$$+160\eta^2 v^{12} xz^7 \sin^3\theta \cos^3\theta v_t^4 - 160\eta^2 v^{12} xz^7 \sin^3\theta \cos^5\theta v_t^4 - 32\eta^2 v^{12} xz^7 \sin^5\theta \cos\theta v_t^4$$
$$+160\eta^2 v^{12} xz^7 \sin^5\theta \cos^3\theta v_t^4 - 32\eta^2 v^{12} xz^7 \sin^7\theta \cos\theta v_t^4 + 4v^{10} x^6 z^2 \sin^4\theta v_t^6 + 16v^{10} x^5 z^3$$
$$\sin^3\theta \cos\theta v_t^6 - 9v^{10} x^4 z^4 \sin^2\theta v_t^6 + 20v^{10} x^4 z^4 \sin^2\theta \cos^2\theta v_t^6 - 18v^{10} x^3 z^5 \sin\theta \cos\theta v_t^6 + 24v^{10}$$
$$x^3 z^5 \sin\theta \cos^3\theta v_t^6 - 8v^{10} x^3 z^5 \sin^3\theta \cos\theta v_t^6 + 4v^{10} x^2 z^6 v_t^6 - 12v^{10} x^2 z^6 \cos^2\theta v_t^6 + 8v^{10} x^2 z^6$$
$$\cos^4\theta v_t^6 - 16v^{10} x^2 z^6 \sin^2\theta \cos^2\theta v_t^6 - 4v^{10} x^2 z^6 \sin^4\theta v_t^6 + 6v^{10} xz^7 \sin\theta \cos\theta v_t^6 - 8v^{10} xz^7$$
$$\sin\theta \cos^3\theta v_t^6 + 8v^{10} xz^7 \sin^3\theta \cos\theta v_t^6 + 4v^{10} z^8 \sin^2\theta \cos^2\theta v_t^6 + 16\eta v^{10} x^6 z^2 \sin^4\theta v_t^6$$
$$+64\eta v^{10} x^5 z^3 \sin^3\theta \cos\theta v_t^6 - 80\eta v^{10} x^5 z^3 \sin^3\theta \cos^3\theta v_t^6 + 48\eta v^{10} x^5 z^3 \sin^5\cos v_t^6 - 18\eta v^{10}$$
$$x^4 z^4 \sin^2 v_t^6 + 50\eta v^{10} x^4 z^4 \sin^2\cos^2 v_t^6 - 56\eta v^{10} x^4 z^4 \sin^2\cos^4 v_t^6 + 80\eta v^{10} x^4 z^4 \sin^4\theta \cos^2\theta v_t^6$$
$$-12\eta v^{10} x^4 z^4 \sin^6\theta v_t^6 - 36\eta v^{10} x^3 z^5 \sin\theta \cos\theta v_t^6 + 120\eta v^{10} x^3 z^5 \sin\theta \cos^3\theta v_t^6 - 56\eta v^{10} x^3$$
$$z^5 \sin\theta \cos^5\theta v_t^6 - 56\eta v^{10} x^3 z^5 \sin^3\theta \cos\theta v_t^6 + 80\eta v^{10} x^3 z^5 \sin^3\theta \cos^3\theta v_t^6 + 16\eta v^{10} x^3 z^5$$
$$\sin^5\theta \cos\theta v_t^6 - 6\eta v^{10} x^2 z^6 \cos^2\theta v_t^6 + 18\eta v^{10} x^2 z^6 \cos^4\theta v_t^6 - 12\eta v^{10} x^2 z^6 \cos^6\theta v_t^6 - 72\eta$$
$$v^{10} x^2 z^6 \sin^2\theta \cos^2\theta v_t^6 + 96\eta v^{10} x^2 z^6 \sin^2\theta \cos^4\theta v_t^6 + 2\eta v^{10} x^2 z^6 \sin^4\theta v_t^6 - 40\eta v^{10} x^2$$
$$z^6 \sin^4\theta \cos^2\theta v_t^6 - 16\eta v^{10} xz^7 \sin\theta \cos^3\theta v_t^6 + 16\eta v^{10} xz^7 \sin\theta \cos^5\theta v_t^6 + 16\eta v^{10} xz^7$$
$$\sin^3\theta \cos\theta v_t^6 - 80\eta v^{10} xz^7 \sin^3\theta \cos^3\theta v_t^6 + 32\eta v^{10} xz^7 \sin^5\theta \cos\theta v_t^6 + 16\eta^2 v^{10} x^6 z^2$$
$$\sin^4\theta v_t^6 + 64\eta^2 v^{10} x^5 z^3 \sin^3\theta \cos\theta v_t^6 - 160\eta^2 v^{10} x^5 z^3 \sin^3\theta \cos^3\theta v_t^6 + 96\eta^2 v^{10} x^5 z^3$$
$$\sin^5\theta \cos\theta v_t^6 - 48\eta^2 v^{10} x^4 z^4 \sin^2\theta \cos^4\theta v_t^6 + 208\eta^2 v^{10} x^4 z^4 \sin^2\theta \cos^6\theta v_t^6 + 160\eta^2$$
$$v^{10} x^4 z^4 \sin^4\cos^2\theta\theta v_t^6,$$

$$\tau_{23} = -544\eta^2 v^{10} x^4 z^4 \sin^4\theta \cos^4\theta v_t^6 - 24\eta^2 v^{10} x^4 z^4 \sin^6\theta v_t^6 + 208\eta^2 v^{10} x^4 z^4 \sin^6\theta \cos^2\theta v_t^6 + 64\eta^2 \tag{A5}$$
$$v^{10} x^3 z^5 \sin\theta \cos^3\theta v_t^6 - 64\eta^2 v^{10} x^3 z^5 \sin\theta \cos^7\theta v_t^6 + 448\eta^2 v^{10} x^3 z^5 \sin^3\theta \cos^5\theta v_t^6 + 32\eta^2 v^{10} x^3 z^5$$
$$\sin^5\theta \cos\theta v_t^6 - 448\eta^2 v^{10} x^3 z^5 \sin^5\theta \cos^3\theta v_t^6 + 64\eta^2 v^{10} x^3 z^5 \sin^7\theta \cos\theta v_t^6 + 16\eta^2 v^{10} x^2 z^6 \cos^4\theta$$
$$v_t^6 - 32\eta^2 v^{10} x^2 z^6 \cos^6\theta v_t^6 + 16\eta^2 v^{10} x^2 z^6 \cos^8\theta v_t^6 + 224\eta^2 v^{10} x^2 z^6 \sin^2\theta \cos^4\theta v_t^6 - 224\eta^2 v^{10} x^2 z^6$$
$$\sin^2\theta \cos^6\theta v_t^6 - 128\eta^2 v^{10} x^2 z^6 \sin^4\theta \cos^2\theta v_t^6 + 480\eta^2 v^{10} x^2 z^6 \sin^4\theta \cos^4\theta v_t^6 - 224\eta^2 v^{10} x^2 z^6$$
$$\sin^6\theta \cos^2\theta v_t^6 + 16\eta^2 v^{10} x^2 z^6 \sin^8\theta v_t^6 + 8v^8 x^7 z \sin^3\theta \cos\theta v_t^8 - 3v^8 x^6 z^2 \sin^2\theta v_t^8 + 12v^8 x^6 z^2 \sin^2\theta$$
$$\cos^2\theta v_t^8 - 18v^8 x^5 z^3 \sin\theta \cos\theta v_t^8 + 24v^8 x^5 z^3 \sin\theta \cos^3\theta v_t^8 - 16v^8 x^5 z^3 \sin^3\theta \cos\theta v_t^8 + 6v^8 x^4 z^4 v_t^8$$
$$-18v^8 x^4 z^4 \cos^2\theta v_t^8 + 12v^8 x^4 z^4 \cos^4\theta v_t^8 - 16v^8 x^4 z^4 \sin^2\theta \cos^2\theta v_t^8 - 8v^8 x^4 z^4 \sin^4\theta v_t^8 + 18v^8 x^3 z^5$$
$$\sin\theta \cos\theta v_t^8 - 24v^8 x^3 z^5 \sin\theta \cos^3\theta v_t^8 + 16v^8 x^3 z^5 \sin^3\theta \cos\theta v_t^8 - 3v^8 x^2 z^6 \sin^2\theta v_t^8 + 12v^8 x^2 z^6$$
$$\sin^2\theta \cos^2\theta v_t^8 - 8v^8 x z^7 \sin^3\theta \cos\theta v_t^8 + 32\eta v^8 x^7 z \sin^3\theta \cos\theta v_t^8 - 6\eta v^8 x^6 z^2 \sin^2\theta v_t^8 + 32\eta v^8 x^6$$
$$z^2 \sin^2\theta \cos^2\theta v_t^8 - 64\eta v^8 x^6 z^2 \sin^2\theta \cos^4\theta v_t^8 + 112\eta v^8 x^6 z^2 \sin^4\theta \cos^2\theta v_t^8 - 16\eta v^8 x^6 z^2 \sin^6\theta$$
$$v_t^8 - 36\eta v^8 x^5 z^3 \sin\theta \cos\theta v_t^8 + 84\eta v^8 x^5 z^3 \sin\theta \cos^3\theta v_t^8 - 32\eta v^8 x^5 z^3 \sin\theta \cos^5\theta v_t^8 - 52\eta v^8 x^5 z^3$$
$$\sin^3\theta \cos\theta v_t^8 + 80\eta v^8 x^5 z^3 \sin^3\theta \cos^3\theta v_t^8 - 18\eta v^8 x^4 z^4 \cos^2\theta v_t^8 + 44\eta v^8 x^4 z^4 \cos^4\theta v_t^8 - 24\eta v^8$$
$$x^4 z^4 \cos^6\theta v_t^8 - 112\eta v^8 x^4 z^4 \sin^2\theta \cos^2\theta v_t^8 + 160\eta v^8 x^4 z^4 \sin^2\theta \cos^4\theta v_t^8 + 4\eta v^8 x^4 z^4 \sin^4\theta v_t^8$$
$$-48\eta v^8 x^4 z^4 \sin^4\theta \cos^2\theta v_t^8 - 52\eta v^8 x^3 z^5 \sin\theta \cos^3\theta v_t^8 + 32\eta v^8 x^3 z^5 \sin\theta \cos^5\theta v_t^8 + 52\eta v^8 x^3 z^5$$
$$\sin^3\cos\theta v_t^8 - 80\eta v^8 x^3 z^5 \sin^3\theta \cos^3\theta v_t^8 + 16\eta v^8 x^2 z^6 \sin^2\theta \cos^2\theta v_t^8 - 64\eta v^8 x^2 z^6 \sin^2\theta \cos^4\theta$$
$$v_t^8 + 112\eta v^8 x^2 z^6 \sin^4\theta \cos^2\theta v_t^8 - 16\eta v^8 x^2 z^6 \sin^6\theta v_t^8 + 32\eta^2 v^8 x^7 z \sin^3\theta \cos\theta v_t^8 + 16\eta^2 v^8 x^6$$
$$z^2 \sin^2\theta \cos^2\theta v_t^8 - 128\eta^2 v^8 x^6 z^2 \sin^2\theta \cos^4\theta v_t^8 + 224\eta^2 v^8 x^6 z^2 \sin^4\theta \cos^2\theta v_t^8 - 32\eta^2 v^8 x^6 z^2$$
$$\sin^6\theta v_t^8 + 32\eta^2 v^8 x^5 z^3 \sin\theta \cos^3\theta v_t^8 + 32\eta^2 v^8 x^5 z^3 \sin\theta \cos^5\theta v_t^8 + 96\eta^2 v^8 x^5 z^3 \sin\theta \cos^7\theta$$
$$v_t^8 - 544\eta^2 v^8 x^5 z^3 \sin^3\theta \cos^5\theta v_t^8 + 544\eta^2 v^8,$$

$$\tau_{24} = x^5 z^3 \sin^5\theta \cos^3\theta v_t^8 - 96\eta^2 v^8 x^5 z^3 \sin^7\theta \cos\theta v_t^8 + 40\eta^2 v^8 x^4 z^4 \cos^4\theta v_t^8 - 24\eta^2 v^8 x^4 z^4 \cos^6\theta v_t^8 \tag{A6}$$
$$-16\eta^2 v^8 x^4 z^4 \cos^8\theta v_t^8 + 160\eta^2 v^8 x^4 z^4 \sin^2\theta \cos^4\theta v_t^8 + 320\eta^2 v^8 x^4 z^4 \sin^2\theta \cos^6\theta v_t^8 - 48\eta^2 v^8 x^4 z^4$$
$$\sin^4\theta \cos^2\theta v_t^8 - 768\eta^2 v^8 x^4 z^4 \sin^4\theta \cos^4\theta v_t^8 + 320\eta^2 v^8 x^4 z^4 \sin^6\theta \cos^2\theta v_t^8 - 16\eta^2 v^8 x^4 z^4 \sin^8\theta$$
$$v_t^8 + 96\eta^2 v^8 x^3 z^5 \sin\theta \cos^5\theta v_t^8 - 96\eta^2 v^8 x^3 z^5 \sin\theta \cos^7\theta v_t^8 - 160\eta^2 v^8 x^3 z^5 \sin^3\theta \cos^3\theta v_t^8 + 544\eta^2$$
$$v^8 x^3 z^5 \sin^3\theta \cos^5\theta v_t^8 - 544\eta^2 v^8 x^3 z^5 \sin^5\theta \cos^3\theta v_t^8 + 96\eta^2 v^8 x^3 z^5 \sin^7\theta \cos\theta v_t^8 + 4v^6 x^8 \sin^2\theta$$
$$\cos^2\theta v_t^{10} - 6v^6 x^7 z \sin\theta \cos\theta v_t^{10} + 8v^6 x^7 z \sin\theta \cos^3\theta v_t^{10} - 8v^6 x^7 z \sin^3\theta \cos\theta v_t^{10} + 4v^6 x^6 z^2 v_t^{10}$$
$$-12v^6 x^6 z^2 \cos^2\theta v_t^{10} + 8v^6 x^6 z^2 \cos^4\theta v_t^{10} - 16v^6 x^6 z^2 \sin^2\theta \cos^2\theta v_t^{10} - 4v^6 x^6 z^2 \sin^4\theta v_t^{10} + 18v^6$$
$$x^5 z^3 \sin\theta \cos\theta v_t^{10} - 24v^6 x^5 z^3 \sin\theta \cos^3\theta v_t^{10} + 8v^6 x^5 z^3 \sin^3\theta \cos\theta v_t^{10} - 9v^6 x^4 z^4 \sin^2\theta v_t^{10} + 20$$
$$v^6 x^4 z^4 \sin^2\theta \cos^2\theta v_t^{10} - 16v^6 x^3 z^5 \sin^3\theta \cos\theta v_t^{10} + 4v^6 x^2 z^6 \sin^4\theta v_t^{10} + 16\eta v^6 x^8 \sin^2\theta \cos^2\theta$$
$$v_t^{10} - 12\eta v^6 x^7 z \sin\theta \cos\theta v_t^{10} + 16\eta v^6 x^7 z \sin\theta \cos^3\theta v_t^{10} - 16\eta v^6 x^7 z \sin\theta \cos^5\theta v_t^{10} - 16\eta v^6 x^7$$
$$z \sin^3\theta \cos\theta v_t^{10} + 80\eta v^6 x^7 z \sin^3\theta \cos^3\theta v_t^{10} - 32\eta v^6 x^7 z \sin^5\theta \cos\theta v_t^{10} - 18\eta v^6 x^6 z^2 \cos^2\theta v_t^{10}$$
$$+34\eta v^6 x^6 z^2 \cos^4\theta v_t^{10} - 12\eta v^6 x^6 z^2 \cos^6\theta v_t^{10} - 72\eta v^6 x^6 z^2 \sin^2\theta \cos^2\theta v_t^{10} + 96\eta v^6 x^6 z^2 \sin^2\theta$$
$$\cos^4\theta v_t^{10} + 2\eta v^6 x^6 z^2 \sin^4\theta v_t^{10} - 40\eta v^6 x^6 z^2 \sin^4\theta \cos^2\theta v_t^{10} - 56\eta v^6 x^5 z^3 \sin\theta \cos^3\theta v_t^{10} + 56$$
$$\eta v^6 x^5 z^3 \sin\theta \cos^5\theta v_t^{10} + 56\eta v^6 x^5 z^3 \sin^3\theta \cos\theta v_t^{10} - 80\eta v^6 x^5 z^3 \sin^3\theta \cos^3\theta v_t^{10} - 16\eta v^6 x^5$$
$$z^3 \sin^5\theta \cos\theta v_t^{10} + 50\eta v^6 x^4 z^4 \sin^2\theta \cos^2\theta v_t^{10} - 56\eta v^6 x^4 z^4 \sin^2\theta \cos^4\theta v_t^{10} + 80\eta v^6 x^4 z^4 \sin^4$$
$$\theta \cos^2\theta v_t^{10} - 12\eta v^6 x^4 z^4 \sin^6\theta v_t^{10} + 80\eta v^6 x^3 z^5 \sin^3\theta \cos^3\theta v_t^{10} - 48\eta v^6 x^3 z^5 \sin^5\theta \cos\theta v_t^{10}$$
$$+16\eta^2 v^6 x^8 \sin^2\theta \cos^2\theta v_t^{10} - 32\eta^2 v^6 x^7 z \sin\theta \cos^5\theta v_t^{10} + 160\eta^2 v^6 x^7 z \sin^3\theta \cos^3\theta v_t^{10} - 64\eta^2$$
$$v^6 x^7 z \sin^5\theta \cos\theta v_t^{10} + 32\eta^2 v^6 x^6 z^2 \cos^4\theta v_t^{10} + 8\eta^2 v^6 x^6 z^2 \cos^6\theta v_t^{10} + 16\eta^2 v^6 x^6 z^2 \cos^8\theta v_t^{10}$$
$$-32\eta^2 v^6 x^6 z^2 \sin^2\theta \cos^4\theta v_t^{10} - 224\eta^2 v^6 x^6 z^2 \sin^2\theta \cos^6\theta v_t^{10} + 48\eta^2 v^6 x^6 z^2 \sin^4\theta \cos^2\theta v_t^{10} + 480$$
$$\eta^2 v^6 x^6 z^2 \sin^4\theta \cos^4\theta v_t^{10} - 224\eta^2 v^6 x^6 z^2 \sin^6\theta \cos^2\theta v_t^{10} + 16\eta^2 v^6 x^6 z^2 \sin^8\theta v_t^{10} + 112\eta^2 v^6$$
$$x^5 z^3 \sin\theta \cos^5\theta v_t^{10} + 64\eta^2 v^6 x^5 z^3 \sin\theta \cos^7\theta v_t^{10} - 160\eta^2 v^6 x^5 z^3 \sin^3\theta \cos^3\theta v_t^{10} - 448\eta^2 v^6 x^5$$
$$z^3 \sin^3\theta$$

and

$$\tau_{25} = \Bigg(\cos^5\theta v_t^{10} + 448\eta^2 v^6 x^5 z^3 \sin^5\theta \cos^3\theta v_t^{10} - 64\eta^2 v^6 x^5 z^3 \sin^7\theta \cos\theta v_t^{10} - 64\eta^2 v^6 x^4 z^4 \sin^2\theta \cos^4\theta v_t^{10} \tag{A7}$$

$$+208\eta^2 v^6 x^4 z^4 \sin^2\theta \cos^6\theta v_t^{10} - 544\eta^2 v^6 x^4 z^4 \sin^4\theta \cos^4\theta v_t^{10} + 208\eta^2 v^6 x^4 z^4 \sin^6\theta \cos^2\theta v_t^{10} + v^4 x^8$$

$$v_t^{12} - 3v^4 x^8 \cos^2\theta v_t^{12} + 2v^4 x^8 \cos^4\theta v_t^{12} - 8v^4 x^8 \sin^2\theta \cos^2\theta v_t^{12} + 6v^4 x^7 z \sin\theta \cos\theta v_t^{12} - 8v^4 x^7 z$$

$$\sin\theta \cos^3\theta v_t^{12} - 9v^4 x^6 z^2 \sin^2\theta v_t^{12} + 20v^4 x^6 z^2 \sin^2\theta \cos^2\theta v_t^{12} - 8v^4 x^5 z^3 \sin^3\theta \cos\theta v_t^{12} + 10v^4 x^4 z^4$$

$$\sin^4\theta v_t^{12} - 6\eta v^4 x^8 \cos^2\theta v_t^{12} + 8\eta v^4 x^8 \cos^4\theta v_t^{12} - 16\eta v^4 x^8 \sin^2\theta \cos^2\theta v_t^{12} + 16\eta v^4 x^8 \sin^2\theta \cos^4\theta$$

$$v_t^{12} - 16\eta v^4 x^8 \sin^4\theta \cos^2\theta v_t^{12} - 20\eta v^4 x^7 z \sin\theta \cos^3\theta v_t^{12} + 40\eta v^4 x^7 z \sin\theta \cos^5\theta v_t^{12} + 20\eta v^4 x^7 z$$

$$\sin^3\theta \cos\theta v_t^{12} - 80\eta v^4 x^7 z \sin^3\theta \cos^3\theta v_t^{12} + 16\eta v^4 x^7 z \sin^5\theta \cos\theta v_t^{12} + 52\eta v^4 x^6 z^2 \sin^2\theta \cos^2\theta v_t^{12}$$

$$-20\eta v^4 x^6 z^2 \sin^2\theta \cos^4\theta v_t^{12} - 16\eta v^4 x^6 z^2 \sin^4\theta \cos^2\theta v_t^{12} + 4\eta v^4 x^6 z^2 \sin^6\theta v_t^{12} + 80\eta v^4 x^5 z^3 \sin^3\theta$$

$$\cos^3\theta v_t^{12} - 56\eta v^4 x^5 z^3 \sin^5\theta \cos\theta v_t^{12} - 32\eta v^4 x^4 z^4 \sin^4\theta \cos^2\theta v_t^{12} + 8\eta^2 v^4 x^8 \cos^4\theta v_t^{12} + 32\eta^2$$

$$v^4 x^8 \sin^2\theta \cos^4\theta v_t^{12} - 32\eta^2 v^4 x^8 \sin^4\theta \cos^2\theta v_t^{12} + 16\eta^2 v^4 x^7 z \sin\theta \cos^5\theta v_t^{12} - 32\eta^2 v^4 x^7 z \sin\theta$$

$$\cos^7\theta v_t^{12} + 160\eta^2 v^4 x^7 z \sin^3\theta \cos^5\theta v_t^{12} - 160\eta^2 v^4 x^7 z \sin^5\theta \cos^3\theta v_t^{12} + 32\eta^2 v^4 x^7 z \sin^7\theta \cos\theta v_t^{12}$$

$$-88\eta^2 v^4 x^6 z^2 \sin^2\theta \cos^4\theta v_t^{12} - 64\eta^2 v^4 x^6 z^2 \sin^2\theta \cos^6\theta v_t^{12} + 192\eta^2 v^4 x^6 z^2 \sin^4\theta \cos^4\theta v_t^{12} - 64$$

$$\eta^2 v^4 x^6 z^2 \sin^6\theta \cos^2\theta v_t^{12} - 192\eta^2 v^4 x^5 z^3 \sin^3\theta \cos^5\theta v_t^{12} + 192\eta^2 v^4 x^5 z^3 \sin^5\theta \cos^3\theta v_t^{12} - 3v^2$$

$$x^8 \sin^2\theta v_t^{14} + 8v^2 x^8 \sin^2\theta \cos^2\theta v_t^{14} + 8v^2 x^6 z^2 \sin^4\theta v_t^{14} + 18\eta v^2 x^8 \sin^2\theta \cos^2\theta v_t^{14} - 28\eta v^2 x^8$$

$$\sin^2\theta \cos^4\theta v_t^{14} + 16\eta v^2 x^8 \sin^4\theta \cos^2\theta v_t^{14} - 8\eta v^2 x^7 z \sin^5\theta \cos\theta v_t^{14} - 44\eta v^2 x^6 z^2 \sin^4\theta \cos^2\theta v_t^{14}$$

$$-24\eta^2 v^2 x^8 \sin^2\theta \cos^4\theta v_t^{14} + 16\eta^2 v^2 x^8 \sin^2\theta \cos^6\theta v_t^{14} - 32\eta^2 v^2 x^8 \sin^4\theta \cos^4\theta v_t^{14} + 16\eta^2 v^2 x^8$$

$$\sin^6\theta \cos^2\theta v_t^{14} + 64\eta^2 v^2 x^6 z^2 \sin^4\theta \cos^4\theta v_t^{14} + 2x^8 \sin^4\theta v_t^{16} - 12\eta x^8 \sin^4\theta \cos^2\theta v_t^{16} + 16\eta^2$$

$$x^8 \sin^4\theta \cos^4\theta v_t^{16} + \left(v^{12} z^6 v_t^6 + 3v^{10} x^2 z^4 v_t^8 + 3v^8 x^4 z^2 v_t^{10} + v^6 x^6 v_t^{12}\right) \sqrt{\frac{x^2 v_t^2 + v^2 z^2}{v^2 v_t^2}} \Bigg)$$

$$\Bigg/ \left(v^6 v_t^6 \left(x^2 v_t^2 + v^2 z^2\right)^3 \sqrt{\frac{x^2 v_t^2 + v^2 z^2}{v^2 v_t^2}} \right).$$

IV

Commun. Comput. Phys.
doi: 10.4208/cicp.OA-2018-0143

Vol. **x**, No. x, pp. 1-27
xxx 201x

Target-Oriented Inversion of Time-Lapse Seismic Waveform Data

Xingguo Huang[1,*], Morten Jakobsen[1,2], Kjersti Solberg Eikrem[2] and Geir Nævdal[2]

[1] *Department of Earth Science, University of Bergen, P.O. Box 7803, 5020 Bergen, Norway.*

[2] *NORCE Norwegian Research Centre, Postboks 22, 5838 Bergen, Norway.*

Received 27 May 2018; Accepted (in revised version) 2 March 2019

Abstract. Full waveform inversion of time-lapse seismic data can be used as a means of estimating the reservoir changes due to the production. Since the repeated computations for the monitor surveys lead to a large computational cost, time-lapse full waveform inversion is still considered to be a challenging task. To address this problem, we present an efficient target-oriented inversion scheme for time-lapse seismic data using an integral equation formulation with Gaussian beam based Green's function approach. The proposed time-lapse approach allows one to perform a local inversion within a small region of interest (e.g. a reservoir under production) for the monitor survey. We have verified that the T-matrix approach is indeed naturally target-oriented, which was mentioned by Jakobsen and Ursin [24] and allows one to reduce the computational cost of time-lapse inversion by focusing the inversion on the target-area only. This method is based on a new version of the distorted Born iterative T-matrix inverse scattering method. The Gaussian beam and T-matrix are used in this approach to perform the wavefield computation for the time-lapse inversion in the baseline model from the survey surface to the target region. We have provided target-oriented inversion results of the synthetic time-lapse waveform data, which shows that the proposed scheme reduces the computational cost significantly.

AMS subject classifications: 81U40, 74J25, 74J20, 45Dxx

Key words: Waveform inversion, time-lapse seismic, seismic inverse scattering, target-oriented inversion, Gaussian beam based Green's function.

*Corresponding author. *Email addresses:* Xingguo.Huang@uib.no, xingguo.huang19@gmail.com (X. Huang), Morten.Jakobsen@uib.no (M. Jakobsen), kjei@norceresearch.no (K. S. Eikrem), gena@norceresearch.no (G. Nævdal)

1 Introduction

Full waveform inversion (FWI) is a powerful tool for reconstructing the subsurface structure and estimating the physical parameters, e.g. P- and S- wave velocities in the subsurface [1]. Advances in full waveform inversion make it possible to do the time-lapse seismic full waveform inversion. Time-lapse seismic is a widely used tool for the dynamic reservoir monitoring and assessing the reservoir changes due to production [2–4]. Recent studies have shown the applicability of the full waveform inversion for the time-lapse seismic problem [5–10].

Essentially, the seismic full waveform inversion can be viewed as a seismic inverse scattering problem since the scattering theory provides the relations between the model parameter perturbation and the seismic waveform [1, 11–14]. Seismic scattering method is an important technique for seismic data processing, in which the scattered wavefield results from a medium perturbation. The perturbation property of the seismic scattering theory renders it useful not only for seismic forward modeling but also for seismic inversion [15–17]. Since the 1980s, the direct inversion approach based on the linearized wave equation using the seismic scattering method has been widely used [18–23].

Jakobsen and Ursin [24] developed the distorted Born iterative T-matrix method (DBIT) for full waveform inversion based on integral equation methods. The underlying idea of this method is to reduce a nonlinear inverse scattering problem to a sequence of linear inverse scattering problems. For this method, there are several important features: (1) the sensitivity matrix is expressed explicitly in terms of the Green's functions, which is helpful to reduce the computational cost [24, 25]; (2) this method can be applied to the cases with multiple sources; (3) the computational cost and convergence problems can be addressed by the T-matrix approach by domain decomposition and renormalization methods [24, 27–29, 61]. These features make the distorted Born iterative T-matrix method more applicable to seismic full waveform inversion. Additional works on this method can be found in Jakobsen and Wu [29, 31] and Wang et al. [32]. Recently, the integral equation formulations were applied to the time-lapse seismic data and to estimate the uncertainty [33]. However, a major limitation of the time-lapse full waveform inversion is that the computational cost is expensive.

The main purpose of this paper is to develop a fast waveform inversion scheme for the time-lapse inversion. We develop a target-oriented inversion method, which is based on the idea of local inversion. Thus, if we develop a fast repeat-inversion scheme, which is only for a small region, the computational cost can be significantly reduced. It makes sense because the effects of the production on the reservoir changes are considered as small perturbations of the earth model [34]. Several studies on the localized full waveform inversion have been proposed to approach this topic. Borisov et al. [35] used the finite-difference injection method to develop an efficient 3-D time-lapse full waveform inversion. Willemsen et al. [36] derive a local solver for full waveform inversion of a small region of interest. Malcolm and Willemsen [37] have developed local solvers for

localized inversion. Broggini et al. [38] derive the immersive boundary conditions for local wavefields computation. Willemsen and Malcolm [39] applied the coupled acoustic-elastic local solver to phase inversion. Yuan et al. [10] performed a localized waveform inversion time-lapse survey by combining the wavefield injection and extrapolation. Unlike the methods above, we develop a target-oriented waveform inversion scheme based on the distorted Born iterative T-matrix method [24] and Gaussian beam based Green's function [40–47].

The integral equation formulation of full waveform inversion provides significant advantages over other methods for the target-oriented inversion since it allows the sensitivity matrix to be expressed explicitly in terms of the Green's functions. The distorted Born iterative T-matrix method was introduced as a general FWI method by Jakobsen and Ursin [24]; but they suggested that it could be very suitable for time-lapse inversion, since the T-matrix approach is naturally target-oriented, in the sense that the inversion can be focused on any target if the rest of the model is assumed known. In this paper, we have performed a numerical study of time-lapse inversion based on the distorted Born iterative T-matrix method, to verify that this method reduce computational time for time-lapse inversion. The use of Gaussian beam based Green's functions for the static Reference medium also represent a novel aspect of the present study. The target-oriented inversion method of this paper has the following advantages: (1) When using integral equation methods, it is only necessary to discretize the target area if the Green's functions for the rest of the model is known. This is in contrast to the finite difference method where it is required to discretize the whole model, unless special grid injection method is used; (2) The scattering volume V in the T-matrix formulation is flexible and can be equal to the target area in time-lapse inversion; (3) Another advantage if that compared to finite difference method, there is no grid dispersion error which exists in numerical differential equation solvers, and the integral equation method has a smaller accumulated error [48]. For our approach, two critical aspects are (1) to calculate the initial local wavefields of the target region and (2) its iterative updating for the local inversion. To this end, we employ two methods, called Gaussian beam based Green's function approach [40, 45] and the T-matrix method. These two methods are used to calculate the initial local wavefields of the target region. For the updating of the wavefields in the local inversion, we use the T-matrix method. The T-matrix method is from quantum mechanical scattering theory [50–55]. Since its introduction into rock physics, the T-matrix method [29, 56–58] has been successfully used to solve the seismic scattering forward problem. More recently, this approach has been extended to seismic inversion [24].

The paper is organized as follows: we first review the seismic scattering forward problem including the Lippmann-Schwinger equation and the T-matrix approach. Then, we review the seismic inverse scattering method for waveform inversion. Further, we present our target-oriented inversion scheme for time-lapse seismic data in Section 4. The new aspects of the paper is described in Section 4 called Time-lapse inversion. Both Sections 4.1 and 4.2 are new compared with the work of [24], but the sequential and double difference strategies are less new than the target-oriented aspects discussed in

Sections 4.2. Finally, we give the inverted results for the full baseline model and the target-oriented inverted results for the time-lapse data.

2 Seismic direct scattering problem

For the inversion of the time-lapse waveform data, we use the seismic scattering method to extrapolate the wavefield. In this section, we review the Lippmann-Schwinger equation, Green's operators and T-matrix theory.

2.1 The Lippmann-Schwinger equation

The Green's function for the scalar wave equation in the frequency domain satisfies [59]

$$\left(\bigtriangledown^2+\frac{\omega^2}{c^2(\mathbf{r})}\right)G\left(\mathbf{r},\mathbf{r}',\omega\right)=-\delta\left(\mathbf{r}-\mathbf{r}'\right), \tag{2.1}$$

where $c(\mathbf{r})$ is the seismic wave velocity, $\mathbf{r}$ is the position vector, $\mathbf{r}'$ is the source position vector, and the Dirac delta function $\delta(\mathbf{r}-\mathbf{r}')$ represents a unit point source at position x′ and $G(\mathbf{r},\mathbf{r}',\omega)$ is the Green's function with an angular frequency ω. We can decompose the actual medium into a background medium and a perturbed medium as

$$\chi(\mathbf{r})=\frac{1}{c^2(\mathbf{r})}-\frac{1}{c_0^2(\mathbf{r})}, \tag{2.2}$$

where $c_0(\mathbf{r})$ is the seismic wave velocity in an arbitrary heterogeneous background medium and $\chi(\mathbf{r})$ is the contrast function. Substituting Eq. (2.2) into Eq. (2.1) yields

$$\left(\bigtriangledown^2+\frac{\omega^2}{c_0^2(\mathbf{r})}\right)G\left(\mathbf{r},\mathbf{r}',\omega\right)=-\delta\left(\mathbf{r}-\mathbf{r}'\right)-\omega^2\chi(\mathbf{r})G\left(\mathbf{r},\mathbf{r}',\omega\right). \tag{2.3}$$

The Lippmann-Schwinger equation can be obtained from Eq. (2.3) as [24, 59]

$$G\left(\mathbf{r},\mathbf{r}',\omega\right)=G^{(0)}\left(\mathbf{r},\mathbf{r}',\omega\right)+\omega^2\int_D d\mathbf{r}''G\left(\mathbf{r},\mathbf{r}'',\omega\right)\chi\left(\mathbf{r}''\right)G\left(\mathbf{r}'',\mathbf{r}',\omega\right), \tag{2.4}$$

where $G^{(0)}(\mathbf{r},\mathbf{r}',\omega)$ is the Green's function for the background medium, D is the scattering domain where $\chi(\mathbf{r}'')$ is non-zero, and the background Green's function $G^{(0)}(\mathbf{r},\mathbf{r}',\omega)$ satisfies the scalar wave equation

$$\left(\bigtriangledown^2+\frac{\omega^2}{c_0^2(\mathbf{r})}\right)G^{(0)}\left(\mathbf{r},\mathbf{r}',\omega\right)=-\delta\left(\mathbf{r}-\mathbf{r}'\right). \tag{2.5}$$

If the background medium is homogeneous, the background Green's function $G^{(0)}(\mathbf{r},\mathbf{r}',\omega)$ can be calculated by analytic methods. If the background medium is inhomogeneous, the background Green's function can be calculated by ray theory [40] or finite

difference method [1]. In this work, we employ the Gaussian beam summation method to calculate the background Green's function. Following the recent approach [45], the method implements an estimate of the Green's function in the inhomogeneous background medium that requires (1) a dynamic ray tracing for Gaussian beam computation, (2) the Green's function calculation by Gaussian beam summation. The reason why we use the Gaussian beam is that (1) we can start the inversion with a smoothed inhomogeneous background model; (2) the boundary reflection can be reduced. The details of the method are shown in Appendix A. For the use of the operator form in the following section, we rewrite the Lippmann-Schwinger equation (2.4) in a form of a product of continuous matrices

$$G\left(\mathbf{r},\mathbf{r}',\omega\right)=G^{(0)}\left(\mathbf{r},\mathbf{r}',\omega\right)+\int_D d\mathbf{r}_1 d\mathbf{r}_2 G^{(0)}\left(\mathbf{r}_1,\mathbf{r}_2,\omega\right)V\left(\mathbf{r}_1,\mathbf{r}_2\right)G\left(\mathbf{r}_2,\mathbf{r}',\omega\right), \tag{2.6}$$

where $V\left(\mathbf{r}_1,\mathbf{r}_2\right)=\omega^2\chi\left(\mathbf{r}_1\right)\delta\left(\mathbf{r}_1-\mathbf{r}_2\right)$, V is a local scattering potential operator, which can be represented by a diagonal matrix in coordinate representation [29, 31].

2.2 The Green's operators and T-matrix approach

Here, we rewrite the Lippmann-Schwinger equation (2.6) in operator notation

$$G=G^{(0)}+G^{(0)}VG. \tag{2.7}$$

Following the recent works [24, 56–58], we introduce the T-matrix approach into the full waveform inversion approach. Referring to Jakobsen and Ursin [24], we introduce the T-matrix approach by

$$VG=TG^{(0)}, \tag{2.8}$$

where represents the T-matrix. Applying the relation (2.8) to the Lippmann-Schwinger equation (2.7), we have

$$G=G^{(0)}+G^{(0)}TG^{(0)}. \tag{2.9}$$

For the Green's operators above, we haven't specified any matrix elements in any particular representation. However, for application to the seismology, we introduce the restricted Green's operators. Note that the above equation is independent of the source-receiver configuration. By applying the relation (2.8) to the Lippmann-Schwinger equation (2.7), we have

$$G_{VS}=G^{(0)}_{VS}+G^{(0)}_{VV}TG^{(0)}_{VS}, \tag{2.10}$$

where $G^{(0)}_{VS}$ and G_{VS} are the source-dependent Green's functions in the background and actual media, respectively. Similarly, we get Green's functions from the source to the receiver, volume to volume, the scattering point to the receiver, respectively:

$$\begin{aligned} G_{RS}&=G^{(0)}_{RS}+G^{(0)}_{RS}TG^{(0)}_{RV},\\ G_{VV}&=G^{(0)}_{VV}+G^{(0)}_{VV}TG^{(0)}_{VV},\\ G_{RV}&=G^{(0)}_{RV}+G^{(0)}_{RV}TG^{(0)}_{VV}. \end{aligned} \tag{2.11}$$

Since in Eq. (2.11) $G_{RS}^{(0)}$ is arbitrary, the T-matrix satisfies the Lippmann-Schwinger type equation [24]

$$T = V + VG_{VV}^{(0)}T. \tag{2.12}$$

Eq. (2.12) has the exact solution

$$T = \left(I - VG_{VV}^{(0)}\right)^{-1} V. \tag{2.13}$$

The computation of the T-matrix by matrix inversion can be very costly. The domain decomposition was proposed by Jakobsen and Wu [29,31] to accelerate the T-matrix approach to seismic full-waveform inversion. Also, if the perturbation is small, we can use an approximated form of the T-matrix [24] to update the background Green's function for every iteration.

3 Seismic inverse scattering problem

3.1 The distorted Born iterative T-matrix inversion method

The distorted Born iterative T-matrix inversion method of [24, 81], which is based on a distorted Born approximation [60, 61] and solves for the scattering potential $\mathbf{V}$, uses an iterative scheme that for each iteration updates the scattering potential. Because the T-matrix is used for the Green's function update, the method has been referred to distorted Born iterative T-matrix inversion method. The relationship between a variation $\delta\mathbf{V}^{(i)} = \mathbf{V} - \mathbf{V}^i$ in the scattering potential $\mathbf{V}$ around a heterogeneous background model with scattering potential $\mathbf{V}^{(i)}$ and a variation $\delta\mathbf{G}_{RS} = \mathbf{G}_{RS} - \mathbf{G}_{RS}^{(i)}$ in the Green's function $\mathbf{G}_{RS}$ around the Green's function $\mathbf{G}_{RS}^{(i)}$ for the background medium is given by [60, 61]

$$\delta\mathbf{G}_{RS}^{(i)} = \mathbf{G}_{RV}^{(i)}\delta\mathbf{V}^{(i)}\mathbf{G}_{VS}^{(i)}, \tag{3.1}$$

where

$$\mathbf{G}_{RS}^{(i)} = \mathbf{G}_{RS}^{(0)} + \mathbf{G}_{RV}\mathbf{T}^{(i)}\mathbf{G}_{VS}^{(0)}, \tag{3.2}$$

$$\mathbf{G}_{VS}^{(i)} = \mathbf{G}_{VS}^{(0)} + \mathbf{G}_{VV}\mathbf{T}^{(i)}\mathbf{G}_{VS}^{(0)}, \tag{3.3}$$

$$\mathbf{G}_{RV}^{(i)} = \mathbf{G}_{RV}^{(0)} + \mathbf{G}_{RV}\mathbf{T}^{(i)}\mathbf{G}_{VV}^{(0)} \tag{3.4}$$

are matrices of Green's functions for the background medium responsible for different parts of the scattering path from the source to the receiver via the volume, and

$$\mathbf{T}^{(i)} = \mathcal{T}\left(\mathbf{V}^{(i)}\right) \tag{3.5}$$

is the corresponding T-matrix. In Eqs. (3.2)-(3.4), the reference Green's functions $\mathbf{G}_{RS}^{(0)}$, $\mathbf{G}_{VS}^{(0)}$, and $\mathbf{G}_{RV}^{(0)}$ are calculated for a heterogeneous medium with Gaussian beams and the

background Green's functions $\mathbf{G}_{RS}^{(i)}$, $\mathbf{G}_{VS}^{(i)}$, and $\mathbf{G}_{RV}^{(i)}$ (typically calculated numerically for an inverted model with scattering potential $\mathbf{V}^{(i)}$ relative to the reference model with zero scattering potential) are static and dynamic, respectively. By dynamic, they are updated after each linearised inversion step.

The observable scattered (data residual) wavefield $\delta d_R^{(i)}$ associated with the perturbation $\mathbf{V}^{(i)}$ can be written as

$$\delta d_R^{(i)} = \delta \mathbf{G}_{RS}^{(i)} \mathbf{s}, \tag{3.6}$$

where $\mathbf{s}$ is an N_s-dimensional vector associated with the source functions at N_s different source positions. By combining Eqs. (3.1) and (3.6), a linear relation between the scattered (data residual) field $\delta d_R^{(i)}$ and the scattering potential variation (or perturbation) $\mathbf{V}^{(i)}$ [24] can be obtained:

$$\delta d_R^{(i)} = \mathbf{G}_{RV}^{(i)} \delta \mathbf{V}^{(i)} \mathbf{G}_{VS}^{(i)} \mathbf{s}. \tag{3.7}$$

From Eq. (3.7), one can observe that when the scattered (data residual) field $\delta d_R^{(i)}$ is known, one can determine the perturbation $\mathbf{V}^{(i)}$ using a regularised least-squares inversion method. Then, the original $\mathbf{V}^{(i)}$ can be replaced with the inverted scattering potential and more accurate solutions can be obtained with iterations in a direct iterative manner. It should be noted that the data residual field and background medium Green's functions can be updated after each iteration by using the exact relations (3.1)-(3.4).

3.2 Some details for implementation

In this work, we use the distorted Born iterative method to solve the inverse problem for the baseline and time-lapse inversions. The underlying idea of the distorted Born iterative inversion method is to reduce a nonlinear inverse scattering problem to a series of linear inverse scattering problem.

Eq. (3.7) can also be expressed as [24]

$$\delta d_{r,s}^{(i)} = \sum_{n=1}^{N} J_{rn,s}^{(i)} \delta \chi_n, \tag{3.8}$$

where the scattered wavefields δd represents the difference between the calculated wavefields in the background medium and the wavefields in the actual medium, $\delta\chi$ is the difference of the contrast potential, and the sensitivity matrix can be written as [24]

$$J_{rn,s}^{(i)} = \left[G_{rn}^{(i)} \delta v_n G_{ns}^{(i)} \right] f_s, \tag{3.9}$$

where $G_{rn}^{(i)}$ and $G_{ns}^{(i)}$ are the Green's functions in a dynamic heterogeneous reference medium associated with the receivers and the sources at ith iteration, respectively. The Green's functions that is updated after each iteration and where we compute the corresponding Green's functions by solving the Lippmann-Schwinger equations (3.2)-(3.4).

Here, f_s is the source function associated with the angular frequency, and δv_n is the Kronecker-delta.

From Eq. (3.8), one can observe that the nonlinear inverse scattering problem has been reduced to a series of linear inverse scattering problem. However, solving inverse problem is an ill-posed problem. In order to obtain a meaningful solution, we can apply generalized Tikhonov regularization to the inverse scattering problem. Thus, the solution can be obtained by solving the following optimization problem [62]

$$E(\delta\chi)=\left\|\delta d^{(i)}-J^{(i)}\delta\chi\right\|^2+\alpha\|\delta\chi\|^2, \tag{3.10}$$

where $\|\|$ represents the $L2$ norm, α is the regularization parameter, which can be chosen by the cooling scheme [24], a modified version of the method described in Lavarello and Oelze [63] and in Hesford and Chew [64], or L-curve method [65]. The regularization parameter is very important for the inversion. Through many numerical tests, we choose to use the cooling scheme as

$$\alpha^{(i)}=\alpha_0 a^{(i-1)}, \tag{3.11}$$

where α_0 is the initial value, and $0.1<a<0.9$. However, to obtain a relatively good result, we should choose different initial values in Eq. (3.11) for the baseline and time-lapse inversion. The details will follow in Section 4. The iterative form solution for the inversion is

$$\chi^{i+1}=\chi^{(i)}+\left(H^i+\alpha^{(i)}I\right)^{-1}V^{(i)}, \tag{3.12}$$

with the gradient

$$V^{(i)}=\Re\left[\left(J^{(i)}\right)^{\dagger}\delta d^{(i)}\right], \tag{3.13}$$

where $\delta d^{(i)}$ is the difference between the observed data and the calculated data, $\dagger$ denotes transpose conjugate, i is the number of iteration, $\Re$ represents the real part, and

$$H^{(i)}=\Re\left[\left(J^{(i)}\right)^{\dagger}J^{(i)}\right] \tag{3.14}$$

is the approximate Hessian matrix. The process of solving the nonlinear inverse scattering problem is essentially similar to the Gauss-Newton optimization methods for FWI (e.g. the process for inverse Hessian, shown as Eq. (3.12) in this paper and Eq. (13) in [76]). Similar to the GN Hessian (equation 10 in [76]), the element of the Hessian in our approach is formed by correlating the two Frechet derivative wavefields at the receivers, which is a approximate Hessian. Actually, it has been demonstrated that the Distorted Born iterative method is consistent with the Gauss-Newton methods of optimization (see Remis and van den Berg [74], Oristaglio and Blok [73], Jakobsen and Ursin [24]. However, different from [75] and [76], we construct the approximate Hessian matrix explicitly in terms of Green's functions based on the integral equations. The main difference between our scattering approach and the conventional adjoint state method is that we have

an explicit representation of the sensitivity matrix in terms of Green's functions, that can easily be updated after each iteration using the variational T-matrix approach, without having to perform a full forward simulation. And also instead of using the conjugate gradient method, we solve a linear system (using Gaussian elimination method) involving our approximate Hessian matrix. Appendix B shows the pseudo code of the algorithm, which is based on the pseudo code of the DBIT inversion algorithm shown in [81].

The above formulations are used to obtain both the full baseline model and the time-lapse model. For the baseline inversion, we formulate the Gaussian beam based distorted Born iterative T-matrix inversion method by using the Gaussian beam based Green's function as the background Green's function. This method incorporates several important features: (1) The Gaussian beam has flexibility in calculating the wavefields and the boundary reflection can be avoided because it is a ray-based method. (2) Due to the use of the complex traveltime [40–46] in Gaussian beam, this method can deal with the problem of caustic, which is a limitation of the conventional ray theory. For this inversion, we use the integral equations as wavefield propagators, which is based on scattering theory. The Gaussian beam is only used to compute the background Green's function, but the scattering theory can address all the wavefields, e.g. multiple scattering. In fact, for relatively simple medium, combining the distorted Born iterative inversion method and the Gaussian beam can be used for the baseline inversion. However, this paper focus on the target-oriented time-lapse inversion. To obtain an accurate baseline model, the T-matrix is used in the baseline inversion.

4 Time-lapse inversion

4.1 Sequential and double difference strategies

After obtaining the baseline model, we can perform the time-lapse inversion using the time-lapse inversion strategies. In this work, we employ two strategies, called sequential difference strategy and double difference strategy.

Sequential difference strategy: Fig. 1 shows the schematic diagrams of the sequential difference method. The sequential difference strategy [6, 7, 33] considers the baseline model as the initial model. Because the perturbation resulting from the reservoir changes is localized and only occur in a small region, starting from the baseline model for the time-lapse inversion is a good candidate and can reduce the computation cost. After completing the time-lapse inversion, the perturbation can be obtained by a subtraction between the inverted baseline and monitor model.

Double difference strategy: Fig. 2 shows the schematic diagrams of the double difference method. The double difference strategy was proposed by Waldhauser and Ellsworth [66] in the traveltime tomography for improving the earthquake source location [7, 67, 68]. It also starts the time-lapse inversion with the baseline model [5, 7]. However, instead of a full-data inversion in the sequential difference strategy, the double

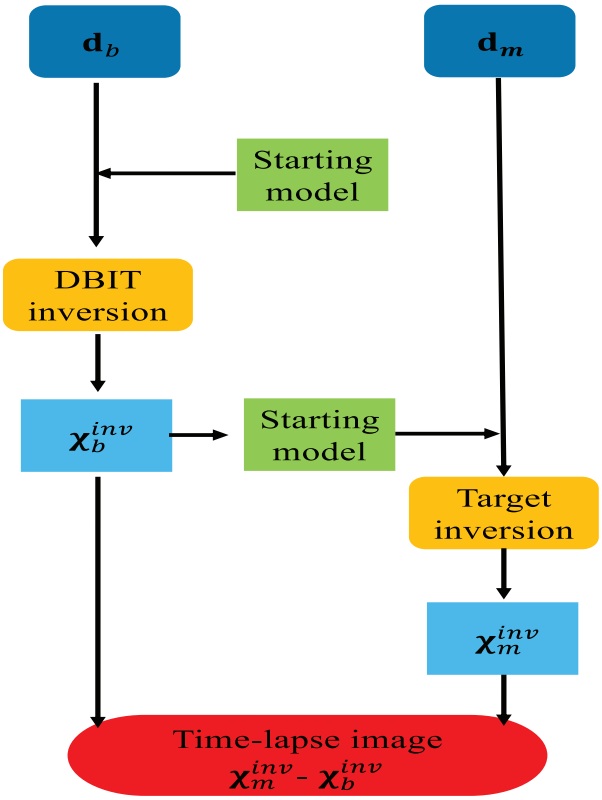

Figure 1: Schematic diagrams of the sequential difference method.

difference strategy only inverts the time-lapse perturbation model using the time-lapse data difference as

$$E(\delta\chi)=\frac{1}{2}\|(u_{monitor}-u_{baseline})-(d_{monitor}-d_{baseline})\|^2, \tag{4.1}$$

where $u_{monitor}$, $u_{baseline}$, $d_{monitor}$ and $d_{baseline}$ are the calculated monitor data set, calculated baseline data set, observed monitor data set and observed baseline data set, respectively. The time-lapse data difference consists of two parts: One is the difference between the observed monitor and baseline data set, and the other is the difference between the calculated monitor and baseline data set. Moreover, there is an assumption that the shot and receiver positions are equal in the data sets.

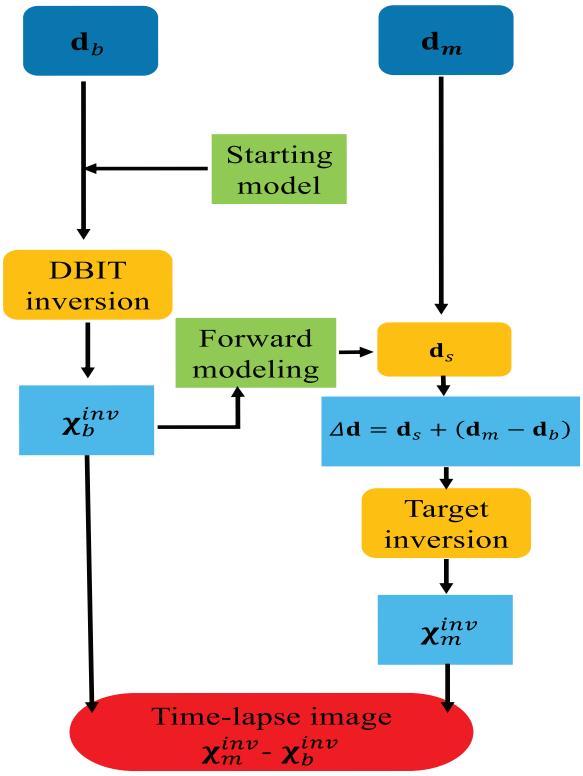

Figure 2: Schematic diagrams of the double difference method.

4.2 The target-oriented scheme

To reduce the computational cost of the time-lapse inversion, we develop a target-oriented inversion scheme. The target-oriented concept was proposed to reduce the computational cost of the wave-equation least-squares migration [69,70] and the reverse time migration [71]. This concept is generalized to the local full waveform inversion [10,35,36]. The scheme of the local inversion is referred to as the target-oriented inversion.

For the target-oriented inversion, there have been several different approaches to perform localized inversion. Borisov et al [35] used the finite-difference injection method to develop a localized full waveform inversion for time-lapse imaging. In this approach, the wavefields are recorded around the local region, and the initial wavefield of the target region are injected. In subsequent target-oriented inversion, the local wavefields are updated. However, the method suffers a limitation that it does not accurately model the

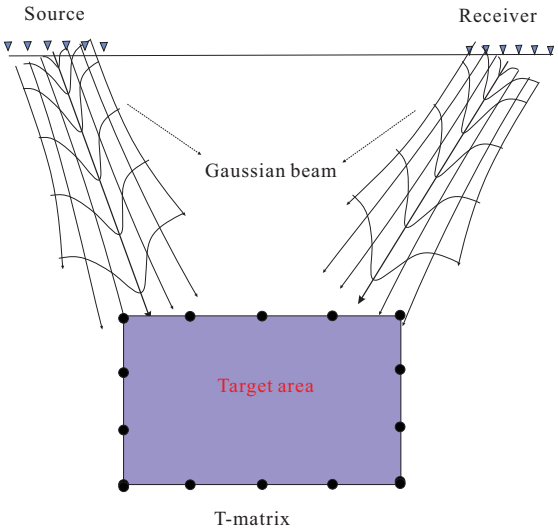

Figure 3: Sketch illustrating the main ideas of the target-oriented inversion. Note that in this scheme, the Gaussian beam and T-matrix are used to propagate the wavefields from the source and receiver and- the wavefields are propagated from the receiver to scattering region by the reciprocity theorem.

higher order long-range interactions between the scattered wavefield propagating into the unaltered exterior domain and then re-enter into the local target domain. Yang et al. [77] developed time-lapse waveform inversion by transforming the original survey into a new survey at the top of the reservoir. The new data sets are synthesized from the recorded data with the re-datumed signals and the new virtual survey geometry. Because of modifying the surface data recordings, they introduce varying degrees of artefacts. Valenciano et al. [70] proposed to explicitly compute an approximation of the Hessian in a target-oriented fashion. After computing a nondiagonal Hessian matrix, they obtain the inverse image using an iterative algorithm. However, this method used the Green's function by solving the one-way wave equation, which has a limited accuracy for large-angle propagation.

Our approach uses integral equations to develop the target-oriented inversion. The method requires only one simulation for the initial Green's functions on the entire subsurface model and the initial Green's functions are computed efficiently since we employ Gaussian beams. For the subsequent target-oriented inversion, the multiple scattering occurring within the target area can be modeled by the T-matrix. The T-matrix approach is naturally target-oriented since the T-matrix refers to the target-region only and is independent of the source-receiver configuration. Our target-oriented inversion is based on the full waveform inversion using the integral equation formulations. Fig. 3 shows the sketch illustrating the main ideas of target-oriented inversion. The underlying idea of

the proposed target-oriented inversion is that we only need to compute the local wavefields of the target region. The initial local scattered wavefields of the target region are computed in the inverted baseline model.

We have developed our time-lapse inversion method adopting the distort Born iterative T-matrix method described in Section 2.3 and using the inversion formulations described in Section 3. Our inversion approach involves a static heterogeneous reference medium (denoted by $\mathbf{G}^{(0)}_{RS}$, $\mathbf{G}^{(0)}_{VS}$,and $\mathbf{G}^{(0)}_{RV}$) for which we use Gaussian beam based Green's functions, and a dynamic heterogeneous reference medium that is updated after each iteration and where we compute the corresponding Green's functions ($\mathbf{G}^{(i)}_{RS}$, $\mathbf{G}^{(i)}_{VS}$,and $\mathbf{G}^{(i)}_{RV}$) by solving the Lippmann-Schwinger equation. The Green's functions have scattering information from the target area. That means that we could estimate the velocity within the target.

For the time-lapse target inversion scheme, there are three main steps:

(1) Compute the background Green's function in the smoothed baseline model;

(2) Compute the static Green's functions in the inverted baseline model using the Gaussian beam based Green's function and T-matrix from the survey surface to the target region;

(3) Perform the local inversion, the local wavefields are updated by the Lippmann-Schwinger equations associated with T-matrix approach within the target region.

5 Numerical results

5.1 Baseline inversion

In this section, we use a subset of the Marmousi 2 P wave velocity model [72] to test the baseline inversion scheme. The model size is 2460 m $\times$ 1620 m. The size of the grid is 20 m $\times$20 m. Fig. 4(a) shows the resampled baseline model. We employ 81 sources and 123 receivers, which are both located at the surface and distributed uniformly from 0 m to 2460 m. We employ a Ricker wavelet with the central frequency of 7.5 Hz. In this example, we use the sequential frequency inversion scheme, which inverts frequency by frequency. Here, we choose a frequency group of 2 Hz, 5 Hz, 8 Hz, 11 Hz, 15 Hz and 18 Hz. For each frequency, the maximum number of iterations is 30. We generated the frequency component synthetic data and used the fast Fourier transform with a sampling interval of 0.004 s and the total record length of 3 s. A key point of this inversion is to choose the regularization parameter. We use the cooling scheme [24] for this test. In the numerical tests, we find that if the regularization parameter is too small in the beginning of the iterative process, artefacts can build-up in the inverted results, to compensate for model errors. This is because in the scattering domain, the initial information about the scattered wavefield is not sufficient. After many tests, we decide to use 10 as the initial value α_0 of the cooling scheme (see Eq. (3.11)). We choose a in the Eq. (3.11) as 0.9. We

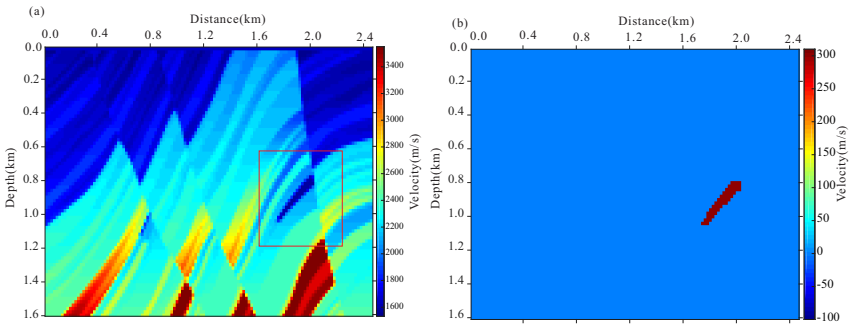

Figure 4: The baseline model and target region. (a) A subset version of the Marmousi2 P- wave velocity model; (b) time-lapse perturbation of 300m/s.

have tested with noise-free and noisy data. For the noisy data, the random noise has been added to each frequency component data [24]

$$\mathbf{d}^{noisy} = \left(\mathbf{d} + \frac{|\mathbf{d}|}{\sqrt{SNR}} \frac{\eta}{|\eta|}\right), \tag{5.1}$$

where η is a vector with independent random numbers taken from a Gaussian distribution, and the decibel (**dB**) is used to measure noise level. We use the signal-to-noise ratio (denoted by SNR) of 30 dB (3 % noise) and 26 dB (5.1 % noise), respectively.

Fig. 5(a) shows the smoothed starting model for the baseline inversion. For field case, the smoothed starting model can be obtained by traveltime inversion. The Gaussian beams have been computed for this model for the initial Green's function. Figs. 5(b), (c) and (d) show the inverted results for the subset of the Marmousi2 baseline model with a smoothed starting model (shown in Fig. 5(a)) with noise-free data and noisy data with the SNR of 30 dB and 26 dB, respectively. From Fig. 5(b), one can observe that the model structure can be distinguished clearly. This implies that the inversion method works well for noise-free data. To quantify the errors between the true model and the inversion results, we compute the differences between the true baseline model and the inverted baseline results with noisy data, shown as Fig. 6. From Fig. 6, one can observe that due to the effect of a stronger noise, the error of the inverted results with signal-to-noise ratio of 26 dB is larger than that with the signal-to-noise ratio of 30 dB.

5.2 Time-lapse inversion

In this section, we focus on the target-oriented inversion of the time-lapse model. Fig. 4(b) shows the time-lapse perturbation model. This model is obtained by adding a perturbation of 300 m/s to the baseline model. For the numerical tests, we use the same sources and receivers as the baseline inversion. Here, we use the same Ricker wavelet, grid size

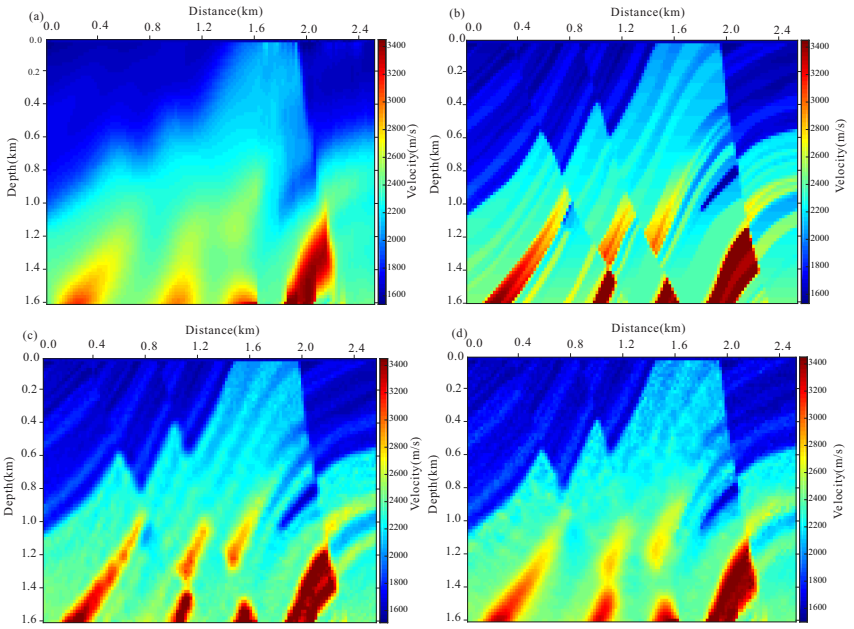

Figure 5: The baseline inversion results using Gaussian beam plus T-matrix method. (a) The smoothed starting model; (b) the inverted result of noise-free data; (c) the inverted result of noisy data (30dB); (d) the inverted result of noisy data (26dB).

and frequency group as the baseline inversion. The size of the target region is 600 m $\times$ 600 m, shown as Fig. 4(b). The locations are from 1600 m to 2200 m and from 600 m to 1200 m in the horizontal and vertical directions, respectively. For the regularization parameter, we use a modified version of the cooling scheme (Jakobsen and Ursin, 2015). In our approach, the initial value is chosen as $\alpha_0 = \sqrt{\text{trace}(H)/\text{length}(H)}$, where H represents the Hessian matrix as before. We choose a in the Eq. (3.11) as 0.9. We generated the frequency component synthetic data and used the fast Fourier transform with a sampling interval of 0.004 s and the total record length of 3 s. The maximum number of iterations is 30 for each frequency.

5.2.1 Comparison of time-lapse inversion strategies

To validate the accuracy of our target-oriented inversion approach, we have carried out the numerical experiments on a time-lapse model in which there is a perturbation due the time-lapse effects, shown as Fig. 4(b). For this experiment, we have tested both the sequential difference strategy and double difference strategy. We employ the baseline model used in the last section, which is shown in Fig. 4(a), as the true baseline model.

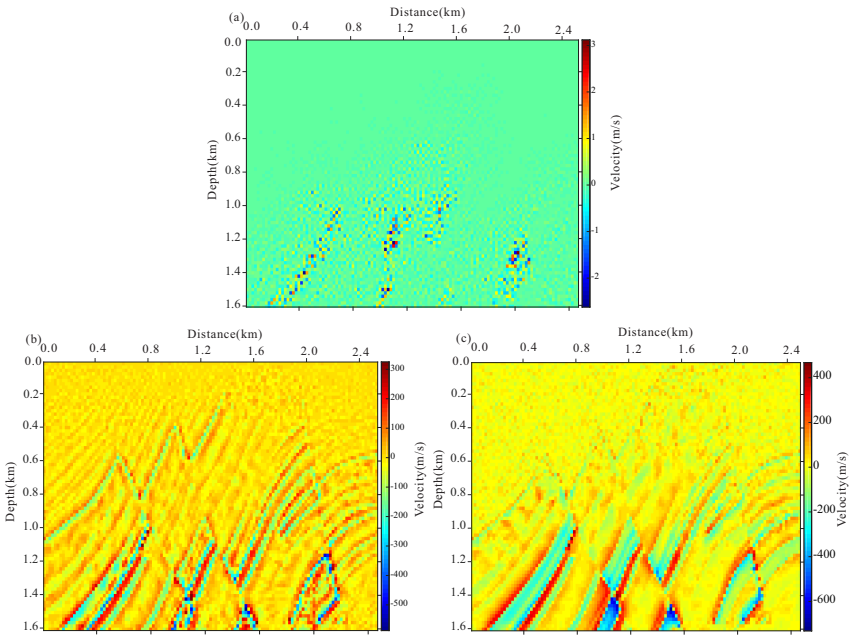

Figure 6: The errors of the baseline inversion. (a) The inversion error with noise-free data; (b) The inversion error with noisy data (30dB); (c) the inversion error with noisy data (26dB).

We have performed the full-model inversion and target-oriented inversion on this time-lapse model. Fig. 7 shows the inverted results of the noise-free data for the time-lapse inversion with the sequential difference strategy and double difference strategy, respectively. All computations were performed on Intel (R) Xeon (R) CPU E5-4650 2.7 GHz. The computational times of the full-model inversion with the sequential difference and double difference strategies are 2.15×10^4 s and 2.11×10^4 s, respectively. The computational times of the target-oriented inversion with the sequential difference and double difference strategies are 418 s and 431 s, respectively. One can see that by using the target-oriented inversion scheme, the computational cost has been reduced by approximately 80%. Comparison of the inversion results shows that, for both of the sequential and double difference strategies, the results of the target-oriented inversion are slightly better than that of full-model inversion. This can easily be explained. The larger area we have in the inversion, the more errors of the inversion will occur. We can observe from Figs. 8(a) and (c) that for the full-model inversion there are some inversion artefacts outside the target region. This is because the full waveform inversion has the problems of high ill-posedness and nonlinearity. However, the potential artifacts can be avoided in the target-oriented inversion because there is no model update outside the target region.

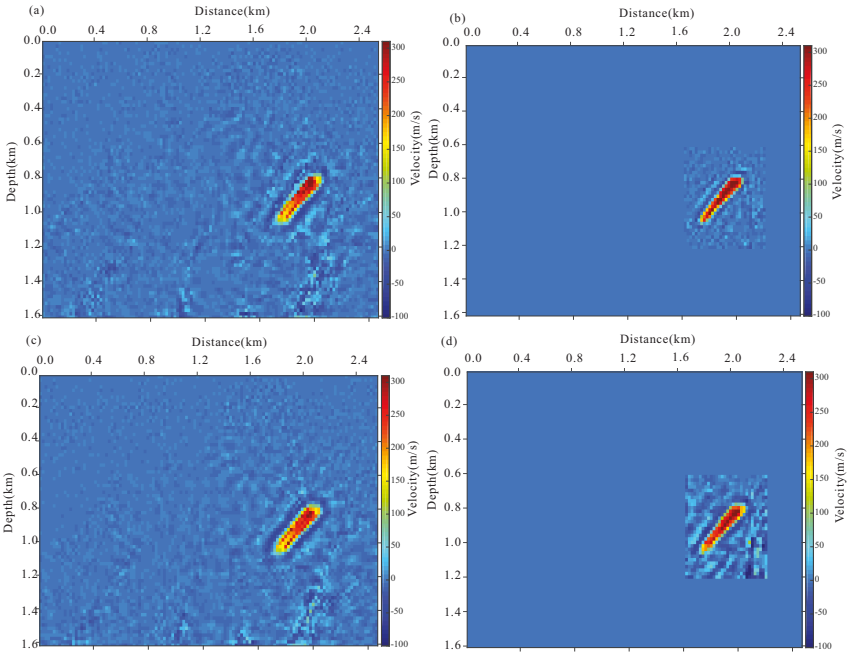

Figure 7: The time-lapse inversion results of the noise-free for a perturbation of 300m/s with the true baseline model as the starting model. (a) The full-model inversion with the sequential difference strategy; (b) the target-oriented inversion with the sequential difference strategy; (c) the full-model inversion with the double difference strategy; (d) the target-oriented inversion with the double difference strategy.

5.2.2 Inversion of noise-free data with the inverted baseline model

In this section, we employ the inverted baseline model of the noise-free data (shown as Fig. 4(b)) as the starting model for the time-lapse inversion and use noise-free data for time-lapse inversion. In this inversion, we use both the sequential difference strategy and double difference strategy as well. Fig. 8 shows the inverted results for the time-lapse inversion using the full-model scheme (Figs. 8(a) and (c)) and target-oriented inversion scheme (Figs. 8(b) and (d)). We also compare the results of the target-oriented inversion and that of the full-model inversion. From Fig. 8, one can make the following observations: (1) whether for the target-oriented inversion or full-model inversion, the results from the double difference strategy are better than that from the sequential difference strategy, which shows that compared with the sequential difference strategy, the double difference strategy works better; (2) for both the sequential difference and double difference strategy, the target-oriented scheme works nearly the same as the full-model scheme. However, the computational cost can be reduced by target-oriented inversion.

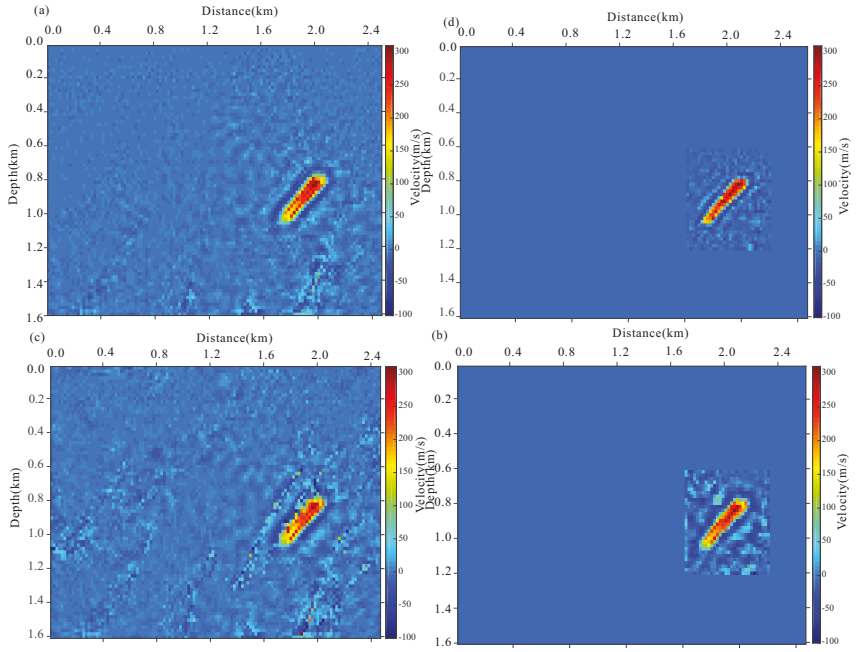

Figure 8: The time-lapse inversion results of noise-free data for a perturbation of 300m/s with the inverted baseline model of noise-free data as the starting model. (a) The full-model inversion with the sequential difference strategy; (b) the target-oriented inversion with the sequential difference strategy; (c) the full-model inversion with the double difference strategy; (d) the target-oriented inversion with the double difference strategy.

The double difference strategy, which inverts with the data difference rather than full-data, requires the starting baseline model that can accurately describe the kinematics and structures, otherwise the time-lapse energy cannot be localized [7].

5.2.3 Inversion of noisy data with the inverted baseline model

To make the numerical experiments more realistic, we perform the numerical tests with the noisy data. Fig. 9 shows the inverted results for the time-lapse inversion of the noisy data (30 dB) using the full-model scheme (Figs. 9(a) and (c)) and target-oriented scheme (Figs. 9 (b) and (d)). Fig. 10 shows the inverted results for the time-lapse inversion of the noisy data (26 dB) using the full-model scheme (Figs. 10(a) and (c)) and target-oriented scheme (Figs. 10(b) and (d)). For the inversion of the noisy data (26 dB), the computational times of the target-oriented inversion with the sequential difference and double difference strategies are 2.01×10^4 s and 2.19×10^4s, respectively. The computational times of the target-oriented inversion with the sequential difference and double difference strategies are 246 s and 602 s, respectively. The computational cost has been reduced from 70

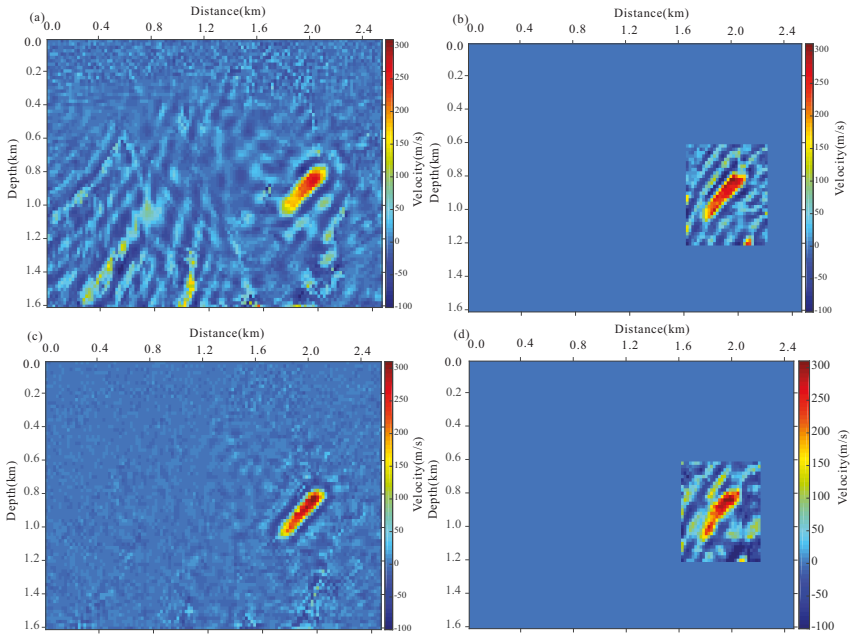

Figure 9: The time-lapse inversion results of noisy data (30dB) for a perturbation of 300m/s with the inverted baseline model using the same noise-level data as the starting model. (a) The full-model inversion with the sequential difference strategy; (b) the target-oriented inversion with the sequential difference strategy; (c) the full-model inversion with the double difference strategy; (d) the target-oriented inversion with the double difference strategy.

% to 80 %. The reason why the computation time is different is that because of the use of different strategies, the computation stops at different iterations for different frequencies. The results in Fig. 10 show clear difference for four numerical experiments from different inversion scheme. For the sequential difference strategy, the inverted time-lapse velocity perturbation from the target-oriented scheme appears more clear, however, the result from the full-model scheme with strong noise is not so clear. The situation improves significantly for the double difference strategy shown in Figs. 10(c) and (d). Also, for the double difference strategy, the results with noisy data from the full-model inversion are slightly better than that from the target-oriented inversion.

Furthermore, we have tested a smaller time-lapse perturbation of 100 m/s. Figs. 11(a) and (b) show the inverted results of noisy data (26 dB) with the double difference and sequential difference strategies. From Figs. 11(a) and (b), one can observe the following features of the inverted time-lapse perturbation: (1) although the time-lapse perturbation can be displayed clearly, there are some artifacts outside the region of time-lapse velocity perturbation; (2) compared with the inverted results of the perturbation of 300 m/s, the

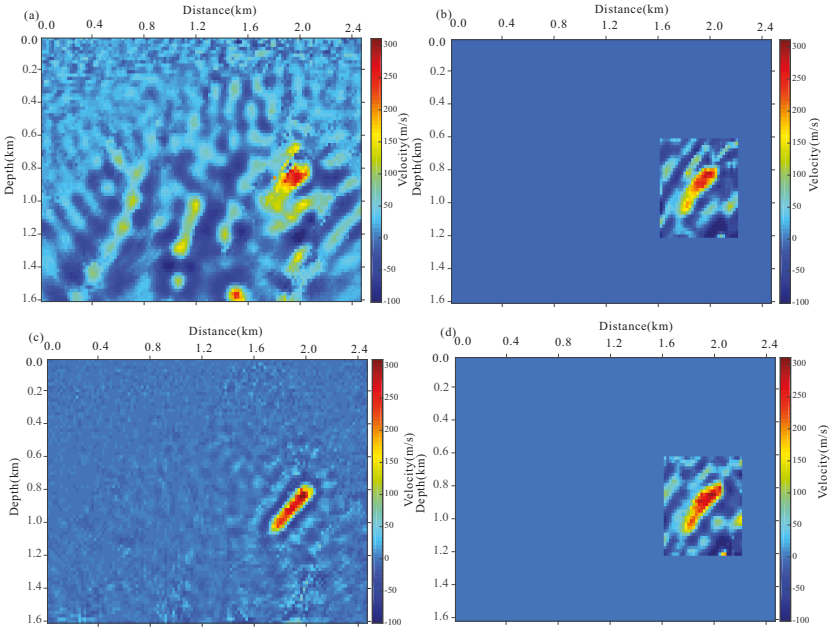

Figure 10: The time-lapse inversion results of noisy data (26dB) for a perturbation of 300m/s with the inverted baseline model using the same noise-level data as the starting model. (a) The full-model inversion with the sequential difference strategy; (b) the target-oriented inversion with the sequential difference strategy; (c) the full-model inversion with the double difference strategy; (d) the target-oriented inversion with the double difference strategy.

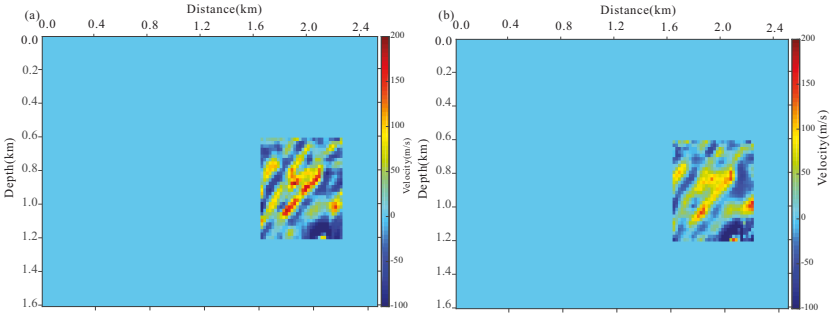

Figure 11: The time-lapse inversion results of noisy data (26dB) for a perturbation of 100m/s with the inverted baseline model using the same noise-level data. (a) The target-oriented inversion with the sequential difference strategy; (b) the target-oriented inversion with the double difference strategy.

inverted results of the perturbation of 100 m/s look less accurate. This indicates that the smaller value of the time-lapse velocity perturbation we have, the more difficult for inversion.

6 Conclusions

Full waveform inversion can be an effective tool for time-lapse seismic data because of its applicability of extracting information on subsurface structure. However, the inversion of the time-lapse seismic waveform data requires to repeat computations for monitor survey. This renders the inversion very expensive for the reservoir monitor. Instead of performing a full-model inversion, we focus on inversion of a target region, where the reservoir changes occur. Jakobsen and Ursin [24] mentioned the possibility of doing T-matrix based time-lapse inversion, but never did this. The main finding is that we have verified that the T-matrix approach is indeed naturally target-oriented and allows one to reduce the computational cost of time-lapse inversion by focusing the inversion on the target-area only. Our approach is based on the DBIT method using the integral equation form. In our scheme, the Gaussian beam has been introduced, which allows to compute the wavefields from the surface to the target region in the smoothed baseline model. Then, by combining the background Green's function using the Gaussian beam with the T-matrix, we obtain the Green's function for the time-lapse inversion. For the local inversion of the target region, the T-matrix is used to update the wavefields within the target region.

Numerical examples are presented, showing that because of the limited size of the target-oriented time-lapse inversion, the computational cost has been reduced by approximately 80%. However, for the double difference strategy, the results with noise-free data from the target-oriented inversion are better than that from the full-model inversion, while the results with noisy data from the full-model inversion are slightly better than that from the target-oriented inversion. That means that the double difference strategy is relatively sensitive to the random noise. For the sequential difference strategy, compared with the results from the full-model inversion, the results of the time-lapse model from the target-oriented inversion are nearly the same. This method should be possible, due to the computational efficiency, to perform a 4-D seismic full waveform inversion. Future works will be also directed toward to a 4-D inversion of the time-lapse waveform data and extended by the domain decomposition method [31].

Acknowledgments

The authors acknowledge the Research Council of Norway for the Petromaks II project 267769 (Bayesian inversion of 4D seismic waveform data for quantitative integration with production data). The third author acknowledges the Research Council of Norway and the industry partners; ConocoPhillips Skandinavia AS, Aker BP ASA, Eni Norge AS,

Maersk Oil Norway AS, Statoil Petroleum AS, Neptune Energy Norge AS, Lundin Norway AS, Halliburton AS, Schlumberger Norge AS, Wintershall Norge AS and DEA Norge AS of The National IOR Centre of Norway for support.

Appendix A: The Green's function using Gaussian beam summation

The Green's function can be computed by a Gaussian beam summation [40,78]

$$G^{(0)}\left(\mathbf{x},\mathbf{x}',\omega\right)=\frac{i}{4\pi}\int\frac{dp_x}{p_z}\mathbf{u}_{GB}\left(\mathbf{x}';\mathbf{x},\mathbf{p};\omega\right), \tag{A.1}$$

where, $\mathbf{x}$ is the source (starting point) position vector, $\mathbf{x}'$ is the subsurface scattering point vector, the ray parameter vector $\mathbf{p}$ is defined by

$$\mathbf{p}=\{p_x,p_z\}, \tag{A.2}$$

where p_x $p_z$are ray parameters, respectively. Further, u_{GB} is a single Gaussian beam [40,41]

$$\begin{aligned}\mathbf{u}_{GB}(q_1,q_2,\tau)&=U^{\Omega}(\tau)\left(\mathbf{det}W\right)^{1/2}\mathbf{exp}\left[-\frac{1}{2}\omega q^T\mathbf{Im}M(\tau)q\right]\\&=\mathbf{exp}\left\{-i\omega\left[t-T(\tau)-\frac{1}{2}q^T\mathbf{Im}M(\tau)q\right]\right\},\end{aligned} \tag{A.3}$$

with

$$W(\tau_0,\tau)=Q_1(\tau_0,\tau)+Q_2(\tau_0,\tau)\left[\mathbf{Re}M(\tau_0)+i\mathbf{Im}M(\tau_0)\right], \tag{A.4}$$

where $T(\tau)$ the traveltime along ray, $Q_1(\tau_0,\tau)$ and $Q_2(\tau_0,\tau)$ are real-valued matrices, which are solutions of the dynamic ray tracing system in matrix form, $q=(q_1,q_2)^T$ and q_1,q_2 are the ray-centred coordinates, which can be constructed along the ray Ω. Moreover $M(\tau_0)$ is the 2×2 complex-valued matrix, which represents the second-order derivatives of the ray traveltime. Following Hill [79,80], the sampling for the horizontal slowness dp_x can be chosen as

$$dp_x=\frac{1}{6l\sqrt{f_{\min},f_{\max}}}, \tag{A.5}$$

where $f_{\min}$ and $f_{\max}$ are the lowest and highest frequencies, respectively. The initial beam width can be chosen as

$$l=\frac{V_{avg}}{f_{\min}}, \tag{A.6}$$

where V_{avg} is the average velocity of the full model.

Appendix B

Algorithm 1 Pseudo code for DBIT inversion algorithm

procedure THE TARGET-ORIENTED INVERSION ALGORITHM OF TIME-LAPSE WAVEFORM DATA USING THE DBIT METHOD WITH THE GAUSSIAN BEAM BASED GREEN'S FUNCTION IS IMPLEMENTED IN THE FOLLOWING PSEUDO CODE

Initialization: define frequency-independent parameters, i.e. convergence condition and initial conditions

m = initial local model;

for $f=1$ **to** $f=N_f$ **do**

$i=0$

$\varepsilon_d=1$

while $\varepsilon >$ TargetDataResidual **do**

$i=i+1$

if $i==1$ **then**

$G_{RS}^{(b)}=G_{RS}^{(0)}+G_{RV}^{(0)}T^{(b)}G_{VS}^{(0)}$

$G_{RV}^{(b)}=G_{RV}^{(0)}+G_{RV}^{(0)}T^{(b)}G_{VV}^{(0)}$

$G_{VS}^{(b)}=G_{VS}^{(0)}+G_{VV}^{(0)}T^{(b)}G_{VS}^{(0)}$

end

$G_{RS}=G_{RS}^{(b)}+G_{RV}^{(b)}TG_{VS}^{(b)}$

$G_{RV}=G_{RV}^{(b)}+G_{RV}^{(b)}TG_{VV}^{(b)}$

$G_{VS}=G_{VS}^{(b)}+G_{VV}^{(b)}TG_{VS}^{(b)}$

dr=DataResidual (G_{RS},f)

J=SensitivityMatrix (G_{RV},G_{VS})

$H=J'J$

end

$\chi=\chi+(\Re(H)+\alpha I)\backslash\Re(J'd)$

$\varepsilon_d=\|u_{monitor}-d_{monitor}\|\,/\,\|d_{monitor}\|$

end while

end for

References

[1] Virieux, J. and Operto, S. An overview of full-waveform inversion in exploration geophysics, Geophysics, 74 (2009), WCC1-WCC26.

[2] Landrø, M., and Stammeijer, J. Quantitative estimation of compaction and velocity changes using 4D impedance and traveltime changes. Geophysics, 69 (2004), 949-957.

[3] Lumley, D. 4D seismic monitoring of CO2 sequestration. The Leading Edge, 29 (2010), 150-155.

[4] Maharramov, M., Biondi, B. L., and Meadows, M. A. Time-lapse inverse theory with applications. Geophysics, 81 (2016), R485-R501.
[5] Zheng, Y., Barton, P., and Singh, S. Strategies for elastic full-waveform inversion of time-lapse ocean bottom cable (OBC) seismic data: 81st Annual International Meeting, SEG, Expanded Abstracts (2011), 4195-4200.
[6] Routh, P., Palacharla, G., Chikichev, I., and Lazaratos, S. Full wavefield inversion of time-lapse data for improved imaging and reservoir characterization: 82nd Annual International Meeting, SEG, Expanded Abstracts, (2012), 1-6.
[7] Asnaashari, A., Brossier, R., Garambois, S., Audebert, F., Thore, P., and Virieux, J. Time-lapse seismic imaging using regularized full waveform inversion with a prior model: which strategy? Geophys. Prospect. 63 (2015), 78-98.
[8] Yang, D., Liu, F., Morton, S., et al. Time-lapse full-waveform inversion with ocean-bottom-cable data: Application on Valhall field. Geophysics 81 (2016), R225-R235.
[9] Kamei, R., and Lumley, D. Full waveform inversion of repeating seismic events to estimate time-lapse velocity changes. Geophysical Journal International, 209 (2017), 1239-1264.
[10] Yuan, S., Fuji, N., Singh, S., and Borisov, D. Localized time-lapse elastic waveform inversion using wavefield injection and extrapolation: 2-D parametric studies. Geophysical Journal International, 209 (2017), 1699-1717.
[11] Tarantola, A., Inversion of seismic reflection data in the acoustic approximation: Geophysics, 34 (1984), 1259-1266.
[12] Tarantola, A., A strategy for nonlinear elastic inversion of seismic reflection data: Geophysics, 51 (1986), 1893-1903.
[13] Oristaglio M. L. and Blok H. Wavefield Imaging and Inversion in Electromagnetics and Acoustics. Cambridge University Press, 2012.
[14] Pike R. and Sabatier P. Scattering and inverse scattering in pure and applied science. Academic Press, 2002.
[15] Weglein, A. B., Araujo, F. V., Carvalho, P. M., Stolt, R. H., Matson, K. H., Coates, R. T., and Zhang, H. Inverse scattering series and seismic exploration. Inverse problems, 19 (2003), R27.
[16] Qu, Y., Li, Z., Huang, J., Li, J., and Guan, Z. Elastic full-waveform inversion for surface topography. Geophysics, 82 (2017), R269-R285.
[17] Hu, Y., Han, L. G., Wu, R. S., Feng, Q. Multi-scale time-frequency domain full waveform inversion with a local correlation-phase misfit function. In SEG Technical Program Expanded Abstracts 2018 (pp. 1058-1062). Society of Exploration Geophysicists.
[18] Clayton, R. W., and Stolt, R. H. A Born-WKBJ inversion method for acoustic reflection data. Geophysics, 46 (1981), 1559-1567.
[19] Cohen, J. K., and Bleistein, N. Velocity inversion procedure for acoustic waves. Geophysics, 44 (1979), 1077-1087.
[20] Weglein, A. B., Boyse, W. E., and Anderson, J. E. Obtaining three-dimensional velocity information directly from reflection seismic data: An inverse scattering formalism. Geophysics, 46 (1981), 1116-1120.
[21] Berkhout, A. J. Seismic resolution: A quantitative analysis of resolving power of acoustical echo techniques (Vol. 12). Geophysical Press, (1984).
[22] Beylkin, G. Imaging of discontinuities in the inverse scattering problem by inversion of a causal generalized Radon transform. Journal of Mathematical Physics, 26 (1985), 99-108.
[23] Stolt, R. H., and Weglein, A. B. Migration and inversion of seismic data. Geophysics, 50 (1985), 2458-2472.

[24] Jakobsen, M. and Ursin, B. Full waveform inversion in the frequency domain using direct iterative T-matrix methods, J. Geophys. Eng., 12 (2015), 400-418.
[25] Tao, Y. and Sen, M. K. Frequency-domain full waveform inversion with a scattering-integral approach and its sensitivity analysis. Journal of Geophysics and Engineering, 10 (2013), 065008.
[26] Wang, Y. M., and Chew, W. C. Accelerating the iterative inverse scattering algorithms by using the fast recursive aggregate T-matrix algorithm. Radio science, 27 (1992), 109-116.
[27] Kouri, D. J., and Vijay, A. Inverse scattering theory: Renormalization of the Lippmann-Schwinger equation for acoustic scattering in one dimension. Physical Review E, 67 (2003), 046614.
[28] Wu, R. S. and Zheng, Y. Nonlinear partial derivative and its DeWolf approximation for nonlinear seismic inversion Geophys. J. Int. 196 (2014), 1827-43.
[29] Jakobsen, M., and Wu, R. S. Renormalized scattering series for frequency-domain waveform modelling of strong velocity contrasts: Geophysical Journal International, 206 (2016), 880-899.
[30] Jakobsen, M., Wu, R. S., Huang, X. Seismic waveform modeling in strongly scattering media using renormalization group theory. In SEG Technical Program Expanded Abstracts 2018 (pp. 5007-5011). Society of Exploration Geophysicists.
[31] Jakobsen, M. and Wu, R. S. Accelerating the T-matrix approach to seismic full-waveform inversion by domain decomposition. Geophysical Prospecting, 66 (2018), 1039-1059.
[32] Wang, B., Jakobsen, M., Wu, R.S., Lu, W. and Chen, X. Accurate and efficient velocity estimation using Transmission matrix formalism based on the decomposition method. Inverse problems, 33 (2017), 035002 (13pp).
[33] Eikrem, K. S., Jakobsen, M. and Nævdal, G. Bayesian Inversion of Time-lapse Seismic Waveform Data Using an Integral Equation Method. In: IOR 2017-19th European Symposium on Improved Oil Recovery, (2017).
[34] Kirchner, A. and Shapiro, S. A. Fast repeat-modelling of time-lapse seismograms. Geophysical prospecting, 49 (2001), 557-569.
[35] Borisov, D., Singh, S. C., and Fuji, N. An efficient method of 3-D elastic full waveform inversion using a finite-difference injection method for time-lapse imaging. Geophysical Journal International, 202 (2015), 1908-1922.
[36] Willemsen, B., Malcolm, A., and Lewis, W. A numerically exact local solver applied to salt boundary inversion in seismic full-waveform inversion. Geophysical Journal International, 204 (2016), 1703-1720.
[37] Malcolm, A., and Willemsen, B. Rapid 4D FWI using a local wave solver. The Leading Edge, 35 (2016), 1053-1059.
[38] Broggini, F., Vasmel, M., Robertsson, J. O., and van Manen, D. J. Immersive boundary conditions: Theory, implementation, and examples. Geophysics, 82 (2017), T97-T110.
[39] Willemsen, B., and Malcolm, A., An efficient coupled acoustic-elastic local solver applied to phase inversion. Geophysics, 82 (2017), R219-R234.
[40] Cerveny, V. Seismic ray theory. Cambridge university press, (2001).
[41] Cerveny, V., Popov M. M., and Psencik, I. Computation of wave fields in inhomogeneous media-Gaussian beam approach. Geophysical Journal International, 70 (1982), 109-128.
[42] Huang, X. and Greenhalgh, S. Linearized formulations and approximate solutions for the complex eikonal equation in orthorhombic media and applications of complex seismic traveltime. Geophysics 83 (2018), C115-C136.
[43] Huang, X. and Sun, H. Numerical modelling of Gaussian beam propagation and diffrac-

tion in inhomogeneous media based on the complex eikonal equation. Acta Geophysica, 4 (2018), 497-508.
[44] Huang, X., Sun, J. and Greenhalgh, S. On the solution of the complex eikonal equation in acoustic VTI media: A perturbation plus optimization scheme. Geophysical Journal International, 214 (2018), 907-932.
[45] Huang, X, Sun, H., and Sun, J. Born modeling for heterogeneous media using the Gaussian beam summation based Green's function. Journal of Applied Geophysics, 131 (2016), 191-201.
[46] Huang, X., Sun, J., and Sun, Z. Local algorithm for computing complex travel time based on the complex eikonal equation. Physical Review E, 93 (2016), 043307.
[47] Huang, X. Extended Beam Approximation for High-Frequency Wave Propagation. IEEE Access, 6 (2018), 37214-37224.
[48] Chew et al. Integral Equation Methods for Electromagnetic and Elastic Waves. San Rafael, CA, USA: Morgan and Claypool, (2008).
[49] Levinson, H.W. and Markel, V. A. Solution to the nonlinear inverse scattering problem by T-matrix completion. I. Theory. Physical Review E 94 (2016a), 043317.
[50] Levinson, H.W. and Markel, V. A. Solution to the nonlinear inverse scattering problem by T-matrix completion. II.Simulations. Physical Review E 94 (2016b), 043318.
[51] March, N.H., Young, W.H. and Sampanthar, S. The Many-Body Problem in Quantum Mechanics. Dover Publications Inc., (1967) New York.
[52] Markel, V. A., and Schotland, J. C. On the convergence of the Born series in optical tomography with diffuse light. Inverse problems 23 (2007), 1445.
[53] Newton, R.G. Scattering Theory of Waves and Particles. Dover Publications Inc., (2002), New York.
[54] Tsang, L., and Kong, J. A.. Multiple scattering of electromagnetic waves by random distributions of discrete scatterers with coherent potential and quantum mechanical formalism. Journal of Applied Physics 51 (1980), 3465-3485.
[55] Gonis, A. and Butler, W. H. Multiple Scattering in Solids. Springer-Verlag, (2000), New York.
[56] Jakobsen, M. T-matrix approach to seismic forward modelling in the acoustic approximation. Studia Geophysica et Geodaetica, 56 (2012), 1-20.
[57] Jakobsen, M., and Hudson J. A. Visco-elastic waves in rock-like composites. Studia Geophysica et Geodaetica 47 (2003), 793-826.
[58] Jakobsen, M., Hudson, J. A., and Johansen T. A. T-matrix approach to shale acoustics. Geophysical Journal International 154 (2003), 533-558.
[59] Morse, P.M. and Feshbach, H. Methods of theoretical physics, (1953), McGraw-Hill New York.
[60] Chew, W. C., and Wang, Y. M. Reconstruction of two-dimensional permittivity distribution using the distorted Born iterative method. IEEE transactions on medical imaging, 9 (1990), 218-225.
[61] Wang, Y. M., and Chew, W. C. Accelerating the iterative inverse scattering algorithms by using the fast recursive aggregate Tmatrix algorithm. Radio science, 27 (1992), 109-116.
[62] Tikhonov, Andrei Nikolaevitch, et al. Numerical methods for the solution of ill-posed problems. Vol. 328. (2013) Springer Science Business Media.
[63] Lavarello R. J. and. Oelze M. L, Density imaging using inverse scattering, J. Acoust. Soc. Am., vol. 125, no. 2, (2009) pp. 793-802.
[64] Hesford, A. J., and Chew, W. C. Fast inverse scattering solutions using the distorted Born

iterative method and the multilevel fast multipole algorithm. The Journal of the Acoustical Society of America, 128 (2010), 679-690.
[65] Hansen, P. C., and O'Leary, D. P. The use of the L-curve in the regularization of discrete ill-posed problems. SIAM Journal on Scientific Computing, 14 (1993), 1487-1503.
[66] Waldhauser, F., and Ellsworth, W. L. A double-difference earthquake location algorithm: Method and application to the northern Hayward fault, California. Bulletin of the Seismological Society of America, 90 (2000), 1353-1368.
[67] Denli, H., and Huang, L. Double-difference elastic waveform tomography in the time domain. SEG Annual Meeting. Society of Exploration Geophysicists, (2009).
[68] Zhang, Z., and Huang, L. Double-difference elastic-waveform inversion with prior information for time-lapse monitoring. Geophysics, 78 (2013), R259-R273.
[69] Tang, Y., Target-oriented wave-equation least-squares migration/inversion with phase-encoded Hessian. Geophysics, 74 (2009), WCA95-WCA107.
[70] Valenciano, A. A., Biondi, B., and Guitton, A. Target-oriented wave-equation inversion. Geophysics, 71 (2006), A35-A38.
[71] Luo, Y., and Schuster, G. T. Bottom-up target-oriented reverse-time datuming: CPS. In SEG Geophysics Conference and Exhibition F (Vol. 55), (2004).
[72] Martin, G.S., Wiley, R. and Marfurt, K.J. Marmousi2: An elastic upgrade for Marmousi. The Leading Edge, 25 (2006), 156-166.
[73] Oristaglio, M. L. and Blok, H. Wavefield Imaging and Inversion in Electromagnetics and Acoustics, Cambridge, Cambridge University Press, (2012).
[74] Remis, R. F. and van den Berg, P. M. On the equivalence of the Newton-Kantorovich and distorted Born iterative methods Inverse Problems, 16 (2000), L1-4.
[75] Métivier, L., Brossier, R., Virieux, J., and Operto, S. Full waveform inversion and the truncated Newton method. SIAM Journal on Scientific Computing 35 (2013): B401-B437.
[76] Pan, W., Kristopher A. Innanen, and W. Liao. Accelerating Hessian-free Gauss-Newton full-waveform inversion via l-BFGS preconditioned conjugate-gradient algorithm. Geophysics 82 (2017), R49-R64.
[77] Yang, D., Zheng, Y., Fehler, M., and Malcolm, A. Target-oriented time-lapse waveform inversion using virtual survey, in 2012 SEG Annual Meeting, Society of Exploration Geophysicists, (2012).
[78] Gray, S. H., Bleistein, N. True-amplitude Gaussian-beam migration. Geophysics, 74 (2009), S11-S23.
[79] Hill, N. R. Gaussian beam migration. Geophysics, 55 (1990), 1416-1428.
[80] Hill, N. R. Prestack Gaussian-beam depth migration. Geophysics, 66 (2001), 1240-1250.
[81] Jakobsen, M., and Tveit, S. Distorted Born iterative T-matrix method for inversion of CSEM data in anisotropic media. Geophysical Journal International. 214 (2018), 1524-1537.

V

BAYESIAN FULL WAVEFORM INVERSION IN ANISOTROPIC ELASTIC MEDIA USING THE ITERATED EXTENDED KALMAN FILTER

Running head: Bayesian full waveform inversion

Bayesian full waveform inversion in anisotropic elastic media using the iterated extended Kalman filter

Xingguo Huang[1], **Kjersti Solberg Eikrem** [2] **Morten Jakobsen** [1 2] **and Geir Nævdal** [2]

[1] *University of Bergen, Department of Earth Science, Allegate 41, 5020 Bergen, Norway.*

Emails: Xingguo.Huang@uib.no

[2] *NORCE Norwegian Research Centre, Postboks 22, 5838 Bergen, Norway.*

(January 17, 2020)

Running head: ***Bayesian seismic full waveform inversion***

ABSTRACT

Uncertainty quantification in the context of seismic imaging is important for interpreting inverted subsurface models and updating reservoir models. The limited illumination, noisy data and poor initial models in the seismic full waveform inversion (FWI) lead to inversion uncertainties. This is particularly true for anisotropic elastic FWI, which suffers from extra parameter trade-off problems. We address the uncertainty quantification of anisotropic elastic FWI problem in the framework of Bayesian inference. Specially, we estimate the uncertainties of the subsurface elastic parameters in the Bayesian anisotropic elastic FWI by combining the iterated extended Kalman filter with an explicit representation of the sensitivity matrix with Green's functions. The sensitivity matrix is based on the integral equation approach, which is also within the context of nonlinear inverse scattering theory. We present the results of numerical tests with examples for anisotropic elastic media. They show that the proposed Bayesian inversion method can provide reasonable reconstructed

results for the elastic coefficients of the stiffness tensor and the framework is suitable for accessing the uncertainties.

INTRODUCTION

Uncertainty quantification of seismic images is important for merging the seismic and production data in the context of history matching of reservoir models. In addition, various factors in the seismic inversion, such as noisy seismic data, nonlinear forward modeling and poor initial models can lead to inversion uncertainties. Thus, uncertainty quantification of velocity fields is clearly essential for interpreting inverted subsurface models. A better understanding and quantification of velocity uncertainties is necessary for making a more justifiable and reliable conclusion on identifying pockets of oil and gas. The full waveform inversion is a popular technique for obtaining high resolution subsurface images by estimating subsurface parameters. Such a method can be used to estimate the velocity uncertainties by finding statistical solutions for the unknown model parameters (Tarantola and Valette, 1982; Gouveia and Scales, 1998; Tarantola, 2005).

Bayesian inference provides a systematic framework for solutions of geophysical inverse problems, which can account for uncertainties. To find the posterior probability distribution of the subsurface model parameters, it is necessary to give a prior probability distribution of the model parameters, which can be velocity, density etc., in the seismic inversion. A critical aspect of the Bayesian inversion is the calculation of the posterior covariance matrix, which is based on the Hessian matrix. Actually, when obtaining the global minimum solution of an optimization problem, the inverse Hessian matrix can be viewed as the posterior covariance matrix. A solution can be obtained within the framework of the linearized approximation, as the problem is nonlinear so the covariance matrix is an approximation (Tarantola, 2005). There are several ways to analyze the uncertainties by means of analyzing the Hessian matrix or utilizing an approximate Hessian. The posterior covariance based on the Hessian was used

to discuss the resolution of seismic inversion (Fichtner and Trampert, 2011a,b), whereas a further application of Bayesian inference to seismic tomography using stochastic probing of the Hessian or resolution operators can be found in Fichtner and Leeuwen (2015). Martin et al. (2012) used the Markov chain Monte Carlo (MCMC) method to obtain the solution of seismic inversion problems in the framework of Bayesian inference, in which the Hessian manipulations were made tractable by a low-rank approximation. There are some reports on estimating the uncertainty for solutions of the linearized infinite-dimensional statistical inverse problems (Bui-Thanh et al., 2013; Petra et al., 2014). Rawlinson et al. (2014) gave a review of uncertainty assessment in the seismic tomography problems. Zhu et al. (2016) described a point spread function method for a priori information from depth migration in the context of Bayesian full waveform inversion. Nawaz and Curtis (2018) applied a Bayesian inversion method to estimate the spatial distribution of geological facies. Zhang et al. (2018a) developed uncertainty estimation in the surface wave tomography.

Advances in seismic full waveform inversion have recently made it possible to estimate velocity uncertainties in the framework of Bayesian full waveform inversion, as an alternative to the classic deterministic optimization methods. Interest in Bayesian full waveform inversion as a method for uncertainty quantification has increased in the past few years due to the development of new computational techniques. Aleardi and Mazzotti (2017) developed a hybrid method that combines the genetic algorithm and a Gibbs sampler to estimate the posterior probability distributions. Ray et al. (2016) presented a promising way to recover the Bayesian posterior model probability density function of subsurface elastic parameters and used it to mitigate the problem of data uncertainty (Ray et al., 2017). The Reversible Jump Hamiltonian Monte Carlo has been successfully applied to uncertainty quantification showing results on the Marmousi model (Sambridge and Mosegaard, 2002;

Mosegaard and Sambridge, 2002; Biswas and Sen, 2017). Fang et al. (2018) presented a method for uncertainty quantification with weak partial-differential-equation constraints. Further, uncertainty assessment in velocity models and images can be found in Ely et al. (2018). Recently, Thurin et al. (2017, 2019) have made significant progress on the original application of ensemble-based Kalman filter method to full waveform inversion and demonstrated impressive results on uncertainty estimation with the Marmousi model. Kotsi et al. (2018) developed the local Bayesian inversion for 4-D time lapse data. Later, Eikrem et al. (2018) developed a method with the iterated extended Kalman filter method for time-lapse seismic full-waveform inversion.

To the best of our knowledge, there is no report in the literature that gives an uncertainty quantification of inverted velocities in the anisotropic elastic medium by means of full waveform inversion. For deterministic FWI, most of the published reconstruction schemes have assumed isotropy of the subsurface medium. Such an assumption is questionable and even not reasonable when dealing with reservoirs with anisotropy, which is due to fine layering (Backus, 1962), aligned fractures (Ali and Jakobsen, 2011; Huang and Greenhalgh, 2019) and aligned clay minerals (Jakobsen and Johansen, 2000; Schoenberg and Sayers, 1995). Generally, it is the potential variation in the velocity with respect to the direction of propagation (Virieux and Operto, 2009; Lee et al., 2010; Plessix and Cao, 2011; Operto et al., 2013; Alkhalifah et al., 2016), which leads to medium anisotropy, that contributes to short and long offset data (Plessix and Cao, 2011). Very few publications have shown the results in the anisotropic situation, only in the acoustic approximation (Plessix and Cao, 2011; Gholami et al., 2013; Alkhalifah and Plessix, 2014; da Silva et al., 2016). This is because solving the anisotropic elastic FWI problem is still a rather challenging task. Although there are a lot of successful applications of acoustic anisotropic FWI, but mainly

in marine data and low frequencies. As frequencies increase the importance of the elastic assumption increases. For describing the wave physics better in such cases, it is better to use the anisotropic elastic medium. Efforts have been made for both anisotropic and elastic FWI in order to consider elastic Earth (Burridge et al., 1998; Lee et al., 2010; Köhn et al., 2015; Kamath and Tsvankin, 2016; Oh and Alkhalifah, 2016; He and Plessix, 2017; Oh and Alkhalifah, 2018; Yang et al., 2018; Jakobsen et al., 2019). However, it is well known that an increase in the number of parameters will further make the non-linear inversion approach more complicated (Tarantola, 1986; Brossier et al., 2009). Also, the lack of low frequencies, the inaccuracy of initial velocity models and noise (Operto et al., 2013) will increase the uncertainty of the inversion.

The aim of this paper is to develop a Bayesian framework for full waveform inversion in anisotropic elastic media for uncertainty quantification. To this end, we apply the Bayesian inference to the earlier elastodynamic generalization of the distorted Born iterative T-matrix (DBIT) method for the anisotropic elastic full waveform inversion (Jakobsen et al., 2019), which is based on the integral equation (IE) method. The integral equation method has several important features: (1) it provides solutions of inverse scattering problems with high-order accuracy, no grid dispersion error, which exists in the numerical differential equation solvers, captures radiation conditions and has a smaller accumulated error (Chew et al., 2008; Djebbi et al., 2016); (2) it requires discretization for the anomalous volume only, which reduces the size of computation, (Malovichko et al., 2017) for the DBIT method, the scattering volume V in the T-matrix formulation is flexible and can be equal to the target area in time-lapse inversion (Huang et al., 2018, 2019a); (3) the sensitivity matrix is expressed explicitly in terms of Green's functions, which is very suitable for the Bayesian framework; (4) the computational cost and convergence problems can also be ad-

dressed by the T-matrix approach using domain decomposition (Jakobsen and Wu, 2018) and renormalization methods (Wu et al., 2015; Osnabrugge et al., 2016; Wu et al., 2016; Jakobsen et al., 2018; Huang et al., 2019b). Further, by employing the iterated extended Kalman filter in the Bayesian framework, the uncertainty characteristics can be exploited simultaneously with the velocity model building.

The iterated extended Kalman filter is a generalization of the Kalman filter (Kalman, 1960). The Kalman filter provides an estimate of the posterior probability density for the state when the data and the dynamical relationships are both linear, and the prior is Gaussian. The extended Kalman filter is an extension of the Kalman filter to nonlinear problems. Because it approximates the nonlinearities using a first-order Taylor expansion around the current estimate, it has become an important tool for state estimation of nonlinear systems. In recent work, Eikrem et al. (2017, 2018) used this method for isotropic FWI. Instead of processing the data sequentially in time, we process the frequencies sequentially, starting with the lowest and end with higher frequencies, which is the same as the multiscale FWI method (Bunks et al., 1995).

In the following, we first review the anisotropic elastic integral equations for the nonlinear scattering problem and their operator formulations. Additionally, we derive the sensitivity matrix in the integral equation method. Then, we present the Bayesian framework and the iterated extended Kalman filter method. The performance of the proposed inversion in the context of full waveform inversion and nonlinear inverse scattering theory is tested on synthetic data sets with increasing complexity, both in three layered and modified Hess models.

BAYESIAN FRAMEWORK FOR FULL WAVEFORM INVERSION

In this section, we give a brief review of Bayesian inference for anisotropic elastic full waveform inversion and use the iterated extended Kalman filter method by connecting the sequential setting in the iterated extended Kalman filter to the sequential strategy in the frequency domain full waveform inversion.

Bayesian inference

The main purpose of this paper is to find the elastic coefficients of stiffness from the observed seismic data by performing Bayesian full waveform inversion in anisotropic elastic media. There are two reasons to choose the Bayesian framework for full waveform inversion. One is that the Bayesian inference can provide an inversion framework for incorporating the uncertainties in prior information, measurements, model parameterization, and forward modeling theory, which can easily be used for solving the full waveform inversion problem, especially for anisotropic elastic full waveform inversion. The other important reason is that the solution of seismic inversion is part of the inputs of joint history matching of seismic and production data. The ensemble-based approach for history matching needs uncertainty information (Aanonsen et al., 2009).

The Bayesian inversion scheme gives a statistical solution of the inverse problem in the form of probability density. In this procedure, a prior density $P(\mathbf{m})$ is chosen for the model parameter $\mathbf{m}$. A likelihood $\mathcal{P}(\mathbf{d} \mid \mathbf{m})$ needs also to be given for the model parameter $\mathbf{m}$ and observation data $\mathbf{d}$. Based on the Bayes' theorem, the mathematical formulation for the posterior distribution can be expressed as

$$\mathcal{P}(\mathbf{m} \mid \mathbf{d}) = \frac{\mathcal{P}(\mathbf{d} \mid \mathbf{m})\,\mathcal{P}(\mathbf{m})}{\int \mathcal{P}(\mathbf{d} \mid \mathbf{m})\,\mathcal{P}(\mathbf{m})\,d\mathbf{m}}, \tag{1}$$

where $\int \mathcal{P}(\mathbf{d} \mid \mathbf{m})\, \mathcal{P}(\mathbf{m})\, d\mathbf{m}$ is the **evidence** (Ray et al., 2017). A common assumption for the Bayesian inversion is that both a priori density and likelihood are Gaussian (Zhang et al., 2018b):

$$\mathcal{P}(\mathbf{m}) \propto \exp\left\{-\frac{1}{2}\left((\mathbf{m}-\mathbf{m}_{\text{prior}})^T \mathbf{C}_M^{-1}(\mathbf{m}-\mathbf{m}_{\text{prior}})\right)\right\}, \tag{2}$$

and

$$\mathcal{P}(\mathbf{d} \mid \mathbf{m}) \propto \exp\left\{-\frac{1}{2}\left((\mathbf{d}-\mathbf{d}_{cal}(\mathbf{m}))^\dagger \mathbf{C}_D^{-1}(\mathbf{d}-\mathbf{d}_{cal}(\mathbf{m}))\right)\right\}, \tag{3}$$

where $\mathbf{m}_{\text{prior}}$ is the prior model that in our case is the initial model in the inversion, and $\mathbf{C}_D$ and $\mathbf{C}_M$ are the data and model covariance matrices, in which the uncertainties in the data and uncertainties related to the subsurface parameters are incorporated, respectively. The symbol † represents the conjugate transpose, $\mathbf{d}$ is the observed data, and $\mathbf{d}_{cal}$ is the calculated data, which is from seismic forward modeling. In our case, $\mathbf{d}_{cal}$ is equivalent to $\delta\mathbf{u}$, which is calculated scattered data.

With nonlinear modeling, this is only an approximation. Combining equations 1-3, we have

$$\begin{aligned}\mathcal{P}(\mathbf{m} \mid \mathbf{d}) \quad \propto \quad & \exp\left\{-\tfrac{1}{2}\left((\mathbf{d}-\mathbf{d}_{cal}(\mathbf{m}))^\dagger \mathbf{C}_D^{-1}(\mathbf{d}-\mathbf{d}_{cal}(\mathbf{m}))\right)\right\} \\ & \exp\left\{-\tfrac{1}{2}\left((\mathbf{m}-\mathbf{m}_{\text{prior}})^T \mathbf{C}_M^{-1}(\mathbf{m}-\mathbf{m}_{\text{prior}})\right)\right\}.\end{aligned} \tag{4}$$

Gouveia and Scales (1998) used a local, nonlinear optimization technique to find the model parameters and then performed a local analysis. The posteriori probability density distribution is approximated by

$$\mathcal{P}(\mathbf{m} \mid \mathbf{d}) \propto \exp\left\{-\frac{1}{2}\left((\mathbf{m}-\mathbf{m}_{\text{map}})^T \widetilde{\mathbf{C}}_M^{-1}(\mathbf{m}-\mathbf{m}_{\text{map}})\right)\right\}, \tag{5}$$

where $\mathbf{m}_{\text{map}}$ is the maximum a posteriori solution that is obtained by the inversion, and the a posteriori covariance matrix is

$$\widetilde{\mathbf{C}}_M = \left(\mathbf{J}^\dagger \mathbf{C}_D^{-1}\mathbf{J} + \mathbf{C}_M^{-1}\right)^{-1}, \tag{6}$$

where $\mathbf{J}$ is the Fréchet derivatives $\mathbf{J} = \frac{\partial \mathbf{d}_{cal}}{\partial \mathbf{m}}$. From the mathematical formulations described in this section, we can observe that one key point for estimating the uncertainties for full waveform inversion is to calculate the Fréchet derivatives and then estimate the covariance matrix.

Iterated extended Kalman filter method

The Kalman filter provides a way to estimate the state of a linear dynamical system from a series of noisy measurements. It is a typical method to solve linear problems with data arriving in batches in time. The seismic data in the full waveform inversion is obtained simultaneously in time, but it can be transformed and processed in batches (van Leeuwen and Herrmann, 2013; Tveit et al., 2016; Thurin et al., 2017; Eikrem et al., 2017, 2018). A generalized version of the Kalman filter, called extended Kalman filter, can be applied to the nonlinear problems . However, the extended Kalman filter uses a first order Taylor expansion around the current estimate status to approximate the nonlinearity. Such an approximation can be questioned for strongly nonlinear cases as Bayesian full waveform inversion. Here we use an iterated extended Kalman filter (Bell and Cathey, 1993; Skoglund et al., 2015), which involves the measurement update repeatedly.

The reason why the iterated extended Kalman filter can be used for Bayesian full waveform inversion in the frequency domain is due to the multi-scale strategy. The multi-scale strategy has been widely used by the seismic community to solve the problem of cycle-skipping in the frequency domain full waveform inversion (Bunks et al., 1995). It relates the large-scale structure and fine-structure by performing inversion from low to high frequency. In this strategy, the inversion for higher frequencies uses the results from lower

frequencies as the starting model. The iterated extended Kalman filter method uses a similar sequential strategy (Eikrem et al., 2018). Thus, it makes sense that the iterated extended Kalman filter method can be extended to anisotropic elastic full waveform inversion.

Taking the similarity between the multi-scale seismic full waveform inversion and the iterated extended Kalman filter method, we start with the prior distribution $\mathcal{P}(\mathbf{m})$, then use equation 4 to update $\mathcal{P}(\mathbf{m} \mid \mathbf{d})$. In the sequential computations, $\mathcal{P}(\mathbf{m} \mid \mathbf{d})$ is the prior for processing the next set of data for the next frequency. A recursive equation for Bayesian full waveform inversion can be written as

$$\mathcal{P}(\mathbf{m} \mid \mathbf{d}_{k,\cdots,1}) \propto \mathcal{P}(\mathbf{d}_k \mid \mathbf{m}) \mathcal{P}(\mathbf{m} \mid \mathbf{d}_{k-1,\cdots,1}). \tag{7}$$

With the assumption that $\mathcal{P}(\mathbf{d}_k \mid \mathbf{m})$ is approximated by a normal distribution with mean $\mathbf{m}_{k-1}$ and covariance $\mathbf{C}_{k-1}$ (Skoglund et al., 2015; Eikrem et al., 2018), we have the recursive form solution for the posterior distribution

$$\begin{aligned} \mathcal{P}(\mathbf{m} \mid \mathbf{d}_{k,\cdots,1}) \quad \propto \quad & \exp\left\{-\tfrac{1}{2}\left((\mathbf{d}_k - \mathbf{d}_{cal}(\mathbf{m}))^{\dagger} \mathbf{C}_{D,k}^{-1} (\mathbf{d}_k - \mathbf{d}_{cal}(\mathbf{m}))\right)\right\} \\ & \exp\left\{-\tfrac{1}{2}\left((\hat{\mathbf{m}}_{k-1} - \mathbf{m})^{T} \mathbf{C}_{M,k-1}^{-1} (\hat{\mathbf{m}}_{k-1} - \mathbf{m})\right)\right\}. \end{aligned} \tag{8}$$

According to Tarantola (2005), the above MAP solutions can be found as

$$\hat{\mathbf{m}}_k = \mathrm{argmin}_{\mathrm{m}} \left((\mathbf{d}_k - \mathbf{d}_{cal}(\mathbf{m}))^{\dagger} \mathbf{C}_{D,k}^{-1} (\mathbf{d}_k - \mathbf{d}_{cal}(\mathbf{m})) + (\hat{\mathbf{m}}_{k-1} - \mathbf{m})^{T} \mathbf{C}_{M,k-1}^{-1} (\hat{\mathbf{m}}_{k-1} - \mathbf{m})\right). \tag{9}$$

Here, we choose the Levenberg-Marquardt iterative extended Kalman filter algorithm (Skoglund et al., 2015) to solve equation (9), the iterative solution is

$$\mathbf{m}^{i+1} = \mathbf{m}^{i} + \left(\mathbf{J}_i^{\dagger} \mathbf{C}_{D,k}^{-1} \mathbf{J}_i + \mathbf{C}_{k-1}^{-1} + \lambda \mathbf{I}\right)^{-1} \left(\mathbf{J}_i^{\dagger} \mathbf{C}_{D,k}^{-1} (\mathbf{d}_k - \mathbf{d}_{cal}(\mathbf{m})) + \mathbf{C}_{M,k-1}^{-1} \left(\mathbf{m}_{k-1} - \mathbf{m}^{i}\right)\right), \tag{10}$$

where λ is a damping factor and $\mathbf{I}$ is the identity matrix. It should be noted that the covariance matrix $\mathbf{C}_{M,k}^{-1} = \mathbf{J}_i^{\dagger} \mathbf{C}_{D,k}^{-1} \mathbf{J}_i + \mathbf{C}_{M,k-1}^{-1}$ is only updated after the new $\hat{\mathbf{m}}_k$ is obtained.

For large λ such as $\lambda = 10^6$, the update is similar to the steepest decent method, and for small λ such as $\lambda = 0.01$, the update is similar to Gauss-Newton method. After each iteration, if the objective function decreases, λ is reduced and if not, it is increased.

DIRECT SCATTERING PROBLEM

The elastodynamic wave equation in the frequency domain can be written as (Aki and Richards, 2002; Cerveny, 2005)

$$\left[\nabla \cdot \mathbf{C}(\mathbf{x}) : \nabla_s - \rho(\mathbf{x})\omega^2 \mathbf{I}\cdot\right] \mathbf{u}(\mathbf{x}) = -\mathbf{S}(\mathbf{x}), \tag{11}$$

where $\mathbf{u}(\mathbf{x})$ is the particle displacement vector at point $\mathbf{x}$, $\mathbf{S}$ is the component of the single-force source, ρ is the mass density, : represents product, ω is the angular frequency, $\mathbf{I}$ is identity matrix and $\mathbf{C}(\mathbf{x})$ is the stiffness tensor component field. In order to derive a volume integral equation for the particle displacement field, we first decompose the stiffness tensor field $\mathbf{C}(\mathbf{x})$ as

$$\mathbf{C}(\mathbf{x}) = \mathbf{C}^{(0)}(\mathbf{x}) + \delta\mathbf{C}(\mathbf{x}), \tag{12}$$

where $\mathbf{C}^{(0)}(\mathbf{x})$ and $\delta\mathbf{C}(\mathbf{x})$ are the stiffness tensors in arbitrary background and perturbed media. It follows from equations (11) and (12) that

$$\left[\nabla \cdot \mathbf{C}^{(0)}(\mathbf{x}) : \nabla_s - \rho(\mathbf{x})\omega^2 \mathbf{I}\right] \mathbf{u}(\mathbf{x}) = -\mathbf{S}(\mathbf{x}) - \nabla \cdot \delta\mathbf{C}(\mathbf{x}) : \epsilon(\mathbf{x}), \tag{13}$$

where $\epsilon(\mathbf{x}) = \nabla_s \mathbf{u}(\mathbf{x})$ is the strain field at point $\mathbf{x}$. By treating the (vectorial contrast-sources) second term on the right-hand side of equation 13 just like ordinary sources and using the concept of Green's functions, we obtain

$$\mathbf{u}(\mathbf{x}) = \mathbf{u}^{(0)}(\mathbf{x}) + \int d\mathbf{x}' \mathbf{G}^{(0)}(\mathbf{x}, \mathbf{x}') \cdot \nabla \cdot \delta\mathbf{C}(\mathbf{x}') : \epsilon(\mathbf{x}'), \tag{14}$$

where

$$\mathbf{u}^{(0)}(\mathbf{x}) = \int d\mathbf{x}' \mathbf{G}^{(0)}(\mathbf{x}, \mathbf{x}') \cdot \mathbf{S}(\mathbf{x}'), \tag{15}$$

and

$$\left[\nabla \cdot \mathbf{C}^{(0)}(\mathbf{x}) : \nabla_s - \rho(\mathbf{x})\omega^2 \mathbf{I} \cdot\right] \mathbf{G}^{(0)}(\mathbf{x}, \mathbf{x}') = -\mathbf{I}\delta(\mathbf{x} - \mathbf{x}'). \tag{16}$$

Here, $\delta(\mathbf{x}-\mathbf{x}')$ is the Dirac delta function, $\mathbf{u}^{(0)}(\mathbf{x})$ is the wavefield in the reference model due to the vectorial source field $\mathbf{S}(\mathbf{x}')$, and $\mathbf{G}^{(0)}(\mathbf{x}, \mathbf{x}')$ is the reference medium Green's function and the domain of integration is the whole domain. If the medium is homogeneous, one can compute the background Green's function analytically; if the medium is inhomogeneous, one can compute the background Green's function using the ray theory based method (Cerveny, 2005; Huang et al., 2016; Huang, 2018; Huang and Greenhalgh, 2018, 2019) or finite difference method (Fichtner, 2010) or the generalized T-matrix approach of Jakobsen et al. (2015).

From equation 14, one can observe that the equation involves the derivates of the stiffness perturbation tensor. By means of partial integration symmetries of the elastic stiffness tensor, the equation can be reformulated as

$$\mathbf{u}(\mathbf{x}) \quad = \quad \mathbf{u}^{(0)}(\mathbf{x}) + \int_D d\mathbf{x}' \mathbf{M}^{(0)}(\mathbf{x}, \mathbf{x}') : \delta\mathbf{C}(\mathbf{x}') : \epsilon(\mathbf{x}'). \tag{17}$$

Here, we have introduced the third-rank tensor $\mathbf{M}^{(0)}(\mathbf{x}, \mathbf{x}')$, which is defined by the following tensor components (Jakobsen and Hudson, 2003):

$$M^{(0)}_{ijk}(\mathbf{x}, \mathbf{x}') = -\frac{1}{2}\left(\frac{\partial G^{(0)}_{ij}(\mathbf{x}, \mathbf{x}')}{\partial x_k} + \frac{\partial G^{(0)}_{ik}(\mathbf{x}, \mathbf{x}')}{\partial x_j}\right). \tag{18}$$

By taking spatial derivatives of equation 17 at position $\mathbf{x}$, one can show that the strain field also satisfies an integral equation of the Lippmann-Schwinger type:

$$\epsilon(\mathbf{x}') = \epsilon^{(0)}(\mathbf{x}') + \int_D d\mathbf{x}'' \Gamma^{(0)}(\mathbf{x}', \mathbf{x}'') : \delta\mathbf{C}(\mathbf{x}'') : \epsilon(\mathbf{x}''), \tag{19}$$

where the components of the fourth-rank tensor $\Gamma^{(0)}(\mathbf{x}', \mathbf{x}'')$ are defined by Jakobsen and Hudson, 2003 and Jakobsen et al., 2003

$$\Gamma^{(0)}_{ijkl}(\mathbf{x}, \mathbf{x}') = \frac{1}{4}\left(\frac{\partial^2 G^{(0)}_{ij}(\mathbf{x}, \mathbf{x}')}{\partial x_k \partial x'_l} + \frac{\partial^2 G^{(0)}_{ik}(\mathbf{x}, \mathbf{x}')}{\partial x_j \partial x'_l} + \frac{\partial^2 G^{(0)}_{ij}(\mathbf{x}, \mathbf{x}')}{\partial x_l \partial x'_k} + \frac{\partial^2 G^{(0)}_{ji}(\mathbf{x}, \mathbf{x}')}{\partial x_l \partial x'_k}\right). \quad (20)$$

Thus, one can calculate the particle displacement vector field at any point by first solving the integral equation 19 for the strain field, and then use the result in conjunction with the integral equation 17. Jakobsen et al. (2015) present a more general integral equation formulation that also allows for density perturbations (see also Jakobsen and Hudson, 2003).

The two coupled integral equations 17 and 19 can be rewritten exactly as

$$\mathbf{u}(\mathbf{x}) = \mathbf{u}^{(0)}(\mathbf{x}) + \int_D d\mathbf{x}_1 \int_D d\mathbf{x}_2 \mathbf{M}^{(0)}(\mathbf{x}, \mathbf{x}_1) : \mathbf{V}(\mathbf{x}_1, \mathbf{x}_2) : \epsilon(\mathbf{x}_2), \quad (21)$$

and

$$\epsilon(\mathbf{x}) = \epsilon^{(0)}(\mathbf{x}) + \int_D d\mathbf{x}_1 \int_D d\mathbf{x}_2 \Gamma^{(0)}(\mathbf{x}, \mathbf{x}_1) : \mathbf{V}(\mathbf{x}_1, \mathbf{x}_2) : \epsilon(\mathbf{x}_2), \quad (22)$$

where

$$\mathbf{V}(\mathbf{x}_1, \mathbf{x}_2) = \delta\mathbf{C}(\mathbf{x}_1)\delta(\mathbf{x}_1 - \mathbf{x}_2), \quad (23)$$

is a non-local stiffness perturbation.

The two coupled integral equations 21-22 can be written as the real-space coordinate representation of the following integral operator equations:

$$u = u^{(0)} + M^{(0)} V \epsilon, \quad (24)$$

and

$$\epsilon = \epsilon^{(0)} + \Gamma^{(0)} V \epsilon. \quad (25)$$

Clearly, the main problem here is to determine the strain field, since the particle displacement field is given explicitly by the integral 24 when ϵ is known. The integral equation 25

for the strain field is similar to the Lippmann-Schwinger equation in quantum scattering theory. This is an agreeable feature because it allows us to modify the well analyzed iterative or perturbation methods that have been developed to solve scattering and inverse scattering problems in quantum physics for seismic use (Zuberi and Alkhalifah, 2014). The full integral equation method based on scattering theory can address all the wavefields, e.g. multiple scattering. The integral equation method is also used for full waveform inversion (Abubakar et al., 2012; Jakobsen and Wu, 2018). Jakobsen and Wu (2016) demonstrated that the finite difference is equivalent to the full integral equation method.

FRÉCHET DERIVATIVES

An important method to formulate the Fréchet derivatives in this work is the distorted Born iterative method (Jakobsen and Ursin, 2015). The nonlinear inverse scattering problem in anisotropic elastic media is based on the distorted Born iterative method and solves for stiffness tensor from measurements of the displacement-strain. This method uses an iterative scheme in which we compute the Green's functions and update the scattering potential in each iteration. The relation between the displacement-strain state vector for the variation in the scattering potential using the distorted Born approximation (Chew and Wang, 1990; Jakobsen and Ursin, 2015; Jakobsen and Wu, 2018):

$$u - u^{(i)} \approx M^{(i)} \left(V - V^{(i)} \right) \epsilon^{(i)}, \tag{26}$$

where $V^{(i)}$ is the updated scattering potential in the inhomogeneous background medium, i is the number of iterations and $u^{(i)}$ and $\epsilon^{(i)}$ in inhomogeneous background media are

$$u^{(i)} = u^{(0)} + M^{(0)} V^{(i)} \epsilon^{(i)}, \tag{27}$$

$$\epsilon^{(i)} = \epsilon^{(0)} + \Gamma^{(0)} V^{(i)} \epsilon^{(i)}, \tag{28}$$

and

$$M^{(i)} = M^{(0)} + M^{(i)} V^{(i)} \Gamma^{(0)}. \tag{29}$$

The details on the derivation of M can be found in Appendix A. Another exact approach to update the $u^{(i)}$ and $\epsilon^{(i)}$ for each iteration is the T-matrix approach, which can be found in Appendix B. The main advantage of using the distorted Born iterative method to formulate the Fréchet derivatives is that it gives the Fréchet derivatives in terms of the modified Green's function and strain field, which can be easily applied to the iterative extended Kalman filter for Bayesian seismic full waveform inversion.

The data residual equation in the real-space coordinate representation is

$$u_k(\mathbf{r}) - u_k^{(i)}(\mathbf{r}) = \int d\mathbf{x} M_{kL}^{(i)}(\mathbf{r}, \mathbf{x}) \left[\Delta C_{LM}^{(i+1)}(\mathbf{x}) - \Delta C_{LM}^{(i)}(\mathbf{x}) \right] \epsilon_M^{(i)}(\mathbf{x}), \tag{30}$$

in the abbreviated sub-script notation, where repeated upper case indices runs from 1 to 6. Here, we have also used Einstein's summation convention and the definition of stiffness and mass density perturbations, $\mathbf{r}$ is the receiver position vector, k is index of components and i is the number of iteration. Equation (30) can be expressed more compactly as

$$\delta u_k^{(i)}(\mathbf{r}) = \int d\mathbf{x} M_{kL}^{(i)}(\mathbf{r}, \mathbf{x}) \, \delta C_{LM}^{(i+1)}(\mathbf{x}) \, \epsilon_M^{(i)}(\mathbf{x}), \tag{31}$$

where $\delta u_k^{(i)}(\mathbf{r}) = u_k(\mathbf{r}) - u_k^{(i)}(\mathbf{r})$ is the data residual wavefield at the ith iteration and $\delta C_{LM}^{(i+1)}(\mathbf{x})$ is the difference in the stiffness (mass density) between the current and following iterations. The next step is to decompose the mass density and stiffness model perturbations as

$$\delta C_{LM}^{(i+1)}(\mathbf{x}) \equiv \Delta C_{LM}^{(i+1)}(\mathbf{x}) - \Delta C_{LM}^{(i)}(\mathbf{x}), \tag{32}$$

with

$$\Delta C_{LM}(\mathbf{x}) = \sum_{p=1}^{21} B_{LM}^{(p)}(\mathbf{x}) \, m^{(p)}(\mathbf{x}), \tag{33}$$

where $m^{(p)}(\mathbf{x})$ represents the perturbation in one of the 21 elastic constants, which is a scalar, and $B_{LM}^{(p)}$ represents the tensor field related to the model (elastic) parameter $m^{(p)}$. The B-matrices in equation 33 associated with different elastic parameters depend on the parameterization of the model. In this study, we parameterize the model by using perturbations in the elastic stiffness elements that are normalized to the corresponding properties in an isotropic reference medium. More specifically, we use the following expression for the normalized stiffness perturbations

$$m^{(p)} = \frac{\left(C_{LM} - C_{LM}^{(0)}\right)}{C_{LM}^{(0)}}, \tag{34}$$

and a similar expression for the normalized mass density perturbations. By using model parameter perturbations that are normalized in this way, we ensure that the different model parameter perturbations are of approximately similar range, which is an advantage for multi-parameter FWI. It follows from equation 30 that

$$\delta u_k^{(i)}(\mathbf{r}) = \sum_{p=1}^{21} \int d\mathbf{x} J_k^{(i,p)}(\mathbf{r},\mathbf{x})\, \delta m^{(i+1,p)}(\mathbf{x}), \tag{35}$$

where the full set of scalar and vectorial Fréchet derivatives after the i th iteration is given by

$$J_k^{(i,p)}(\mathbf{r},\mathbf{x}) = M_{kL}^{(i)}(\mathbf{r},\mathbf{x})\, B_{LM}^{(p)}(\mathbf{x})\, \epsilon_M^{(i)}(\mathbf{x}). \tag{36}$$

After a discretization of the seismic model involving N_r receivers and N grid blocks, equation (35) can be expressed as

$$\delta \mathbf{u}^{(i)} = \sum_{p=1}^{21} \mathbf{J}^{(i,p)} \delta \mathbf{m}^{(i+1,p)}, \tag{37}$$

where $\mathbf{m}^{(i+1,p)}$ represents the inverted perturbation in the pth model parameter relative to a static reference medium, whereas $\delta \mathbf{m}^{(i,p)}$ is the variation of this quantity between two successive iterations. It should be noted that dimensions in the summation should

not include p. Here, $\dim\left(\delta\mathbf{u}^{(i)}\right) = 3N_r$, $\dim\left(\mathbf{J}^{(i,p)}\right) = 3N_r \times 21N$ and $\dim\left(\delta\mathbf{m}^{(i+1,p)}\right) = 21N \times 21N$, which is an explicit matrix. It should be noted that in the numerical examples, we use VTI media. Thus, $\dim\left(\mathbf{J}^{(i,p)}\right) = 3N_r \times 5N$ and $\dim\left(\delta\mathbf{m}^{(i+1,p)}\right) = 5N \times 5N$. Then, we rewrite equation (27) into matrix form as

$$\delta\mathbf{u}^{(i)} = \mathbf{J}^{(i)}\delta\mathbf{m}^{(i+1)}, \tag{38}$$

where

$$\mathbf{J}^{(i)} = \left(\mathbf{J}^{(i,1)}, \mathbf{J}^{(i,2)} \cdots, \mathbf{J}^{(i,21)}\right)^T, \tag{39}$$

and

$$\delta\mathbf{m}^{(i)} = \left(\delta\mathbf{m}^{(i,1)}, \delta\mathbf{m}^{(i,2)} \cdots, \delta\mathbf{m}^{(i,21)}\right), \tag{40}$$

are block-matrices of Fréchet-derivatives and model parameters, respectively.

This work reports a Bayesian full waveform inversion based on integral equation method with iterated extended Kalman filter. A key aspect is that performing Bayesian inversion using iterated extended Kalman filter requires the Fréchet-derivatives 39 utilizing integral equations 24 and 25. In other words, inserting equation 39 into equation 10 leads to the formulation for inversion.

NUMERICAL RESULTS

Noisy data are an important source of the uncertainties in seismic full waveform inversion. To make the data represent realizations of the uncertainty, we add complex Gaussian noise to the synthetic data. The definition of signal to noise ratio S_N is as follows (Eikrem

et al., 2018):

$$S_N = \frac{\|\mathbf{d}\|^2}{\|\mathbf{w}\|^2}, \tag{41}$$

where $\mathbf{d}$ is the data in the frequency domain and $\mathbf{w}$ is the noise, which can be estimated from the data. The desired signal to noise ratio S_N is obtained by scaling it in the following way

$$\mathbf{d}_{noise} = \mathbf{d} + \frac{\|\mathbf{d}\|}{\sqrt{\left(S_N \mathrm{E}\left(\|\mathbf{w}\|^2\right)\right)}}\mathbf{w}, \tag{42}$$

where E is the expectation.

Three-layered model

To validate our Bayesian inversion approach, we have carried out the numerical experiments on a three-layer VTI model in which there are five independent Voigt stiffness parameters C_{11}, C_{33}, C_{55}, C_{13} and C_{66} perturbations shown in Figure 1. Table 1 shows the values of Voigt stiffness parameters of the three-layered model. The model size is 875 m $\times$ 350 m. The size of each grid cell is 25 m $\times$25 m. We employ 14 sources and 35 receivers, which are both located at the surface and distributed uniformly from 0 m to 875 m. We employ a Ricker wavelet with a central frequency of 7.5 Hz. We use the seismic forward modeling method described in Jakobsen et al. (2019) to generate the dataset. We use all three components of the particle displacement vector at the surface as data. In this example, we use the sequential frequency inversion scheme, which inverts frequency by frequency. Here, we choose frequencies of 4 Hz, 5 Hz, 6 Hz, ..., 20 Hz, and start by inverting the lowest frequency. We start with a large λ in the first iteration for the first frequency to make the first step small. We use the initial value in the first iteration for the first frequency as $\lambda = 10,000$ and reduced it by a factor of 2 after each iteration. For other

frequencies, we start with $\lambda = 100$ and change it by a factor of 10. For this experiment, the prior mean model is a homogeneous isotropic elastic medium. The background Green's functions in such media are computed by analytic methods. The initial mean (the values of the initial model) for the inversion is zero. In this model, a strongly anisotropic VTI medium is sandwiched between two weakly anisotropic VTI media.

Figure 2 show the a priori model covariance matrix and a priori covariance matrix for one parameter (the order from upper part to lower part on the diagonal line is C_{11}, C_{33}, C_{55}, C_{13} and C_{66}). The covariance matrix for the prior distribution was constructed from an exponential variogram with a practical range of 5 grid blocks vertically and horizontally. The practical range for an exponential variogram is defined as the distance where 95% of the sill is reached (Eikrem et al., 2018). The covariance matrix was scaled to be 1.0 or 0.5 on the diagonal. Figure 3 shows the maximum a posteriori solution (Example 1), Figure 4 shows a posteriori standard deviation, Figure 5 the full posterior covariance matrix (the order from upper part to lower part on diagonal line is C_{11}, C_{33}, C_{55}, C_{13} and C_{66}) and Figure 6 shows the error (difference between the inverted model and the true model) of maximum a posteriori solution with noisy data with a signal to noise ratio of 4. From Figure 3, one can observe that the inverted results are very similar to the true model. That means that the anisotropic model can be recovered by the proposed approach despite the fact that the multiparameter reconstruction with noisy data is challenging. From Figure 6, one can observe that in the region close to the edges of the model and sharp boundaries, the errors involved are relatively large.

Figure 7 shows the maximum a posteriori solution (mean) using the same model with the experiment shown in Figure 3 except that the a priori covariance matrix is obtained by multiplying 0.5 with the covariance matrix (Example 2). Figure 8 shows a posteriori

standard deviation, Figure 9 shows the full posterior covariance matrix and Figure 10 shows the error of the maximum a posteriori solution with noisy data with a signal to noise ratio of 4. An exponential variogram with a practical range of 5 grid blocks vertically and horizontally is used to construct the covariance matrix for the prior distribution. From the results shown in Figure 7, the similar observation can be made with Figure 3. We observe that the a posteriori standard deviation is reduced as a consequence of the reduction in the a priori standard deviation.

A subset of Hess model

To make the numerical experiments more realistic, we perform the inversion on a subset of SEG Hess model, shown in Figure 11. We use the same model size, number of sources and receivers, source with Ricker wavelet as the previous example. Here, we choose the same frequencies as the previous example and invert in an increased order. For each frequency, the maximum number of iterations is 20 in the iterated extended Kalman filter method. For this experiment, the prior mean model is the same as the one used in the previous example.

Figure 12 shows the maximum a posteriori solution (Example 3), Figure 13 shows the posteriori standard deviation, Figure 14 shows the full covariance matrix and Figure 15 shows the error of mean (maximum a posteriori solution) with noisy data with a signal to noise ratio of 4. We use the same prior distribution as shown in Figure 2. The standard deviations are the square root of the diagonal of the covariance matrices. Figure 12 shows that the Bayesian full waveform inversion method in this paper can give reasonable results in anisotropic elastic cases. From the results shown in Figure 13, one can observe that compared with the uncertainties shown in the prior covariance matrix, the a posteriori

standard deviation shows that the uncertainties have been reduced significantly. However, different parameters show different degrees of uncertainty.

It is interesting to see the results for uncertainty estimation using different prior covariance matrices. Figure 16 shows the results with the same cases as Figure 13 but with a different prior covariance matrix, which is the same prior distribution as shown in Figure 2 (Example 4). From Figure 17, one can observe that there are smaller uncertainties compared with the results shown in Figure 13 since the smaller values of the prior covariance matrix are used. From the posteriori covariance matrices shown in Figures 14 and 18, one can observe that C_{13} has correlation with C_{11} and C_{33}, which is consistent with the deterministic anisotropic full waveform inversion that the anisotropic inversion is highly sensitive to C_{13} (Lee et al., 2010). On the other hand, C_{55} has much smaller relation with other elastic stiffness parameters. That means that very little parameter trade-off would exist (Operto et al., 2013; Kazei and Alkhalifah, 2019) for the Bayesian inversion of this parameters. We also test the method in the resampled SEG Hess model, shown in Figure 20. Figure 21 shows the maximum a posteriori solution (Example 5), Figure 22 shows the posteriori standard deviation, and Figure 23 shows the error of mean (maximum a posteriori solution) with noisy data with a signal to noise ratio of 4. One can observe that the model can be well reconstructed.

DISCUSSION

Analysis and interpretation of the multiparameter Hessian matrix

The exact Hessian involves the superposition of the correlatation of the first-order and second-order partial derivatives with respect to the data residuals, which is related to the

first-order and second-order scattering (Pan et al., 2016). In our approach, $\mathbf{J}^{\dagger}\mathbf{C}_D^{-1}\mathbf{J}$ is similar to the Gauss Newton Hessian (Pratt et al., 1998), the element of the Hessian in our approach is formed by correlating two Fréchet derivative wavefields at the receivers, which is an approximate Hessian, meaning that we ignore the second-order influence. However, we construct the approximate Hessian matrix explicitly. The main difference between our scattering integral approach and the conventional adjoint state method with finite difference method is that we have an explicit representation of the sensitivity matrix in terms of Green's functions, that can easily be updated after each iteration using the variational T-matrix approach.

Application of the Hessian matrix as as the inverse Hessian operator is equivalent to the posterior covariance of the minimization problem when the solution is close to the global minimum. Fichtner and Trampert (2011) provided the interpretation of the Hessian in terms of the inverse posterior covariance in the Bayesian framework sense. Since the approximate Hessian is used in this work, it cannot account for strongly non-linear relation between the model parameters and the seismic data.

Computational cost

We use the distorted Born iterative method to construct the sensitivity matrix, which is expressed explicitly in terms of Green's functions based on the integral equations. The relation between the displacement-strain state vector for the variation in the scattering potential is constructed using the distorted Born approximation. The sensitivity matrix can easily be updated after each iteration using the variational T-matrix approach. After each iteration, the sensitivity matrix is updated. Actually, it has been demonstrated

that the Distorted Born iterative method is consistent with the Gauss-Newton methods of optimization (see Remis and van den Berg, 2003, Oristaglio and Blok, 2012, Jakobsen and Ursin, 2015). Currently, the Green's functions are based on the full integral equation solution of the wave equation (exact solution of Lippmann-Schqinger type equation), which is relatively costly although in principle, the method can be applied to large scale models. A potential extension for efficient computation of Green's functions is to use the iterative solution of the Lippmann-Schwinger equation. As discussed by Osnabrugge et al., (2016), the operation of Green's function with contrast-source terms has a convolution structure that can be implemented more efficiently by using the wave vector representation; that is, by using the Fast Fourier Transform (FFT) algorithm. This is because convolution in real-space is equivalent to multiplication in the Fourier space, and the computational cost of the FFT-operation is much smaller than that of matrix multiplication and inversion.The memory requirements scales like N^2 and N when using the position and wave vector representations, respectively. The computational cost should theoretically scale like N^3 and $N\log N$ when using the position and wave vector representations, respectively. The iterative solution with FFT implementation is much faster and can be used for practical large-scale problems (Huang et al., 2019; Jakobsen et al., 2019).

Uncertainty analysis

The main difference in uncertainty analysis between the isotropic case and the proposed multiparameter case is that the covariance matrix in multiparameter case can indicate how errors are correlated between pairs of model parameters. The uncertainty is described by the model covariance, which shows that uncertainty in the data leads to uncertainty in the estimated model parameters. In multiparameter uncertainty analysis, the covariance matrix

is a square symmetric matrix, whose off-diagonal entries indicate how errors are correlated between pairs of model parameters and the diagonal entries show the variance of corresponding parameters, such as the influence of data noise. Another important application of the covariance is that the off-diagonal entries indicate strong trade-offs in the variables.

The inverted C_{55} is better than others. This is because C_{55} is related to S-wave, which leads to higher resolution due to the shorter wavelength (Zhang et al., 2018). From the perspective of radiation patterns of different elastic parameters (Wu and Aki, 1985; Tarantola, 1986; Virieux et al., 2009), the S-wave has more low-wavenumber components than that of P-waves. The low-wavenumber components have stronger amplitudes and prevent from the inversion getting trapped in a local minimum (Virieux et al., 2009; Liu and Peter, 2019).

The standard deviation is the square root of the diagonal of the covariance matrices. One can observe that the standard deviation increases with depth. The fact that the uncertainty increases with the depth is particularly noticeable for both the layered model and a subset of hess model tests. This can be explained by wave propagation theory, the geometrical spreading effect. According to the physical interpretation of the Hessian (Pratt et al., 1998), its energy decreases with the increase of depth due mainly to the geometrical spreading effect. Whereas high uncertainty values are concentrated in the region of relatively high perturbation, the values of the uncertainty is particularly large near the boundary and in the region of the perturbation interface. This is because the wave path will bend in the region of high perturbation.

Multiparameter trade-off quantification

The posterior covariance obtained by Kalman filter method in the Bayesian framework provides a direct measure of trade-off in the anisotropic elastic full waveform inversion. Actually, the diagonal element of the posterior covariance defines the local resolution in the full waveform inversion and off-diagonal blocks provide the measure of trade-off of the multi-parameter full waveform inversion. In the inversion, it can be observed that the posterior covariance shows correlation between C_{11} and C_{33}, which is consistent with the deterministic anisotropic full waveform inversion that the anisotropic inversion is highly sensitive to C_{13} our data are not independently sensitive to it, and probably there is a combination with C_{11} and C_{33} that SVD can highlight in the linear sense, that has a relative independence of influence on the data (Kazei and Alkhalifah, 2019). On the other hand, C_{55} has much smaller relation with other elastic stiffness parameters.

In any case, by employing the iterated extended Kalman filter in the Bayesian framework, the uncertainty characteristics can be exploited simultaneously with the velocity model building. Uncertainty quantification in full waveform inversion is important for interpretation of the inversion results. There is still a need for further development because currently, our Bayesian inversion methods are not applicable to large scale FWI problem. All these issues need to be investigated in the future research.

CONCLUSIONS

We have presented a new Bayesian inference framework for full waveform inversion and estimation of the uncertainties in anisotropic elastic media, in which the integral equations in the context of nonlinear inverse scattering and iterated extended Kalman filter are used.

Using the integral equation approach based on scattering theory enables us to easily construct the explicit sensitivity matrix in the covariance matrix in terms of Green's functions. The iterated extended Kalman filter method can be frequency friendly because the multi-scale full waveform inversion in the frequency domain uses a sequential strategy, which is very similar with the data assimilation process in the iterated extended Kalman filter. The Bayesian full waveform inversion involves a full covariance matrix, which is used to describe the uncertainty.

Synthetic results are presented, showing that the Bayesian full waveform inversion framework is suitable for the anisotropic elastic medium, in which the independent Voigt stiffness parameters are reconstructed. Specifically, despite of the fact that the prior mean is far from the true model, and noisy data with anisotropic elastic model is used, the reconstruction can provide an acceptable solution. A posteriori standard deviation provides uncertainty quantification in the Bayesian full waveform inversion. The next steps will be directed to efficient methods with applications on real data.

REFERENCES

Aanonsen, S. I., G. Nævdal, D. S. Oliver, A. C. Reynolds, B. Vallès, et al., 2009, The ensemble Kalman filter in reservoir engineering–a review: SPE Journal, **14**, 393–412.

Abubakar, A., M. Li, Y. Lin, and T. Habashy, 2012, Compressed implicit Jacobian scheme for elastic full-waveform inversion: Geophysical Journal International, **189**, 1626–1634.

Aki, K., and P. G. Richards, 2002, Quantitative seismology.

Aleardi, M., and A. Mazzotti, 2017, 1D elastic full-waveform inversion and uncertainty estimation by means of a hybrid genetic algorithm–Gibbs sampler approach: Geophysical Prospecting, **65**, 64–85.

Ali, A., and M. Jakobsen, 2011, On the accuracy of Rüger's approximation for reflection coefficients in HTI media: implications for the determination of fracture density and orientation from seismic AVAZ data: Journal of Geophysics and Engineering, **8**, 372–393.

Alkhalifah, T., N. Masmoudi, and J.-W. Oh, 2016, A recipe for practical full-waveform inversion in orthorhombic anisotropy: The Leading Edge, **35**, 1076–1083.

Alkhalifah, T., and R.-É. Plessix, 2014, A recipe for practical full-waveform inversion in anisotropic media: An analytical parameter resolution study: Geophysics, **79**, R91–R101.

Backus, G. E., 1962, Long-wave elastic anisotropy produced by horizontal layering: Journal of Geophysical Research, **67**, 4427–4440.

Bell, B. M., and F. W. Cathey, 1993, The iterated Kalman filter update as a Gauss-Newton method: IEEE Transactions on Automatic Control, **38**, 294–297.

Biswas, R., and M. Sen, 2017, 2D full-waveform inversion and uncertainty estimation using the reversible jump Hamiltonian Monte carlo, *in* SEG Technical Program Expanded Abstracts 2017: Society of Exploration Geophysicists, 1280–1285.

Brossier, R., S. Operto, and J. Virieux, 2009, Seismic imaging of complex onshore struc-

tures by 2D elastic frequency-domain full-waveform inversion: Geophysics, **74**, WCC105–WCC118.

Bui-Thanh, T., O. Ghattas, J. Martin, and G. Stadler, 2013, A computational framework for infinite-dimensional Bayesian inverse problems Part i: The linearized case, with application to global seismic inversion: SIAM Journal on Scientific Computing, **35**, A2494–A2523.

Bunks, C., F. M. Saleck, S. Zaleski, and G. Chavent, 1995, Multiscale seismic waveform inversion: Geophysics, **60**, 1457–1473.

Burridge, R., M. V. de Hoop, D. Miller, and C. Spencer, 1998, Multiparameter inversion in anisotropic elastic media: Geophysical Journal International, **134**, 757–777.

Cerveny, V., 2005, Seismic ray theory: Cambridge university press.

Chew, W. C., M. S. Tong, and B. Hu, 2008, Integral equation methods for electromagnetic and elastic waves: Synthesis Lectures on Computational Electromagnetics, **3**, 1–241.

Chew, W. C., and Y.-M. Wang, 1990, Reconstruction of two-dimensional permittivity distribution using the distorted Born iterative method: IEEE transactions on medical imaging, **9**, 218–225.

da Silva, N. V., A. Ratcliffe, V. Vinje, and G. Conroy, 2016, A new parameter set for anisotropic multiparameter full-waveform inversion and application to a North Sea data set: Geophysics, **81**, U25–U38.

Djebbi, R., R.-É. Plessix, and T. Alkhalifah, 2016, Analysis of the traveltime sensitivity kernels for an acoustic transversely isotropic medium with a vertical axis of symmetry: Geophysical prospecting, **65**, 22–34.

Eikrem, K. S., G. Nævdal, and M. Jakobsen, 2018, Iterated extended Kalman filter method for time-lapse seismic full-waveform inversion: Geophysical Prospecting, **67**, 379–394.

Eikrem, K, S., M. Jakobsen, and G. Nævdal, 2017, Bayesian inversion of time-lapse seismic waveform data using an integral equation method: Presented at the IOR 2017-19th European Symposium on Improved Oil Recovery.

Ely, G., A. Malcolm, and O. V. Poliannikov, 2018, Assessing uncertainties in velocity models and images with a fast nonlinear uncertainty quantification method: Geophysics, **83**, R63–R75.

Fang, Z., C. Da Silva, R. Kuske, and F. J. Herrmann, 2018, Uncertainty quantification for inverse problems with weak partial-differential-equation constraints: Geophysics, **83**, R629–R647.

Fichtner, A., 2010, Full seismic waveform modelling and inversion: Springer Science & Business Media.

Fichtner, A., and T. v. Leeuwen, 2015, Resolution analysis by random probing: Journal of Geophysical Research: Solid Earth, **120**, 5549–5573.

Fichtner, A., and J. Trampert, 2011a, Hessian kernels of seismic data functionals based upon adjoint techniques: Geophysical Journal International, **185**, 775–798.

———, 2011b, Resolution analysis in full waveform inversion: Geophysical Journal International, **187**, 1604–1624.

Gholami, Y., R. Brossier, S. Operto, A. Ribodetti, and J. Virieux, 2013, Which parameterization is suitable for acoustic vertical transverse isotropic full waveform inversion? Part 1: Sensitivity and trade-off analysis: Geophysics, **78**, R81–R105.

Gouveia, W. P., and J. A. Scales, 1998, Bayesian seismic waveform inversion: Parameter estimation and uncertainty analysis: Journal of Geophysical Research: Solid Earth, **103**, 2759–2779.

He, W., and R.-É. Plessix, 2017, Analysis of different parameterisations of waveform inver-

sion of compressional body waves in an elastic transverse isotropic Earth with a vertical axis of symmetry: Geophysical Prospecting, **65**, 1004–1024.

Huang, X., 2018, Extended beam approximation for high-frequency wave propagation: IEEE Access, **6**, 37214–37224.

Huang, X., and S. Greenhalgh, 2018, Linearized formulations and approximate solutions for the complex eikonal equation in orthorhombic media and applications of complex seismic traveltime: Geophysics, **83**, C115–C136.

———, 2019, Traveltime approximation for strongly anisotropic media using the homotopy analysis method: Geophysical Journal International, **216**, 1648–1664.

Huang, X., M. Jakobsen, K. S. Eikrem, and G. Nævdal, 2018, A target-oriented scheme for efficient inversion of time-lapse seismic waveform data, *in* SEG Technical Program Expanded Abstracts 2018: Society of Exploration Geophysicists, 5352–5356.

Huang, X., M. Jakobsen, G. Naevdal, and K. S. Eikrem, 2019a, Target-oriented inversion of time-lapse seismic waveform data: Communications in Computational Physics, doi: 10.4208/cicp.OA–2018–0143.

Huang, X., M. Jakobsen, and R.-S. Wu, 2019b, Taming the divergent terms in the scattering series of Born by renormalization: SEG Technical Program Expanded Abstracts 2019, In press.

Huang, X., J. Sun, and Z. Sun, 2016, Local algorithm for computing complex travel time based on the complex eikonal equation: Physical Review E, **93**, 043307.

Jakobsen, M., E. Ivan, Psencik, Iversen, and B. Ursin, 2019, Transition operator approach to seismic full-waveform inversion in arbitrary anisotropic elastic media: Communications in Computational Physics, in press.

Jakobsen, M., and T. A. Johansen, 2000, Anisotropic approximations for mudrocks: A

seismic laboratory study: Geophysics, **65**, 1711–1725.

Jakobsen, M., and B. Ursin, 2015, Full waveform inversion in the frequency domain using direct iterative T-matrix methods: Journal of Geophysics and Engineering, **12**, 400.

Jakobsen, M., and R. Wu, 2016, Renormalized scattering series for frequency-domain waveform modelling of strong velocity contrasts: Geophysical Journal International, **206**, 880–899.

Jakobsen, M., and R.-S. Wu, 2018, Accelerating the T-matrix approach to seismic full-waveform inversion by domain decomposition: Geophysical Prospecting, **66**, 1039–1059.

Jakobsen, M., R.-S. Wu, and X. Huang, 2018, Seismic waveform modeling in strongly scattering media using renormalization group theory: SEG Technical Program Expanded Abstracts 2018, **1**, 5007–5011.

Kalman, R. E., 1960, A new approach to linear filtering and prediction problems: Journal of basic Engineering, **82**, 35–45.

Kamath, N., and I. Tsvankin, 2016, Elastic full-waveform inversion for VTI media: Methodology and sensitivity analysis: Geophysics, **81**, C53–C68.

Kazei, V., and T. Alkhalifah, 2019, Scattering radiation pattern atlas: What anisotropic elastic properties can body waves resolve?: Journal of Geophysical Research: Solid Earth, **124**, 2781–2811.

Köhn, D., O. Hellwig, D. De Nil, and W. Rabbel, 2015, Waveform inversion in triclinic anisotropic media-a resolution study: Geophysical Journal International, **201**, 1642–1656.

Kotsi, M., A. Malcolm, and G. Ely, 2018, 4D full-waveform metropolis hastings inversion using a local acoustic solver, *in* SEG Technical Program Expanded Abstracts 2018: Society of Exploration Geophysicists, 5323–5327.

Lee, H.-Y., J. M. Koo, D.-J. Min, B.-D. Kwon, and H. S. Yoo, 2010, Frequency-domain

elastic full waveform inversion for VTI media: Geophysical Journal International, **183**, 884–904.

Malovichko, M., N. Khokhlov, N. Yavich, and M. Zhdanov, 2017, Approximate solutions of acoustic 3D integral equation and their application to seismic modeling and full-waveform inversion: Journal of Computational Physics, **346**, 318–339.

Martin, J., L. C. Wilcox, C. Burstedde, and O. Ghattas, 2012, A stochastic Newton MCMC method for large-scale statistical inverse problems with application to seismic inversion: SIAM Journal on Scientific Computing, **34**, A1460–A1487.

Mosegaard, K., and M. Sambridge, 2002, Monte Carlo analysis of inverse problems: Inverse problems, **18**, R29.

Nawaz, M. A., and A. Curtis, 2018, Variational bayesian inversion (vbi) of quasi-localized seismic attributes for the spatial distribution of geological facies: Geophysical Journal International, **214**, 845–875.

Oh, J.-W., and T. Alkhalifah, 2016, Elastic orthorhombic anisotropic parameter inversion: An analysis of parameterization elastic orthorhombic anisotropic FWI: Geophysics, **81**, C279–C293.

———, 2018, Optimal full-waveform inversion strategy for marine data in azimuthally rotated elastic orthorhombic media: Geophysics, **83**, R307–R320.

Operto, S., Y. Gholami, V. Prieux, A. Ribodetti, R. Brossier, L. Metivier, and J. Virieux, 2013, A guided tour of multiparameter full-waveform inversion with multicomponent data: From theory to practice: The Leading Edge, **32**, 1040–1054.

Osnabrugge, G., S. Leedumrongwatthanakun, and I. M. Vellekoop, 2016, A convergent Born series for solving the inhomogeneous Helmholtz equation in arbitrarily large media: Journal of computational physics, **322**, 113–124.

Pan, W., K. A. Innanen, G. F. Margrave, M. C. Fehler, X. Fang, and J. Li, 2016, Estimation of elastic constants for HTI media using Gauss-Newton and full-Newton multiparameter full-waveform inversion: Geophysics, **81**, R275–R291.

Petra, N., J. Martin, G. Stadler, and O. Ghattas, 2014, A computational framework for infinite-dimensional Bayesian inverse problems, Part ii: Stochastic Newton MCMC with application to ice sheet flow inverse problems: SIAM Journal on Scientific Computing, **36**, A1525–A1555.

Plessix, R.-E., and Q. Cao, 2011, A parametrization study for surface seismic full waveform inversion in an acoustic vertical transversely isotropic medium: Geophysical Journal International, **185**, 539–556.

Rawlinson, N., A. Fichtner, M. Sambridge, and M. K. Young, 2014, Seismic tomography and the assessment of uncertainty, *in* Advances in Geophysics: Elsevier, **55**, 1–76.

Ray, A., S. Kaplan, J. Washbourne, and U. Albertin, 2017, Low frequency full waveform seismic inversion within a tree based Bayesian framework: Geophysical Journal International, **212**, 522–542.

Ray, A., A. Sekar, G. M. Hoversten, and U. Albertin, 2016, Frequency domain full waveform elastic inversion of marine seismic data from the Alba field using a bayesian trans-dimensional algorithm: Geophysical Journal International, **205**, 915–937.

Sambridge, M., and K. Mosegaard, 2002, Monte Carlo methods in geophysical inverse problems: Reviews of Geophysics, **40**, 3–1.

Schoenberg, M., and C. M. Sayers, 1995, Seismic anisotropy of fractured rock: Geophysics, **60**, 204–211.

Skoglund, M. A., G. Hendeby, and D. Axehill, 2015, Extended Kalman filter modifications based on an optimization view point: 2015 18th International Conference on Information

Fusion (Fusion), IEEE, 1856–1861.

Tarantola, A., 1986, A strategy for nonlinear elastic inversion of seismic reflection data: Geophysics, **51**, 1893–1903.

———, 2005, Inverse problem theory and methods for model parameter estimation: SIAM, **89**.

Tarantola, A., and B. Valette, 1982, Generalized nonlinear inverse problems solved using the least squares criterion: Reviews of Geophysics, **20**, 219–232.

Thurin, J., R. Brossier, and L. Métivier, 2017, An ensemble-transform Kalman filter: Full-waveform inversion scheme for uncertainty estimation, *in* SEG Technical Program Expanded Abstracts 2017: Society of Exploration Geophysicists, 1307–1313.

———, 2019, Ensemble-based uncertainty estimation in full waveform inversion: Geophysical Journal International, **219**, 1613–1635.

Tveit, S., T. Mannseth, and M. Jakobsen, 2016, Discriminating time-lapse saturation and pressure changes in CO2 monitoring from seismic waveform and csem data using ensemble-based bayesian inversion, *in* SEG Technical Program Expanded Abstracts 2016: Society of Exploration Geophysicists, 5485–5489.

van Leeuwen, T., and F. J. Herrmann, 2013, Fast waveform inversion without source-encoding: Geophysical Prospecting, **61**, 10–19.

Virieux, J., and S. Operto, 2009, An overview of full-waveform inversion in exploration geophysics: Geophysics, **74**, WCC1–WCC26.

Wu, R.-S., J. Luo, and G. Chen, 2016, Seismic envelope inversion and renormalization group theory: Nonlinear scale separation and slow dynamics, *in* SEG Technical Program Expanded Abstracts 2016: Society of Exploration Geophysicists, 1346–1351.

Wu, R.-S., B. Wang, and C. Hu, 2015, Renormalized nonlinear sensitivity kernel and in-

verse thin-slab propagator in T-matrix formalism for wave-equation tomography: Inverse Problems, **31**, 115004.

Yang, Q., A. Malcolm, H. Rusmanugroho, and W. Mao, 2018, Analysis of radiation patterns for optimized full waveform inversion in fluid-saturated porous media: Geophysical Journal International, **216**, 1919–1937.

Zhang, X., A. Curtis, E. Galetti, and S. de Ridder, 2018a, 3-D Monte Carlo surface wave tomography: Geophysical Journal International, **215**, 1644–1658.

Zhang, Z.-d., T. Alkhalifah, E. Z. Naeini, and B. Sun, 2018b, Multiparameter elastic full waveform inversion with facies-based constraints: Geophysical Journal International, **213**, 2112–2127.

Zhu, H., S. Li, S. Fomel, G. Stadler, and O. Ghattas, 2016, A Bayesian approach to estimate uncertainty for full-waveform inversion using a priori information from depth migration: Geophysics, **81**, R307–R323.

Zuberi, M., and T. Alkhalifah, 2014, Generalized internal multiple imaging (gimi) using feynman-like diagrams: Geophysical Journal International, **197**, 1582–1592.

Table 1: Values of three-layered model

Layer	C_{11}	C_{33}	C_{55}	C_{13}	C_{66}
1	0.0296	-0.0630	0.0889	-0.3556	0.0889
2	0.2519	-0.1889	-0.3333	-0.1111	-0.3333
3	0.1519	-0.1222	0.0667	-0.5778	0.0667

MODIFIED GREEN'S FUNCTIONS

It follows from equations (11) and (12) that the corresponding integral operator equations for Green's functions can be expressed as

$$G = G^{(0)} + M^{(0)} V N \tag{A-1}$$

and

$$N = N^{(0)} + \Gamma^{(0)} V N. \tag{A-2}$$

The integral equation (A.2) for the N-tensor has the following exact formal solution:

$$N = \left(I - \Gamma^{(0)} V \right)^{-1} N^{(0)}. \tag{A-3}$$

By inserting the exact formal solution (A.3) into equation (A.1) for modified Green's function, we have

$$G = G^{(0)} + M^{(0)} V \left(I - \Gamma^{(0)} V \right)^{-1} N^{(0)}. \tag{A-4}$$

It follows from equation (A.4) and the identity (Jakobsen et al., 2019)

$$V \left(I - \Gamma^{(0)} V \right)^{-1} = \left(I - V \Gamma^{(0)} \right)^{-1} V, \tag{A-5}$$

then we get

$$G = G^{(0)} + M V N^{(0)}, \tag{A-6}$$

where

$$M = M^{(0)} \left(I - V \Gamma^{(0)} \right)^{-1} \tag{A-7}$$

is the solution of the following integral equation for M-tensor:

$$M = M^{(0)} + M V \Gamma^{(0)}. \tag{A-8}$$

Thus, the two coupled integral equations (A.1) and (A.2) are equivalent to the two coupled integral equations (A.6) and (A.8). For the inversion, equations (A.3) and (A.8) can be used to update the N and M-tensors after each iteration.

T-MATRIX PERSPECTIVE

In this Appendix, we give the formulations for updating Green's functions in the T-matrix representation. The two coupled integral equations (11-12) can be interpreted as the real-space coordinate representation of the following integral operator equations:

$$u = u^{(0)} + M^{(0)} V \epsilon \tag{A-9}$$

and

$$\epsilon = \epsilon^{(0)} + \Gamma^{(0)} V \epsilon. \tag{A-10}$$

Following the standard approach of potential scattering theory (Taylor, 1972; Jakobsen and Hudson, 2003; Jakobsen, 2012; Jakobsen and Ursin, 2015), we now introduce the transition operator (or T-matrix)) T by

$$V\epsilon = T\epsilon^{(0)}, \tag{A-11}$$

It follows from equation (B.1) that

$$u = u^{(0)} + M^{(0)} T \epsilon^{(0)}, \tag{A-12}$$

where

$$T = V + V\Gamma^{(0)} T. \tag{A-13}$$

Thus, we have eliminated the strain field from the equations and reduced the problem to the determination of the transition operator T, that we have a long experience with from both rock physics and seismic full waveform inversion (e.g., Jakobsen and Hudson, 2003; Jakobsen and Ursin, 2015). Here, $u^{(i)}$ and $\epsilon^{(i)}$ in inhomogeneous background media can be updated by

$$u^{(i)} = u^{(0)} + M^{(0)} T^{(i)} \epsilon^{(0)}, \tag{A-14}$$

and

$$\epsilon^{(i)} = \epsilon^{(0)} + \Gamma^{(0)} T^{(i)} \epsilon^{(0)}, \tag{A-15}$$

where the T-matrix is

$$T^{(i)} = \left(I - V^{(i)} \Gamma^{(i)} \right)^{-1} V^{(i)}. \tag{A-16}$$

LIST OF FIGURES

17 Example 4: The posteriori standard deviation.

18 Example 4: The full covariance matrix.

19 Example 4: The error of maximum a posteriori solution with noisy data with a signal to noise ratio of 4.

20 A resampled Hess model.

21 Example 5: The maximum a posteriori solution.

22 Example 5: The posteriori standard deviation.

23 Example 5: The error of maximum a posteriori solution with noisy data with a signal to noise ratio of 4.

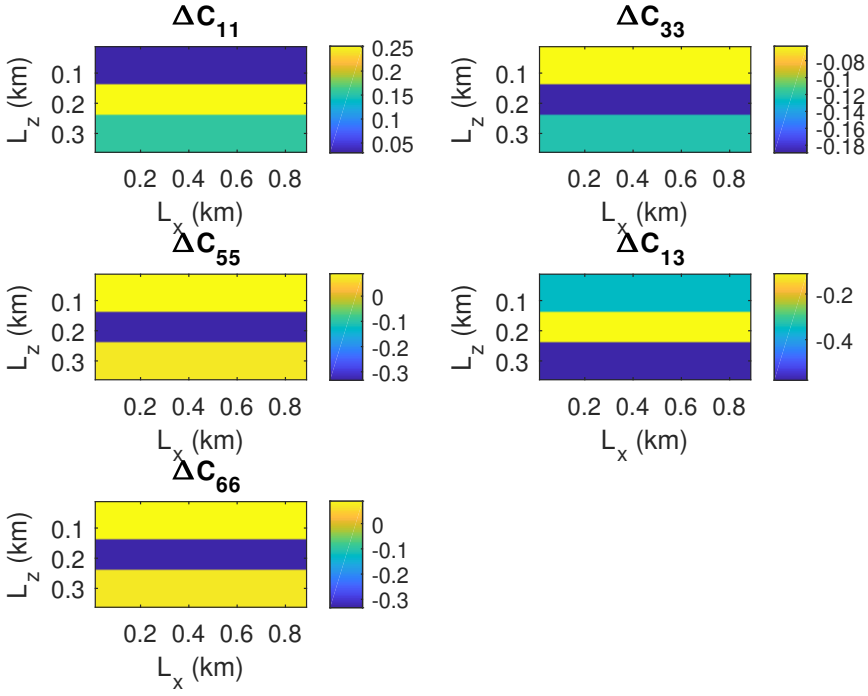

Figure 1: A three-layered anisotropic elastic model. The size of the model is 0.875km×0.35km.

–

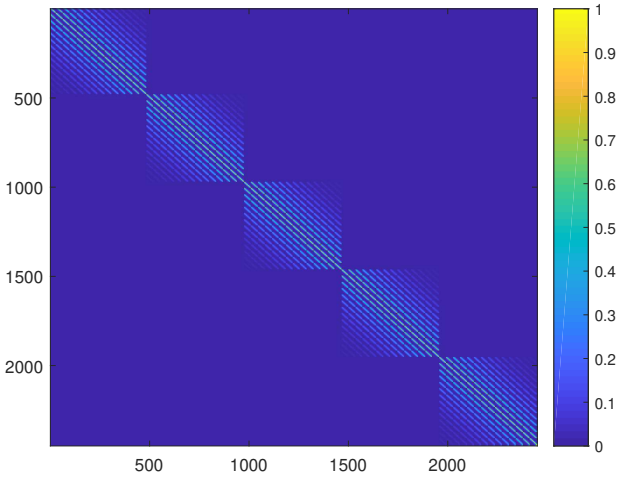

(a)

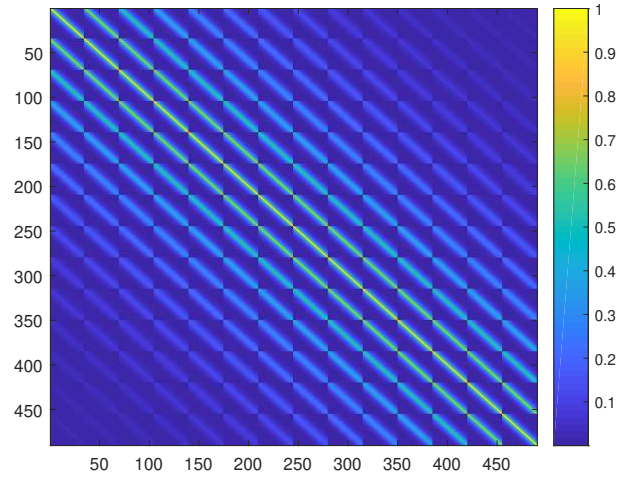

(b)

Figure 2: (a) The full a priori model covariance matrix. (b) A priori covariance matrix for one of the parameters.

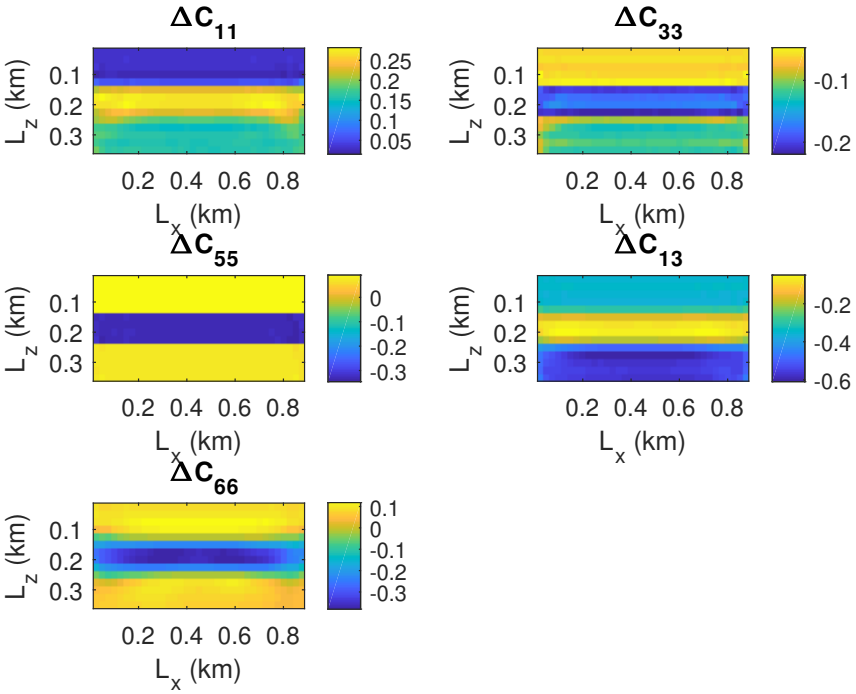

Figure 3: Example 1: The maximum a posteriori solution.

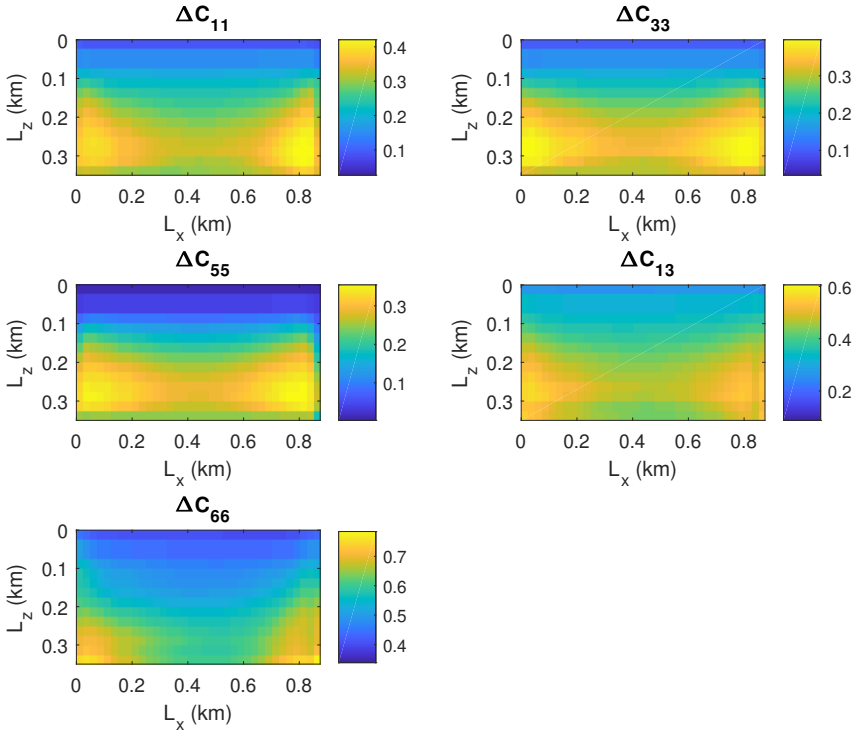

Figure 4: Example 1: The posteriori standard deviations.

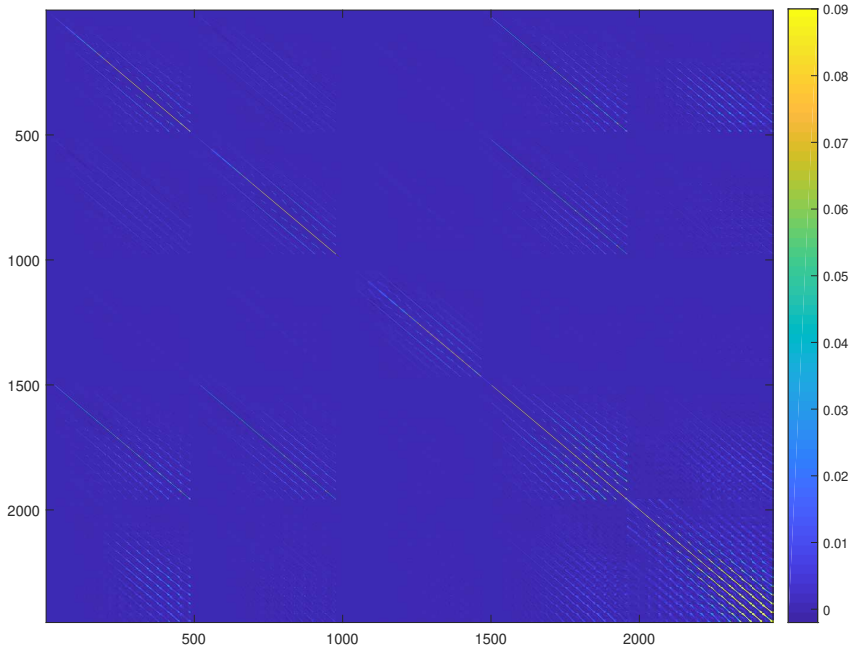

Figure 5: Example 1: The full a posteriori covariance matrix (The order from upper part to lower part on diagonal line is C_{11}, C_{33}, C_{55}, C_{13} and C_{66}).

–

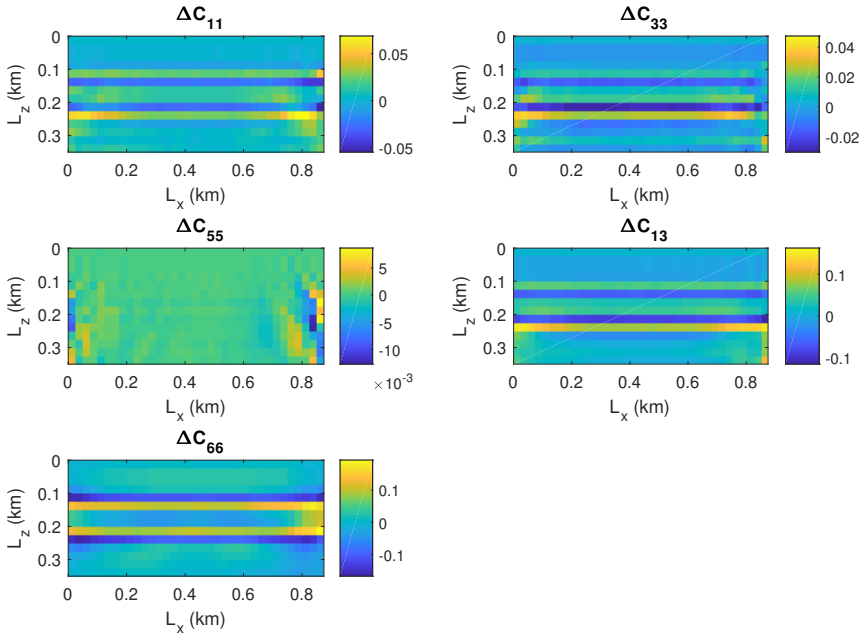

Figure 6: Example 1: The error of maximum a posteriori solution with noisy data with a signal to noise ratio of 4.

–

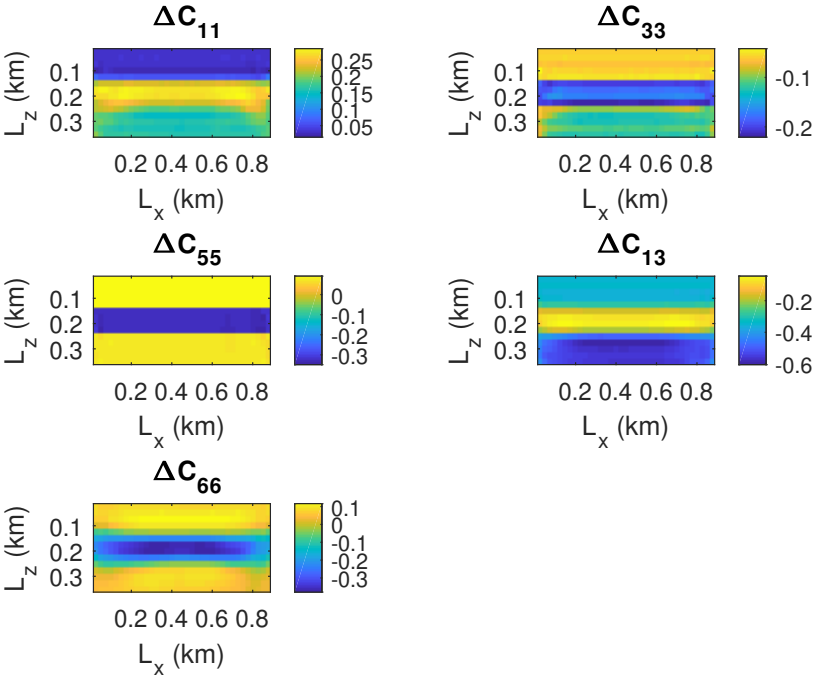

Figure 7: Example 2: The maximum a posteriori solution.

–

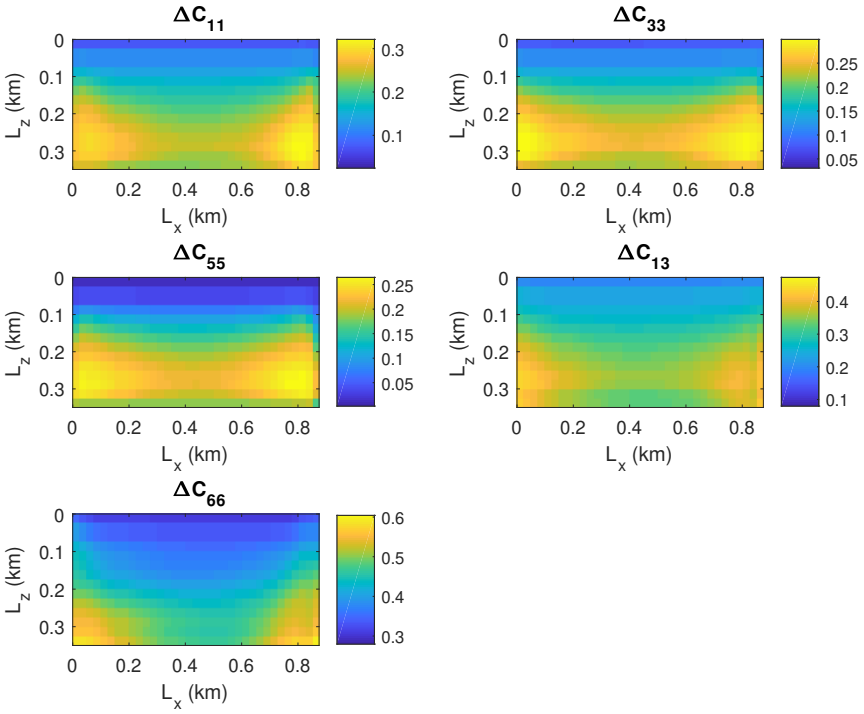

Figure 8: Example 2: The posteriori standard deviation.

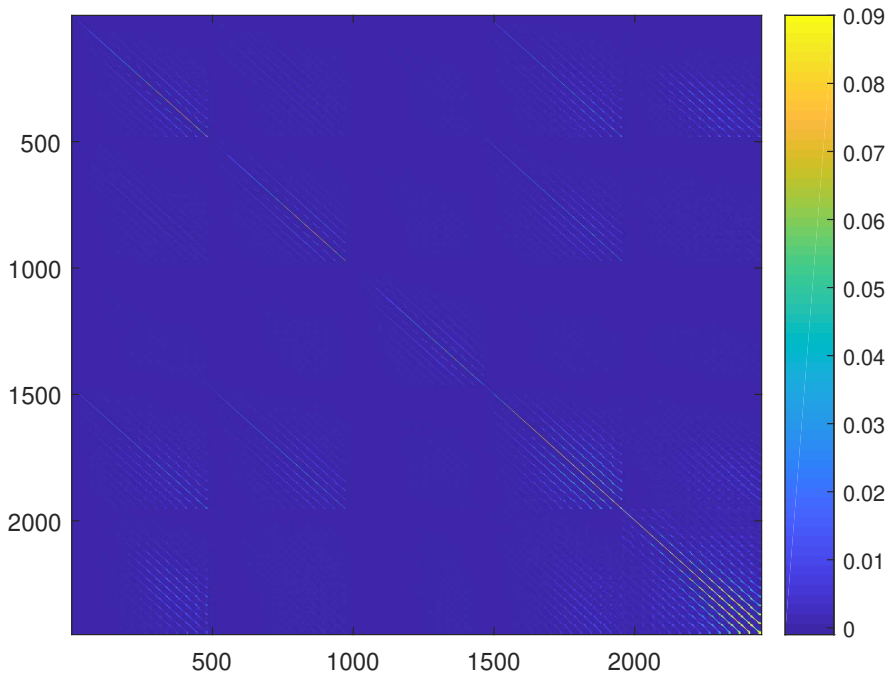

Figure 9: Example 2: The full covariance matrix (The order from upper part to lower part on diagonal line is C_{11}, C_{33}, C_{55}, C_{13} and C_{66}).

–

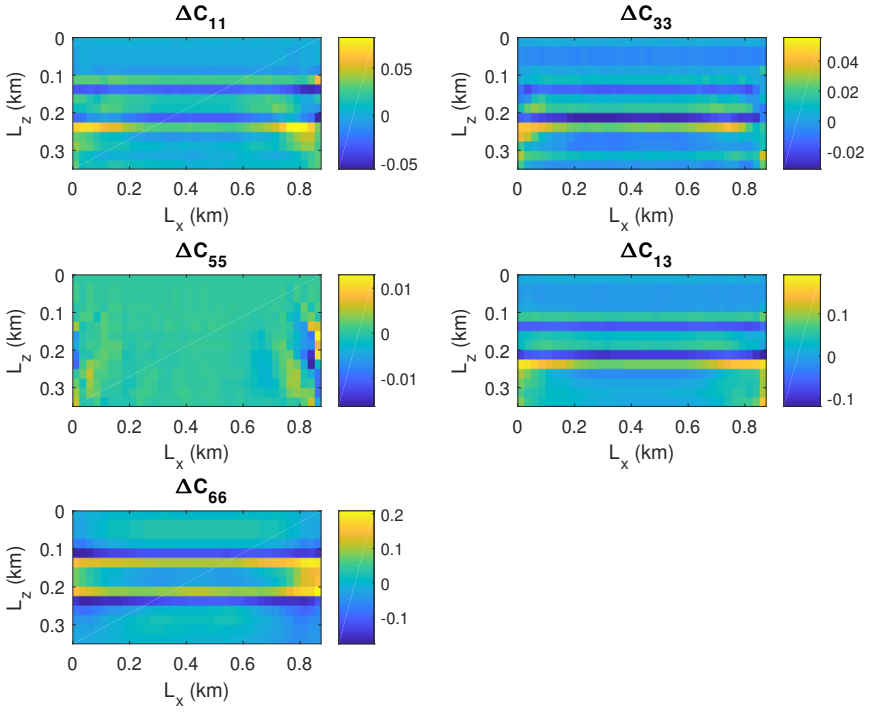

Figure 10: Example 2: The error of maximum a posteriori solution with noisy data with a signal to noise ratio of 4.

–

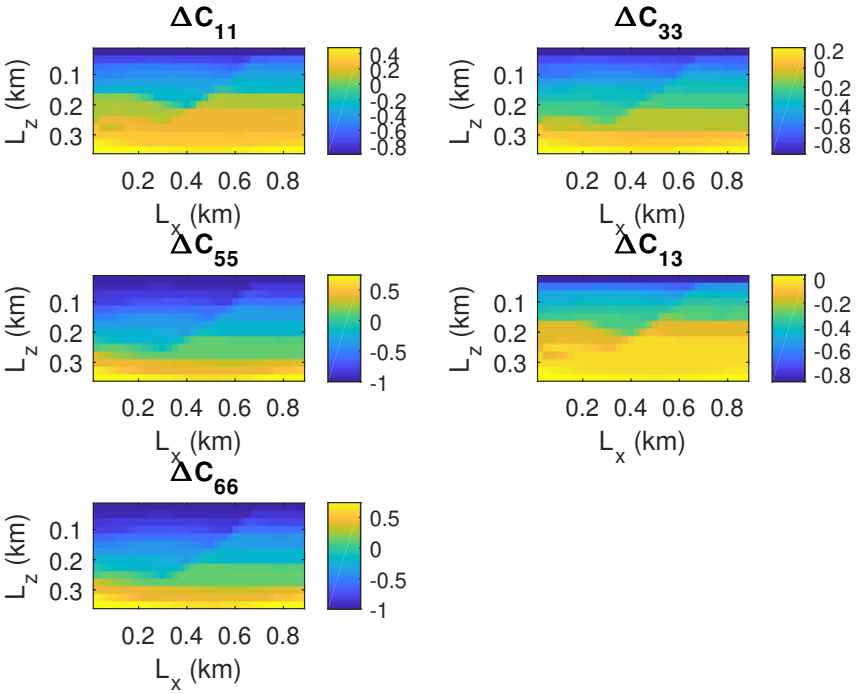

Figure 11: A subset of Hess model.

–

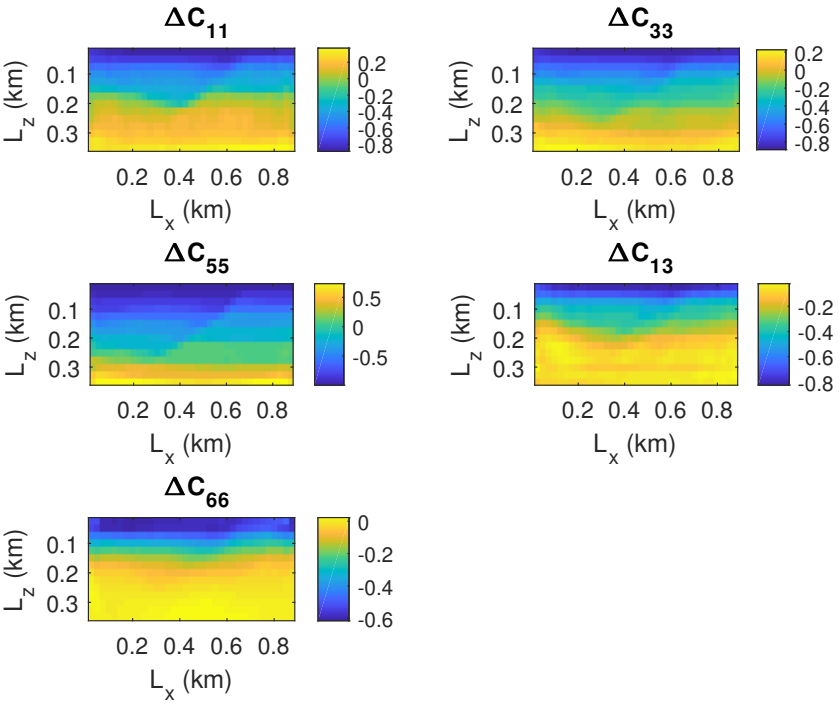

Figure 12: Example 3: The maximum a posteriori solution.

–

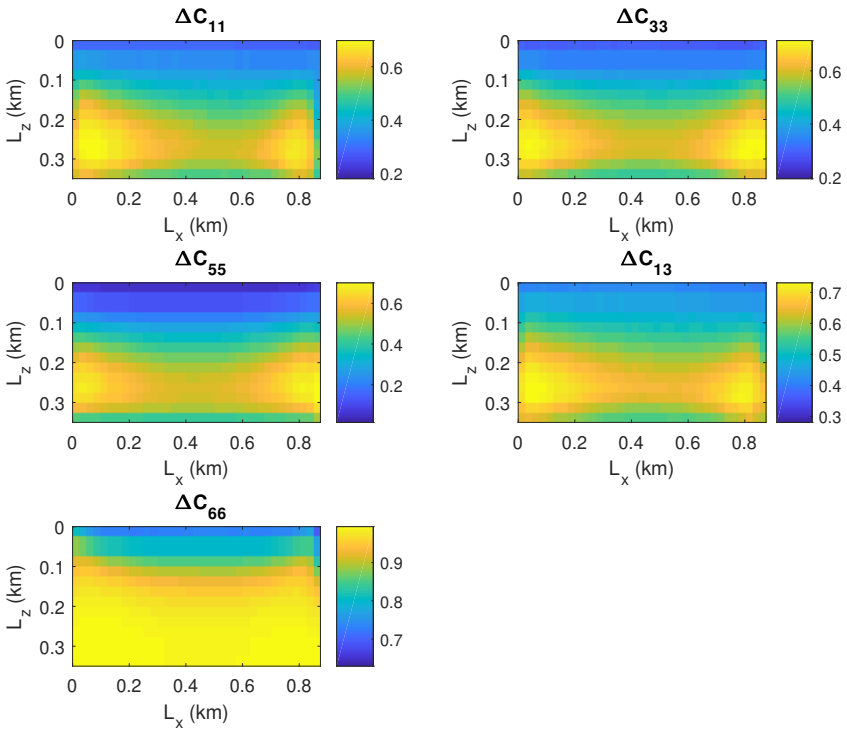

Figure 13: Example 3: The posteriori standard deviation.

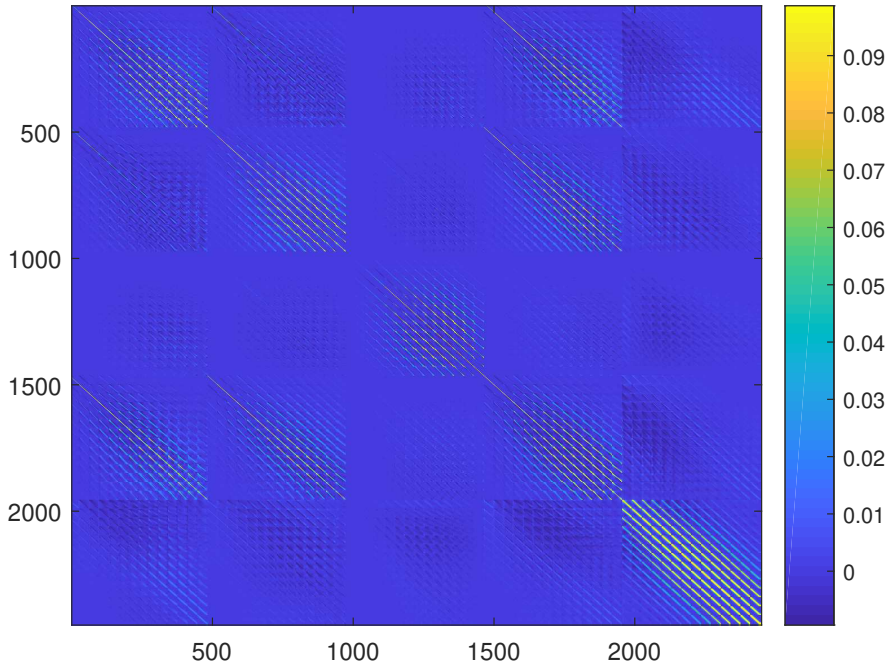

Figure 14: Example 3: The full covariance matrix.

–

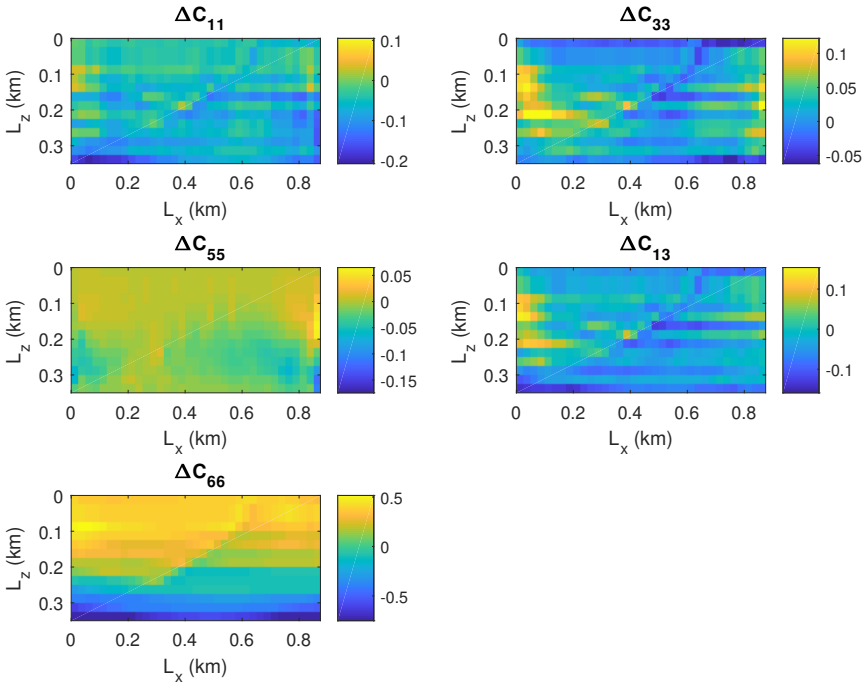

Figure 15: Example 3: The error of maximum a posteriori solution with noisy data with a signal to noise ratio of 4.

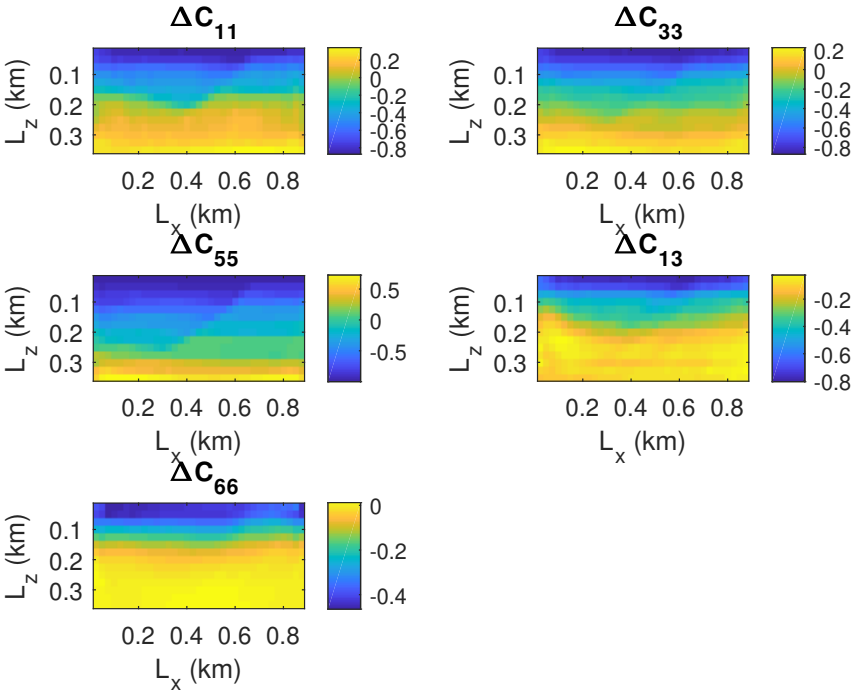

Figure 16: Example 4: The maximum a posteriori solution.

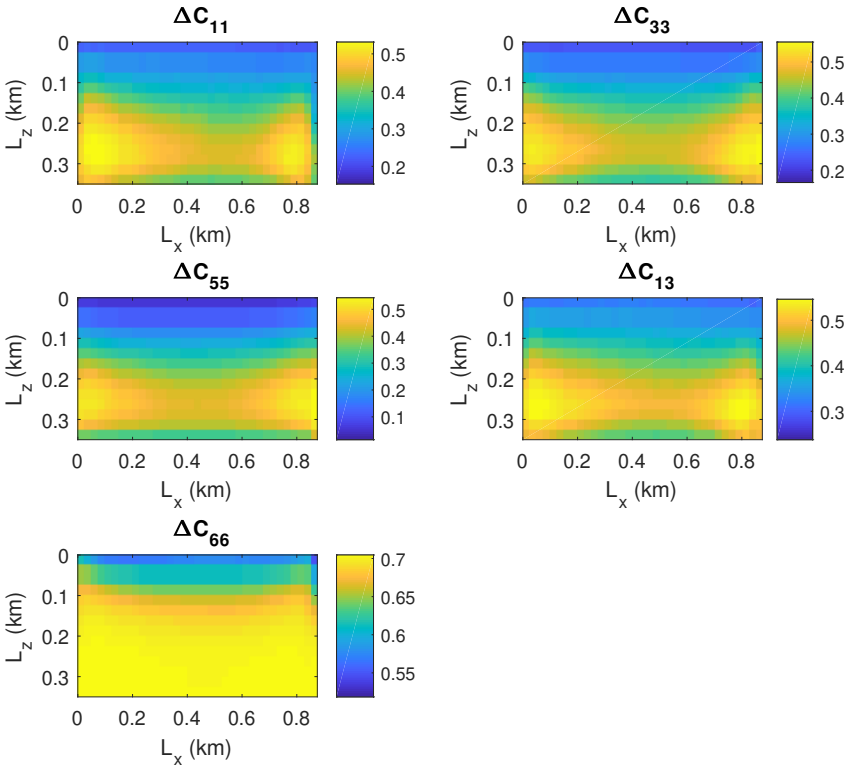

Figure 17: Example 4: The posteriori standard deviation.

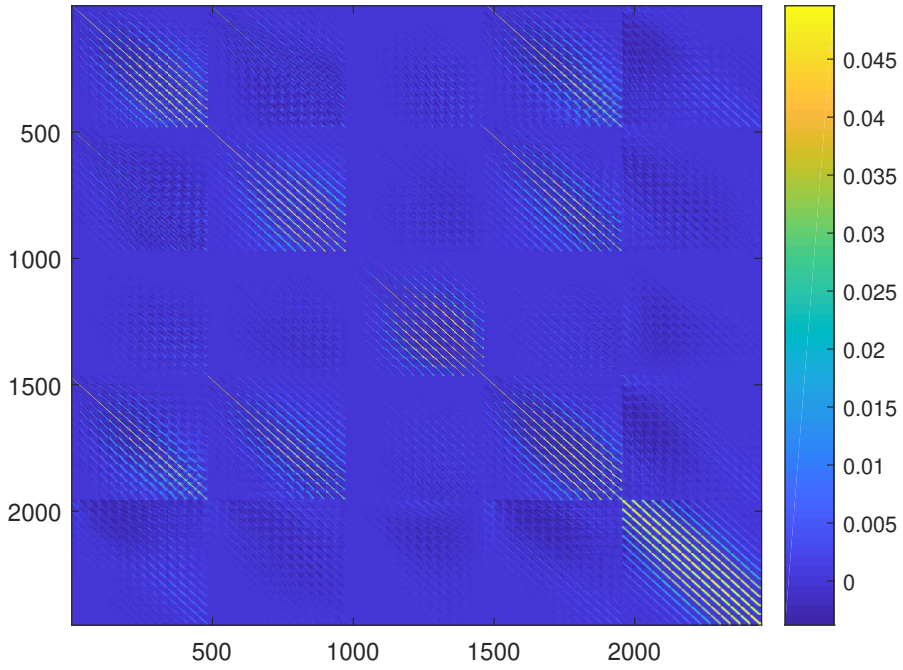

Figure 18: Example 4: The full covariance matrix.

–

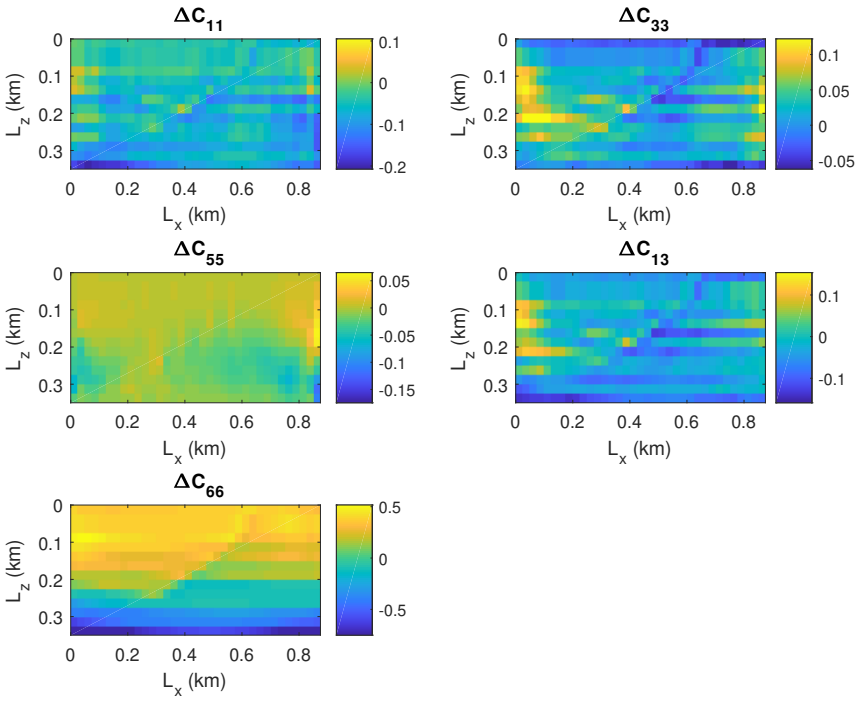

Figure 19: Example 4: The error of maximum a posteriori solution with noisy data with a signal to noise ratio of 4.

–

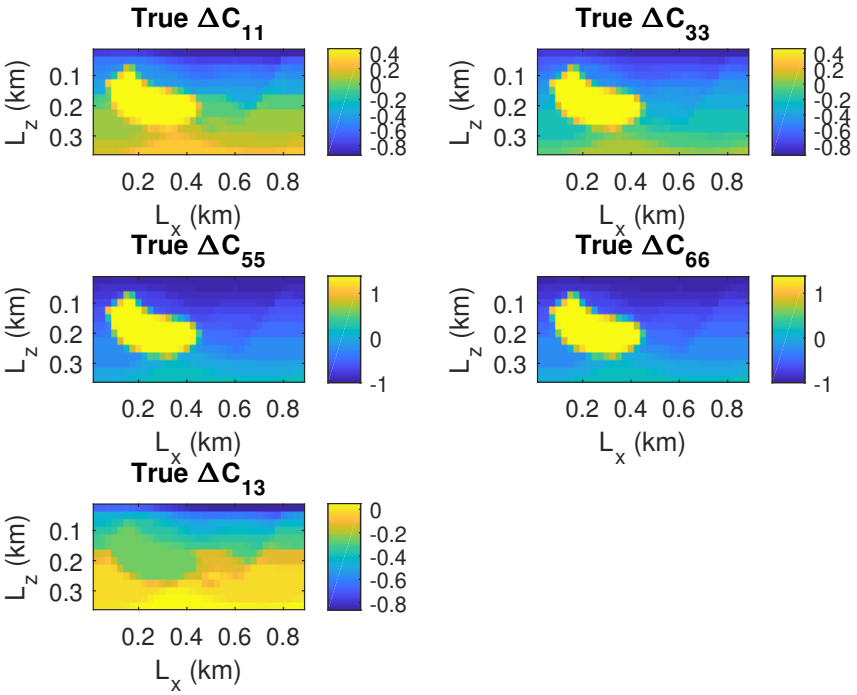

Figure 20: A resampled Hess model.

–

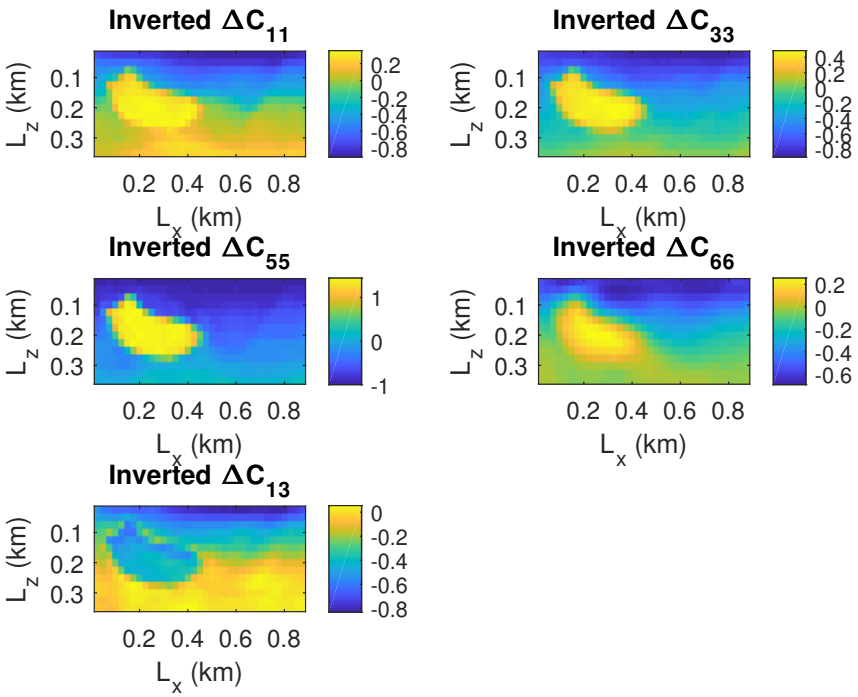

Figure 21: Example 5: The maximum a posteriori solution.

–

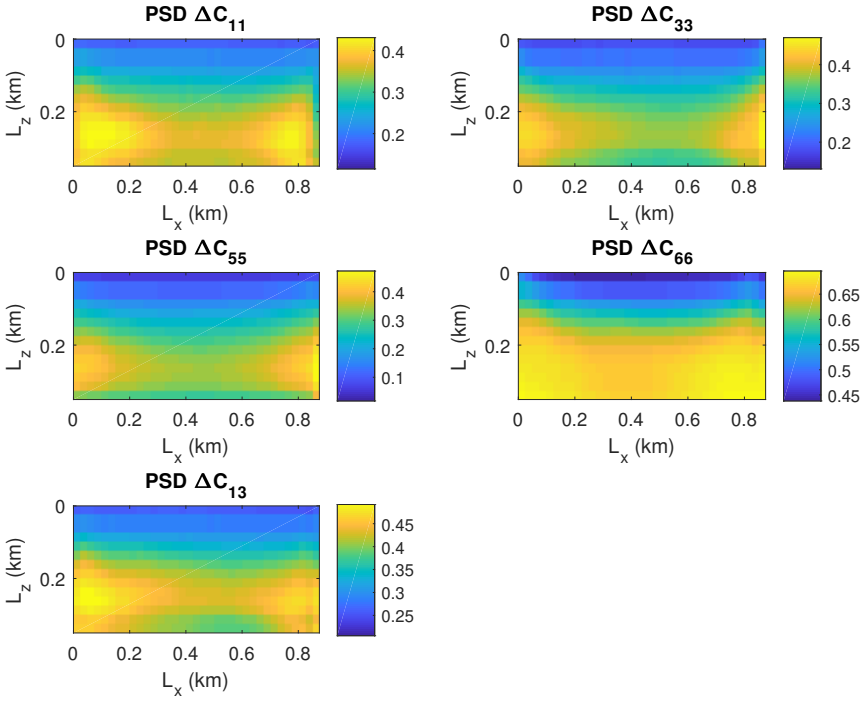

Figure 22: Example 5: The posteriori standard deviation.

–

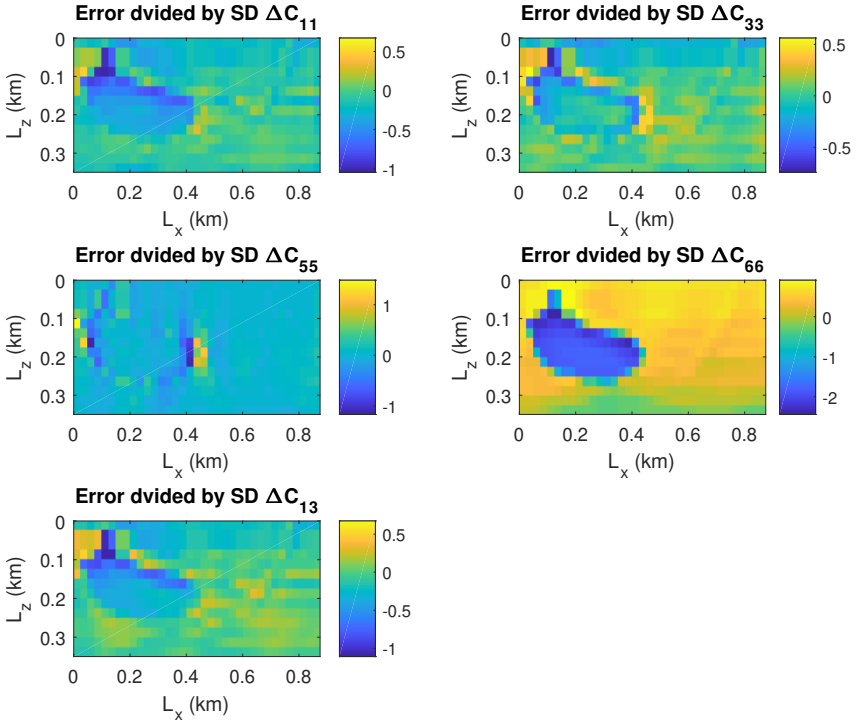

Figure 23: Example 5: The error of maximum a posteriori solution with noisy data with a signal to noise ratio of 4.

–

List of publications

Here, I give a full list of papers I have published during my PhD study, which includes some more work that was outside the scope of the thesis.

Journal publications

Paper 1. **Huang X.**, Jakobsen M., and Wu R. S. (2019). On the applicability of a renormalized Born series for seismic wave modelling in strongly scattering media. *Journal of Geophysics and Engineering*, doi:10.1093/jge/gxz105.

Paper 2. **Huang X.** and Greenhalgh S. (2019). Traveltime approximation for strongly anisotropic media using the homotopy analysis method. *Geophysical Journal International*, 216 (3): 1648-1664.

Paper 3. **Huang X.**, Jakobsen M., Eikrem K. S. and Nævdal G. (2019). Target-oriented inversion of time-lapse seismic waveform data, 2019, *Communication in Computational Physics*, doi: 10.4208/cicp.OA-2018-0143.

Paper 4. **Huang X.**, Eikrem K. S., Jakobsen M., and Nævdal G. (2020). Bayesian seismic full waveform inversion in anisotropic elastic media using an integral equation approach. *Geophysics*, in revision.

Paper 5. **Huang X.**, Sun H., Sun Z. and da Silva N. V. (2020). A complex point-source solution of the acoustic eikonal equation for Gaussian beams in transversely isotropic media. *Geophysics*, in press.

Paper 6. **Huang X.** and Greenhalgh S. (2019). Linearized formulations and approximate solutions for the complex eikonal equation in orthorhombic media and applications of complex seismic traveltime.*Geophysics*, 83(3), C115-C136.

Paper 7. **Huang X.**, Sun J. and Greenhalgh S. (2018). On the solution of the complex eikonal equation in acoustic VTI media: a perturbation plus optimization scheme. *Geophysical Journal International*, 214 (2), 907–932.

Paper 8. **Huang X.** (2018). Extended beam approximation for high-frequency wave propagation. *IEEE Access*, 2018, 6, 37214 – 37224.

Paper 9. **Huang X.** and Sun H. (2018). Numerical modelling of Gaussian beam propagation and diffraction in inhomogeneous media based on the complex eikonal equation. *Acta Geophysica*, 66, 497-508.

Paper 10. Jakobsen M., Wu R. S. and **Huang. X.** (2020). Convergent scattering series solution of the inhomogeneous Helmholtz equation via renormalization group and homotopy continuation approaches. *Journal of Computational Physics*, 109343.

Paper 11. Jakobsen M., **Huang. X.**, Wu R. S. (2020). Homotopy analysis of the Lippmann-Schwinger equation for seismic wavefield modeling in strongly scattering media. *Geophysical Journal International*, Minor Revision.

Paper 12. Hu Y., Wu R. S., Long Y., **Huang. X.**,Yang L. (2020) Instantaneous Phase Encoded Joint Direct Envelope Inversion of Phase and Amplitude in the Time-Frequency Domain, in review.

Paper 13. Yan B., Wang S., Ji Y., Yuan S., **Huang X.**, and da Silva N. V. (2020). Frequency-dependent spherical-wave reflection coefficient inversion in acoustic media: From theory to practice. *Geophysics*, in revision.

Paper 14. Zhang. R., Li T., Deng X. and **Huang X.** (2019). 2D data-space joint inversion of MT, gravity, magnetic, and seismic data with cross-gradient constraints. *Geophysical Prospecting*, doi.org/10.1111/1365-2478.12858.

Conference abstracts

Paper 15. **Huang X.** Jakobsen M. and Wu R. S. (2019). Taming the divergent terms in the scattering series of Born by renormalization. *SEG Technical Program Expanded Abstracts 2019*, pp 5065-5069.

Paper 16. **Huang X.**, Jakobsen M., Eikrem K. S. and Nævdal G. (2018). A target-oriented scheme for efficient inversion of time-lapse seismic waveform data. *SEG Technical Program Expanded Abstracts 2018*, pp. 5352-5356.

Paper 17. Jakobsen M., Wu R. S. and **Huang X.** (2018). Seismic waveform modelling in strongly scattering media using renormalization group theory. *SEG Technical Program Expanded Abstracts 2018*, pp. 5007-5011.

Graphic design: Communication Division, UiB / Print: Skipnes Kommunikasjon AS

uib.no

ISBN: 9788230854198 (print)
9788230867297 (PDF)